Dewetting Dynamics of Heavy Crude Oil: Contributions from Surface and Interfacial Forces

Suparit Tangparitkul

Submitted in accordance with the requirements for the degree of

Doctor of Philosophy

University of Leeds

School of Chemical and Process Engineering

August 2019

The candidate confirms that the work submitted is his own, except where work which has formed part of jointly-authored publications has been included. The contribution of the candidate and the other authors to this work has been explicitly indicated below. The candidate confirms that appropriate credit has been given within the thesis where reference has been made to the work of others.

Theory background on oil droplet dewetting and literature review on enhanced oil recovery fluids is presented in Chapter 2 and the related research to oil droplet dewetting dynamics at elevated temperatures and surfactant addition is presented in Chapter 4 which has been published in Paper 1.

Published Journal Papers

1. Tangparitkul, S.; Charpentier, T. V. J.; Pradilla, D.; Harbottle, D. Interfacial and Colloidal Forces Governing Oil Droplet Displacement: Implications for Enhanced Oil Recovery. *Colloids Interfaces 2018, 2 (3), 30.*

2. James, E.; Tangparitkul, S.; Brooker, A.; Amador, C.; Graydon, A.; Vaccaro, M.; Cayre, O. J.; Hunter, T. N.; Harbottle, D. Accelerated spreading of inviscid droplets prompted by the yielding of strongly elastic interfacial films. *Colloids and Surfaces A: Physicochemical and Engineering Aspects 2018, 554, 326 – 333.*

3. Zhang, H.; Tangparitkul, S.; Hendry, B.; Harper, J.; Kim, Y. K.; Hunter, T. N.; Lee, J. W.; Harbottle, D. Selective separation of cesium contaminated clays from pristine clays by flotation. *Chemical Engineering Journal 2019, 355, 797 – 804.*

Conference Presentations

1. Tangparitkul, S.; Pradilla, D.; Cayre, O. J.; Wen, D.; Charpentier, T. V. J.; Harbottle, D. Insights into Thermal EOR: the dewetting dynamics of heavy oil. *UK Colloids 2017: An International Colloids and Interface Science Symposium. 10 – 12 July 2017, Manchester, UK.*

2. Tangparitkul, S.; Pradilla, D.; Charpentier, T. V. J.; Harbottle, D. Droplet Dynamics in Low-Salinity Enhanced Oil Recovery. *Special Interest Group on Drop Dynamics Conference. 16 – 17 April 2019, Leeds, UK.*

3. Tangparitkul, S.; Niu, Z.; Pradilla, D.; Charpentier, T. V. J.; Xu, Z.; Harbottle, D. Oil Droplet Displacement in Low-salinity Environments: Effect of Temperature and Pressure. *The 20th International Conference on Petroleum Phase Behavior & Fouling (PetroPhase 2019). 2 – 6 June 2019, Kanazawa, Japan.*

The candidate performed all experimental work and prepared the first draft of Paper 1. Experimental training on the high-pressure tensiometer and atomic force microscope was provided by Zhen Niu (University of Alberta) and Dr Chris S. Hodges (University of Leeds), respectively. Co-authors, Dr Thibaut V. J. Charpentier (University of Leeds), Dr Diego Pradilla (Universidad de Los Andes), Prof. Zhenghe Xu (University of Alberta) and Associate Prof. David Harbottle (University of Leeds), supervised the research and provided guidance to improve the quality of the manuscript.

Acknowledgements

A very special thanks is given to my supervisors who have guided and supported me throughout my study. I would like to thank Associate Prof. David Harbottle for his critical discussions and encouragement on research of shared our interest. He has provided me with opportunities to visit two more continents concluding my academic pilgrimage around the world. He hammered my work into shape and challenged me, and often provided another perspective to the work. I learned a lot from him especially how he runs his group. I would like to thank Dr Thibaut Charpentier for his kindly support and discussions. We normally have a meeting in The Library pub where I probably still owe him a few pints.

During my visit to the University of Alberta, I would like to thank Professor Zhenghe Xu who gave me a meeting time even though he has a busy schedule to discuss my research and accommodated me with all nice people in his group and world-class facilities. In that extremely cold weather, their extremely warm kindness allowed me to finish my work under extremely hot and extremely pressurised conditions.

I thank all previous and current members of the Colloids and Polymer Engineering Research Group who guided me in the lab and discussed my research in the group meetings and the following pub chats. EJ who trained me on the tensiometer, my main PhD equipment. And a big thank you to all especially Olivier, Tim, Nick, Chris, Huagui, James, Kai, Calum, Andy, Shafeeq, Mo, MY, Assim, Ghinwa, Laura, Tom, Dewi, David, Stefanos and Mohammed.

I would like to thank my home affiliation Chiang Mai University for granting me the scholarship the White-Elephant Academics Scheme since my masters. Special thanks has to be given to all my superiors and senior colleagues who have always supported me. The Dean, Assistant Prof. Nat Vorayos, who sorted out the funding issue at the beginning of the PhD and whom I am determined to thank by finishing my PhD before the end of his second term as Dean. The Head of Department, Associate Prof. Pirat Jaroonpattanapong, who has kindly welcomed me to his department and allowed me to work on my own interests. The Associate Dean, Associate Prof. Juggapong Natwichai, who advised me from his experiences in Australia and visited me in England. Associate Dean and my mentor Assistant Prof. Cheowchan Leelasukseree, who offered me this whole opportunity and successfully got me in the second trial while I was in Melbourne busily finding my life. He has given me two origami 50-Australian-dollar-note shirts when I left to Adelaide for my masters.

Also, a massive thanks goes to my family. Especially my father who let me rebel and find my own path but anyway he loaned me money to use in advance prior to the scholarship being granted. I might now pretend to forget and not return it. Thank you to all my Thai friends during my time in Leeds: Pom, Ohm, Card, Kwang and Gang. And Alex whom I met in Adelaide and we are here now in Leeds.

Lastly let me say with Rupert Brooke: “Now, God be thanked Who has matched us with His hour...”

Abstract

The research considers the dewetting dynamics of heavy crude oil on solid substrates in the presence of chemical additives and at elevated temperatures and pressures. Increasing the temperature from 40 to 80 °C was found to increase the initial receding rate of an oil droplet on substrate from 0.07 to 3.73 °/s, a consequence of the reduced oil viscosity. Higher temperatures also induced release of natural surfactants and thus decreased the oil-water interfacial tension (σ_{OW}), promoting increased oil droplet dewetting (equilibrium contact angle (θ) decreased from 63.7° to 51.3°), with the effect described by the Young's equation. At high pressure (200 bar at 140 °C), asphaltenes partition less at the oil-water interface leading to slightly higher σ_{OW} (14.4 mN/m at 10 bar to 17.6 mN/m at 200 bar). Increase in σ_{OW} led to less oil dewetting as the θ increased from 17.9° to 23.1°. Adding a surfactant demonstrated the benefit of reducing σ_{OW} and increasing oil-substrate electrostatic repulsion. At high surfactant concentration the oil droplet attained low θ, and eventually pinched-off from the surface when the ultra-low oil-surface adhesion was exceeded by droplet buoyancy.

Oil droplet dewetting was studied in brine fluids at 60 °C where the addition of salt was shown to change σ_{OW} depending on the synergistic interfacial adsorption of salt ions and native surface-active species (*i.e.* naphthenic acids and asphaltenes). However, the oil droplet contact angles in brines were more influenced by the disjoining pressure and not σ_{OW} as described by the Young's equation. Increased oil droplet dewetting (θ: 43.2° in water $\rightarrow$ 18.1°) was observed in low-salinity NaCl fluid (2,000 ppm), with hydration forces strongly influencing repulsion between the oil droplet and substrate. In contrast, attractive hydrophobic forces, as measured in $CaCl_2$ brines, acting between the

oil droplet and hydrophobised substrate (*via* divalent cation bridging), reduced the oil droplet dewetting rate and increased θ (≥ 27.2° at 60 °C). Initial droplet receding rates were increased by a strong oil-substrate repulsion and low steady-state θ, without the influence of changing σ_{OW}.

Surface-active nanoparticles, poly(*N*-isopropylacrylamide) (PNIPAM), were synthesised to study their effect on lowering σ_{OW} and enhancing the dewetting dynamics in the presence of surfactant. Blends of PNIPAM and SDS (1:1 mass ratio) were considered at different bulk concentrations. At low concentration (5×10^{-4} wt%), SDS interfacial adsorption was greater than PNIPAM with the dominance reversed at high concentration (5×10^{-3} wt%). The difference in interfacial activity was shown to influence the oil dewetting process, but is not fully described by the Young's equation. Increased oil dewetting by nanoparticles was shown at low concentration, with the PNIPAM and SDS blend displacing the oil droplet at 5.66 °/s and attaining low θ (37.0°), while σ_{OW} remained relatively high (25.3 mN/m). This was due to PNIPAM particles remaining in the bulk fluid and self-assembling in the oil-water-substrate "wedge", thus inducing a structural disjoining pressure, which promoted oil dewetting. In the presence of NaCl (2,000 ppm), contributions from PNIPAM induced further structural forces that led to a gradual liberation of oil from the substrate, even though the droplet buoyant force was less than the oil-substrate adhesion force.

Table of Contents

List of Figures

List of Tables

Nomenclature

Latin

a	Particle radius or contact radius, nm
A	Interfacial area, m^2 *or*
	Surface-active contribution, %
A_f	Projected area of droplet when crumpling is first observed, mm^2
A_i	Projected area of initial droplet before volume contraction, mm^2
A_{SWB}	Hamaker constant, J
C_0	Material bulk concentration, wt%
C_s	Concentration of surface-active species, mol/L
CR	Crumpling ratio
d	Nanoparticle diameter, nm
D	Droplet width perpendicular to droplet moving direction, mm
D_{Bulk}	Bulk diffusion coefficient, m^2/s
$D_{Interface}$	Diffusion coefficient at the interface, mol^4·m^{-4}·s^{-1}
e	Elementary charge, C
E	Particle detachment energy, J
E'	Electrical field strength, N/C
f_i	Fractional area of the surface
f_R	Retention force, μN
F	Force, μN
F_A	Adhesion force, μN
F_R	Receding force, μN
g	Acceleration due to gravity, m/s^2
G	Interfacial energy, J
h	Water film thickness, nm
h_{cr}	Critical film thickness, nm
h_e	Equilibrium film thickness, nm
k	Slope of σ_t versus $\sqrt{t}$ *or*
	Numerical constant of droplet shape
k_B	Boltzmann constant, m^2·kg·s^{-2}·K^{-1}

K	Elastic modulus, GPa *or*
	Adsorption constant
L	Characteristic length of the oil droplet, mm
L_S	Slip length, mm
m	Dimensionless pore shape multiplier
M	Instrument (density meter) constant
N	Instrument (density meter) constant
P	Osmotic pressure, Pa
P_c	Capillary pressure, Pa
r	Radius of oil-solid surface contact area, nm
r_m	Minimum radius of the hole, nm
r_p	Pore radius, µm
R	Universal gas constant, $\mathrm{J \cdot K^{-1} \cdot mol^{-1}}$ *or*
	Colloidal (oil-coated) sphere radius, µm
R_0	Drop radius of curvature at the apex, m
R_1 or R_2	Drop curvature, m
R'	Ratio of the true area of the solid to its planar projection
R_a	Arithmetical mean deviation, nm
R_h	Particle hydrodynamic radius, nm
S	Spreading coefficient, mN/m
t	Time, s
t_e	Equilibrium time, s
t_i	Initial time, s
T	Absolute temperature, K
U	Three-phase contact line velocity, mm/s
v	Dispersed colloidal (electrophoretic) velocity, m/s
V	Droplet volume, µL
W_A	Work of adhesion, J

Greek

β	Shape factor
Γ	Surface excess, $\mathrm{mol/m^2}$
Γ_s	Surface excess of surface-active species, $\mathrm{mol/m^2}$
Γ_t	Interfacial concentration of material at time t, $\mathrm{mol/m^2}$
δ	Fitting parameter for structural disjoining pressure

Δ	Least-squares difference
$\Delta\rho$	Density difference, kg/m^3
$\Delta\sigma$	Decrease in interfacial tension or surface pressure, mN/m
ε	Dielectric permittivity of vacuum
ε_0	Relative dielectric permittivity of water
ζ	Coefficient of contact-line friction, Pa·s
θ	Contact angle *or* equilibrium contact angle *or* steady-state contact angle, °
θ^0	Contact angle in pure water (no brine), °
θ_a	Advancing contact angle, °
θ_{CB}	Cassie-Baxter contact angle, °
θ_d	Dynamic contact angle, °
θ_{exp}	Experimental dynamic contact angle, °
θ_i	Initial contact angle, °
θ_{IFT}	Calculated contact angle that solely depends on the σ_{OW}^{Brine}, °
θ_m	Theoretical dynamic contact angle, °
θ_r	Receding contact angle, °
θ_W	Wenzel contact angle, °
κ	Debye length, nm *or* Fitting parameter for structural disjoining pressure
κ^0	Frequency of adsorption/desorption events, Hz
λ	Distance between adsorption sites, nm
μ	Viscosity, mPa·s
μ_o	Oil viscosity, mPa·s
Π	Disjoining pressure, Pa
Π_0	Fitting parameter for structural disjoining pressure
Π_1	Fitting parameter for structural disjoining pressure
Π_{el}	Electrostatic disjoining pressure, Pa
Π_H	Hydration disjoining pressure, Pa
Π_{st}	Structural disjoining pressure, Pa
Π_{vdW}	van der Waals disjoining pressure, Pa
ρ	Density, kg/m^3
σ	Interfacial tension, mN/m
σ_0	Interfacial tension of pure system (no surfactant), mN/m
σ_{OS}	Oil-solid interfacial tension, mN/m
σ_{OW}	Oil-water or oil-brine interfacial tension, mN/m

σ_{OW}^{0}	Oil-water interfacial tension in pure water (no brine), mN/m
σ_{OW}^{Brine}	Oil-brine interfacial tension, mN/m
σ_{SW}	Solid-water interfacial tension, mN/m
σ_{t}	Oil-water interfacial tension at time t, mN/m
τ	Oscillation period, s
φ	Tangent angle, °
$\emptyset_2$	Fitting parameter for structural disjoining pressure
ψ	Zeta potential, mV
ω	Fitting parameter for structural disjoining pressure

Abbreviations

ΔBS: backscattered signal

AFM: atomic force microscopy

CMC: critical micelle concentration

DLVO: Derjaguin-Landau-Verwey-Overbeek Theory

EOR: Enhanced Oil Recovery

FT-IR: Fourier transform infrared

H/C: hydrogen to carbon (H/C) ratio

HD: Hydrodynamic theory

HPHT: high pressure and high temperature

LCST: lower critical solution temperature

MK: Molecular-kinetic theory

NMR: nuclear magnetic resonance

PNIPAM: poly(*N*-isopropylacrylamide)

QCM: quartz crystal microbalance

RMS: root mean square

SARA: saturate, aromatic, resin and asphaltene analysis

SDS: sodium dodecyl sulfate

SEM: scanning electron microscope

SEM-EDX: scanning electron microscopy with energy dispersive X-ray spectroscopy

TAN: total acid number

Chapter 1

Introduction

This chapter introduces droplet dewetting dynamics in the context of oil recovery, and considers the importance of oil-water interfacial tension and contact angle. Subsequently the research novelty, research aims and objectives are described. An outline of the thesis Chapters is provided.

1.1 Droplet in Oil Recovery

Oil recovery where the oil phase is displaced by an immiscible wetting phase (*i.e.* water) is governed by a number of surface and interfacial phenomena. Following natural drive in primary oil recovery, if the oil-water interfacial tension is sufficiently low and decreases the capillary pressure, oil droplets can form. This potentially leads to the formation of an oil-in-water emulsion which is then recovered.[1] The oil-rock interaction influences the ease by which oil droplets detach from the rock substrate.[2] **Figure 1.1** shows oil droplets and subsequent recovery from inside the porous media of reservoir rock.

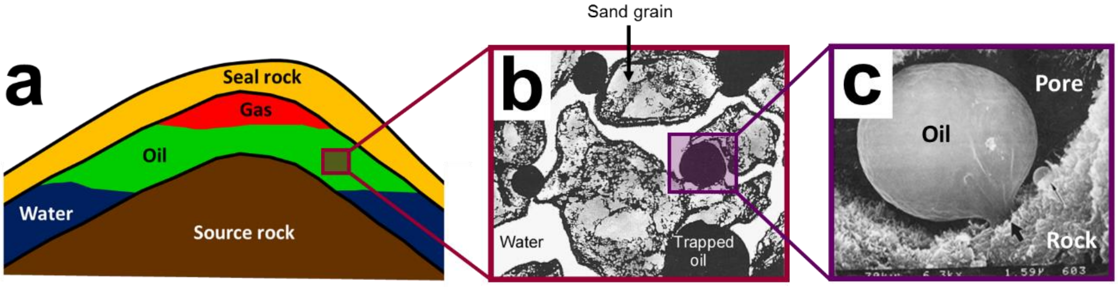

Figure 1.1. Schematic of a petroleum reservoir (a) with macroscopic view of oil droplets in porous media (b) and microscopic view showing spherical oil droplets detaching from the rock substrate (c). Images (b) and (c) were adapted from Török *et al*.[3] and O'Brien *et al*.[4], respectively.

To increase oil production, Enhanced Oil Recovery (EOR) is frequently used following water-flooding or after depletion of natural drive.[5, 6] Sophisticated EOR processes involve a modification of the injecting fluid to detach or repel the oil droplet from the rock surface (*e.g.* surfactant injection), and increase the sweep or 'flood' of residual oil in the reservoir (*e.g.* polymer flooding).[7, 8] The former is of particular interest and relies on oil dewetting, which is governed by wettability and the oil-water interfacial tension.[5] As the oil droplet-substrate contact area increases, so does the droplet-substrate adhesion force, hence a greater 'lifting force' is needed to liberate the oil droplet from the substrate.[2] To minimise the droplet-substrate adhesion force, the contact area can be reduced by decreasing the oil-water interfacial tension[9, 10] and decreasing the oil droplet contact angle.

It is worth noting that in oil recovery the dewetting process is one contributing factor to increase oil recovered. While not necessarily important in primary recovery, the dewetting process becomes more relevant in secondary and tertiary production. Oil dewetting is a governing mechanism in the recovery of oil from strongly water-wet or neutrally-wet environments, *e.g.* sandstone and oil-sands, while it is less likely to contribute to oil recovery from strongly oil-wet environments, where the majority of oil is recovered *via* enhanced sweep efficacy.

1.2 Research Novelty and Opportunities

Injection of additives (*e.g.* surfactants) in the flood water has been shown to promote oil dewetting. Oil droplet dewetting can be quantified by the contact angle (substrate-water-oil) and is associated with the balance of interfacial energies as described by the Young's equation.[9] However, it has been shown that some EOR fluids induce other effects that lead to greater oil dewetting which is not simply described by the Young's equation alone.[11, 12] Hence, greater understanding of these effects is needed *via* a systematic study of interfacial and colloidal forces. For example, nanofluids have shown additional affinity at the three-phase contact line where nanoparticles accumulate to induce a structural disjoining pressure.[11] New mechanisms for oil droplet displacement by introducing additional colloidal species is leading to greater recovery of oil from depleted reservoirs, and as such, a greater understanding of these resulting forces is needed to optimise flooding strategies. The contribution of these forces can be highlighted when studying the dynamics of oil dewetting. However, most studies only consider the steady-state condition, and thus a mechanistic understanding of the forces governing oil droplet dewetting has not been established.[13, 14, 15, 16]

It is known that the petroleum sub-surface environment at high temperatures and pressures is not necessarily represented by studying phenomena at ambient conditions.[17] This leads to challenges when predicting behaviour under such harsh conditions. For example, low-salinity water flooding has shown promise to increase oil recovered. Yet the fundamental understanding of this process and the interfacial/surface forces governing droplet behaviour is limited to only a few studies at ambient conditions. In order to optimise the low-salinity flooding, research is needed under more relevant conditions.

In addition, the scientific community is increasingly interested in nanofluids for use as EOR fluids.[18] However, nanoparticles (*e.g.* SiO_2) typically have negligible surface activity and thus are not effective at lowering the apparent oil-water interfacial tension.[19] In order for EOR fluids to function, nanoparticles must be blended with a surfactant. Therefore, there is an opportunity to consider surface-active nanoparticles (*e.g.* *N*-isopropylacrylamide nanogel) and their impact to recede oil in the absence and presence of surfactants.[20, 21]

1.3 Research Aim and Objectives

Aim: To elucidate the governing role of surface and interfacial forces in oil droplet displacement, and optimise the water chemistry to promote rapid oil droplet dewetting as well as minimising oil droplet-surface contact area. To achieve this, the following objectives were defined.

Objectives:

1. Determine the dominant parameters that govern oil droplet dewetting on model substrates at ambient and reservoir-like conditions (*i.e.* high pressure and high temperature), and assess the variation in surface and interfacial properties at extreme conditions.

2. Elucidate the critical mechanism for brine-enhanced oil droplet dewetting. Brine solutions are considered for improved oil recovery, yet the fundamental interfacial and

surface forces governing this enhancement, and how those forces correlate to the optimum brine concentration is not yet understood.

3. Fabricate nanoparticles that exhibit strong interfacial activity for application to improve oil recovery. Nanofluids have shown great promise in enhancing oil droplet dewetting, yet the fluids are often a complex mix of nanoparticles and surfactants. The added performance is achieved through the synergistic activity of both components, which can be simplified by using strongly surface-active nanoparticles.

1.4 Thesis Outline

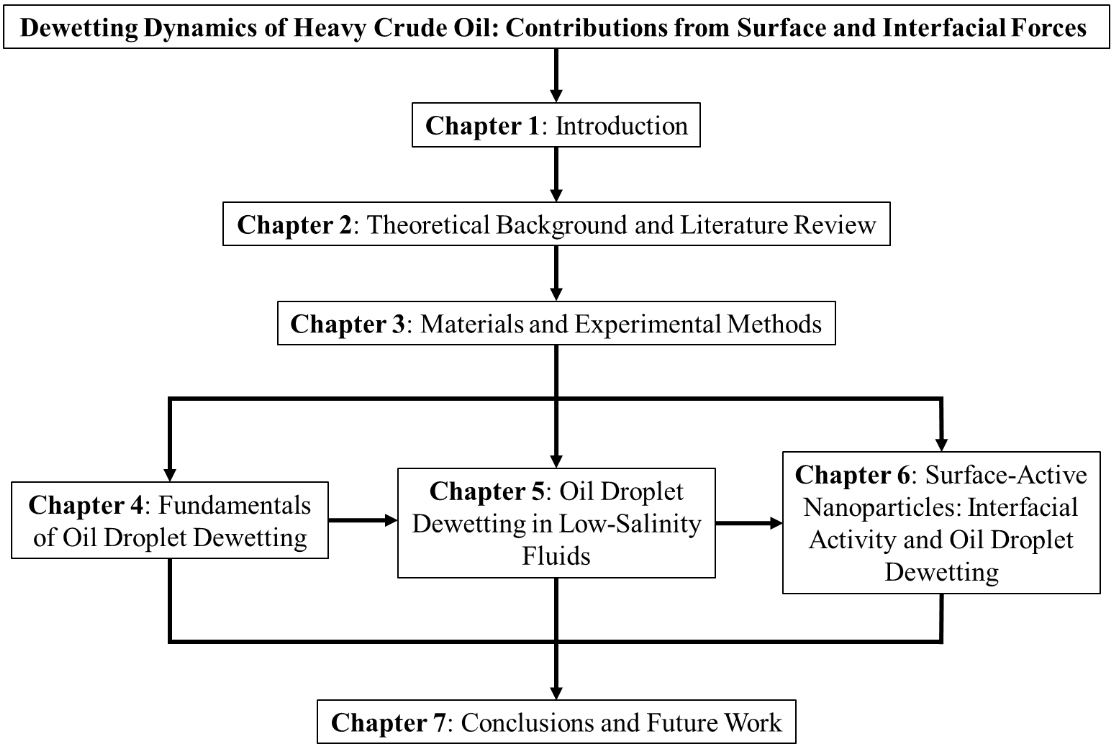

Figure 1.2. Structure of the PhD thesis.

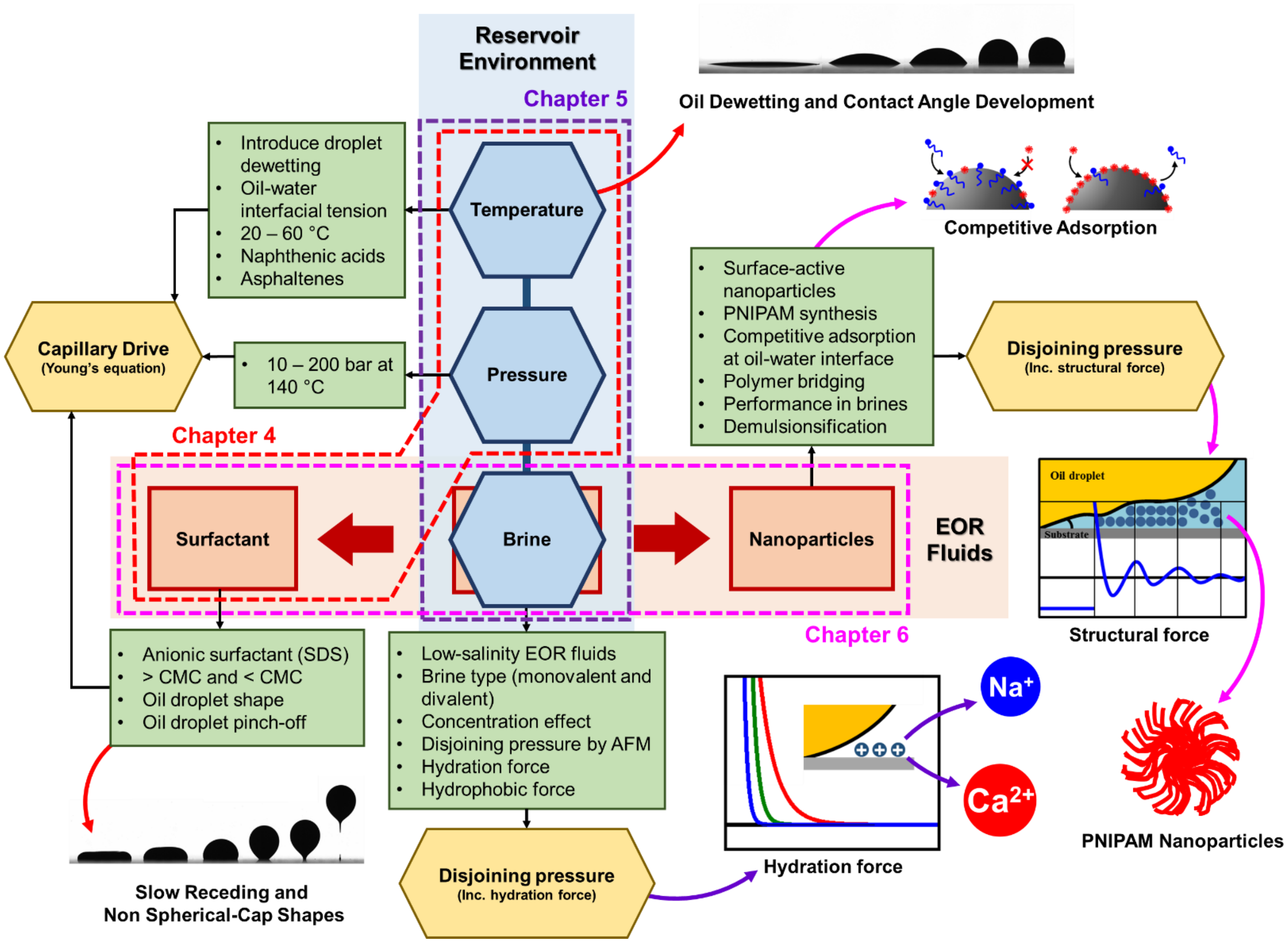

Figure 1.3. Pictorial diagram of the research undertaken and integration of research findings to meet the research aim.

A flow chart outlining the thesis structure is shown in **Figure 1.2** with Chapters 4 – 6 presenting the main contributing result chapters that are schematically illustrated in **Figure 1.3**. Chapter 2 summarises oil film and droplet theory, along with oil film recession including a review of oil displacement in EOR fluids. Chapter 3 describes the materials and experimental techniques used throughout the study.

In Chapter 4, the dewetting dynamics of heavy crude oil films coated on model glass substrates were studied using the tensiometry technique, with oil film dewetting promoted by carefully flooding the oil-coated substrate with water. The effect of temperature was studied over the range 40 – 80 °C. The dynamic contact angles were measured and fitted by two theoretical models, namely hydrodynamic and molecular-kinetic models, to better understand parameters governing oil droplet dewetting. The contribution of interfacial tensions to the equilibrium contact angle, as described by the Young's equation, were addressed and the influence of high temperature (≤ 140 °C) and high pressure (≤ 200 bar) considered, with pressure effects shown to be minimal but temperature effects more significantly influencing the oil-water interfacial tension and substrate wettability. Oil-water interfacial tension was decreased and oil droplet surface charge increased when surfactant (sodium dodecyl sulfate) was added to the water phase, leading to increased oil dewetting. At surfactant concentration > CMC, the ultra-low interfacial tension and continual reduction in oil-substrate contact led to eventual droplet pinch-off when the buoyant force exceeded the adhesion force. This chapter provides a fundamental understanding of oil droplet dewetting dynamics and the relevant interfacial properties that are considered in more detail in Chapters 5 and 6.

In Chapter 5, heavy crude oil droplet dewetting was studied in brine solutions of increasing concentration from 2,000 to 60,000 ppm (also 0 ppm in the absence of brine) to elucidate the low-salinity mechanism for EOR. Two brine types were considered;

monovalent (NaCl) and divalent ($CaCl_2$). The oil-brine interfacial tension showed a negligible effect on oil droplet dewetting, indicating the weak influence of interfacial tensions (Young’s equation). However, the substrate-water-oil disjoining pressure as measured by atomic force microscopy (AFM) was shown to significantly govern oil droplet dewetting dynamics in the presence of brine solutions. The influence of high pressure and high temperature was also studied and clearly showed an effect when studying oil droplet dewetting dynamics at more relevant (reservoir-like) conditions.

Chapter 6 describes the effect of surface-active nanoparticles, using Poly(*N*-isopropylacrylamide), on the displacement of a heavy crude oil droplet on hydrophilic smooth surfaces. The competitive adsorption between the nanoparticle and surfactant was studied at the oil-water interface and showed two-step adsorption, with the PNIPAM particles increasingly prevalent at the oil-water interface with increasing total bulk component concentration. Oil droplet dewetting was studied as a function of the total component concentration. The mechanism for oil dewetting by nanoparticles was described based on the structural disjoining pressure. The optimal brine concentration as elucidated in Chapter 5 was also considered in the presence of PNIPAM nanoparticles to examine the combined contribution from structural and hydration forces on oil droplet dewetting.

Chapter 7 provides a summary of the research conclusions and future work. The research was aimed at promoting rapid oil droplet dewetting and minimising the oil droplet-surface contact area (as inferred from the oil droplet contact angle). Research findings are summarised.

Chapter 2

Theoretical Background and Literature Review

2.1 Synopsis

This chapter describes the interfacial and colloidal forces governing oil film displacement from solid surfaces. Direct contact of oil with the reservoir rock transforms the solid surface from a water-wet to neutrally-wet and oil-wet as a result of the deposition of polar components of crude oil, with lower oil recovery from oil-wet reservoirs. To enhance oil recovery, chemicals can be engineered and added to the injection water to modify the oil-water interfacial tension and solid-oil-water contact angle. In the presence of certain surfactants and nanoparticles, a ruptured oil film will dewet to a new equilibrium contact angle, reducing the work of adhesion to detach an oil droplet from the solid surface. Similar oil dewetting enhancement is also expected from low-salinity water injection. Dynamics of contact-line displacement are reviewed and the effect of surface-active agents on enhancing oil displacement discussed. The chapter is intended to provide an overview of the interfacial and colloidal forces controlling the process of oil film displacement and droplet detachment for enhanced oil recovery. A comprehensive summary of chemicals tested at various stages of development is provided.

2.2 Reservoir wettability and contact angle

Before describing the underlying principles that govern each step, it is worth considering the likely interaction between the oil and solid surface, *i.e.* the reservoir wettability. The reservoir environment can be characterised as either: (i) water-wet (water droplet contact angle, θ = 0° to ~ 70°), (ii) oil-wet (θ = ~110° to ~ 180°) and (iii) neutrally-wet (θ = ~70° to ~ 110°) exhibiting a similar affinity to both water and oil.[22, 23, 24] While it is understood that most reservoir environments were initially water-wet, the reservoir rock can evolve to become more oil-wet due to the deposition/adsorption of several indigenous organic polar species (asphaltenes, resins and naphthenic acids) present in crude oil.[25, 26, 27, 28] For oil-wet reservoirs, oil recovery is poor due to no capillary imbibition. Hence, one of the criteria for successful EOR is to enhance capillary imbibition and alter the wettability change by using chemical additives, although complete reversal to strongly water-wet surfaces might be not favoured for EOR with the pore occupancy and permeability need to be accounted for.[29, 30, 31, 32]

2.2.1 Oil film stability

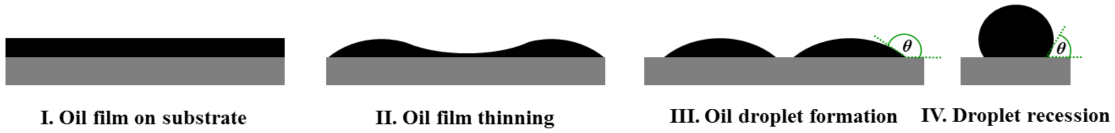

Figure 2.1. Schematic showing the four stages of oil film dewetting from a uniform thick film (I) to film thinning (II), formation of discrete oil patches (III), and recession of oil patches to form oil droplets at the new equilibrium wetting condition (IV).

Oil recovery from the reservoir rock occurs by either displacement from squeezing or oil film thinning and rupture to form discrete oil droplets (**Figure 2.1**) that are removed by shear; the latter is of interest here.

The long-time transformation from water-wet to an oil-wet reservoir occurs following the collapse of a thin aqueous layer separating the solid surface and oil layer. The stability of the thin water layer is attributed to the disjoining pressure which accounts for surface forces between the solid-water and water-oil interfaces. According to the classical DLVO theory, the total disjoining pressure (Π) includes contributions from electrostatic (Π_{el}) and van der Waals (Π_{vdW}) forces[33]

$$\Pi = \Pi_{el} + \Pi_{vdW} \tag{2.1}$$

with the thin water layer collapsing when Π is negative. The disjoining pressure as a function of aqueous layer thickness has been calculated for a silica-water-oil (bitumen) system of salinity 1 mM KCl and pHs 3, 5 and 9, see **Figure 2.2**. While Π_{vdW} depends on the interaction Hamaker constant, Π_{el} is sensitive to pH and salinity, with the magnitude of the electrostatic force dependent on the surface (zeta) potentials of silica and bitumen, and the Debye length. For crude oil, the pH dependent surface potentials result from ionisation and surface activity of natural surfactants (naphthenic acids).[34, 35, 36] At higher pHs, dissociation of the carboxylic-type surfactant increases the surface potential (negative) of the oil-water interface, with the magnitude increasing as more surfactant partitions at the interface. The high surface potentials at pH 9 form very stable thin-water layers, whereas in more acidic conditions, the disjoining pressure maxima decrease, and the thin-water layer in pH 3 is entirely unstable.

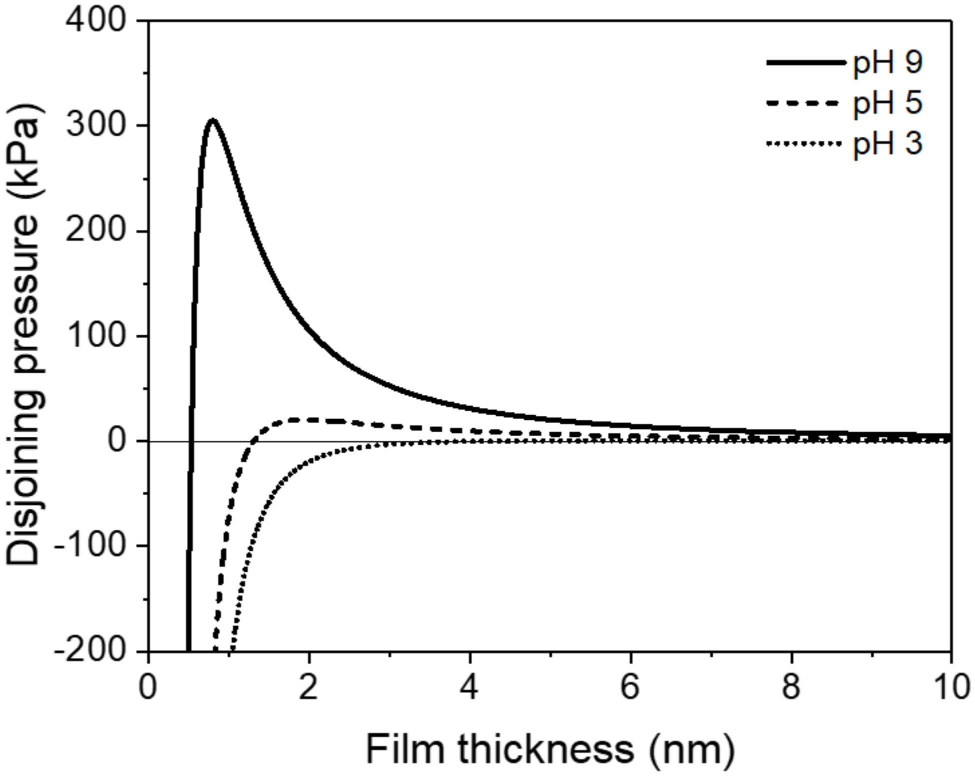

Figure 2.2. Disjoining pressure ($\Pi = \Pi_{el} + \Pi_{vdW}$) as a function of thin-water layer thickness (h) and pH. Zeta potentials (ψ) at pH 3, 5 and 9 are: 2.5, -55.6 and -78.2 mV for oil (bitumen),[37] and -12, -30 and -38 mV for silica, respectively. The Hamaker constant (A_{SWB}) for silica-water-oil system is 5.7 × 10^{-21} J.[10] $\Pi_{vdW} = \frac{A_{SWB}}{6\pi h^3}$, $\Pi_{el} = \frac{1}{2}\varepsilon\varepsilon_0\kappa^2\frac{2\psi_1\psi_2\,cosh(\kappa h)-\psi_1^2-\psi_2^2}{sinh^2(\kappa h)}$, where ε and ε_0 are the dielectric permittivity of vacuum and relative dielectric permittivity of water, respectively. κ is the Debye length which accounts for changes in salinity.

The stability of thick oil films is governed by the balance of gravity and capillary forces, with instability and the formation of discrete oil patches having been described analytically by Sharma,[38] with the critical film thickness, h_{cr}, (Equation (2.2)) dependent on the oil-water interfacial tension (σ_{OW}), the contact angle (θ), and the minimum radius of the hole (r_m)

$$h_{cr} = r_m ln\left(\frac{2sin(\pi-\theta)}{r_m[1+cos(\pi-\theta)]}\sqrt{\frac{\sigma_{OW}}{g\rho}}\right) \tag{2.2}$$

where g is the acceleration due to gravity and ρ the density of oil. For a typical oil-wetted solid surface of contact angle of 145° and σ_{OW} = 30 mN/m, h_{cr} is 0.05 mm for a stable minimum hole radius of 10 µm. Dependence on the fluid and surface properties is rather weak over the range of general applicability, with h_{cr} strongly influenced by the size of the stable hole in the oil film.[10] For very thick films (h >> h_{cr}), thinning of the oil film is needed for dewetting, otherwise holes formed in the film will spontaneously collapse. The mechanisms for film thinning have not been extensively considered but are most likely to result from fluid shear in confined environments. Other factors which can influence the onset of film rupture include gas bubbles trapped in the oil film,[39] and surface asperities which lead to non-uniform film thickness.

2.2.2 Oil droplet energy balance

With the oil film ruptured, the circular hole begins to expand at a rate dependent on the fluid and interfacial properties (to be discussed in Section 2.3).[40] Away from equilibrium, the process of droplet dewetting is driven by a change in energy following the creation of new solid-water interface and the loss of oil-solid interface, assuming the change in oil-water interface during droplet recession can be considered negligible, that is

$$\frac{dG}{dA} = \sigma_{SW} - \sigma_{OS} \tag{2.3}$$

where σ is the interfacial tension and subscripts S, W and O describe the solid, water and oil phases, respectively. Equation (2.3) can be simplified by the Young's equation for an oil droplet on a solid surface given by

$$cos\theta = \frac{\sigma_{OS} - \sigma_{SW}}{\sigma_{OW}} \tag{2.4}$$

to express the energy change during oil recession in terms of the equilibrium contact angle and oil-water interfacial tension (two measurable properties)

$$\frac{dG}{dA} = -\sigma_{OW} cos\theta. \tag{2.5}$$

With σ_{OW} always greater than zero, Equation (2.5) confirms that oil recession is a spontaneous process when $\theta < 90°$, *i.e.* the wetted solid surface is more water-wet (hydrophilic). The simple form of Equation (2.5) provides fundamental insight for effective EOR, highlighting the value of modifying surface wettability and oil-water interfacial tension.[30] The smaller the θ, the more favourable the condition for oil recession. Once the oil droplet has reached equilibrium, the work of adhesion (W_A) between oil and solid surface must be exceeded to liberate the oil droplet. By the reduction in area of oil-solid interface and generation of oil-water and solid-water interfaces, W_A is given by

$$W_A = \sigma_{SW} + \sigma_{OW} - \sigma_{OS} \tag{2.6}$$

which when combined with the Young's equation leads to

$$W_A = \sigma_{OW}(1 - cos\theta) \geq 0. \tag{2.7}$$

With the unlikely condition of $\theta = 0$ for spontaneous liberation (droplet detachment from the solid surface), Equation (2.7) confirms the need for energy to detach oil droplets from the wetted surface. In order to detach an oil droplet from the solid surface the hydrodynamic lift force must exceed contributions from the body and adhesion forces. An approximation of the adhesion force for a partially wetting droplet is, $F_A = \pi r \sigma_{OW} \sin(\pi - \theta)$, where r is the radius of oil-solid surface contact area.[2] The contour map in **Figure 2.3** indicates strongest adhesion (red colour) when the oil-water interfacial tension and water droplet contact angle are high. Therefore, reducing both the oil-water interfacial tension and oil-water-solid contact angle leads to more favourable oil droplet liberation.

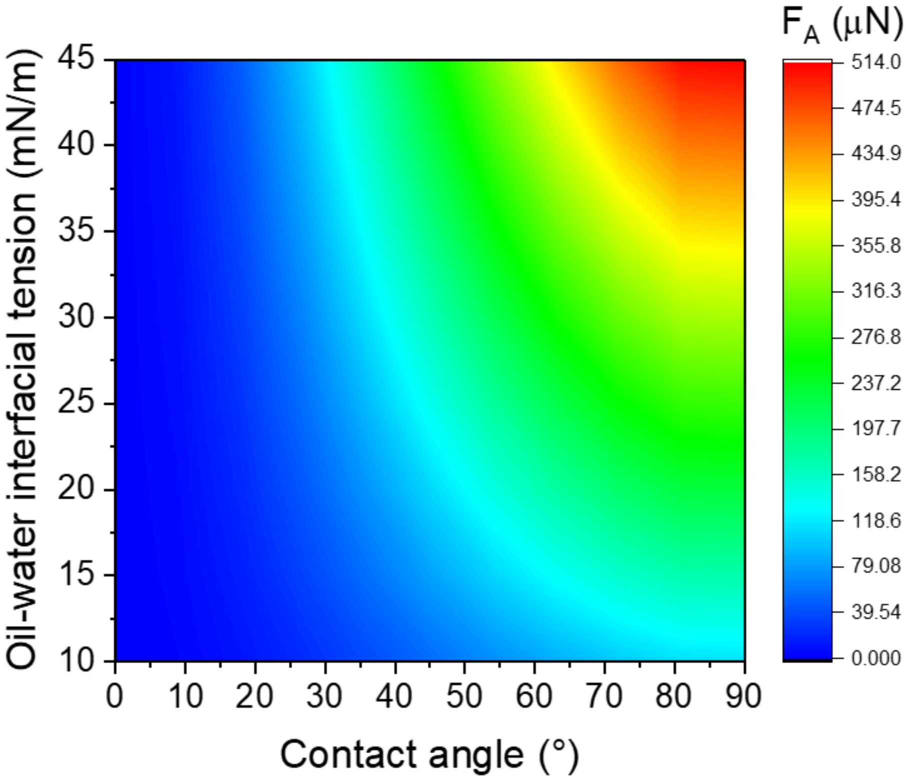

Figure 2.3. Apparent adhesion force for a partially wetting droplet (10 μL droplet).

2.3 Dynamics of Oil Film Recession

After creation of a hole in the oil film, the oil film recedes rapidly, governed by the receding force, $F_R = \sigma_{OW}[\cos(\pi - \theta_d) - \cos(\pi - \theta)]$, acting at the three-phase contact line (θ_d is the dynamic contact angle and θ the equilibrium contact angle), with F_R diminishing towards the new equilibrium wetted-state, hence, the velocity of three-phase contact line decreases with time. The dynamics of oil displacement on a solid surface are frequently described using the (i) hydrodynamic (HD), (ii) molecular-kinetic (MK), or (iii) combined models.

2.3.1 Hydrodynamic model

For more viscous fluids, such as heavy crude oil, the hydrodynamic model relies on the solution of creeping flow in the vicinity of the three-phase contact line, with the no slip boundary condition relaxed to allow for finite slipping of the fluid-fluid contact line on a solid surface. Considering an effective slip length (L_S), Cox presented a comprehensive hydrodynamic solution by segmenting the dynamic three-phase contact line into inner, intermediate, and outer regions, and correlated the apparent contact angle to the three-phase contact line displacement velocity (U),[41, 42]

$$U = \frac{\sigma_{OW}}{9\mu_o}[(\pi - \theta)^3 - (\pi - \theta_d)^3]\left[ln(\frac{L}{L_S})\right]^{-1} \tag{2.8}$$

where μ_o is the oil viscosity, θ the contact angle measured through the water phase, and L and L_S are the characteristic length of the oil droplet and the slip length, respectively. While determination of the slip length is nontrivial, the term is often used as a fitting parameter of the experimental data.

2.3.2 Molecular-kinetic model

The molecular-kinetic model accounts for molecular displacements (adsorption/desorption) in the vicinity of the dynamic three-phase contact line. The model assumes that the solid surface behaves as a source of identical adsorption sites, and liquid molecules can detach and attach to neighbouring sites by overcoming an energy barrier to molecular displacements.[43] The work to overcome the energy barrier is provided by a driving force governed by σ_{OW} and an imbalance between the equilibrium and dynamic wetting states. The three-phase contact line displacement is described in terms of molecular displacement, defined as the distance between adsorption sites (λ) and a frequency (κ^0) of adsorption/desorption events at equilibrium, as shown in **Figure 2.4**.

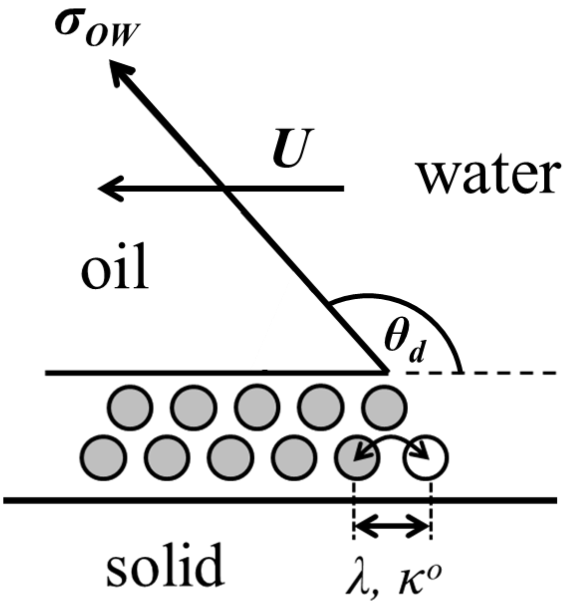

Figure 2.4. Molecular-kinetic model describes the distance between adsorption sites (λ) and a frequency (κ^0) of adsorption/desorption events. Figure adapted from Blake.[44]

The relationship between the dynamic contact angle and the three-phase contact line velocity is given by

$$U = 2\kappa^0 \lambda sinh\left(\frac{\sigma_{OW}[cos(\pi - \theta_d) - cos(\pi - \theta)]\lambda^2}{2k_B T}\right) \tag{2.9}$$

where k_B is the Boltzmann constant and T the absolute temperature. The molecular displacement parameters (λ and κ^0) are often combined and treated as the coefficient of contact-line friction, $\zeta = \frac{k_B T}{\kappa^0 \lambda^3}$, to describe the energy dissipated at the three-phase contact line, and neglecting any viscous dissipation in the bulk liquid.[44, 45] Similar to the HD model, ζ is treated as an adjustable parameter of the experimental data. Simplification of Equation (2.9) then follows when $sinh$ function is small, *i.e.* not far from equilibrium, and Equation (2.9) reduces to the linear form

$$U = \frac{\sigma_{OW}}{\zeta}[cos(\pi - \theta_d) - \cos(\pi - \theta)] \tag{2.10}$$

2.3.3 Combined model

Since each model neglects a contributing factor, a combined model approach can be considered to account for both the contact-line friction and viscous dissipation. As described by de Gennes and Brochard-Wyart,[46, 47] the combined model for contact-line displacement is given by

$$U = \frac{\sigma_{OW}[cos(\pi - \theta_d) - cos(\pi - \theta)]}{\zeta + \frac{6\mu_o}{\theta_d} ln(\frac{L}{L_S})} \tag{2.11}$$

2.3.4 Influencing parameters on the dewetting process

Contributing factors relevant to the reservoir environment and their influence on oil dewetting performance are briefly summarised here. Chemical additives which provide a performance enhancement for oil displacement are discussed in Section 2.4.

Temperature: The contribution from temperature can be simply viewed as a decrease in oil viscosity which leads to an increase in oil droplet receding rate. However, when studying bitumen droplets, Basu *et al.* showed that not only is the oil dewetting rate influenced by temperature but the equilibrium contact angle also decreased slightly due to the increased solubility of naphthenic acids (natural surfactants in crude oil) in the aqueous phase, therefore lowering the oil-water interfacial tension,[13, 48] see **Figure 2.5**.

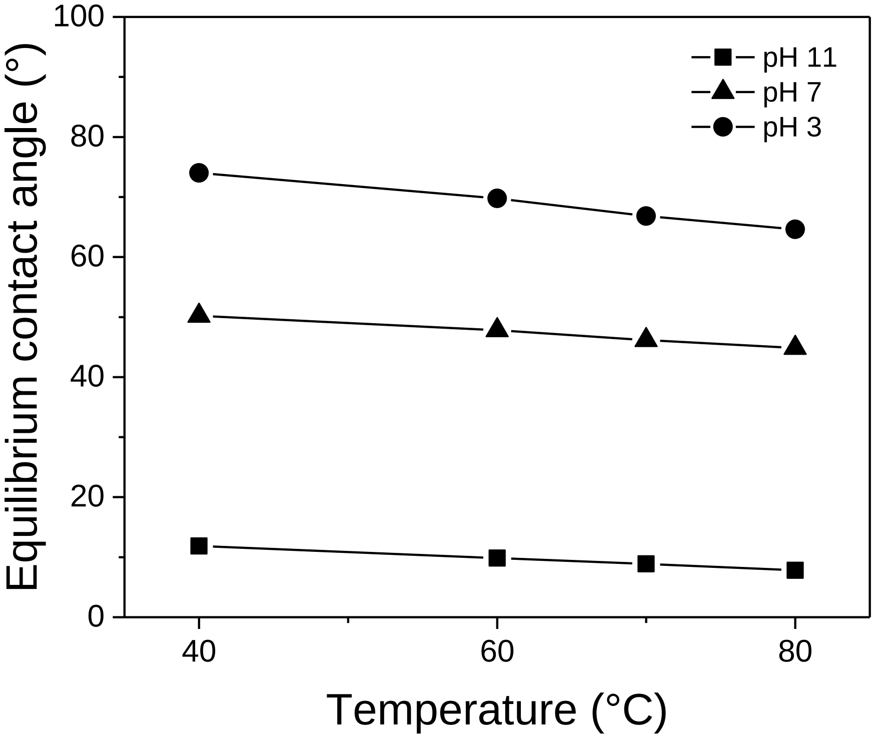

Figure 2.5. Equilibrium contact angle as a function of pH at elevated temperatures. The figure is adapted from Basu *et al.*[13]

pH: The aqueous phase chemistry has been shown to have a marked effect on the dynamic and equilibrium contact angles. The rate of bitumen droplet recession was shown to increase in acidic rather than basic conditions, but the equilibrium contact angle was found to be lower in basic conditions.[13] Basu *et al.* has also shown that pH strongly influences the oil droplet equilibrium contact angle compared with temperature (**Figure 2.5**). The strong pH dependence can again be attributed to the contribution from naphthenic acids which readily partition at the oil-water interface when soluble in the aqueous phase.[49] Beyond the pKa (~4.5), the concentration of anionic naphthenic acids increases as highlighted by a reduction in the oil-water interfacial tension.[50, 51] Surfactant partitioning at the oil-water interface increases the negative surface charge of bitumen (from –36.0 mV up to –80.4 mV).[35] Furthermore, increasing pH also leads to increased ionisation of hydroxyl groups on silica (sand) which increases surface negative charge and hydrophilicity, thus enhancing oil dewetting.[35, 52] These strongly negatively charged surfaces result in a greater electrostatic repulsion between the droplet and substrate (disjoining pressure), repelling the droplet away from the wetted surface as discussed in Section 2.2.1.

Pressure: While pressure is an important property to consider given the reservoir conditions, few studies have considered the effect of pressure on oil droplet dewetting. One recent study of crude oil dewetting on sandstone between pressures of 200 – 500 bar showed that the equilibrium contact angle was insensitive to pressure,[17] similar to Zhang *et al.*[53] who studied the pressure effect on oil dewetting from a range mineral substrates. On the contrary, Nowrouzi *et al.*[54] reported a substantial decrease in contact angle at slightly high pressure (≤ 140 bar) which also reduced the oil-water interfacial tension. Yang *et al.*[55] studied the crude oil-carbonated brine-rock system and found the contact angle decreased at high pressure (≤ 200 bar). The decreased contact angle at high pressure could be attributed to oil swelling due to CO_2 diffusion while the oil-substrate contact area remained unchanged. Such conflicting findings require further systematic study under high pressure conditions to better understand the effect of pressure on oil dewetting.

Fine Particles (clays): Although clays are widely encountered in reservoir environments, their presence has been shown to have a negative impact on the equilibrium oil droplet wetting condition. In the presence of a swelling clay (montmorillonite), the equilibrium contact angle was shown to increase as a function of clay concentration, although the effect on the dynamic contact angle was found to be negligible.[56] Similar trends were observed in the presence of kaolinite (a non-swelling clay) but to a lesser extent.[15, 57] While clays are hydrophilic, they can become hydrophobic by organic matter contamination.[27, 58] This change in particle wettability and increased affinity for the oil-water interface appear to have a negative effect on the oil droplet displacement dynamics,[15, 57] although the impact of particle-stabilised interfaces on oil droplet recession has not yet been considered. Furthermore, no observable effect of salt addition (on clay swelling) was found to change the effect of clay on oil droplet recession.[56]

2.4 Oil Droplet Displacement by EOR Fluids

2.4.1 Surfactants

Surfactants are widely used in EOR to reduce σ_{OW} and enhance water-wetting of the solid surface. Surfactants are often described as amphiphilic molecules composed of a hydrophilic head and a hydrophobic tail, thus surfactants favourably partition at solid-liquid and liquid-liquid interfaces. The accumulation of surfactants at an interface is a function of the surfactant concentration in the bulk fluid as described by the general form of the Gibbs' adsorption equation for a binary, isothermal system,

$$d\sigma = -RT\Gamma_s d\ln C_s \tag{2.12}$$

where Γ_s is the surface excess of surfactant, C_s the surfactant concentration in the bulk fluid, and RT the thermal energy of the system. As a function of concentration, surfactants in solution exist in the monomer-form at low surfactant concentrations, reaching a concentration of maximum solubility of the monomer-form, forming micelles *via* self-association. This concentration is termed the critical micelle concentration (CMC). Surfactant adsorption and displacement of organic species on solid surfaces and the resultant wettability modification is dependent on the surfactant concentration. At extremely low concentrations, surfactant monomers adsorb as individual molecules with no interaction between the adsorbed molecules. At higher concentrations (< CMC) surfactant molecules associate to form patchy hemi-micelles on the solid surface, with surfactants coordinating in the tail-tail confirmation. Further increases in concentration lead to saturation of all available surface sites and the formation of a surfactant bi-layer at the CMC.[59] Formation of a bi-layer would orientate the surfactant hydrophilic head group away from the solid surface, thus increasing the water-wetting nature of the reservoir rock, favourable for oil droplet displacement (Equations (2.5) and (2.7)). Mechanisms for wettability modification by different surfactants are described below.

Composition of the reservoir surface (sandstone, carbonate and deposited organic species) often dictates the surfactant selection for wettability modification, with surfactants categorised as cationic, anionic and non-ionic, based on the charge characteristics of hydrophilic groups. Surfactant adsorption on the solid surface can occur *via* electrostatic, van der Waals forces, and hydrogen bonding, with the extent of wettability modification a function of several properties including surfactant adsorption kinetics, surfactant structure, temperature, pH, salinity. A brief summary of surfactants considered for EOR is provided in **Table 2.1** with remarks provided for changes in solid surface wettability and interfacial tension.

While electrostatic interactions are often considered to describe surfactant-solid surface adsorption, such simplicity does not describe the potential for surfactants to modify solid surface wettability, when many other factors such as oil saturation, clay content, divalent cations, pH and temperature influence the action of the surfactant.

Cationic surfactants are frequently used to treat carbonate reservoirs and include permanently charged ammonium groups (ammonium bromide, ammonium chloride).[60] Adsorbed polar components of crude oil (*i.e.* negatively charged naphthenic acids) can be removed from the solid surface by forming ion pairs with cationic surfactants *via* strong ionic interaction. Removal of contaminants transforms the solid surface wettability to more water-wet.[60, 61] The use of cationic surfactants to treat sandstone has also been demonstrated, although the chemical effectiveness in carbonate reservoirs is greater.[62]

Anionic surfactants including sulfates, sulfonates, phosphates and carboxylates, have been shown to modify wettability in both carbonate and sandstone reservoirs. Wettability modification occurs *via* two mechanisms:[60, 61] (i) anionic surfactants interact with the organic species *via* hydrophobic forces, exposing the surfactant head group to make the solid surface more water-wet (wettability modification for sandstone reservoirs), and (ii) *via* strong electrostatic forces with carbonate surfaces, anionic surfactants can displace organic species exposing the underlying water-wet surface.[62]

Non-ionic surfactants such as alcohols, esters and ethers have been used to modify the wettability of carbonate and sandstone surfaces,[63] being highly effective in high salinity water. With no contribution from electrostatic forces, non-ionic surfactants interact *via* hydrophobic forces with deposited organic species, and hydrogen bonding with hydroxyl groups on the solid surface.[64, 65] Research has shown that non-ionic

Table 2.1. Surfactants.

Surfactants	Conc.	Solid surface	Oil type	Remarks ^{a}	Ref.
Cationic surfactants					
n-C$_8$-N(CH$_3$)$_3$Br (C8TAB) in brine	4.0 wt%	Chalk	Crude oil mixed with heptane	Contact angle = 57°, σ_{OW} ^{b} = 2.85 mN/m	60
n-C$_{10}$-N(CH$_3$)$_3$Br (C10TAB) in water	0.4 wt%	Calcite	Decane mixed with naphthenic acids	σ_{OW} = 2.67 mN/m	61
n-C$_{12}$-N(CH$_3$)$_3$Br (C12TAB) in water	0.4 wt%	Calcite	Decane mixed with naphthenic acids	σ_{OW} = 0.59 mN/m	61
n-C$_{12}$-N(CH$_3$)$_3$Br (C12TAB) in brine	5.0 wt%	Chalk	Crude oil mixed with heptane	Contact angle = 12°, σ_{OW} = 0.81 mN/m	60
n-C$_{16}$-N(CH$_3$)$_3$Br (C16TAB) in brine	1.0 wt%	Chalk	Crude oil mixed with heptane	Contact angle = 27°, σ_{OW} = 0.38 mN/m	60
Cetyltrimethylammonium bromide (CTAB) in brine	0.3 wt%	Quartz	Crude oil	Contact angle = 57°	66
n-Decyl triphenylphosphonium bromide (C10TPPB) in water	0.4 wt%	Calcite	Decane mixed with naphthenic acids	σ_{OW} = 3.56 mN/m	61
Cocoalkyltrimethyl ammonium chloride (CAC) in brine	75 – 2620 ppm (0.0075 – 0.262 wt%)	Dolomite	Crude oil		63
Dodecyltrimethylammonium bromide (DTAB) in brine	0.5 wt%	Calcite	Crude oil	Contact angle = 69°, σ_{OW} = 4.8 mN/m	67
Dodecyltrimethylammonium bromide (DTAB) in brine	0.06 wt%	Quartz	Crude oil	Contact angle = 95°, σ_{OW} = 2.49 mN/m	68
n-(C$_8$-C$_{18}$)-N(CH$_3$)$_2$(CH$_2$-Ph)Cl (ADMBACl) in brine	0.5 wt%	Chalk	Crude oil mixed with heptane	Contact angle = 26°, σ_{OW} = 0.41 mN/m	60
n-C$_8$-Ph-(EO)$_2$-N(CH$_3$)$_2$(CH$_2$-Ph)Cl (Hyamine) in brine	0.2 wt%	Chalk	Crude oil mixed with heptane	Contact angle = 21°, σ_{OW} = 0.48 mN/m	60
Coconut oil alkyl trimethylammonium chloride (ARQUAD C-50) in water	0.4 wt%	Calcite	Decane mixed with naphthenic acids	σ_{OW} = 0.53 mN/m	61

Table 2.1. Surfactants. (Cont.)

Surfactants	**Conc.**	**Solid surface**	**Oil type**	**Remarks** [a]	**Ref.**
Trimethyl tallowalky ammonium choride (ARQUAD T-50) in water	0.4 wt%	Calcite	Decane mixed with naphthenic acids	σ_{OW} = 0.69 mN/m	61
Methyldodecylbis ammonium tribromide	0.0001 – 1 mM	Mica	Kerosene mixed with decane	Contact angle = 87°, σ_{OW} = 0.18 mN/m	69
Anionic surfactants					
n-(C_{12}-C_{15})-$(EO)_{15}$-SO_3Na (S-150) in brine	0.5 wt%	Chalk	Crude oil mixed with heptane	Contact angle = 63°, σ_{OW} = 2.29 mN/m	60
n-C_{13}-$(EO)_8$-SO_3Na (B 1317) in brine	0.5 wt%	Chalk	Crude oil mixed with heptane	Contact angle = 40°, σ_{OW} = 0.78 mN/m	60
n-C_8-$(EO)_3$-SO_3Na (S-74) in brine	0.5 wt%	Chalk	Crude oil mixed with heptane	Contact angle = 49°, σ_{OW} = 6.72 mN/m	60
n-(C_{12}-C_{15})-$(PO)_4$-$(EO)_2$-OSO_3Na (APES) in brine	1.0 wt%	Chalk	Crude oil mixed with heptane	Contact angle = 44°, σ_{OW} = 0.082 mN/m	60
n-($C_8O_2CCH_2$)(*n*-C_8O_2C)CH-SO_3Na (Cropol) in brine	0.5 wt%	Chalk	Crude oil mixed with heptane	Contact angle = 55°, σ_{OW} = 8.77 mN/m	60
n-C_8-$(EO)_8$-OCH_2-COONa (Akypo) in brine	0.5 wt%	Chalk	Crude oil mixed with heptane	Contact angle = 48°, σ_{OW} = 2.99 mN/m	60
n-C_9-Ph-$(EO)_x$-PO_3Na (Gafac) in brine	0.5 wt%	Chalk	Crude oil mixed with heptane	Contact angle = 75°, σ_{OW} = 0.42 mN/m	60
Sodium dodecyl sulfate (SDS) in brine	0.1 wt%	Chalk	Crude oil mixed with heptane	Contact angle = 39°, σ_{OW} = 2.95 mN/m	60
Sodium dodecyl sulfate (SDS) in water	0.4 wt%	Calcite	Decane mixed with naphthenic acids	σ_{OW} = 4.77 mN/m	61
Sodium dodecyl 3EO sulfate in brine	0.05 wt%	Calcite	Crude oil	Contact angle ~ 45°, σ_{OW} = 0.003 mN/m	70
Alkyldiphenyloxide disulfonate in Na_2CO_3/NaCl	0.05 wt%	Calcite	Crude oil	Contact angle ~ 110°, σ_{OW} = 0.0011 mN/m	71

Table 2.1. Surfactants. (Cont.)

Surfactants	Conc.	Solid surface	Oil type	Remarks [a]	Ref.
Polyether sulfonate in Na_2CO_3/NaCl	0.30 wt%	Calcite	Crude oil	Contact angle ~ 80°, σ_{OW} = 0.00812 mN/m	71
Sodium nonyl phenol ethoxylated sulfate (4EO) in Na_2CO_3/NaCl	0.05 wt%	Calcite	Crude oil	Contact angle ~ 60°, σ_{OW} = 0.003 mN/m	71
C_{12}-C_{13} propoxy sulfate (8PO) in Na_2CO_3/NaCl	0.05 wt%	Calcite	Crude oil	Contact angle ~ 40°, σ_{OW} = 0.0001 mN/m	71
Alkyldiphenyloxide disulphonate + C_{14}T-isofol propoxy sulfate (8PO) in Na_2CO_3/NaCl	0.075 wt%	Calcite	Crude oil	Contact angle ~ 70°, σ_{OW} = 0.116 mN/m	71
Methyl alcohol+Proprietary sulfonate in brine	0.02 – 0.20 wt%	Shale (siliceous)	Crude oil	Contact angle = 38°, σ_{OW} = 0.4 mN/m)	72
Sodium laureth sulfate in brine	0.02 – 0.05 wt%	Quartz	Crude oil	Contact angle ~ 110°, σ_{OW} = 2.007 mN/m	66
Sodium lauryl monoether sulfate in brine	0.035 wt%	Quartz	Crude oil	Contact angle = 116.1°, σ_{OW} = 2.49 mN/m	68
Nonionic surfactants					
Poly-oxyethylene alcohol (POA) in brine	750 – 1050 ppm (0.075 – 0.105 wt%)	Dolomite	Crude oil	σ_{OW} = 2.0 mN/m	63
Ethoxylated C_{11}-C_{15} secondary alcohol (Tergitol 15-S-3) in water	0.4 wt%	Calcite	Decane mixed with naphthenic acids	σ_{OW} = 4.44 mN/m	61
Ethoxylated C_{11}-C_{15} secondary alcohol (Tergitol 15-S-7) in water	0.4 wt%	Calcite	Decane mixed with naphthenic acids	σ_{OW} = 1.39 mN/m	61
Ethoxylated C_{11}-C_{15} secondary alcohol (Tergitol 15-S-40) in water	0.4 wt%	Calcite	Decane mixed with naphthenic acids	σ_{OW} = 11.5 mN/m	61
Nonylphenoxypoly(ethyleneoxy)ethanol (Igepal CO-530) in water	0.4 wt%	Calcite	Decane mixed with naphthenic acids	σ_{OW} = 0.33 mN/m	61
C_{12}-C_{15} linear primary alcohol ethoxylate (Neodol 25-7) in water	0.4 wt%	Calcite	Decane mixed with naphthenic acids	σ_{OW} = 2.02 mN/m	61

Table 2.1. Surfactants. (Cont.)

Surfactants	Conc.	Solid surface	Oil type	Remarks [a]	Ref.
Secondary alcohol ethoxylate in Na_2CO_3/NaCl	0.10 wt%	Calcite	Crude oil	Contact angle ~ 20°, σ_{OW} = 0.0017 mN/m	71
Nonyl phenol ethoxylate in Na_2CO_3/NaCl	0.10 wt%	Calcite	Crude oil	Contact angle ~ 80°, σ_{OW} = 0.0006 mN/m	71
Branched alcohol oxyalkylate in brine	0.02 – 0.20 wt%	Shale (siliceous)	Crude oil	Contact angle = 60°, σ_{OW} = 9.8 mN/m	72
Polyoxyethylene octyl phenyl ether in brine	0.04 wt%	Quartz	Crude oil	Contact angle = 95°, σ_{OW} = 4.05 mN/m	66
Alkylpolyglycosides in brine	0.05 wt%	Quartz	Crude oil	Contact angle = 58.8°, σ_{OW} = 2.49 mN/m	68

[a]not all studies report contact angle or interfacial tension data. [b]σ_{OW} is interfacial tension.

surfactants can modify highly oil-wet carbonate to weakly oil-wet or even water-wet ($\theta < 80°$) following the addition of 0.1 wt% surfactant.[71]

2.4.2 Low-salinity water

Low-salinity EOR or dilution of connate water has shown great promise in oil recovery, despite the mechanism for enhanced recovery remaining controversial and discussed in relation to fines migration,[73, 74] mineral dissolution,[75, 76] double-layer expansion,[77] multi-ion exchange,[78] emulsion stabilisation,[79] reduction in oil-water interfacial tension and wettability alteration.[12, 17, 76, 80] The latter two are of interest to oil film displacement and the reduction of oil droplet-substrate adhesion force, where the presence of salt ions can modify both surface and interfacial properties through the interactions with native surface-active species (naphthenic acids and asphaltenes). **Table 2.2** summarises the role of low-salinity fluids on oil droplet dewetting.

The oil-water interfacial tension has been shown to depend on the surface-active species (component type) and salt ions.[81, 82, 83, 84] High brine concentrations were shown to promote adsorption of surface-actives species at the oil-water interface by charge neutralisation. Cation adsorption at the oil-water interface reduces the surface charge and hence the surface-active species (*i.e.* mostly negatively charged) are more favourably adsorbed. At very high ion concentration, the oil-water interface can become saturated with ions resulting in excess ions in the bulk. As such, a negative surface excess leads to an increase in interfacial tension, also known as the Jones-Ray effect.[85] It has been reported that the dipole-ion interaction between cations and water molecules increases at high salt concentrations, due to reduced asphaltene ionisation and associated interaction

Table 2.2. Low-salinity water.

Brines	Conc.	Solid surface	Oil type	Remarks [a]	Ref.
NaCl	0.058 – 58,440 ppm	Mica	Crude oil	Contact angle ~ 0° (pH = 8), Contact angle increased up to 58.4 ppm (55° at pH < 8)	12
NaCl and $CaCl_2$	0 – 30,000 ppm	Muscovite	Decane	Contact angles slightly decreased with dilution (NaCl: up to 5°, $CaCl_2$: up to 55°)	80
NaCl and $CaCl_2$	0 – 200,000 ppm	*NA* [b]	Crude oil	σ_{OW} [c] decreased and then increased with concentration. NaCl had σ_{OW} lower than $CaCl_2$ ~ 2 mN/m	81
NaCl, Na_2SO_4 and $CaCl_2$	0 – 284,080 ppm	*NA*	Decane	σ_{OW} decreased and then increased with concentration, Na_2SO_4 had σ_{OW} lower than NaCl and $CaCl_2$, respectively	86
NaCl, Na_2SO_4 and $CaCl_2$	142 – 142,040 ppm	Quartz	Octane, decane and dodecane mixed with crude-oil acids	Pure oils: contact angles decreased slightly up to ~14,000 ppm and then increased $\Delta\theta = 5°$ with brine concentration, Crude-oil acid mixed: contact angle increased with brine concentration, $\Delta\theta = 50°$	87
NaCl, $MgCl_2$ and $CaCl_2$	0 – 30,000 ppm	*NA*	Pentane, hexane, heptane, benzene and toluene	σ_{OW} decreased and then increased with concentration, Divalent brines found higher σ_{OW} reduction than monovalent in aromatic oils and vice versa	88
NaCl, $MgCl_2$ and $CaCl_2$	1,182 – 100,000 ppm	Sandstone	Crude oil	Contact angles decreased with dilution, More decrease without divalent salts	89
NaCl, $MgCl_2$ and $CaCl_2$	3,432 – 34,322 ppm	Carbonate	Crude oil	Contact angles and σ_{OW} decreased with dilution, Contact angle at 10% higher than 25 – 50% dilutions	90
Formation water [d]	57,670 – 213,734 ppm	Calcite	Crude oil	Diluting brines decreased contact angle from 50° to ~ 0°, σ_{OW} slightly decreased with concentration $\Delta\sigma$ ~2 mN/m)	76
Formation water and seawater	1,751 – 179,855 ppm	Carbonate	Crude oil	Contact angle decreased ~10° – 15° with brine dilution	91

Table 2.2. Low-salinity water. (Cont.)

Brines	**Conc.**	**Solid surface**	**Oil type**	**Remarks** [a]	**Ref.**
Formation water	2,522 – 252,244 ppm	Carbonate	Crude oil	Contact angle increased from 30° to 81° with brine dilution	92
Formation water	1,424 – 142,431 ppm	Quartz	Crude oil	Contact angles decreased from 53° to 28° with brine dilution	17
Synthetic brine	3,587 – 18,739 ppm	Quartz	Crude oil	Contact angles decreased from 84° to 11° with brine dilution, σ_{OW} reduced from 32 to 2 mN/m	93
Formation brine and seawater	1,759 – 179,855 ppm	Carbonate	Crude oil	σ_{OW} decreased from 11.8 to 7.2 mN/m with brine dilution, Contact angles decreased with brine dilution	94
Seawater	731 – 29,260 ppm	Carbonate	Crude oil	Contact angles decreased from 150° up to 20 times dilution (=30°) and increased slightly at 40 times dilution (=45°)	95
Synthetic brine	108 – 10,780 ppm	Calcite and dolomite	Crude oil	Contact angles decreased with brine dilution	96
Formation water	1,679 – 136,855 ppm	Sandstone	Crude oil	Contact angles decreased with brine dilution ($\Delta\theta$ = 10 - 35°)	97
Formation brine and seawater	1,270 – 198,428 ppm	Calcite	Crude oil	Contact angles decreased (120° to 75° for NaCl; slight decrease in $MgCl_2$ and $CaCl_2$), σ_{OW} reduced (50 to 30 mN/m) with brine dilution	98
Formation water	1,954 – 164,473 ppm	Carbonate	Crude oil	Contact angles and σ_{OW} decreased with dilution	99
Formation brine and seawater	1,238 – 35,720 ppm	Quartz and mica	Crude oil	Contact angles decreased with dilution, At brine without divalent contact angle was lowest but σ_{OW} was highest	100
Synthetic brine	1,000 – 100,072 ppm	Carbonate	Crude oil	Contact angles decreased with dilution, Divalent decreased contact angles better than monovalent.	101

[a]not all studies report contact angle or interfacial tension data. [b]*NA* is not available. [c]σ_{OW} is interfacial tension. [d]includes monovalent and divalent salts.

with cations.[82] Asphaltenes become more soluble in the oil phase and prefer aggregate rather than partition at the oil-water interface.

Wettability alteration by brine solutions is attributed to changes in interfacial forces (*i.e.* the extended-DLVO theory) and includes the repulsive hydration force. Equation (2.1) can then be modified to include this force as follows:

$$\Pi = \Pi_{el} + \Pi_{vdW} + \Pi_H \tag{2.13}$$

where Π_H is the hydration force. The hydration force exists at intermediate brine concentrations and results from hydrated ions (salt) increasing the hydration free energy in the water film leading to a strong repulsion. This hydration force often dominates the van der Waals and electrostatic forces, thus governing the contact angle which cannot simply be described by the Young's equation.[102]

Brine dilution from very-high salinity has been reported to decrease the contact angle due to strong hydration and electrostatic forces. The hydration force in brine fluids has been measured by atomic force microscopy and reported to correspond to changes in surface wettability.[12, 76] High brine concentration promotes the development of a hydration force but very high brine concentrations (*i.e.* above a critical concentration) weakens the hydration repulsion due to the cations requiring more energy to hydrate, hence reducing the hydration force.[103] Electrostatic repulsion is increased since the oil-water and solid-water surface (zeta) potentials are larger in low-salinity brines due to electric double-layer expansion (increased Debye length).[104, 105, 106] Some research suggests that the zeta potentials of the solid-water and oil-water interfaces govern the oil droplet contact angle in brine solutions, since dilution of brines led to more negatively charged surfaces and lower oil droplet contact angles.[94, 107, 108, 109, 110]

It has been reported that the brine type influences oil displacement. Greater oil dewetting (*i.e.* less contact angle) has been reported for a monovalent ion due to increased double-layer thickness and electrostatic repulsion compared to divalent ion at the same concentration.[105, 111, 112] The hydration force was also shown to depend on the brine type.[102, 108] Monovalent ion would lead to higher hydration force compared to divalent ion which has a higher hydration energy. Moreover, divalent cations (*e.g.* Ca^{2+} and Mg^{2+}) were found to bind with dissociated acidic materials (*e.g.* naphthenic acids), asphaltenes ($R–COO–Ca^{2+}$) and the negatively charged silica surface to form a 'bridge' which is not observed for monovalent ions (*e.g.* NaCl). This so-called 'bridging' was reported to reduce oil dewetting by increasing the strength of interaction between the oil droplet and wetted-substrate.[80, 113]

2.4.3 Nanoparticles

The use of ultra-small particles (nanoparticles) to enhance oil film displacement has been demonstrated. Nanoparticles are typically 1 to 100 nm and are ideal for EOR applications with particle sizes smaller than the pore diameter, hence nanofluids flow through the porous media without obstructing the porous network. In addition, their high surface area to volume ratio increases their effectiveness at low particle concentrations, and promotes their kinetic stability.[114] An overview of nanoparticles (nanofluids) used to displace oil films is provided in **Table 2.3**.

For oil film displacement, different nanoparticles have been considered including metal oxides, organic, inorganic and composite particles. Metal oxides nanoparticles (*e.g.* Al_2O_3, CuO, TiO_2 and Fe_2O_3) have been shown to lower σ_{OW}[115] and increase the disjoining pressure between the solid surface and oil-water interface.[116]

Table 2.3. Nanoparticles/fluids.

Nanoparticles/fluids	Solid surface	Oil type	Remarks [a]	Ref.
Metal oxides				
TiO_2 (0.01 – 1 wt%)	Sandstone	Heavy oil	Contact angle = 90°	117
TiO_2 (0.01 – 0.10 wt%)	Sandstone	Heavy crude oil	Slight σ_{OW} [b] reduction ~ $\Delta\sigma = 1$ mN/m	115
TiO_2 (0.01 – 0.05 wt%)	Sandstone	Heavy oil	Contact angle change from 127° to 81°, Slight σ_{OW} reduction	116
Al_2O_3 (0.01 – 0.10 wt%)	Sandstone	Heavy crude oil	Slight σ_{OW} reduction ~ $\Delta\sigma = 1$ mN/m	115
NiO (0.01 – 0.10 wt%)	Sandstone	Heavy crude oil	Slight σ_{OW} reduction ~ $\Delta\sigma = 1$ mN/m	115
Organic				
Janus nanoparticles (0.0025 – 0.0004 mM)	*NA* [c]	Hexane	σ_{OW} = 12 mN/m	118
Carbon nanotubes (0.05 – 0.50 wt%)	Glass	Crude oil	σ_{OW} reduction ~ 3 mN/m	119
Nanocellulose (0.2 – 1.0 wt%)	Glass	Crude oil	σ_{OW} = 0.7 mN/m	120
Inorganic				
SiO_2 (0.1 – 0.6 wt%)	Carbonate	Crude oil	Contact angle = 51°	121
SiO_2 (0.5 – 4.0 wt%)	Calcite (oil-wet)	Decane	Contact angle = 20°	122
SiO_2 (0.1 – 5 wt%)	Glass	Crude oil	Contact angle = 0°	123
SiO_2 (0.025 – 0.2 wt%)	Calcite (oil-wet)	Heptane	Contact angle = 41.7°	124

Table 2.3. Nanoparticles/fluids. (Cont.)

Nanoparticles/fluids	**Solid surface**	**Oil type**	**Remarks** [a]	**Ref.**
SiO_2 (0.4 effective volume fraction)	Glass	Model oil		11
SiO_2 (0.01 – 0.10 wt%)	Sandstone	Crude oil	Contact angle = 22°, σ_{OW} = 7.9 mN/m	125
SiO_2 (0.10 wt%)	Sandstone	Light crude oil	Contact angle change from 34° to 32°, σ_{OW} reduced from 20 to 10 mN/m	126
SiO_2 (0.01 – 0.10 wt%)	Sandstone	Heavy crude oil	Slight σ_{OW} reduction ~ $\Delta\sigma = 1$ mN/m	115
Hydrophilic silica (0.01 – 0.10 wt%)	Glass/Sandstone	Light crude oil	Contact angle ~ 20°, σ_{OW} ~ 8 mN/m	127
Hydrophilic, neutralized, and hydrophobic silica (0.2 – 0.3 wt%)	Sandstone	Crude oil	Contact angle ~ 35°	125
Hydrophobic silica (0.1 – 0.4 wt%)	Sandstone	Crude oil	Contact angle = 95.4°, σ_{OW} = 1.75 mN/m	128
Nanostructure particles (0.05 – 0.50 wt%)	Sandstone	Light crude oil	Wettability index = 0.36 (wettability index = 1 is water-wet)	129
Silica colloidal nanoparticles (0.05 – 0.50 wt%)	Sandstone	Light crude oil	Wettability index = 0.57 (wettability index = 1 is water-wet)	129

[a]not all studies report contact angle or interfacial tension data. [b]σ_{OW} is interfacial tension. [c]*NA* is not available.

The interfacial tension decreases as nanoparticles partition at the oil-water interface from the aqueous phase. Unlike surfactants, nanoparticles are not amphiphilic and their affinity to partition at an oil-water interface is governed by their particle size and surface wettability. The general expression of $E = \pi a^2 \sigma_{OW}(1 \pm cos\theta)^2$, describes the particle detachment energy from an oil-water interface (± describes detachment into either liquid phase), where a is the particle radius.[19] When $cos\theta$ = 0 the particle detachment energy is maximised, although for nanoparticles E can be of the order of a few k_BT which theoretically can result in reversible adsorption, similar to a surfactant molecule. The reduction in oil-water interfacial tension has been shown to correlate to the nanoparticle size and the particle specific surface area.[130] It is important to note that the reduction in oil-water interfacial tension is apparent since the oil-water interfacial area is occupied by particles without changing in interfacial energy (unlike a surfactant).[19] Al_2O_3 nanoparticles of diameter 20 nm and 45 nm were shown to lower the oil-water interfacial tension to ~13.6 mN/m and ~8.6 mN/m, respectively.[131] Compared to surfactants, interfacial tension reduction by nanoparticles is often smaller. For example, silica nanoparticles (7 – 14 nm) dosed at 0.01 – 0.10 wt% reduced σ_{OW} to ~10 mN/m from ~15 – 20 mN/m,[125, 126, 127] while TiO_2 nanoparticles (58 nm) reduced σ_{OW} from 23 mN/m to 18 mN/m when dosed at 0.01 – 0.05 wt%.[116] As such, enhanced oil film displacement by nanoparticles is likely to occur *via* other mechanisms, *i.e.* structural disjoining pressure and wettability modification.

Structural disjoining pressure is a consequence of nanofluids exhibiting super-spreading behaviour. Nanoparticles self-assemble in the vicinity of the three-phase contact line to form a liquid wedge at the de-pinning point, see **Figure 2.6**. As nanoparticles accumulate in the liquid wedge a structural disjoining pressure (Equation (2.15)) gradient is established with the highest pressure at the oil droplet-solid surface vertex, driving the nanofluid to spread and cause the oil film to recede. As explained by Wasan and co-workers,[11, 132] the spreading coefficient (S) of the nanofluid is determined by the sum of the capillary pressures at the equilibrium film thickness ($\Pi_0(h_e)$) and disjoining pressure ($\Pi(h)$)

$$S = \Pi_0(h_e)h_e + \int_{h_e}^{\infty} \Pi(h)dh \qquad (2.14)$$

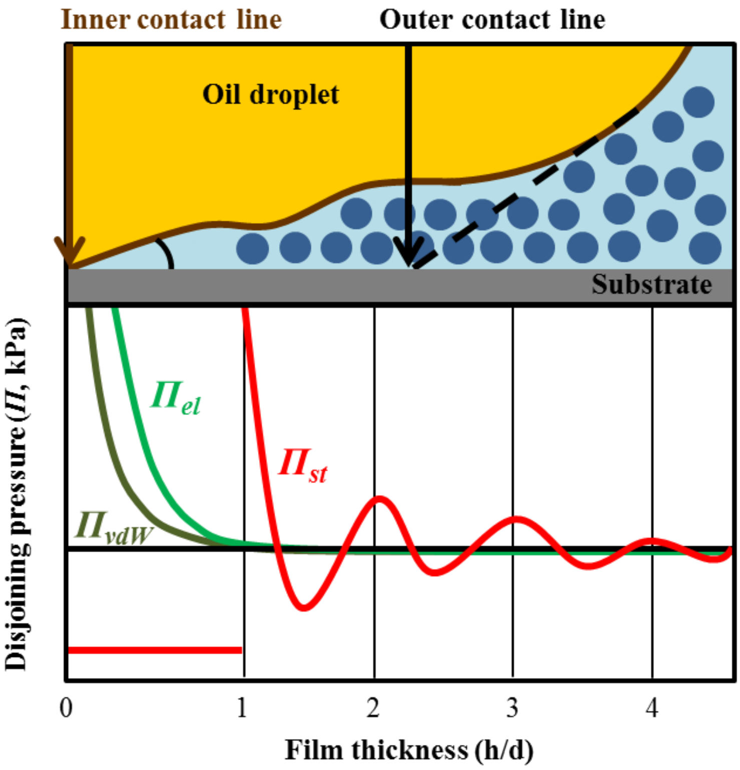

Figure 2.6. Schematic showing the ordered accumulation of nanoparticles to form a liquid wedge. The structural disjoining pressure increases towards the de-pinning point. The structural disjoining pressure exceeds the Laplace pressure, deforming the meniscus profile as represented by inner and outer contact lines. The contribution from the long range structural disjoining pressure dominates the short range electrostatic and van der Waals forces. The figure has been modified from Zhang *et al.*[133] and Chengara *et al.*[33]

When the thickness of the liquid wedge exceeds one particle diameter, nanoparticles accumulate in ordered layers. This layered arrangement of nanoparticles increases the excess pressure in the liquid wedge with the structural disjoining pressure (Π_{st}) described based on the theory of thin liquid films:[134]

$$\Pi_{st}(h) = \Pi_0 \, cos(\omega h + \emptyset_2) \, e^{-\kappa h} + \Pi_1 e^{-\delta(h-d)}, h \geq d \tag{2.15}$$
$$\Pi_{st}(h) = -P, 0 < h < d$$

where d is the nanoparticle diameter, P the osmotic pressure of nanofluid, and all other parameters ($\Pi_0, \Pi_1, \omega,\ \emptyset_2, \kappa$ and δ) are fitted as cubic polynomials varying with particle concentration. Contributions from van der Waals, electrostatic and structural forces have been considered by Chengara *et al.*[33] (**Figure 2.6**). The extended-DLVO theory of the thin film becomes:

$$\Pi = \Pi_{el} + \Pi_{vdW} + \Pi_{st}. \tag{2.16}$$

The structural forces are long-range and govern the behaviour of thick liquid films, with nanoparticle size, concentration, temperature, fluid salinity all contributing to the magnitude of the structural disjoining pressure.

Wettability modification by nanoparticles enhances oil droplet displacement when nanoparticles deposit on the solid surface. The deposition/adsorption is influenced by electrostatic forces, with the nanoparticle decorated solid surface more water-wet when hydrophilic particles deposit to form a heterogeneous surface with increased nano/micron-scale roughness.[135, 136, 137, 138, 139] Wettability of heterogeneous surfaces has been described by Cassie-Baxter,[140] with the apparent contact angle on a composite solid surface given by,

$$cos\theta_{CB} = f_1 cos\theta_1 + f_2 cos\theta_2 \tag{2.17}$$

where f_1 is the fractional area of the surface with contact angle θ_1, f_2 is the fractional area of the surface with contact angle θ_2, and θ_{CB} is the Cassie-Baxter contact angle. The Cassie-Baxter model can be combined with the Wenzel wetting model[141] to account for surface roughness effects,

$$
\begin{gathered}
cos\theta_W = R'cos\theta \\
cos\theta_W = R'cos\theta_{CB}
\end{gathered}
\tag{2.18}
$$

where R' is the ratio of the true area of the solid to its planar projection and θ_W the Wenzel contact angle. With R' always greater than 1, the Wenzel model confirms nano/micron-scale roughness lowers the contact angle of a water-wet surface, thus increasing the potential for oil droplet displacement. For example, metal oxide nanoparticles (ZrO_2 and NiO < 50 nm) were shown to deposit on an oil-wet surface and modifying the contact angle from 152° (untreated surface) to 44° and 86° for ZrO_2 and NiO, respectively. The mean roughness of those surfaces was shown to increase from 70.6 nm (untreated surface) to 2.32 µm (ZrO_2 treated surface) and 330 nm (NiO treated surface).[142]

Oil film displacement can be enhanced when nanoparticles are mixed with surfactants. Fluid blends lower the oil-water interfacial tension below a surfactant only system, with surfactants increasing the interfacial activity of the nanoparticles.[143] The decrease in oil-water interfacial tension depends on the surfactant-particle interaction and surfactant concentration.[144] The contribution of nanoparticles is weakened at surfactant concentrations greater than the CMC. The use of surfactant blends and composite particles (polymer-coated particles) to enhance oil film displacement have also been considered.[145, 146] Recent studies have considered composite fluids (particles) which are summarised in **Table 2.4**.

Table 2.4. Composite fluids.

Composite fluids	Solid surface	Oil type	Remarks [a]	Ref.
Blend systems				
SDS and SiO_2 (Patented nanofluid – No reported concentration)	Glass	Crude oil	Contact angle = 1.2°	[133]
SDS and hydrophilic and hydrophobic SiO_2 (Surfactant: 100 – 6000 ppm, particle: 1000 – 2000 ppm)	Sandstone	Kerosene	σ_{OW} [b] = 1.81 mN/m	[143]
SDS and ZrO_2 (Surfactant: 0.001 – 5 CMC, particle: 0.001 – 0.050 wt%)	*NA* [c]	Heptane	σ_{OW} = 10 mN/m	[147]
Composite nanoparticles				
Zwitterionic polymer and SiO_2 (coated) (No reported concentration)	Sandstone	Decane	σ_{OW} = 35 mN/m	[145]

[a] not all studies report contact angle or interfacial tension data. [b] σ_{OW} is interfacial tension. [c] *NA* is not available.

2.5 Conclusion

The theory of oil film collapse and oil droplet recession has been considered. Changes in interfacial energy and the corresponding change in droplet contact angle are frequently described by the Young's equation, however, through addition of certain chemical additives other forces such as the disjoining pressure dominate behaviour. This chapter clarifies the contribution of surface and interfacial forces on oil droplet dewetting, with forces strongly influenced by the water-phase chemistry. Two theories for dynamic droplet dewetting, hydrodynamic and molecular-kinetic, were presented. Influencing parameters on the process of oil droplet dewetting have been considered, with the effect of temperature, pH, pressure and fine particles (clays) introduced. Different approaches to EOR fluids such as surfactant, low-salinity fluids and nanoparticle fluids, have been summarized in the context of oil droplet dewetting performance. While surfactants significantly decrease the oil-water interfacial tension, low-salinity fluids and nanoparticle fluids contribute to the disjoining pressure that also enhances removal of oil droplets from surfaces.

Chapter 3

Materials and Experimental Methods

3.1 Synopsis

This chapter provides an overview of the materials used throughout the study and discusses the main experimental techniques used. The heavy crude oil properties including density and viscosity are provided along with SARA analysis of the oil. General experimental procedures are described along with more detailed discussion relating to the measurement principles and data analysis. This chapter describes the core materials and experimental methods used, while further specific details relating to the experimental methods set-up, reproducibility are provided in the relevant results chapters.

3.2 Materials

3.2.1 Heavy crude oil

Heavy crude oil was obtained from a Colombian oilfield *via* primary recovery (without addition of any chemicals) and was used throughout the study. Prior to its use, the oil sample was shaken and de-gassed to obtain the homogenous oil without any dissolved gas (*i.e.* dead oil). To prevent further loss of volatile organic components (*e.g.* lightweight hydrocarbons), the oil container was kept sealed using Parafilm (Bemis, USA) and stored in a cool environment. The oil density, viscosity and component analysis are discussed below.

Oil density: The oil density at ambient pressure (~1 bar) was measured using the U-tube oscillation technique (Y-shaped oscillator, see **Figure 3.1**) which is a specific density meter for measuring the density of crude oils (DMA 4200M, Anton Paar, UK). The technique provides a density value based on a precise liquid volume and has been shown to be highly accurate. The measurement technique is based on the correlation between fluid density (ρ) and oscillation period (τ) of the oil-filled U-tube:

$$\rho = M\tau^2 - N \tag{3.1}$$

where M and N are constants based on the instrument geometry. At least two known fluids (*e.g.* dry air and pure degassed water) are used to calibrate with a specific oscillation period.

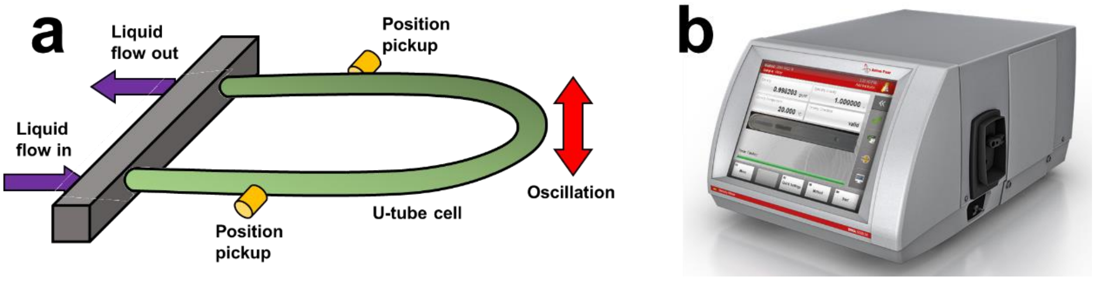

Figure 3.1. Schematic of U-tube oscillation cell (a) and DMA 4200M digital density meter (Anton Paar, UK) (b).

To measure the oil density at a desired temperature, a 5 mL oil sample was first pre-heated to the desired temperature and then injected into the U-tube cell (injection volume ~3 mL). With the sample and U-tube cell environment at the set-point temperature (controlled by a built-in thermostat), the U-tube was electronically excited to oscillate at its characteristic frequency. The oscillation frequency was measured by detecting a light beam that was interrupted by a small coating on the oscillating glass sensor and the oscillation period (τ) determined (reciprocal of frequency). Toluene was used to clean the oil sample from the U-tube cell by injecting excess toluene until the U-tube cell effluent became clear. The oil density was measured at 20, 40, 60 and 80 °C with density values reported in **Table 3.1**.

Table 3.1. Oil density as a function of temperature (ambient pressure).

Temperature (°C)	**Density (g/cm^3)**
20	0.97504
40	0.96564
60	0.94631
80	0.93801

For the high pressure studies, the oil density at high temperature and high pressure was estimated as follows. The oil density at 140 °C and 1 bar was estimated by extrapolating the oil density measured at 20, 40, 60 and 80 °C and 1 bar and was found to be 0.9131 g/cm^3. The oil density at high pressure (ranging from 10 to 200 bar) was determined from the pressure-density relation determined for Athabasca bitumen and reported by Nourozieh *et al*.[148] The estimated oil densities are shown in **Table 3.2**.

Table 3.2. Oil density at elevated pressures.

Pressure (bar)	Density (g/cm^3)
1	0.9131
10	0.9138
100	0.9207
200	0.9285

Oil viscosity: A rheometer (DHR-2, TA Instruments, USA) equipped with a 2° cone geometry was used to measure the oil viscosity as a function of temperature, see **Figure 3.2**. Prior to measurement, the oil sample was shaken for 24 h to obtain a homogenous oil at ambient conditions. To measure the oil viscosity at a given temperature, the oil sample was heated in a water bath to a desired temperature and then ~2 mL oil was pipetted and placed on the rheometer base which was pre-heated to the same temperature. The geometry was then positioned over the oil sample to the predetermined geometry gap and any excess oil removed using a spatula. The oil and geometry were left in contact undisturbed until the set-point temperature was reached. To minimise evaporative loss of light oil fractions, the sample was covered using the geometry cell which was saturated with the same oil. With the sample at the desired temperature the measurement is initiated and the viscosity measured during a shear ramp between 0.1 to 1000 s^{-1}.

Three repeat measurements at each temperature were conducted and the average viscosities provided in **Figure 3.3**. Each measurement was conducted with a new oil sample to prevent contamination and any influence from possible evaporation of light oil fractions at high temperatures. At a given temperature, the oil viscosity was shown to be independent of the shear rate and behaved as a Newtonian fluid.

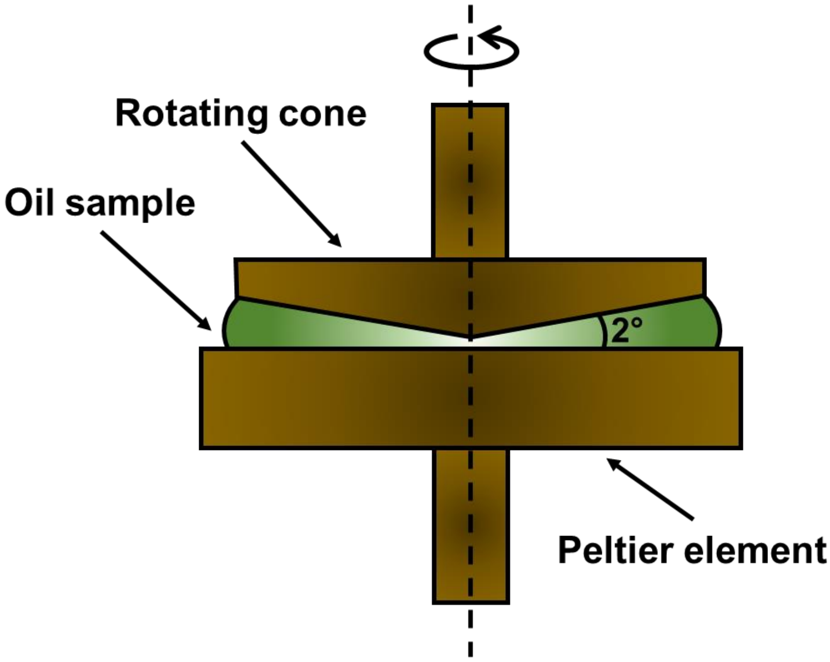

Figure 3.2. Schematic of the rheometer set-up with the oil sample positioned between the Peltier plate and 2° cone geometry.

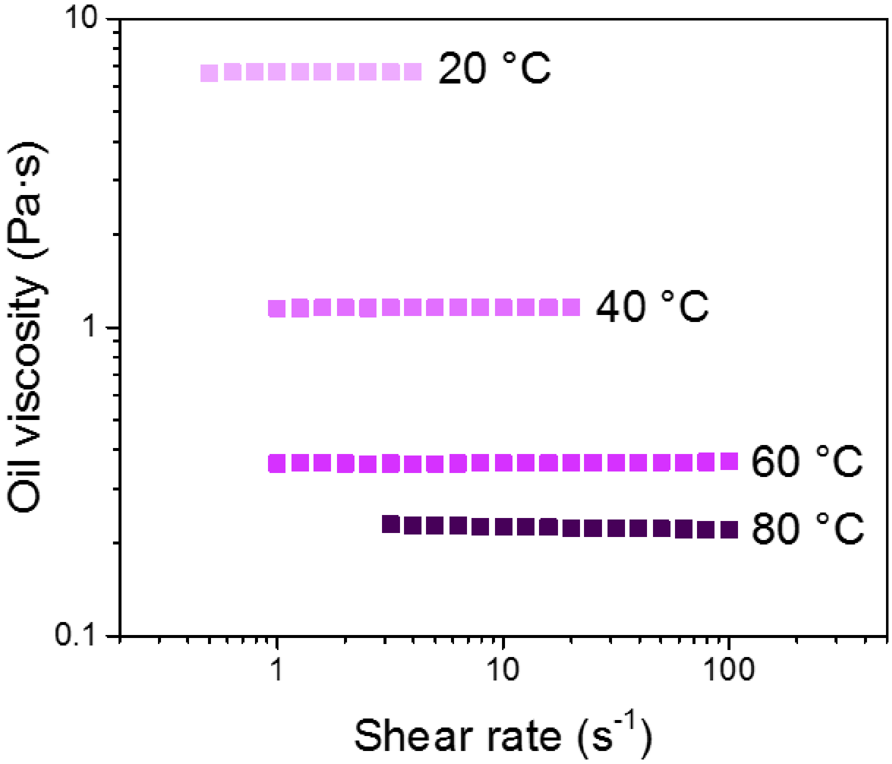

Figure 3.3. Heavy crude oil viscosity as a function of shear rate and temperature.

SARA: The composition of the heavy crude oil was determined by the SARA method to determine the saturate, aromatic, resin and asphaltene content by thin layer chromatography using IP 469 standard.[149] The method separates fractions by solubility (asphaltenes and maltenes) and chromatography to separate fractions based on polarity.

Firstly, asphaltenes are precipitated using heptane. The remaining factions (maltenes) are then separated using a chromatographic column and running solvents of different polarity. The saturate fraction consisting of nonpolar linear hydrocarbons and cyclic alkanes is removed by flushing the maltenes with alkanes through the column while all others fractions are adsorbed onto the column. The aromatic fraction is then washed-off the column to separate this fraction from the adsorbent using an aromatic solvent, *i.e.* benzene. Resins are then eluted from the column using a polar solvent, such as methanol. The polarizability increases from the saturate to asphaltene fractions. All four crude oil components are reported as wt%. The SARA analysis of the heavy crude oil used in the current study is given in **Table 3.3**.

Table 3.3. Properties of heavy crude oil.

SARA analysis (IP 469)				**TAN (ASTM D664)**	**H/C**
Saturate	***Aromatic***	***Resin***	***Asphaltene***		
7.4%	37.8%	15.3%	39.5%	0.134 mg KOH/g	1.34

TAN: Following ASTM D664, the acid number of the heavy crude oil was determined by potentiometric titration. The method determines the acidic components in the heavy crude oil by titrating the oil with potassium hydroxide (KOH). The mass of base needed to titrate the sample is expressed as mg of KOH per one g of oil sample and defines the total acid number (TAN).

The heavy crude oil was dissolved in a mixture of toluene, isopropanol and a small amount of water and then titrated potentiometrically with 0.1 M alcoholic potassium hydroxide (dissolved in propanol). A glass electrode and reference electrode were immersed in the sample to measure the voltage or potential as an acid or base indicator. The volume of KOH used to neutralise the oil sample was converted into unit of mg of KOH per one g of oil sample. The heavy crude oil used in the current study has TAN of 0.134 mg KOH/g as reported in **Table 3.3**.

H/C: An Elemental Analyser (CHNS-O, Flash EA2000, CE Instruments, UK) was used to determine the organic elements in the heavy crude oil. The oil was combusted in a furnace with excess oxygen. Then, the produced gases were separated through a chromatography column and passed through a thermal conductivity detector to obtain the elements (*e.g.* H and C elements) and their amounts.

The hydrogen to carbon (H/C) ratio was determined with a high H/C ratio indicating saturated hydrocarbons in the crude oil (*e.g.* H/C of alkane > 2) and a low H/C ratio implying unsaturated or aromatic hydrocarbons (*e.g*. H/C of benzene = 1). The heavy crude oil sample had a H/C ratio of 1.34 (shown in **Table 3.3**), suggesting high aromatic and less saturated hydrocarbons present in the oil, qualitatively in agreement with the SARA analysis.

3.2.2 Chemicals

Sodium dodecyl sulfate (SDS; Sigma-Aldrich, UK) was used as an anionic surfactant without any purification. Sodium chloride (NaCl ≥ 99.5%, Sigma-Aldrich, UK) and calcium chloride dehydrate ($CaCl_2$ ≥ 99.5%, Sigma-Aldrich, UK) were used as received to prepare the brine solutions. Ultrapure Milli-Q water (Merck Millipore, USA) was used in all experiments with a resistivity of 18.2 MΩ·cm and pH of 5.5 ± 0.5.

Brine density: The density of NaCl and $CaCl_2$ solutions at relevant concentrations and 60 °C and ambient pressure (~1 bar) were determined from the temperature-concentration-density relationship for each specific brine as described by Green and Perry,[150] shown in **Table 3.4**. The brine density at elevated pressures from 10 to 200 bar and 140 °C was estimated using the high pressure equation of state for seawater given by Millero *et al*,[151] see **Table 3.5**.

Table 3.4. Brine density at various concentrations and 60 °C and ambient pressure.

Concentration (ppm)	**Density (g/cm^3)**	
	NaCl	***$CaCl_2$***
2,000	0.9846	0.9847
25,000	1.0001	1.0035
60,000	1.0242	1.0325

Table 3.5. Brine density at various concentrations and 140 °C and elevated pressures.

Pressure (bar)	**Density (g/cm^3)**					
	NaCl			***$CaCl_2$***		
	2,000 ppm	***25,000 ppm***	***60,000 ppm***	***2,000 ppm***	***25,000 ppm***	***60,000 ppm***
1	0.9285	0.9443	0.9685	0.9200	0.9401	0.9709
10	0.9292	0.9450	0.9694	0.9208	0.9408	0.9718
100	0.9358	0.9521	0.9783	0.9273	0.9478	0.9807
200	0.9427	0.9596	0.9879	0.9342	0.9553	0.9903

The density of brine + nanofluids were assumed to be equivalent to the brine fluid density at a given brine concentration, temperature and pressure, since the nanofluids concentration was very low and therefore considered to have a negligible effect on the fluid density.

Density of aqueous fluids with particles and surfactants: On several occasions, fluids were prepared with very low concentrations of PNIPAM, SDS and blends of PNIPAM + SDS (*i.e.* at concentrations $\leq 5 \times 10^{-3}$ wt%). For these fluids the pure water density was used at the given temperature and pressure. Water density at elevated temperatures ranging from 20 to 80 °C and 1 bar was measured using the U-tube oscillation density meter (DMA 4200M, Anton Paar, UK). The water density at 140 °C (ambient pressure) was determined by extrapolating the measured density at 20, 40, 60 and 80 °C. The water density at elevated pressures and 140 °C was calculated from the high pressure equation of state given by Millero *et al.*[151] The water density at elevated temperatures and pressures are given in **Table 3.6** and **Table 3.7**.

Table 3.6. Water density at various temperatures (ambient pressure).

Temperature (°C)	**Density (g/cm^3)**
20	0.99867
40	0.99667
60	0.98476
80	0.98164

Table 3.7. Water density at various pressures (140 °C).

Pressure (bar)	**Density (g/cm^3)**
1	0.9273
10	0.9280
100	0.9346
200	0.9415

3.2.3 Nanoparticle synthesis

Poly(*N*-isopropylacrylamide) was synthesised to test the performance of the nanoparticles to enhance oil droplet dewetting dynamics and equilibrium state. *N*-isopropylacrylamide (NIPAM, Sigma-Aldrich), N,N' Methylenebisacrylamide (BA, Fluka) and potassium persulfate (KPS, Merck) were used as received to synthesise PNIPAM particles following the method published by Li *et al.*[20, 152]

To synthesis the nanoparticles, NIPAM (2.25 g) was dissolved in 250 mL Milli-Q water in a 500 mL three-necked flask. BA (75 mg) was then added under nitrogen bubbling through for 30 min with continuous magnetic stirring at 300 rpm. The temperature was raised to 70 °C *via* a thermostatically-controlled aluminium heating block and held for a further 30 min. During this time, KPS (0.25 g) was dissolved in 10 mL of water and degassed *via* nitrogen. This solution was then added dropwise to initiate the reaction *via* a gas-tight syringe. The reaction was left to polymerise at 70 °C for 3.5 h. The resulting dispersion was passed through glass wool to remove any agglomerated material and then further purified 5 times by centrifugation at 10,000 rpm.

3.2.4 Model substrate

Glass microscope slides (Fisher Scientific, UK) of borosilicate (> 80% SiO_2, **Figure 3.4**) were used as model substrates without any surface modification (unless specified). The ~1 mm thick glass slides were cut into squares of ~25 × 25 mm. It should be noted that the model glass substrates were used to represent the clastic reservoir (*i.e.* sandstone rock) which consists of silicate minerals and represents the majority of conventional petroleum reservoirs.

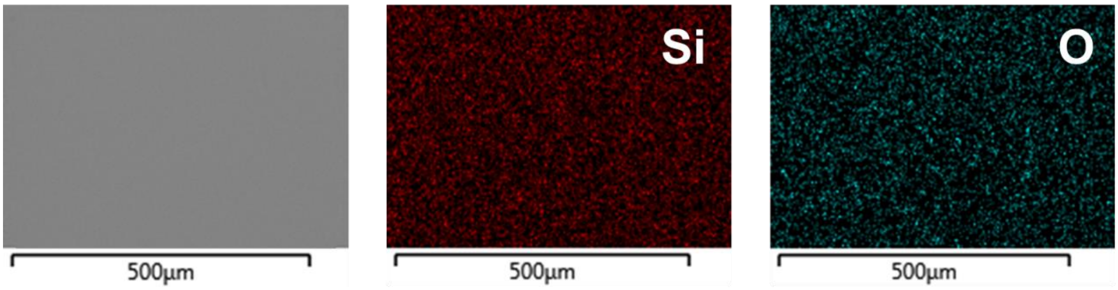

Figure 3.4. SEM-EDX of glass slide showing main compounds (silica and oxygen).

It should be acknowledged that reservoir rocks are porous with significant roughness that can influence the nature of heavy oil droplet dewetting. The former describes the porethroat and governs capillary pressure due to small pore radius,[153] while the latter is known to affect the degree of wetting as discussed in Chapter 2. Since the study is focused on the fundamental nature of oil droplet dewetting at elevated conditions (*i.e.* high pressure, high temperature and high salinity) and in the presence of chemical additives, the solid substrate was chosen to be non-porous and smooth to enable greater interpretation of the data and provide more reliance on understanding the influence of experimental parameters.

The model substrate surface roughness was measured using a surface profilometer (Form Talysurf PGI 800, Taylor Hobson, UK) and had a RMS of 1.3 nm and an arithmetical mean deviation (R_a) of 0.9 nm. These surfaces are considered to be very flat and smooth in comparison to reservoir rocks.[153]

3.3 Experimental Methods

3.3.1 Substrate preparation

All substrates were prepared following the same treatment protocol of rinsing with Milli-Q water, drying with nitrogen and 15 min UV/Ozone (Procleaner^{TM}, Bioforce Nanosciences, USA) of the dry substrates to remove any residual organic components. Glass substrates were verified to be clean when the water contact angle in air was < 1°. Glass substrates were prepared on the day of experiments to minimise any possible interaction with organic materials or contamination by dust.

3.3.2 Oil-water interfacial tension measurement

Although there are several techniques to measure the oil-water interfacial tension including force measurements (*e.g.* Du Noüy ring and Wilhelmy plate), optical tensiometry using pendant drop shape analysis was used in the current study. The pendant drop technique for measuring liquid-liquid interfacial adsorption was favoured since it (i) allows the measurement of dynamic adsorption, (ii) verifies that the steady-state is attained and (iii) is independent of solid-liquid interactions. Using this approach, the interfacial tension can also be measured in relation to the droplet contact angle using the droplet shape analysis method.

The interfacial tension between two immiscible liquids is determined by the force balance of the pendent drop protruding from a needle.[154] Balance of interfacial and buoyant forces enables the interfacial tension (σ) to be determined as follows:

$$\sigma = \frac{\Delta\rho g {R_0}^2}{\beta} \tag{3.2}$$

where $\Delta\rho$ is the density difference between the two immiscible fluids, g the gravitational constant, R_0 the drop radius of curvature at the apex and β the shape factor (**Figure 3.5**).

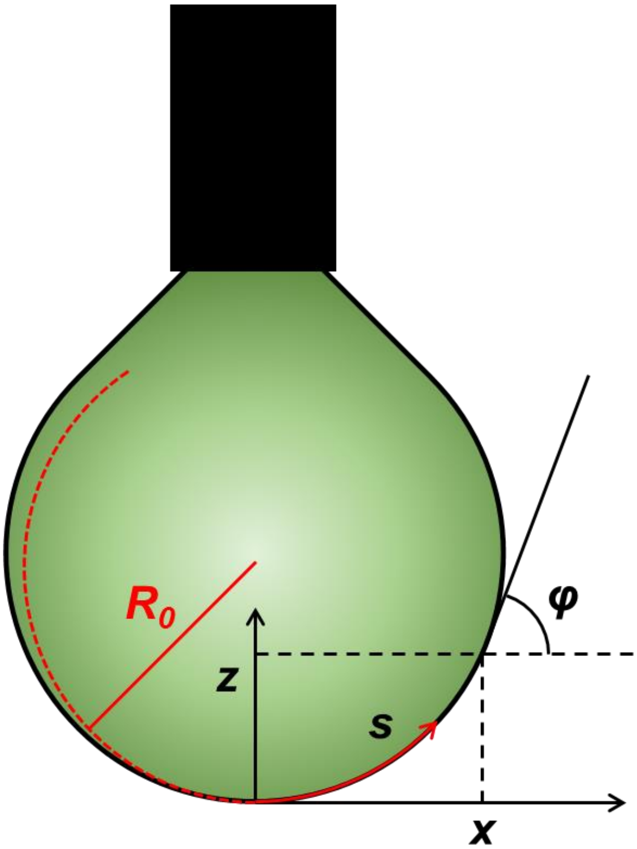

Figure 3.5. Schematic of a pendent drop hanging from a needle with the droplet shape described by cylindrical coordinates, tangent angle (φ) and the apex curvature (R_0).

The pendent drop obeys the Young-Laplace equation[155] balancing the Laplace pressure across the interface with curvature of the interface. The pendent drop is assumed to be axisymmetric, with the shape factor (β) expressed in the cylindrical coordinates:

$$\frac{dx}{ds} = \cos(\varphi) \tag{3.3}$$

$$\frac{dz}{ds} = \sin(\varphi) \tag{3.4}$$

$$\frac{d\varphi}{ds} = 2 + \beta z - \frac{sin(\varphi)}{x} \tag{3.5}$$

The solution is an iterative approximation of fitting a perimeter line to the droplet shape (image capture: OneAttension, Biolin Scientific, Finland). The size of the pendent drop is important to ensure reliable data. For the correct determination of interfacial tension, the droplet volume should be large enough to induce a pendent drop shape (becomes increasingly problematic for fluids of equivalent density). For the heavy crude oil-water system, drop volumes of ~10 µL were found to be sufficient to induce pendant shapes. An inverted or hooked needle was used for the oil-in-water system to allow the oil droplet to be visible in the water phase.

In the current study, interfacial tension between heavy crude oil and water was measured using a Theta Optical Tensiometer (Attension®, Biolin Scientific, Finland) equipped with thermal cell (C217W, Biolin Scientific, Finland) and operated at desired temperatures, with the temperature monitored by k-type thermocouples (TC-08 data logger, Pico Technology, UK). A stainless inverted needle (Gauge 22) with a 1 mL gas-tight syringe (Hamilton Co., USA) was filled with 1 mL of heavy crude oil and submerged in the aqueous solution at the experimental temperature for 10 min to ensure the needle and crude oil were at the desired experimental temperature. The oil drop was subsequently discharged from the needle using a micro-syringe pump (C201, Biolin Scientific, Finland) to form a 10 µL droplet instantaneously. The droplet shape profile was recorded at a constant frame rate (2 fps) to capture the dynamics of interfacial tension as surface-active species partition at the oil-water interface. The measurement was stopped once steady-state conditions were reached.

3.3.3 Oil droplet deposition

A 10 µL heavy crude oil droplet was deposited on a clean glass substrate in the centre of the substrate using a 100 µL auto-pipette. It is noted that at the experimental temperature of 60 °C, both gravitational and inertial effects on the 10 µL oil droplet dewetting can be neglected compared to the interfacial tension due to very low Bond and Weber numbers, respectively.[13, 156] The substrate was warmed (~50 °C) to enhance heavy crude oil droplet spreading on the surface to form a thin circular oil film of approximately 8 – 10 mm diameter (**Figure 3.6**) and having a contact angle ~172.7° (measured through air phase). The oil film was left undisturbed for ~2 h allowing the wettability of the strongly water-wet glass substrate to be slightly altered (although this change was not measured). Prior to each experiment the droplet contact angle measured through the air phase was ~172.7°, which was assumed to be the initial contact angle (θ_i) of the oil-water-substrate system once air is displaced by water to induce oil droplet dewetting. It is noted that the initial contact angle (θ_i) of the oil-water-substrate is not equivalent to the contact angle of air-oil-substrate, however due to limitations of the experimental set up and data acquisition rates, the initial contact angle of the oil-water-substrate system could not be obtained (images compared in **Figure 3.10**a and c).

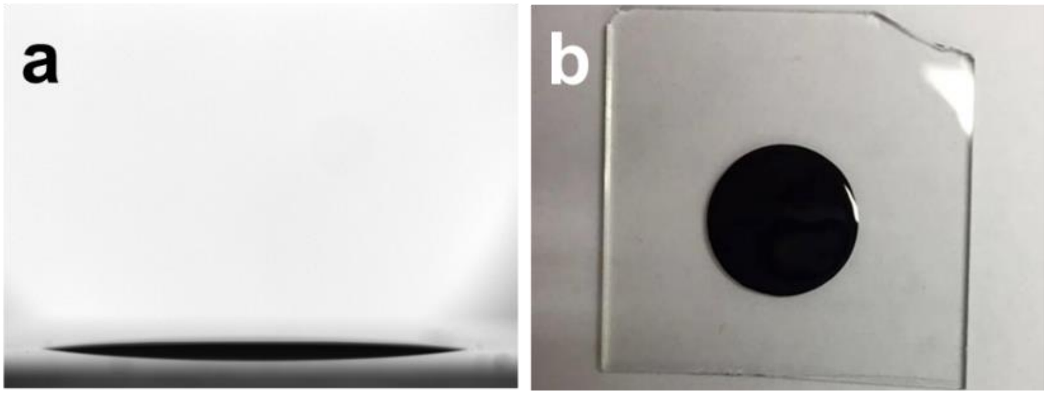

Figure 3.6. Thin oil film deposited on glass substrate: side view (a) and top view (b).

3.3.4 Contact angle measurement

The contact angle (θ) is determined by drop shape analysis using a sessile droplet positioned on the substrate. The angle formed between the substrate baseline and the tangent line to the droplet interface is the contact angle (determined using the Theta software; OneAttension, Biolin Scientific, Finland), see **Figure 3.7**. The software fits the Young-Laplace equation (Equation (3.6)) to the droplet shape using multiple points on the droplet profile. Intersect of the tangent line at the three-phase contact point and the baseline defines the contact angle. It is worth noting that the contact angle is normally defined through the dense fluid phase, *i.e.* measuring the contact angle in the dense fluid phase relative to light fluid phase. In the present work, for the oil-water-substrate system, the contact angle is measured through the water (aqueous) phase.

$$\Delta P = \sigma \left(\frac{1}{R_1} + \frac{1}{R_2} \right) \tag{3.6}$$

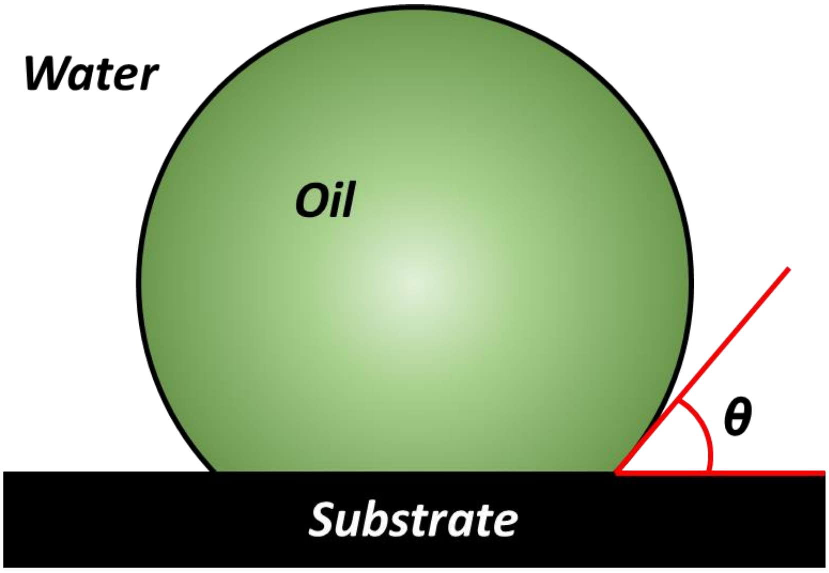

Figure 3.7. Schematic of sessile oil droplet on a substrate submerged in water. The contact angle (θ) is measured through the water phase.

After the thin oil film is deposited on the substrate, the glass substrate is then placed on a fabricated base in the middle of the insulated thermal cell and the cover lid added until the desired experimental temperature was reached and remained constant (~10 min). A thermocouple (TC-08 data logger, Pico Technology, UK) with 2 sensors was used to monitor fluid temperature inside the cell during the measurement both above the substrate and near the cell bottom, see **Figure 3.8**.

The water (aqueous solution) was pre-heated to the desired temperature and added to the thermal cell at 1,400 mL/min for 60 mL with the fluid discharged onto the base of the cell, below the glass substrate. The water flow rate was chosen to ensure that water quickly flowed over the oil thin film to prevent any air bubbles from being generated on the oil droplet, which was a problem with a slow water influx (the oil prefers to wet air rather than water). The oil droplet then dewetted spontaneously due to a negative spreading coefficient and the rate of dewetting was independent of the water influx.

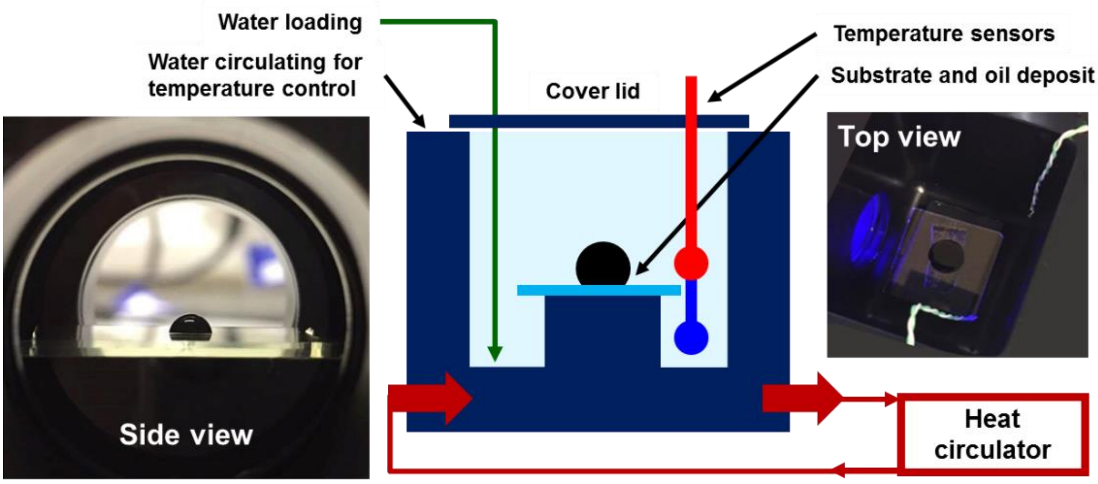

Figure 3.8. Insulated thermal cell and heat circulator with the oil-deposited substrate placed in the centre of the measurement cell. Two temperature sensors are placed above the substrate and near the cell bottom to monitor fluid temperature.

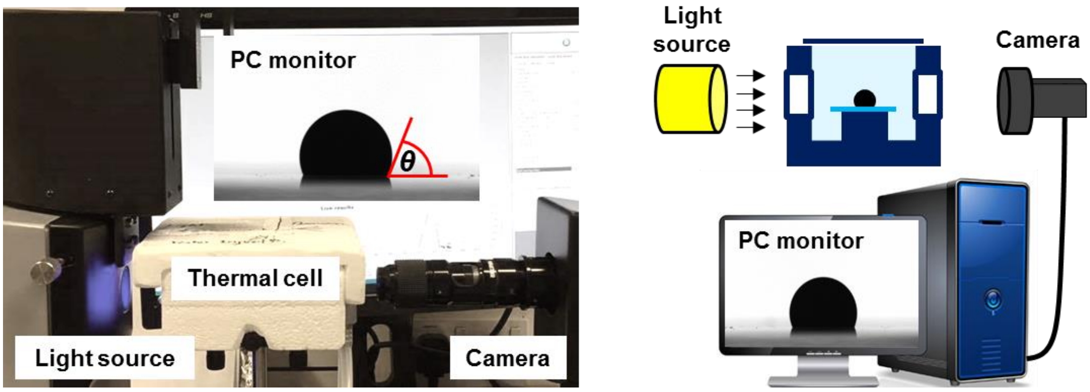

Figure 3.9. Image and schematic of the Attension Theta Optical Tensiometer with the thermal cell used to observe oil droplet dewetting (monitored by the contact angle). The oil droplet is illuminated by a back light source through transparent optical windows.

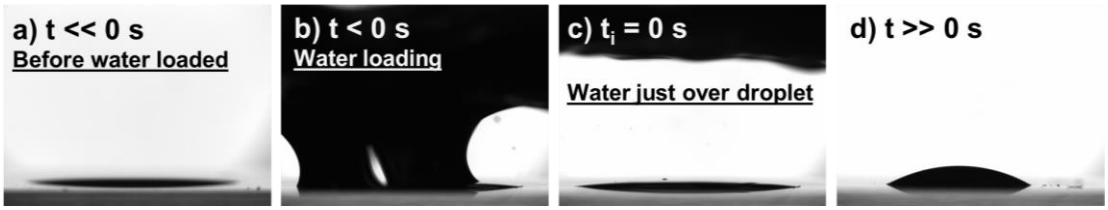

Figure 3.10. Images showing the process of water flooding in the measurement cell. Before water flooding (a); immediately prior to water contacting the thin oil film (b); water in contact with the thin oil film with the condition defined as $t = 0$ (c); droplet recession following complete submergence of the thin oil film by water (d).

The tensiometer camera (Theta Attension®, Biolin Scientific, Finland) was triggered prior to oil droplet recession (**Figure 3.9**) and images of the droplet dewetting were collected until a steady-state condition was reached (*i.e.* the contact angle remained constant). The time when water phase fully submerged the oil phase was defined as the initial dewetting time ($t_i = 0$) with an initial contact angle (θ_i), shown in **Figure 3.10**. The substrate-water-oil contact angle (measured through the water phase) was determined from image analysis using the OneAttension software.

The thin oil film receded inwards in the radial direction to form a droplet, contributing to the perfect axisymmetric and spherical-cap shape (**Figure 3.11**a). On occasions the oil droplet was observed to pin and did not recede due to imperfections on the surface or resulting from air trapped within the oil droplet (**Figure 3.11**b). These data were not considered in the analysis. Two to four repeat experiments were made to ensure good reproducibility for each test condition.

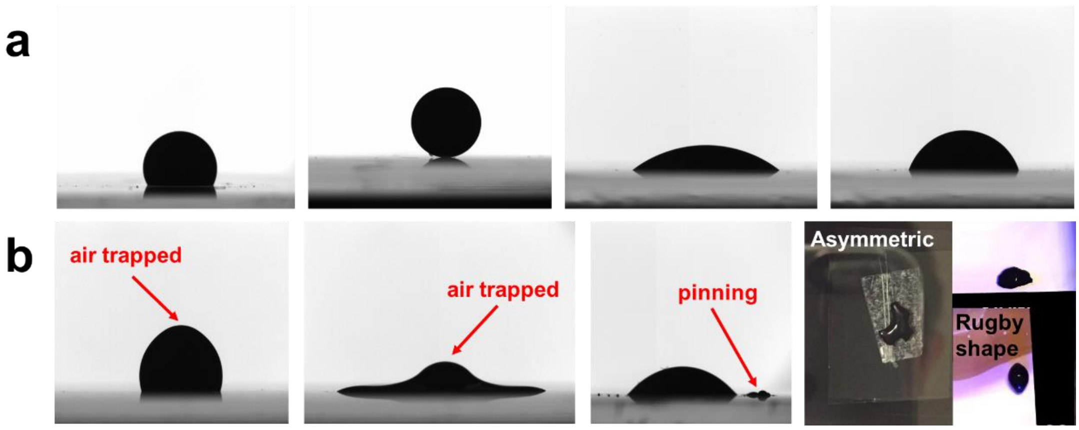

Figure 3.11. Oil droplet shape during dewetting. The droplet maintains axisymmetric and spherical shape during dewetting (a). The droplet is asymmetric due to air bubbles being engulfed in the oil droplet, or pining of the oil droplet due to surface asperities (b).

3.3.5 Zeta potential measurement

Zeta potential (ψ) is an electric potential measured at the slip plane as colloid particles/droplets migrate in an electric field (**Figure 3.12**). The zeta potential represents a potential difference between the attached fluid layer to the dispersed colloid and dispersing medium. It is noted that the zeta potential is smaller in magnitude than the true electrostatic surface potential as it measured at a distance away from the colloid surface.

The zeta potential is not measured directly but determined from the electrophoretic mobility of the dispersed colloids.[157] An electric field is applied across the colloidal dispersion promoting colloids to migrate towards the electrode of opposite charge. The zeta potential is proportional to the migration velocity and is calculated by the Smoluchowski's theory[158]

$$v = \frac{\varepsilon\varepsilon_0\psi}{\mu}E' \tag{3.7}$$

where v is the colloid migration velocity (electrophoretic), μ the dispersing fluid (water) viscosity and E' the electrical field strength. The migration velocity (v) is measured using laser Doppler electrophoresis.

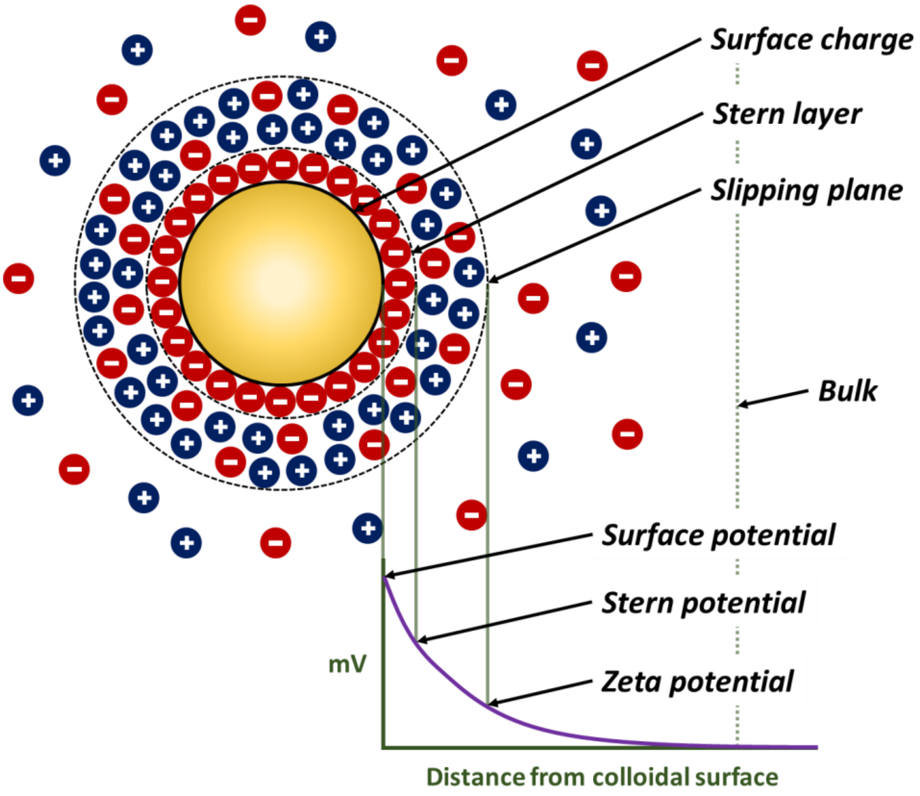

Figure 3.12. Schematic showing the decay in surface charge due to ion screening and the location of the slipping plane that describes the surface zeta potential.

In the current study, the zeta potentials of oil droplets, silica particles (representative of the glass substrate) and PNIPAM nanoparticles dispersed in aqueous (water or brine solutions) media were measured using the Zetasizer Nano ZS (Malvern Instruments, UK). The experimental temperature was controlled within ± 1 °C by the instrument thermostat. For each solution, 12 measurements were performed and the data averaged.

A very low concentration oil-in-water emulsion was prepared by adding 10 µL crude oil in 60 mL Milli-Q water and homogenised (T18 digital ULTRA-TURRAX®, IKA, Germany) at 70,000 rpm for 5 min, producing oil droplets of ~80 µm diameter. Only stable oil droplets were sampled at 5 min after homogenisation for the measurement. The refractive index of the crude oil was taken to be 1.50.[159, 160] 100 nm silica particles (AngstromSphere, USA) and PNIPAM nanoparticles were prepared at 1,000 ppm in the aqueous solutions and ultra-sonicated (FB120, Fisher Scientific, USA) for 5 min prior to measurement.

3.3.6 Atomic Force Microscopy

Interaction forces between an oil-coated colloidal probe and glass substrate were measured in brine solutions. To prepare the oil-coated probes, silica spheres (30 ± 2 µm diameter; Duke Scientific, USA) were dip-coated in oil solution.[161] Oil solution was prepared by dissolving heavy crude oil in 1:1 heptol solution to a concentration of 0.5 g/L. The solution was centrifuged at 10,000 rpm for 30 min to remove any contained ultra-fine solids. The silica spheres were dipped into the solution for 1 min. Heptol solution was allowed to evaporate for 24 h. The oil-coated silica spheres were glued onto a tipless AFM cantilever (TL-CONT-10, Nanosensors, Switzerland) using a two-part epoxy and allowed to cure overnight. The probes were then examined by SEM (Hitachi TM3030, UK) to verify that colloidal probe was appropriately orientated (**Figure 3.13**a). The hydrophobicity of oil-coated silica spheres was examined by measuring the water contact angle in air (on representing glass slide after the same dip-coating treatment) to verify that it was sufficiently coated by oil components (**Figure 3.13**b and c).

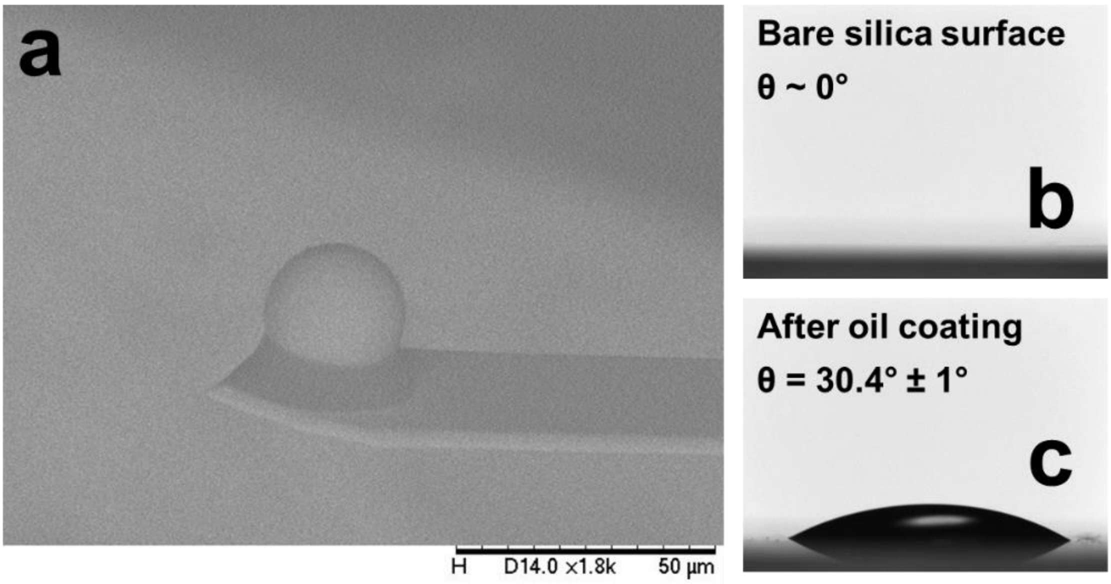

Figure 3.13. SEM of colloidal probe glued on a tipless AFM cantilever confirming the central location of the silica sphere and free of glue contamination (a). Oil components sufficiently coated on silica surface were confirmed by the increase in water contact angle after coating (b) – (c).

The glass substrate was prepared following the method described for oil dewetting experiments. Substrate topography and high profiles were obtained by an Innova AFM (Bruker, USA), see **Figure 3.14**. RMS and R_a determined by AFM ~2.5 ± 4 and 1.9 ± 2 nm, respectively, agree with measurement from surface profilometer.

To ensure the brine solutions were representative of those used in dewetting experiments, 60 mL brine solution was contacted with 10 µL heavy crude oil at 60 °C for 3 h, to allow exchange of soluble species (such as naphthenic acids) into the brine solution.[34]

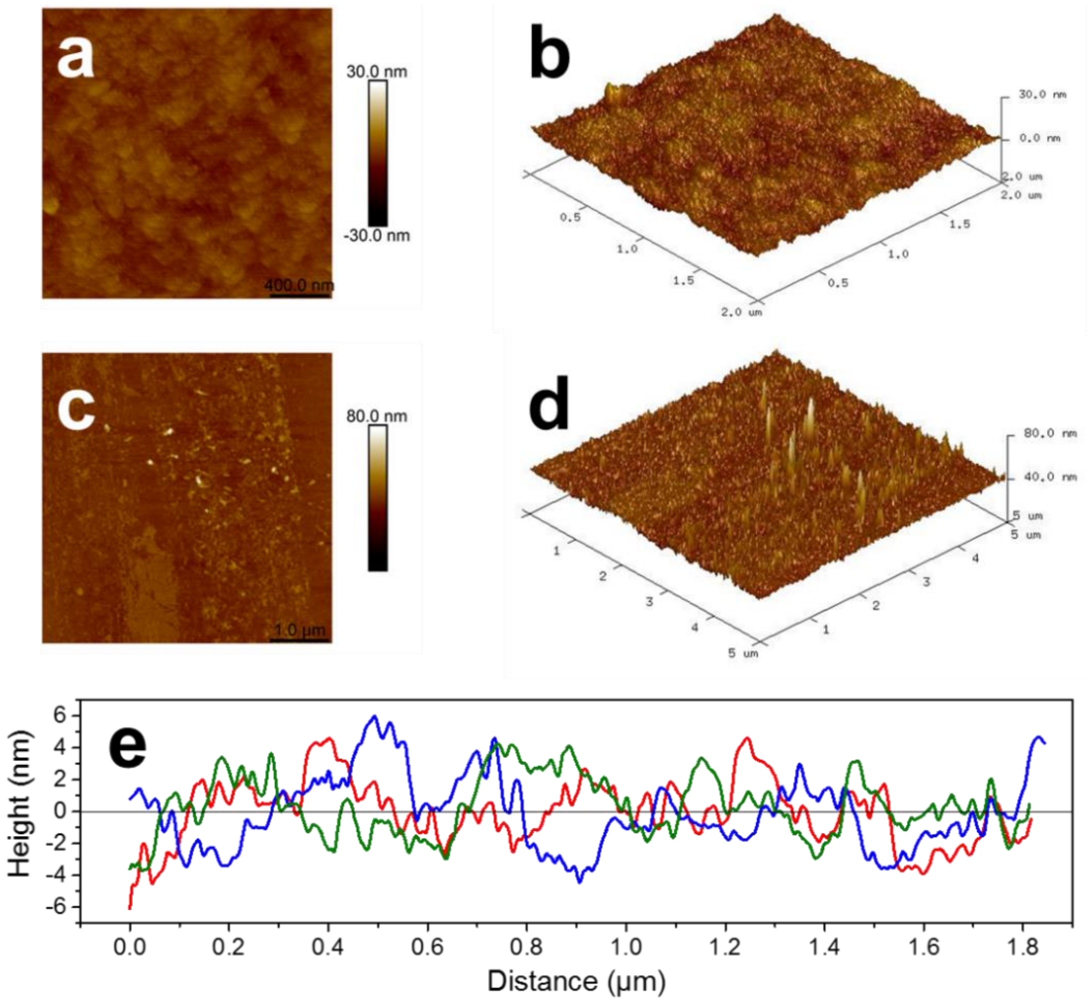

Figure 3.14. Solid substrate topography (a) – (d) and high profiles (e) obtained by AFM.

Force-distance measurements were performed using a Bioscope II AFM (Bruker, USA) at ambient conditions. The cantilevers spring constant were 0.21 – 0.35 N/m as determined by the thermal tune method. Two or three drops of the brine solution were deposited onto the glass substrate before the colloidal probe was immersed into the brine solution. Force curves were obtained at 0.2 Hz at a minimum of three different surface locations. A minimum of 10 force curves per area were collected. Disjoining pressure between oil-coated sphere and glass substrate was determined from the approaching force curve assuming the Hertz theory.[162]

$$a^3 = \frac{RF}{K} \tag{3.8}$$

$$\Pi = \frac{3F}{2\pi a^2} \tag{3.9}$$

where a is contact radius, R the colloidal (oil-coated) sphere radius, F the force, K the elastic modulus of colloidal probe and glass substrate (taken to be 70 GPa),[103] and Π the disjoining pressure.

Chapter 4

Fundamentals of Oil Droplet Dewetting

4.1 Synopsis

The dynamics of oil droplet dewetting can be dramatically influenced by the environment and water chemistry (for example: temperature, pressure and chemical additives). This chapter considers a simple set-up to study the recession of a thin oil film forming a droplet on a model substrate. Heavy crude oil film recession was studied at ambient pressure and increasing temperatures from 40 to 80 °C, with the rate of oil droplet recession increasing with temperature (initial receding rate increased from 0.07 to 3.73 °/s over the 40 – 80 °C temperature range). This effect was mostly attributed to the reduction in oil viscosity (1,150 to 220 mPa·s for 40 °C and 80 °C, respectively). Further contributions from the release of natural surfactants from the heavy crude oil slightly decreased the oil-water interfacial tension from 28.3 to 25.5 mN/m, which lead to a decrease in the equilibrium contact angle from 63.7° to 51.3°. Dynamic dewetting theories were used to model the experimental data where the role of oil viscosity was confirmed to predominantly influence oil droplet dewetting dynamics.

Experiments were conducted at high pressure (≤ 200 bar) and high temperature (140 °C) to better represent the reservoir environment. At elevated pressures, surface-active species such as asphaltenes were dissolved in the heavy crude oil as confirmed by the slight increase in oil-water interfacial tension from 14.4 to 17.6 mN/m when the

pressure was increased from 10 to 200 bar. As a result, the oil droplet showed less droplet recession at high pressures (contact angle increased from 17.9° to 23.1° over the same pressure range) and was attributed to the change in the interfacial tension.

Finally, the role of surfactants for improving oil dewetting was considered. The reduction in oil-water interfacial tension and increase in oil-substrate electrostatic repulsion led to an increase in the rate of oil droplet dewetting and lower equilibrium contact angles. However, at concentrations > CMC, the surfactant concentration was sufficiently high to promote droplet pinch-off due to the very low oil-surface adhesion (2.01 µN) being exceeded by the oil droplet buoyancy force (3.77 µN).

4.2 Introduction

Understanding the fundamental mechanisms for oil film rupture and subsequent oil droplet displacement on reservoir rock is critical to improve oil recovery from challenging environments.[163, 164] Interfacial properties such as substrate wettability and oil-water interfacial tension are often targeted to improve oil recovery from the field.[6, 7, 165] For a single oil droplet on a substrate, the solid-water-oil contact angle (θ) is often considered to describe the potential for oil removal. As previously discussed, the interfacial energies govern the contact angle as described by the Young's equation. To reduce the oil-substrate contact area, the oil-water interfacial tension should be decreased (maximising the oil-water contact area) to increase the probability of oil droplet detachment from the substrate.[7, 166]

Although the equilibrium contact angle (θ_e) is used to define rock wettability in the reservoir environment (oil-connate water-rock), the dynamic contact angle (θ_d) (changing droplet contact angle with time) is rarely considered, although this may be thought of as a better indicator for oil recovery.[16] Basu *et al.*[13] established a simple experimental method to observe spontaneous oil (bitumen) droplet recession by water displacement at elevated temperatures in order to understand the hot water extraction process in oil sands mining. The authors noted that the preferential water wetting on oil sands occurs if the free energy of the water-sand interface is exceeded by the oil-sand interface, hence oil is displaced and released from the sand. A bitumen thin film on a model glass substrate receded spontaneously upon contact with water to form a spherical droplet. High temperatures were shown to increase the droplet receding rate, while high pH reduced the initial droplet receding rate. The reduction in oil viscosity at high temperature was found to promote faster droplet receding.[156, 167] However, the contribution of the oil-water interfacial tension on the contact angle remained to be considered.

To better understand oil dewetting at subsurface conditions, the influence of high pressure and high temperature needs to be studied. Only a few groups have studied the contact angle and oil-water interfacial tension at such extreme conditions, but their findings remain controversial. Yang *et al.*[55] studied a crude oil-carbonated brine-rock system and found the contact angle decreased at high pressure (≤ 200 bar), with the behaviour attributed to oil swelling due to CO_2 diffusion, and the oil-substrate contact area remaining unchanged. Xie *et al.*[17] did not find any influence of pressure (≤ 500 bar) when studying a crude oil-brine-rock system, but showed a slight increase in oil droplet contact angle at high temperature (≤ 140 °C), similar to the findings of Zhang *et al.*[53] who studied oil droplet contact angles on a range of mineral substrates. On the contrary, Nowrouzi *et al.*[54] showed a significant decrease in contact angle and oil-water interfacial tension with increasing pressure. Although some studies attribute the high temperature effects to a disjoining pressure,[17, 54, 168] while the pressure effects remain controversial.

The methodology established by Basu *et al*.[13, 14] has been adopted to study the dewetting of heavy crude oil as a function of temperature, with the experimental data compared to the dewetting dynamic theories previously discussed. The study is extended to high pressure and high temperature environments to assess the dewetting dynamics under extreme conditions, as well as the addition of surfactants that are commonly used to promote droplet recession *via* a reduction in oil-water interfacial tension.

4.3 Experimental Methods

Experimental techniques to measure the oil-water interfacial tension and contact angle were described in Chapter 3. For the study at elevated temperatures, the fluid temperature was set to either 40, 60 and 80 °C at ambient pressure (~1 bar). For the surfactant study the fluid temperature remained constant at 60 °C and ambient pressure. To study the effect of high pressure and high temperature, the high pressure chamber was used with the temperature fixed at 140 °C and the pressures increased from 10, 100 to 200 bar.

The high-pressure chamber (HPC1, Attension® Theta High Pressure, Biolin Scientific, Finland) was equipped with a manual hydraulic pump which was used to pressurise the measurement cell (**Figure 4.1**). The fluid temperature was measured and controlled by the OneAttension software. Due to the complexity of operating at a desired pressure and temperature (pressure-volume-temperature integration), a 10 µL oil droplet was first deposited on a glass substrate before completely filling the high-pressure chamber with the test fluid, which was then sealed at ambient pressure prior to increasing the pressure or temperature.

Preliminary testing of a heavy crude oil droplet in water showed an increase in oil-water interfacial tension and oil droplet contact angle (measured through water) with increasing pressure or decreasing temperature. The pressure was first increased to either 10, 100 or 200 bar (order of minutes) before the test fluid was heated to 140 °C (order of hours). This method of first increasing pressure followed by increasing temperature was adopted to minimise adsorption of surface-active species during experimental set-up (adsorption at room temperature < adsorption at 140 °C). At high temperatures, adsorption of surface-active species is substantial, and due to irreversibly adsorbed asphaltenes,[169, 170] this would lead to results that are not meaningful. Fluid expansion during heating slightly increased the cell pressure, so the desired cell pressure was attained by using the manual hydraulic pump.

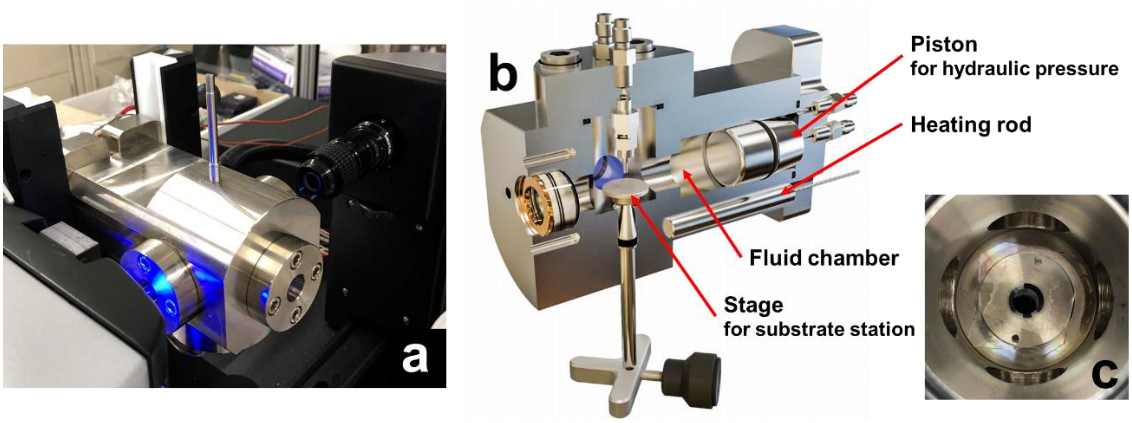

Figure 4.1. Picture showing the high-pressure chamber mounted on the tensiometer (a). Schematic of high-pressure chamber (b) showing the stage where the oil droplet is deposited, and shows the location of the oil droplet on the substrate in the high-pressure chamber (c).

For the high-pressure tests, the oil-water interfacial tension was measured using the sessile drop method rather than the pendent drop method. Due to the nature of the heavy crude oil (very high viscosity ~6,700 mPa·s at 20 °C), the oil could not be injected into the high-pressure chamber using a syringe/needle. For contact angle measurements, the sessile drop method was used. Once at steady-state (~3,600 s after the test conditions were reached), the oil-water interfacial tension and contact angle were determined using the Young-Laplace equation.[154]

4.4 Results and Discussion

4.4.1 Oil droplet dewetting dynamics at elevated temperatures

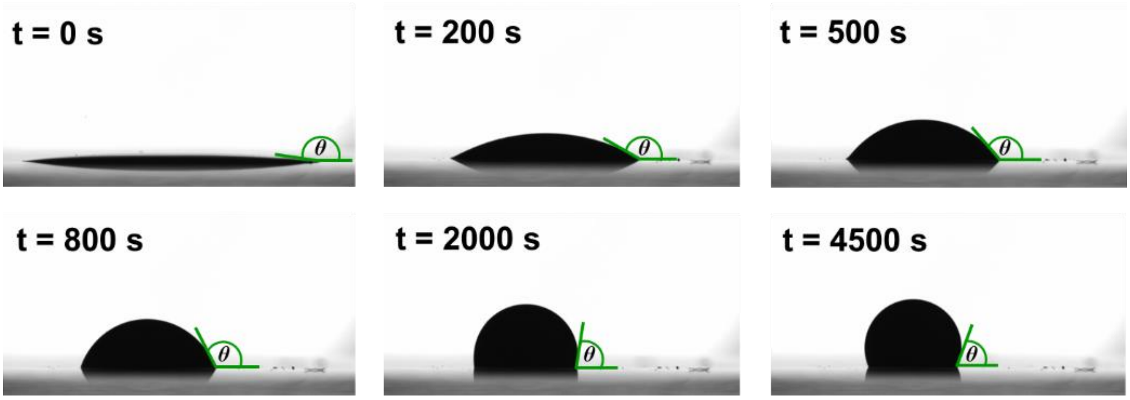

Figure 4.2. Time-dependent dewetting of a heavy oil droplet on a hydrophilic solid surface. For these images the solid surface and water temperature were constant at 40 °C.

The sequence of images in **Figure 4.2** show the dewetting process for an oil droplet deposited on a solid surface. Since $\frac{dG}{dA} < 0$, oil droplet recession occurs spontaneously and the oil-solid contact area reduced to attain a new equilibrium wetted-state, as described by the Young's equation (Equation (2.4)).

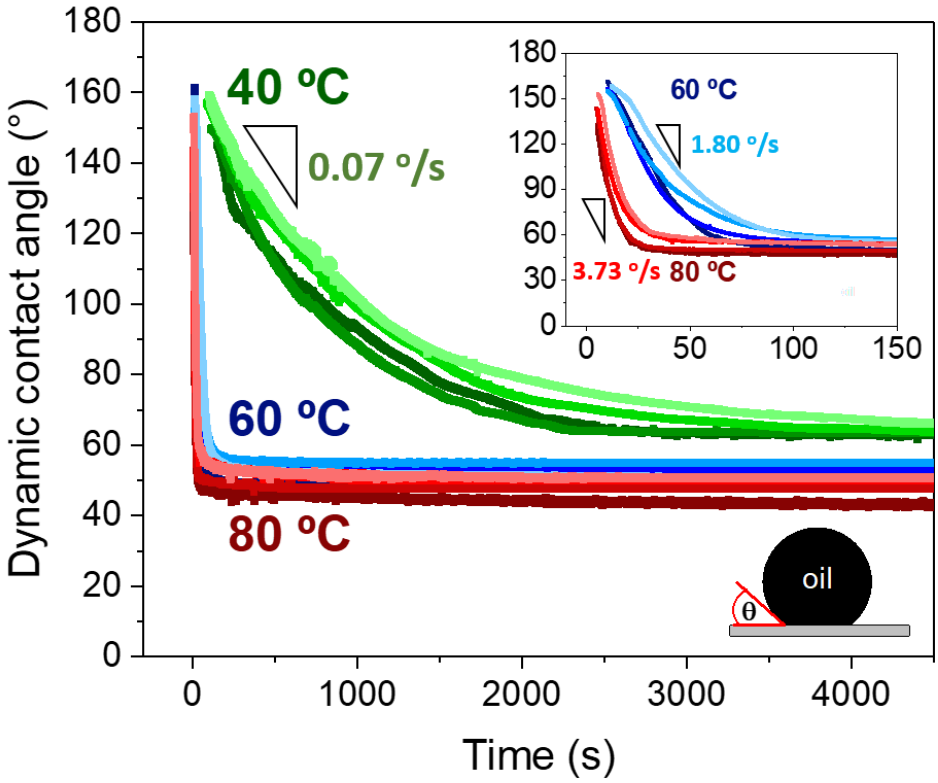

Figure 4.3. Dewetting dynamics of an extra heavy oil film immersed in Milli-Q water at different temperatures: 40 °C, 60 °C and 80 °C. Inset is an expanded region of the initial dewetting dynamics to differentiate between the two higher temperatures. Each experimental condition was repeated four times with measurement variability considered to be negligible.

The rate of oil film dewetting can be determined from the dynamic contact angle, see **Figure 4.3**, with faster dewetting dynamics observed for higher temperature environments. Clearer differentiation between 60 °C and 80 °C is shown in the inset of **Figure 4.3**, with the new equilibrium wetted-states (oil-water-solid surface) attained within a few minutes, contrasting the 40 °C sample which required more than 1 h to reach equilibrium. Moreover, the contact angles at equilibrium were shown to depend on temperature, decreasing from 63.7° to 54.1° and 51.3° with increasing temperature from

40 °C to 60 °C and 80 °C, respectively. Equation (2.4) shows that changes in equilibrium wetted-state result from a change in the balance of energies acting on the three interfaces. Measuring σ_{OW} at equivalent temperatures, **Figure 4.4** confirms a small decrease in σ_{OW} with increasing temperature. Hence, if it were assumed that σ_{OS} and σ_{SW} remained independent of temperature, then θ would decrease, in good agreement with the Young's equation. Previous studies showed variation in the oil-water interfacial tension as a function of pH and temperature,[34, 35, 171, 172, 173, 174] with the effect attributed to the partial solubility of naphthenic acids in water[175, 176] and adsorption of asphaltenes at the oil-water interface.[177, 178, 179]

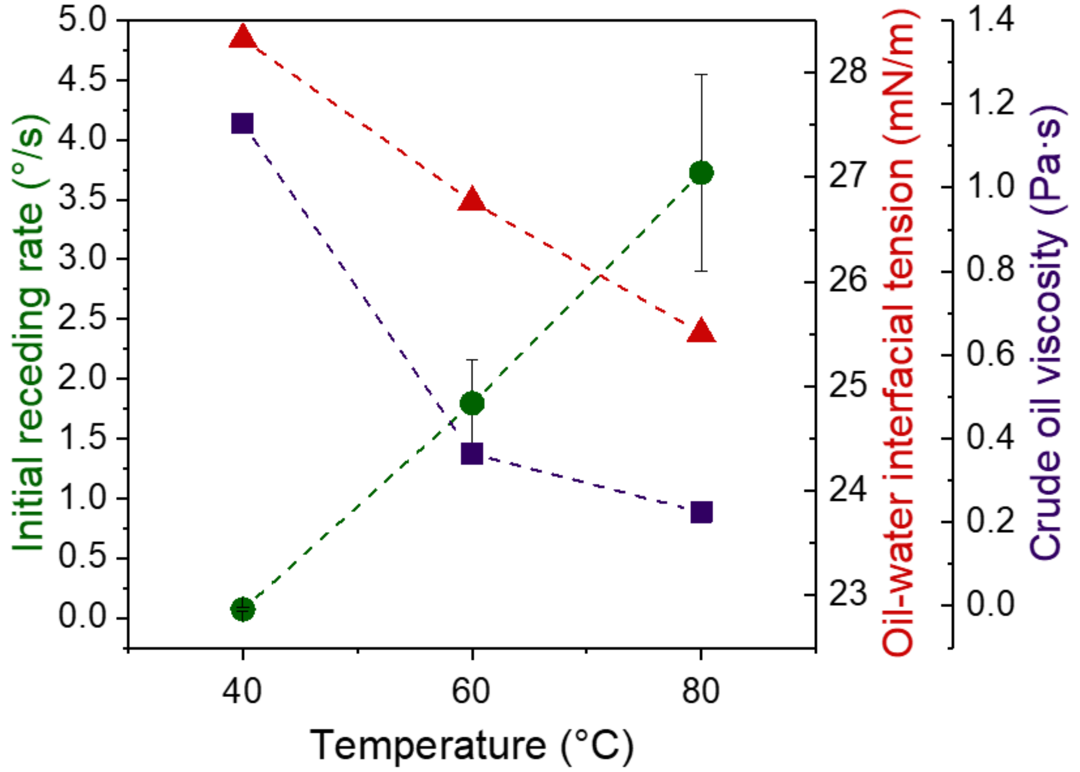

Figure 4.4. Initial oil droplet receding rate as a function of temperature, correlated to changes in oil viscosity and oil-water interfacial tension (error ± 0.03 mN/m). Symbols: circle – oil droplet receding rate, triangle – σ_{OW}, square – μ_o.

Naphthenic acids are considered to be cyclic carboxylic acids of the general form R-COOH, where R can be any cyclo-aliphatic group.[180] Compared to asphaltenes, naphthenic acids are of lower molecular weight, typically less than 450 g/mol, spanning mainly C_{10} to C_{50} compounds with up to six fused ring structures that are mostly saturated.[181]

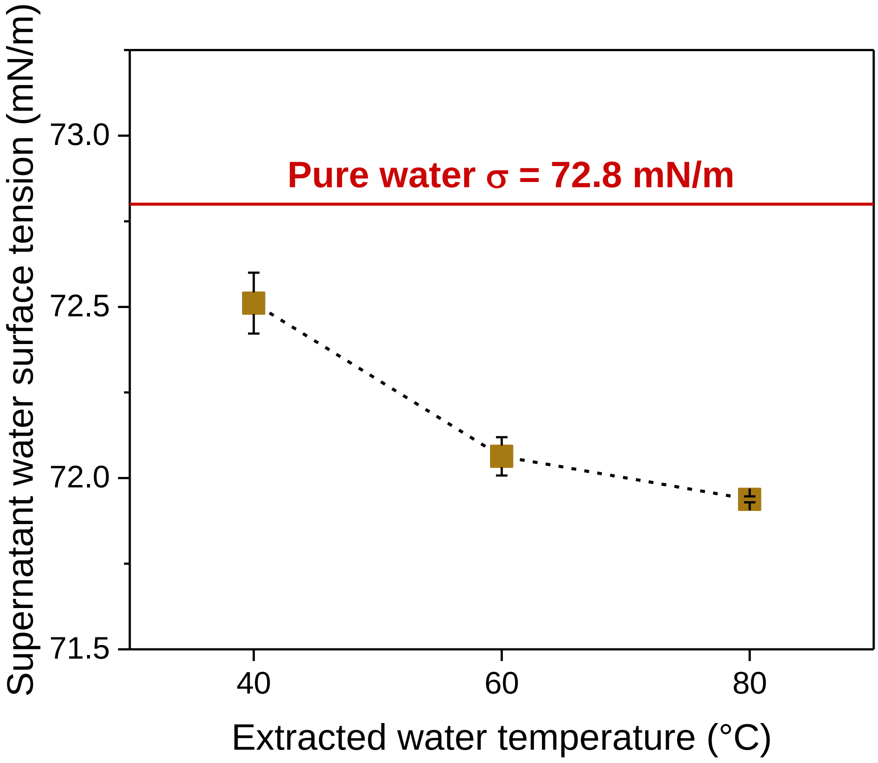

Figure 4.5. Surface tension of extracted water from an oil-water interfacial tension test conducted at 40, 60 and 80 °C. All surface tension measurements are completed at 20 °C. The red line denotes the surface tension of pure water at 20 °C, ~72.8 mN/m.

The surface tension of water extracted from an oil-water interfacial tension measurement at different temperatures (10 µL droplet of heavy crude oil in 60 mL of test fluid) was measured at 20 °C. **Figure 4.5** shows the surface tension of extracted water decreased slightly with increasing experimental temperature (droplet receding test), thus confirming the presence of more naphthenic acids in the water phase at higher temperatures.

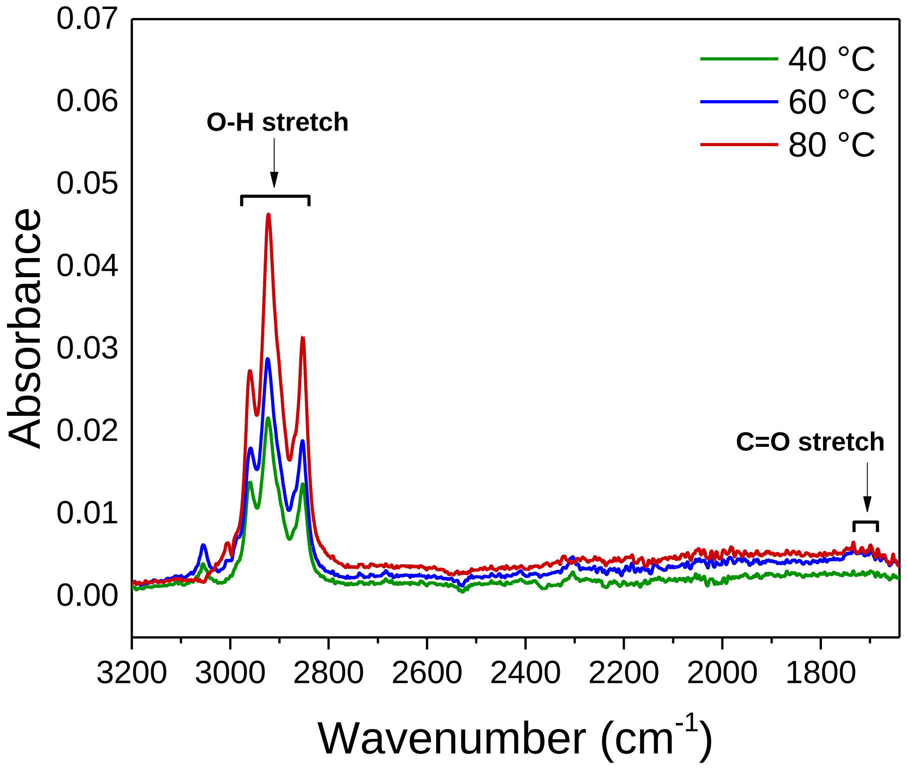

Figure 4.6. Fourier transform infrared (FT-IR) spectrum shows O–H and C=O stretches of naphthenic acids (carboxylic acids) functional groups in extraction of supernatant water containing dissolved naphthenic acids.

To pseudo-quantitatively assess the naphthenic acids dissolved in the water phase, a standard liquid-liquid extraction was performed using Fourier transform infrared (FT-IR).[34, 182] The extracted water was acidified to pH 2.3 using 1 M HCl. Then, the carboxylic acids were extracted from the acidified water into dichloromethane (DCM, Fisher Scientific, UK) using 2:1 volume ratio. The extraction was repeated three times to recover almost all of the carboxylic acids.[34] The DCM extractions were combined and left to evaporate off the solvent in a vented fume hood. The remaining residue was re-dissolved in 20 g of DCM and analysed by FT-IR (Nicolet iS10, Thermo Scientific) with a DCM background. **Figure 4.6** shows the FT-IR spectra confirming O–H and C=O stretches of naphthenic acids (carboxylic acids). The higher absorbance for the higher extracted water temperatures implies more naphthenic acids present in the water phase, thus increased adsorption at the oil-water interface lowering the oil-water interfacial tension at higher temperatures.[174]

Asphaltenes are the heavy component of crude oil that can adsorb at the oil-water interface. Compared to surfactants, asphaltenes are much larger in molecular weight, from 400 to 1,500 g/mol, are polyaromatic with alkyl side-chains and contain heteroatoms and trace metals. It has been shown that higher temperatures increase asphaltene adsorption to the oil-water interface.[177, 183, 184] Orientation of asphaltenes at the oil-water interface is likely to be more perpendicular than parallel with increasing temperature, resulting in more asphaltenes being adsorbed.[185, 186, 187] Also at high temperatures, asphaltenes are more dispersed (less aggregated) which leads to a greater surface excess (denser packing) and hence decreases the oil-water interfacial tension relative to low temperatures.[177]

The equilibrium contact angles measured in the current study are in good agreement with the research by Basu *et al.*[13] With pH increasing, the concentration of naphthenic acids in the water phase increased, resulting in greater reduction in the oil-water interfacial tension and increased electrostatic repulsion between the oil droplet and substrate, see discussion in Section 2.3.4. Data collected at pH 5.5 were compared with the pH tests conducted by Basu *et al.*[13] at pH 3, 7 and 11, as shown in **Figure 4.7**. The data is in excellent agreement with the trend in pH and can be attributed to the variation in naphthenic acid concentration. In addition, the trends in pH are also consistent over the temperature range 40 to 80 °C, with the equilibrium contact angle slightly decreasing at higher temperatures, which can again be attributed to the increased solubility of naphthenic acids.

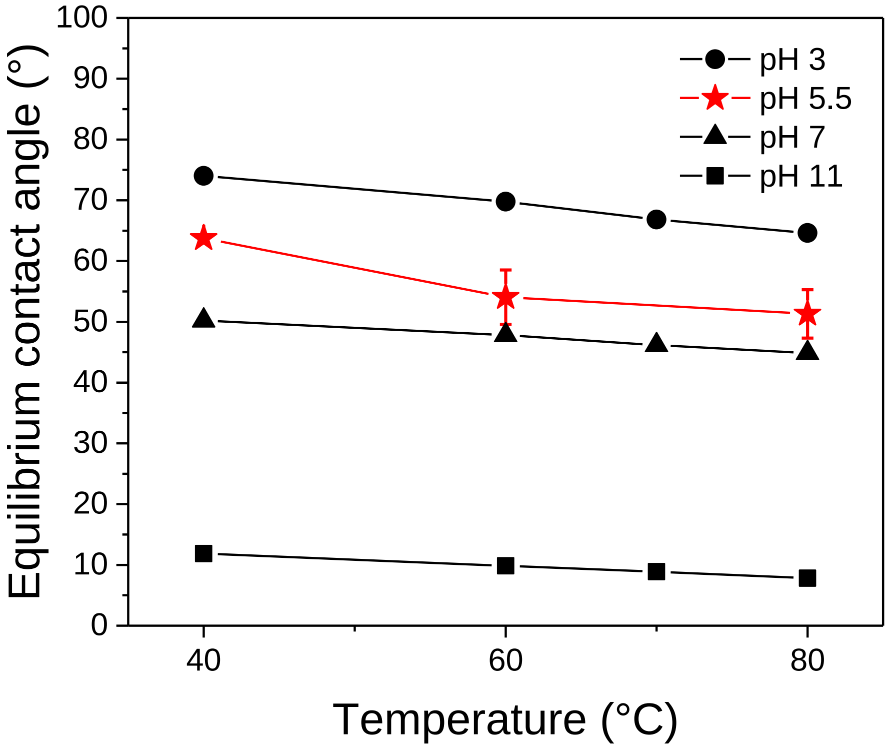

Figure 4.7. Equilibrium oil droplet contact angles (measured through the water phase) in water at pH 5.5 (red symbols) and compared to the pH-dependent data published by Basu *et al.*[13] Lines are included to guide the eye.

The initial receding rate $(\frac{d\theta}{dt})$ of the oil film was compared for each temperature with the rates correlated to changes in σ_{OW} and μ_o, see **Figure 4.4**. Based on the HD model for contact-line displacement (Equation (2.8)), which includes both parameters, the oil viscosity is the rate dependent parameter since the change in oil viscosity (-80.9%) with temperature is more significant than that of oil-water interfacial tension (-9.9%);

between 60 °C and 80 °C the oil viscosity decreased by 38.9% and the initial receding rate increased by 107.2%. The same oil displacement data was fitted to both the HD and MK models (**Figure 4.8**). A least-squares difference between the experimental and theoretical θ_d was made

$$\Delta = \sum_{t=0}^{t_e} (\theta_m - \theta_{exp})^2 \tag{4.1}$$

where θ_m and θ_{exp} are the theoretical and experimental dynamic contact angles at time t, respectively, and the model fitting parameters were determined by minimising the least-squares value.

During the process of oil film dewetting, the model fits appear in reasonable agreement with the experimental data. Slight variation is magnified at higher temperatures when the receding dynamics can be considered rapid for extra heavy crude oil, and experimental variability is more evident. The adjustable fitting parameters for each model (HD – $ln(\frac{L}{L_S})$, MK – ζ) reduced with increasing temperature, suggesting that the slip length of fluid-fluid contact line on a solid surface (L_S) increases and the coefficient of contact-line friction (ζ) decreases when the oil viscosity is reduced, in good agreement with previous findings.[156, 167]

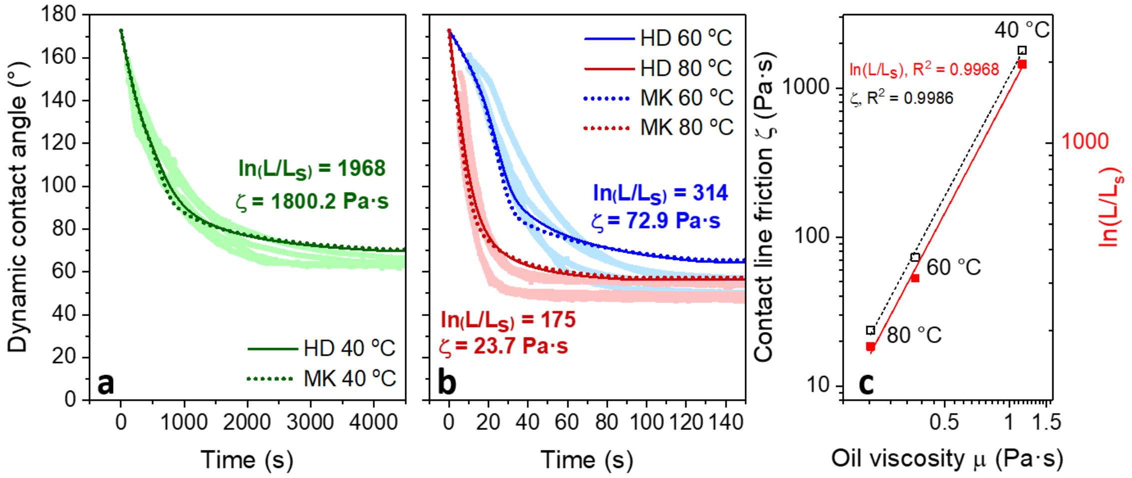

Figure 4.8. HD and MK model fittings of oil film dewetting at 40 °C (a), 60 °C and 80 °C (b). Shaded lines represent the experimental data and the HD and MK models identified by the solid and dash lines, respectively. (c) Optimal fitting parameters, HD (closed symbols) – $ln(\frac{L}{L_S})$, MK (open symbols) – ζ.

4.4.2 Oil droplet dewetting under high pressure and high temperature

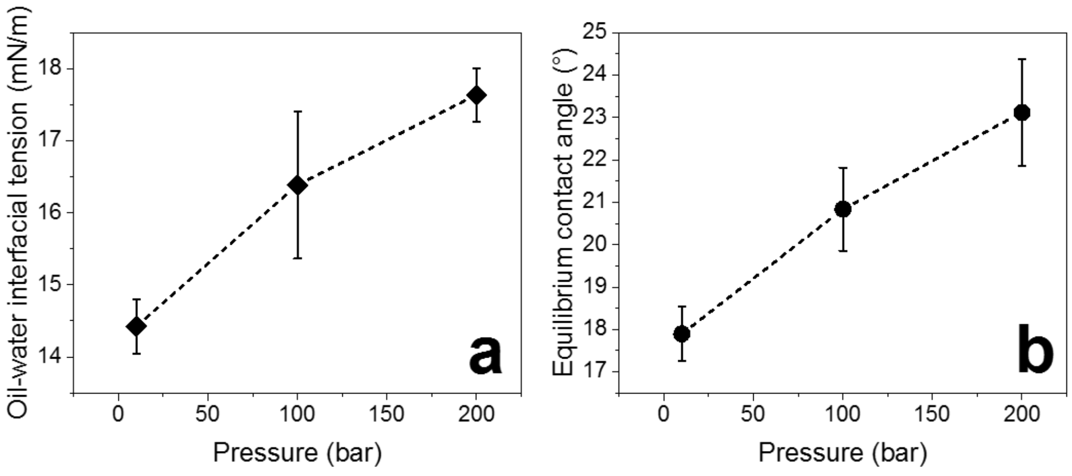

Figure 4.9. Oil-water interfacial tension (a) and equilibrium contact angle (b) in Milli-Q water at 140 °C as a function of pressure. Lines to guide the eye.

Very high temperature and high pressure conditions were studied to better represent the real reservoir conditions. To study behaviour at 140 °C it was necessary to increase the pressure to 10 bar to avoid boiling (water boiling point = 351 °C), whereas the study at 60 °C was conducted at ambient pressure (**Figure 4.4**). Based on the results, the contribution from the pressure difference (10 → 200 bar at 140 °C) can be neglected when compared to the contribution from the temperature difference (60 °C at 1 bar → 140 °C at 10 bar), since changes in σ_{OW} and θ due to pressure (+22.3% $\Delta\sigma_{OW}$ and +29.0% $\Delta\theta$) were smaller than the changes due to temperature (-46.1% $\Delta\sigma_{OW}$ and -66.9% $\Delta\theta$).

Increasing temperature from 60 °C to 140 °C led to a significant reduction in σ_{OW} (26.8 → 14.4 mN/m) indicating a greater partition of surface-active species (*e.g.* asphaltenes and naphthenic acids) at the oil-water interface as discussed in previous section. Reduction in the oil-water interfacial tension accordingly promoted the oil dewetting and the contact angle decreased from 54.1° to 17.9° due to the Young's law.

Increase in σ_{OW} with increasing pressure (**Figure 4.9**a) suggests that the surface-active molecules (*i.e.* asphaltenes) partition less at the oil-water interface. At high pressures asphaltenes are more soluble in the oil phase and thus their interfacial affinity is less.[188, 189] In addition, at high pressure the water and oil molecules at the interface become more confined which contributes to increased intermolecular forces and hence higher interfacial tension.[81, 190] The increase in σ_{OW} was only slight even at very high pressure (200 bar). **Figure 4.9**b shows a reduction in oil dewetting with increasing pressure and this effect can be attributed to the increase in σ_{OW}. The direct contribution of pressure on the contact angle was considered to be negligible since the oil contained no dissolved gas (dead oil) and the water contained negligible dissolved gas.

These initial findings suggest that oil droplet dewetting dynamics observed at ambient condition may not describe the behaviour under reservoir-like conditions. The σ_{OW} still has a relationship with the contact angle *via* the Young's equation.

4.4.3 Oil droplet dewetting dynamics in surfactant

SDS, an anionic surfactant, was used to displace an oil film deposited on a glass substrate at 60 °C (**Figure 4.10**a). Adding SDS to the aqueous phase reduced σ_{OW}, and the CMC was found to be ~0.1 wt% (3.5 mM) at 60 °C (**Figure 4.11**a). The measured oil-water interfacial tension was fitted using the Langmuir isotherm model (Equation 4.2), see **Figure 4.11**a.[191, 192]

$$\sigma = \sigma_0 + RT\Gamma_s ln\left(\frac{1}{1 + KC_s}\right) \tag{4.2}$$

where σ_0 is the interfacial tension of the pure fluid (*i.e.* no surfactant), K the adsorption constant.

The CMC was verified by measuring the conductivity of the SDS solutions (**Figure 4.11**b) and was found to be in good agreement with the CMC ~0.15 wt%. The slightly lower CMC determined from measuring the oil-water interfacial tension likely results from the contribution of natural surfactants (naphthenic acids) adsorbed at the oil-water interface.[48, 193] At 20 °C, the CMC of SDS is ~0.24 wt% and a reduction in CMC at higher temperature is expected and agrees with published literature.[194] Since higher temperatures decrease surfactant-chain hydration, owing to weaker hydrogen bonding, these conditions favour micellisation and thus the surfactant CMC is lower.[195]

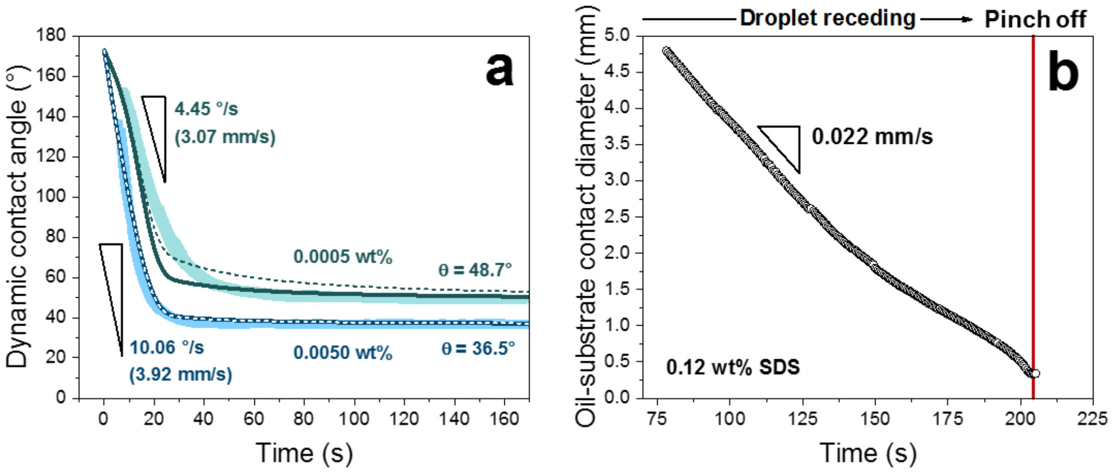

Figure 4.10. Oil film dewetting at 60 °C with increasing SDS concentration (5 × 10^{-4} wt% and 5 × 10^{-3} wt%) (a). Shaded lines represent the experimental data with the HD and MK models identified by the solid and dash lines, respectively. Oil film dewetting at 60 °C with the SDS concentration > CMC (SDS = 0.12 wt%) (b). The surface-oil droplet contact diameter reaches a minimum of 0.34 mm at the point of oil droplet pinch-off.

Increasing the SDS concentration from 5×10^{-4} wt% to 5×10^{-3} wt% increased the rate of oil film displacement and decreased the equilibrium contact angle (θ). The equilibrium contact angle decreased from 54.1° in the absence of SDS to 48.7° and 36.5° for 5×10^{-4} wt% and 5×10^{-3} wt% SDS, respectively, as a result of charge repulsion between the SDS anionic head group and negatively charged silica surface. While surfactant is added, the reduction in σ_{OW} is small over the concentration range 5×10^{-4} to 5×10^{-3} wt%, $\Delta\sigma$ ~ 2 mN/m, and therefore is unlikely to be the main contributor to the substantial decrease in θ. Fitting the HD and MK models confirmed an increased slip length (L_S) and reduced coefficient of contact-line friction (ζ) at higher SDS concentrations (**Table 4.1**).

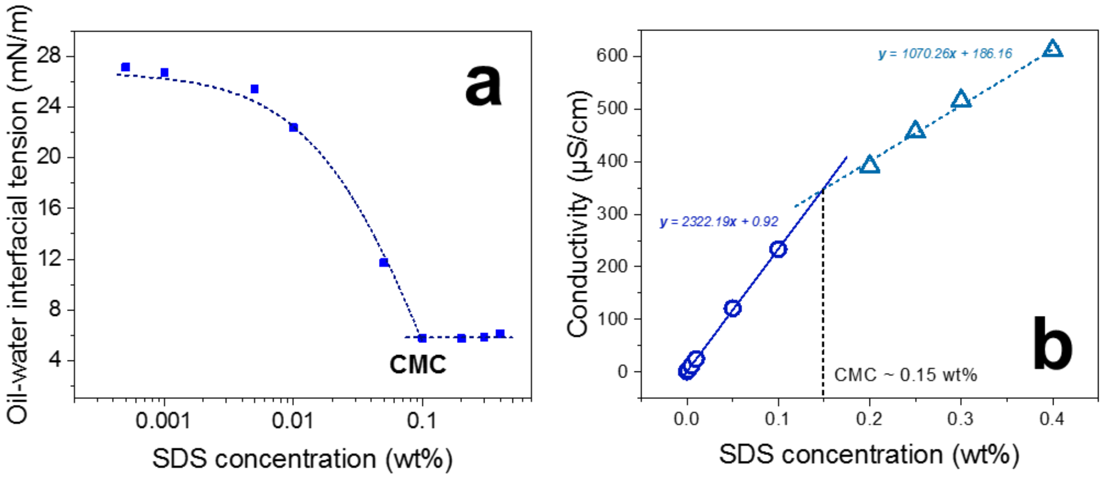

Figure 4.11. Crude oil-water interfacial tension as a function of SDS concentration (a). The CMC was ~0.1 wt% at 60 °C. Conductivity of SDS solution as a function of the SDS concentration at 60 °C (b). The intercept of two linear lines denotes the CMC (~0.15 wt%).

Table 4.1. Model fitting parameters for oil droplets in SDS solutions.

Concentration (wt%)	$\boldsymbol{ln(\frac{L}{L_S})}$	**ζ (Pa·s)**
5×10^{-4}	83.7	33.5
5×10^{-3}	35.0	3.7

Figure 4.10b confirms the benefit of injecting surfactants at concentrations higher than the CMC. The very low σ_{OW} (~5.75 mN/m) caused the oil film to continually recede and eventually pinch off from the solid surface when the oil droplet buoyant force (3.77 µN) exceeds the oil droplet-substrate adhesion force (2.01 µN). Due to very low oil-water interfacial tension, when the oil droplet was deposited onto the glass substrate, the droplet did not form a spherical-cap but more a disk-shape (**Figure 4.12**).[196] As a result the contact angle is not defined, this receding dynamics was determined from the oil droplet contact diameter on the substrate. Compared to the lower surfactant

concentration solutions, the oil droplet receding rate was much slower (0.022 mm/s at 0.12 wt% SDS), see **Figure 4.10**.

Delayed recession of the oil droplet was due to hindrance at the three-phase contact line resulting from a very low capillary force (capillary force: $\sigma_{OW} cos\theta$), which, due to the flattened oil droplet disk-shape (t < 105 s), initially opposed to the direction of oil droplet dewetting, and thus slowed the initial receding rate. In addition, the very low oil-water interfacial tension meant that the driving force to minimise the surface area to volume ratio (*i.e*. form a sphere) was low.

With ultra-low σ_{OW} and small oil-substrate contact area at t = 192 s, the oil droplet buoyancy started to exceed the oil-substrate adhesion and thus the oil droplet pinched off from the substrate before complete droplet recession (much slower process). This led to oil droplet filament elongation and eventual liberation (at t = 194 s) leaving a secondary daughter droplet attached to the surface. The σ_{OW} and oil viscosity have been shown to control the kinetics of droplet pinch-off.[197, 198] As reported in literature and seen in this study, the low σ_{OW} reduced the rate of thinning of the filament neck (due to low capillary force), and high oil viscosity led to a highly elongated oil filament, with slow detachment, ~2,000 ms compared to < 10 ms for a water droplet.[197, 199] It is worth noting, and as discussed in Chapter 6, a real oil droplet detachment could be observed without the generation of a secondary droplet. Such detachment was controlled by a complete receding process and no pinch-off.

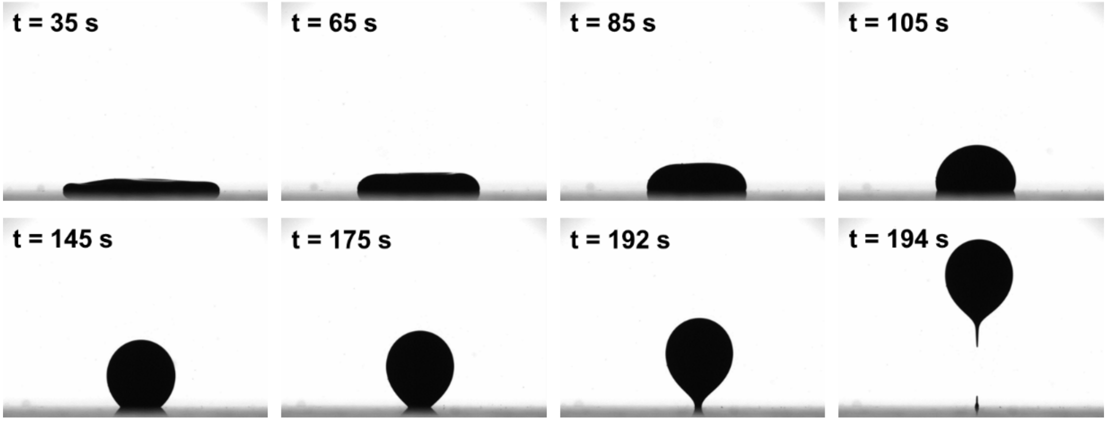

Figure 4.12. Oil droplet dewetting development in 0.12 wt% SDS (> CMC) at 60 °C. The oil droplet receded in axisymmetric shape but not in spherical-cap shape.

4.5 Conclusion

The current chapter has examined the nature of oil film recession on a model surface in pure water fluid. When changing from air-oil-solid to water-oil-solid system, the oil droplet dewetted spontaneously in spherical-cap shape in order to balance the free surface energy towards a new equilibrium. Also revealed is the importance of relevant parameters that alter the phenomena. In the study of temperature, oil viscosity was found to govern the dynamic dewettting of oil droplets (*i.e.* the oil droplet receding rate) while the oil-water interfacial tension mainly altered the equilibrium state of the Young's contact angle. In a high pressure environment, the oil-water interfacial tension slightly increased, which further contributed to reduced adsorption of surface-active species. The contact angle was found to increase according to the interfacial tension change. Significantly low oil-water interfacial tension was demonstrated by adding surfactant and resulted in much lower contact angle. At higher CMC, ultra-low interfacial tension was obtained where the oil droplet pinched off from the substrate spontaneously. This was because the oil-surface adhesion was lower than the critical value allowing the oil droplet buoyancy to overcome. Oil dewetting phenomena in this chapter exhibited the Young's concept by using pure water and normal surfactant additive. The findings here represent a controlled system to compare with further investigations in the later chapters.

Chapter 5

Oil Droplet Dewetting in Low-Salinity Fluids

5.1 Synopsis

Low-salinity EOR shows a great promise, yet the mechanism for its performance remains unclear. To better understand the interfacial interactions promoting EOR under various brine environments, a systematic study on the oil droplet dynamic dewetting was considered with monovalent (NaCl) and divalent ($CaCl_2$) brines under temperatures ≤ 140 °C and pressures ≤ 200 bar.

Increasing brine concentration induced salt ion adsorption and hence neutralised the oil-water interfacial charge, leading to higher adsorption of negatively charged surface-active species (e.g. asphaltenes and naphthenic acids) and oil-water interfacial tension reduced. Such reduction in the interfacial tension with increasing brine concentration was found up to ~25,000 ppm, where a trend reversed to increase with further increasing concentration because salt ion saturated the interface and preferred to interact with water molecule via dipole-ion interaction hence less adsorption of the surface-active species. Contact angles observed were governed by disjoining pressure rather than the oil-water interfacial tension. Decreasing contact angles (43.2° in Milli-Q water → ≥ 18.1°) in brine confirms greater oil dewetting in the presence of NaCl, with hydration force strongly influencing the repulsion between oil and substrate. In contrast, attractive hydrophobic force, constructing in $CaCl_2$ brines between the oil and *hydrophobised substrate (via divalent cation bridging the natural surfactants onto substrate), demotes the oil dewetting and thus higher contact angles (≥ 27.2°). Dynamic dewetting of oil droplet at the initial period was accelerated by a stronger oil-substrate repulsion and lower steady-state contact angle, without the interfacial tension effect.*

For both brines, the oil-water interfacial tension decreased with increasing salinity and temperature (21.6 → 3.9 mN/m from 60 to 140 °C at 60,000 ppm NaCl), which attributed to increasing adsorption of the surface-active species by charge neutralisation from the partitioning of salt ions. Higher pressure (10 → 200 bar) increased the oil-water interfacial tension due to decrease in interfacial adsorption ($\Delta\sigma_{OW}$ ~3 mN/m). This led to slightly higher contact angles ($\Delta\theta$ ~6°), i.e. reduced oil dewetting, although it should be noted that the pressure effect was minimal, especially in $CaCl_2$ *brines due to the dominant effect of hydrophobic attraction.*

Fluid temperature and brine type were shown to have a much greater influence on oil droplet dewetting than pressure. Based on our recent findings, the present study confirms that salt-dependent trends observed under ambient conditions do not fully represent those interfacial behaviours at conditions which are closer to the real reservoir at high temperature and pressure.

5.2 Introduction

Secondary and tertiary oil recovery methods are increasingly used in crude oil production to meet the growing global energy and chemical feedstock demands. Chemical EOR is used in both conventional and unconventional oilfields to alter connate-water chemistry. Injecting engineered water (chemical-doped water) can lead to greater oil recovery by decreasing capillary pressure following surfactant injection and increasing sweep efficiency from polymer flooding. There are however limitations to this practice, most notably the environmental impact as well as increased operational costs due to frequent chemical injections.[200] Proposed in the 1990s, Morrow *et al*.[201, 202] demonstrated an alternative to EOR by diluting connate water, leading to what is now more commonly known as low-salinity EOR. Considered to be greener and cheaper than conventional chemical EOR, many studies have considered low-salinity EOR from a molecular scale through to field trials. Mechanisms to improve oil displacement by low-salinity water injection include interfacial interactions, namely a reduction in oil-water interfacial tension and wettability alteration.[12, 17, 76, 80]

Displacement of crude oil is partly influenced by the solid-liquid and liquid-liquid interfacial energies of the interacting three phases: crude oil, connate water and reservoir rock.[203, 204, 205] Saline water (up to ~30,000 ppm) has been shown to promote adsorption of crude oil surface-active species such as asphaltenes and naphthenic acids, lowering oil-water interfacial tension.[54, 81, 82] However, for high-salinity water both an increase[54, 81, 82] and decrease[84, 206] in oil-water interfacial tension has been observed controversially. The increasing interfacial tension is attributed to the salt-ion negative adsorption.[85]

The effect of salinity on the contact angle (wettability) is debated. Haagh *et al*.[80, 113] showed that low brine concentrations decreased the water contact angle (surface becomes more water-wet), attributing changes to the increasing electrostatic forces, and suggested that lower surface hydrophilicity resulted from cation bridging between surface-active materials in the oil and substrate. Basu *et al.*[15, 56] studied both monovalent and divalent salts for bitumen droplet recession on glass substrates, and showed higher water contact angles for higher brine concentrations. Drummond and Israelachvili[12] considered contact angle alteration in different fashion by brine solutions and argued that interaction forces (classical DLVO forces) should also account for structural forces in brine solutions. Their contribution agreed with Basu and Sharma[102] who showed wettability in brines depends on both capillary and structural (hydration) forces. Israelachvili and co-workers[76] considered the effect of brine dilution on the contact angle of crude oil-brine-rock. Diluting formation water to ~80,000 ppm decreased the contact angle to ~12°, with further dilutions causing an increase in contact angle (~80° at ~500 ppm). A 'wettability map' (oil droplet wettability) was used to describe the influence of interfacial forces acting between oil-water and water-substrate interfaces as a function of brine concentration. Applying DLVO forces to quantify the contact angle, the authors concluded that hydration force dictates wettability behaviour.

Low-salinity brines have been considered at high temperatures and pressures to better understand mechanisms at subsurface conditions, though the findings remain controversial. Yang *et al.*[55] studied crude oil-rock-carbonated brine and showed a decreasing contact angle at high pressure (≤ 200 bar), a result of oil swell due to CO_2 diffusion, while the oil droplet-substrate contact area remained constant. Xie *et al.*[17] showed no pressure effect in crude oil-quartz rock-brine solution but observed a slight increase in contact angle at higher temperature (≤ 140 °C). Zhang *et al.*[53] observed a similar temperature effect for oil droplets on mineral surfaces, although noting that the brine salinity effect was more pronounced than any temperature and pressure contributions. Nowrouzi *et al.*[54] reported substantial reductions in the contact angle at higher pressure (≤ 14 bar) using different brines, with behaviour attributed to a decrease in the oil-water interfacial tension. Although some study has reported the temperature effect on the contact angle in associated with disjoining pressure, discussions on direct effects of pressure and interfacial adsorption on the contact angle were still short of. Thus, the integrated study including all main factors are needed to address the mechanism and clarify whether the study in ambient condition can really represent the one under reservoir condition.

To understand oil dewetting mechanism in low-salinity EOR, the current study considers the dewetting dynamics of heavy crude oil droplet on hydrophilic glass substrates with the effect of monovalent (NaCl) and divalent ($CaCl_2$) brines ranging from 2,000 to 60,000 ppm. Investigation into effect of high pressure and high temperature (reservoir condition) under low-salinity environment has not yet been reported. In this study, the oil dewetting in the brine system was observed as a function of temperature ($\leq$ 140 °C) and pressure ($\leq$ 200 bar). The disjoining pressure between oil-coated particle and glass substrate was also examined to elucidate the prominent behaviours governing heavy crude oil droplet dewetting in brine environment.

5.3 Experimental Methods

To study the dynamic oil dewetting in brines, the techniques to measure the oil-water interfacial tension and contact angle were as described in Chapter 3. The experimenting temperature was set to be 60 °C at ambient pressure.

In the later section, the effect of high pressure and high temperature was also examined on the oil-water interfacial tension and contact angle. The experimenting environment was set at 140 °C with pressures of 10, 100 and 200 bar using the high-pressure chamber whereas the experimental detail was described in Chapter 4.

Zeta potentials of oil-water and silica-water interfaces were measured as described in Chapter 3. The disjoining pressure between oil-coated colloidal probe and glass substrate under brine environment was determined as discussed in Chapter 3.

It is the fact that the heavy crude oil used throughout the thesis is the same but the oil used in this chapter was sampled a long time apart from the other chapters, which could lead to change in the oil properties (*e.g.* due to loss of some light oil components). The oil dewetting control system of Milli-Q water at ambient condition was then conducted specifically with this oil (**Figure 5.1**) to only compare with the data in this chapter. The oil dewetting results and model fittings were in a good agreement with Chapter 4.

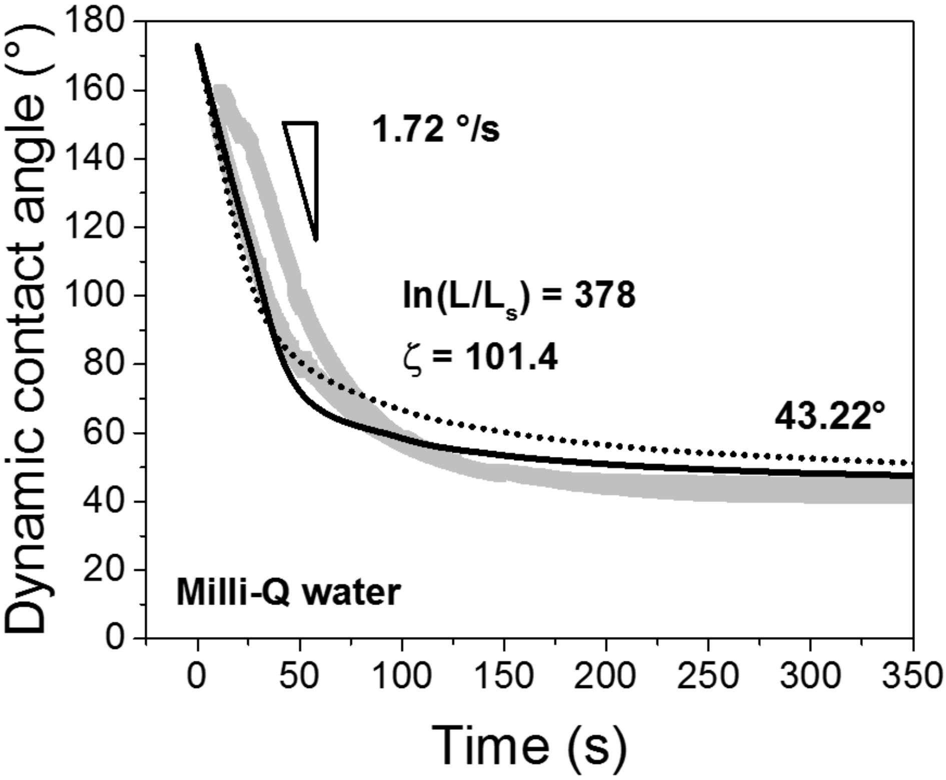

Figure 5.1. Dynamic oil droplet dewetting in a control system of Milli-Q water. Light-coloured symbols are two repetitive experimental plots. The initial receding rate and the equilibrium contact angle are shown next to the plot. Solid and dash lines are HD and MK model fittings, respectively. The fitting parameters are shown next to the fitted lines.

5.4 Results and Discussion

5.4.1 Oil droplet dewetting

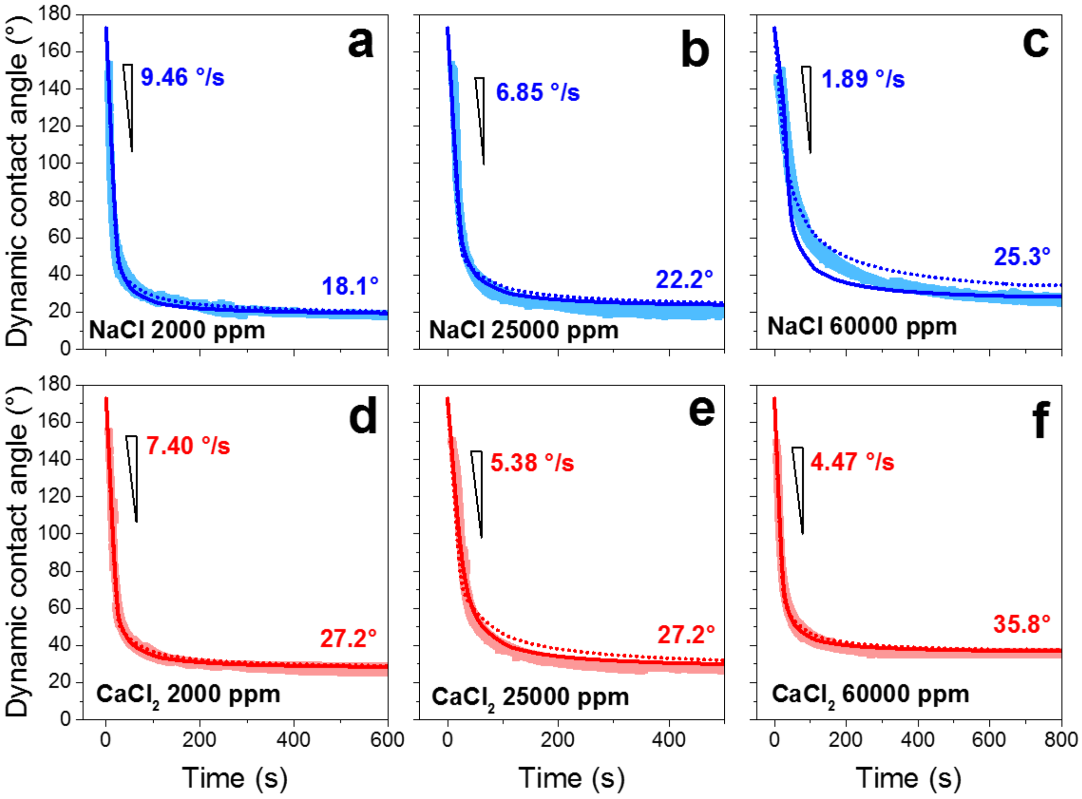

Figure 5.2. Dynamic contact angle of heavy crude oil droplet dewetting on glass substrate in brine solutions at 60 °C. NaCl brine at 2,000, 25,000 and 60,000 ppm, respectively (a) – (c). $CaCl_2$ brine at 2,000, 25,000 and 60,000 ppm, respectively (d) – (f). The light-coloured symbols represent two repeat measurements. The initial receding rate and equilibrium contact angle are shown inset. Solid and dash lines are the HD and MK models, respectively.

The effect of brine concentration on heavy crude oil dewetting is shown in **Figure 5.2** and summarised in **Table 5.1**. Three brine concentrations were considered: case (I) 2,000 and 60,000 ppm were selected due to the fluids exhibiting similar oil-water interfacial tensions (σ_{OW} ~21.6 mN/m and 20.5 mN/m for NaCl and $CaCl_2$); and case (II) 25,000 ppm was chosen as this produced the lowest oil-water interfacial tension, see **Figure 5.4** (σ_{OW} = 21.0 mN/m for NaCl and 20.1 mN/m for $CaCl_2$). Hence for case (I), the effect of brine concentration independent of σ_{OW} is compared and case (II) compares changes in σ_{OW} for both brine types.

During the oil dewetting, the thin film of crude oil recedes axis-symmetrically in the radial direction to form a spherical cap as reported in Chapter 4. The droplet dewetting is represented by the dynamic contact angle (θ_d), with the initial receding rate (°/s) and steady-state contact angle (θ_e) of particular interest.

Table 5.1. Summary of experimental data and model fitting parameters at 60 °C.

Aqueous phase	**Experimental data**			**Model parameters**	
	θ_e ***(°)***	σ_{OW} ***(mN/m)***	***Initial receding rate (°/s)***	$ln(L/L_S)$	***ζ (Pa·s)***
0 ppm (Milli-Q water)	43.2	22.7	1.72	378	101.4
NaCl 2,000 ppm	18.1	21.7	9.46	237	18.7
NaCl 25,000 ppm	22.2	21.0	6.85	259	23.6
NaCl 60,000 ppm	25.3	21.6	1.89	622	139.9
$CaCl_2$ 2,000 ppm	27.2	20.7	7.40	201	21.7
$CaCl_2$ 25,000 ppm	27.2	20.1	5.38	362	49.1
$CaCl_2$ 60,000 ppm	35.8	21.3	4.47	220	33.3

The initial receding rate of heavy crude oil droplet dewetting strongly depends on the brine concentration. Compared to Milli-Q water (initial receding rate = 1.72 °/s), at 2,000 ppm brine (NaCl and $CaCl_2$) the rates of oil droplet dewetting increase substantially, with the fastest rate (9.46 °/s) measured for NaCl at 2,000 ppm (**Figure 5.3**). Further increases in brine concentration reduce the initial rate of oil droplet dewetting, and for 60,000 ppm NaCl the rate is almost equivalent to salt-free water. The increase-decrease in initial rate of oil droplet dewetting with brine concentration is also observed for $CaCl_2$, although the rates are slightly lower than NaCl brine, except at 60,000 ppm where an initial oil droplet dewetting rate of 4.47 °/s is greater than that for NaCl and equivalent brine concentration.

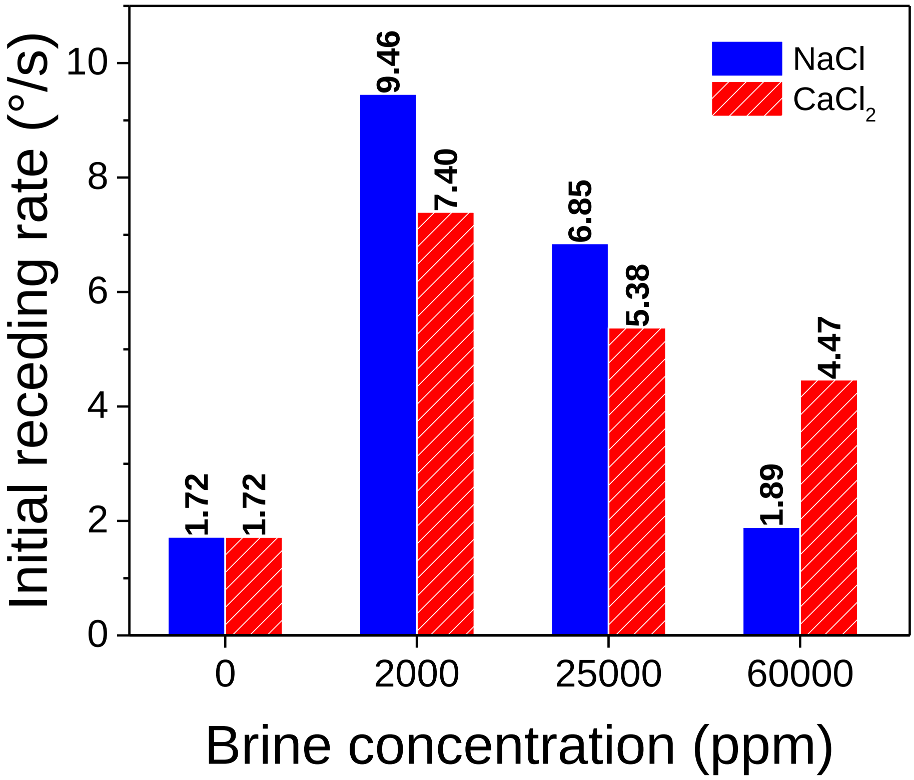

Figure 5.3. Initial receding rate of heavy crude oil dewetting in NaCl and $CaCl_2$ brines as a function of concentration at 60 °C.

Considering Equations (2.8) and (2.10), contact-line velocity depends on the fluid and surface properties: μ_o, σ_{OW} and θ_e. For the data shown in **Figure 5.3**, the contribution from oil viscosity on droplet receding rate can be neglected since the fluid viscosity is constant at 60 °C. The contribution from brine viscosity is also negligible since the brine viscosity varies within 0.1 mPa·s for the different brine types and concentrations considered.[207, 208] For case I (equivalent σ_{OW} at 2,000 and 60,000 ppm brines), significant differences in the initial receding rate of oil droplet confirm that behaviour is not only influenced by σ_{OW}. Better agreement between the initial receding rate and θ_e is generally observed, with the initial receding rate decreasing as θ_e increases, although this simple parameter assessment is not comprehensive to describe the observed differences between NaCl and $CaCl_2$.

The dynamic dewetting models considered two further parameters: (i) $ln(L/L_S)$ for HD model and (ii) ζ MK model. Generally there is good agreement between the heavy crude oil droplet receding rate and the fitting parameter values, with higher values of $ln(L/L_S)$ and ζ corresponding to a reduced rate of oil droplet recession. This is sensible since both parameters describe a contact-line friction or hindrance to oil droplet displacement. From the HD theory, a higher brine concentration shortens the slip length and consequently reduces the rate of oil displacement. Many hydrated salts near the solid surface[103, 209] might demote the elongation of the slip length rather than enhance the fluid slip. Due to its bigger hydrated radius, Ca^{2+} was found to hinder the slip length elongation more than Na^+.[210] From the MK model, increasing contact-line friction (ζ) at higher brine concentrations reduces the oil dynamic displacement due to a higher solid-liquid friction at the three-phase contact line. According to the MK concept,[43, 44] Many hydrated salt ions in water near the solid surface might disrupt the liquid molecule jumping as an obstacle and consequently slow down the oil droplet recession. As discussed above, bigger hydrated size Ca^{2+} implies a higher disruption than the smaller size Na^+.

It should be noted that 60,000 ppm $CaCl_2$ fitting does not appear to agree with the general trend, that is the $ln(L/L_S)$ and ζ values are lower than 25,000 ppm $CaCl_2$ even though the oil droplet dewetting rate is slower. However, when compared to 2,500 ppm $CaCl_2$ the behaviour is consistent. The goodness of fit for the 25,000 ppm data ($R^2 \leq 0.98$) may contribute to this inconsistency.

However, compared to the pure water system, the 'optimum' brines (*i.e.* 2,000 ppm) showed remarkable ability to elongate the slip length and believably energise the oil-water molecular shuffle, hence attained a faster oil recession with low fitting model parameters.

5.4.2 Oil-brine interfacial tension

Oil-water interfacial tension was measured in NaCl and $CaCl_2$ brine solutions of increasing salt concentration from 2,000 ppm to 100,000 ppm at 60 °C (**Figure 5.4**). An initial increase in brine concentration reduced the oil-water interfacial tension relative to no brine, σ_{OW} = 22.7 mN/m. For both NaCl and $CaCl_2$ a minima in the oil-water interfacial tension was measured at ~25,000 ppm and found to be independent of the salt type. At > 25,000 ppm, the oil-water interfacial tension increased and at the highest brine concentration (100,000 ppm) the oil-water interfacial tensions approximated to that of the no-brine interfacial tension, as found in literature.[81, 82, 83, 84]

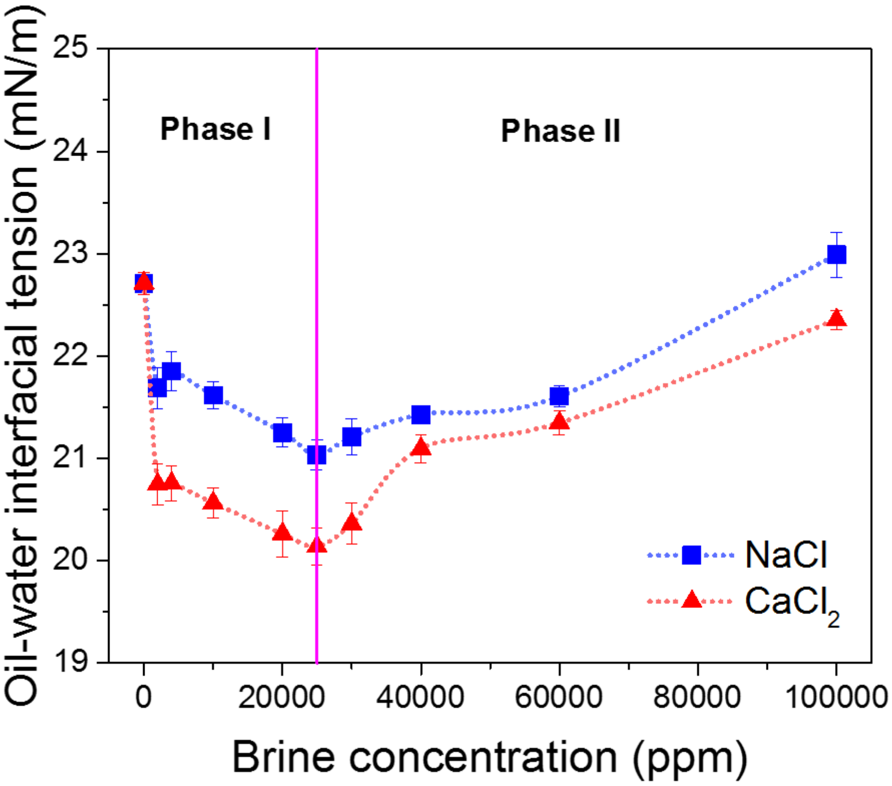

Figure 5.4. Oil-water interfacial tension as a function of brine type and concentration at 60 °C. The pink line at 25,000 ppm divides two phases which define the interfacial tension reduction and increase, respectively. Error bars are standard deviation. Dashed lines are used to guide the eye.

The interfacial tension behaviour can be divided into two phases. Phase I (0 – 25,000 ppm) describes the reduction in oil-water interfacial tension and can be attributed to increased adsorption of surface-active species (*e.g.* naphthenic acids and asphaltenes) at the oil-water interface, which is promoted by charge neutralisation of the heavy crude oil-water interface by increased partitioning of cations at the oil-water interface.[81, 82, 112] Increased salt partitioning at the oil-water interface can be described by the Gibbs' adsorption isotherm, Equation (2.12). The surface excess of salt ions increases ($\Gamma > 0$) leading to the interfacial tension decrease ($\sigma < \sigma_0$). Phase II (25,000 – 100,000 ppm) describes the increase in oil-water interfacial tension. At higher brine concentrations, the oil-water interface becomes saturated by cations and higher brine concentration lead to an increase in the salt excess in the bulk fluid.[81] This condition leads to a negative surface excess ($\Gamma < 0$) and an increase in the interfacial tension, also known as the Jones-Ray effect.[85, 88, 211] It has also been reported that very high brine concentrations, the dipole-ion interaction between cations and water molecules increases at interface thus the asphaltenes are less ionised or bound by the cations.[82] This leads asphaltenes to stay in the oil bulk rather than partition. This was confirmed by the less interfacial skin formed (quantifying amount of asphaltene adsorbed at the interface) studied by crumpling experiment) as follows.

According to Gao *et al.*,[212] crumpling is observed during the droplet volume contraction since asphaltene rigid skin is formed at the interface. The higher crumpling (skin formation) indicates the asphaltene adsorption at higher amount at the interface, quantifying by the crumpling ratio ($CR = \frac{A_f}{A_i}$) where A_f is the projected area of droplet when crumpling is first observed and A_i is the projected area of initial droplet before volume contraction. To ascribe the asphaltene interfacial behaviour in the present study, the crumpling test was examined as a function of $CaCl_2$ brine concentration. Asphaltenes were precipitated and dissolved in 1:1 heptol at 0.3 g/L. Asphaltene droplet (~10 µL) was suspended in water phase at different brine concentration for 1 h and then the droplet was retracted to observe the interfacial crumpling.

Figure 5.5 shows the result of that crumpling ratio increased from 0 up to 25,000 ppm (Phase I) and then inversely decrease to 60,000 ppm (Phase II). This suggests that asphaltene adsorption was enhanced with brine in Phase I where the higher brine concentration in Phase II prevented the adsorption as discussed previously. This finding well agrees with the interfacial tension results shown in **Figure 5.4**, ascribing the asphaltene adsorption is a dominant factor at the oil-water interface.

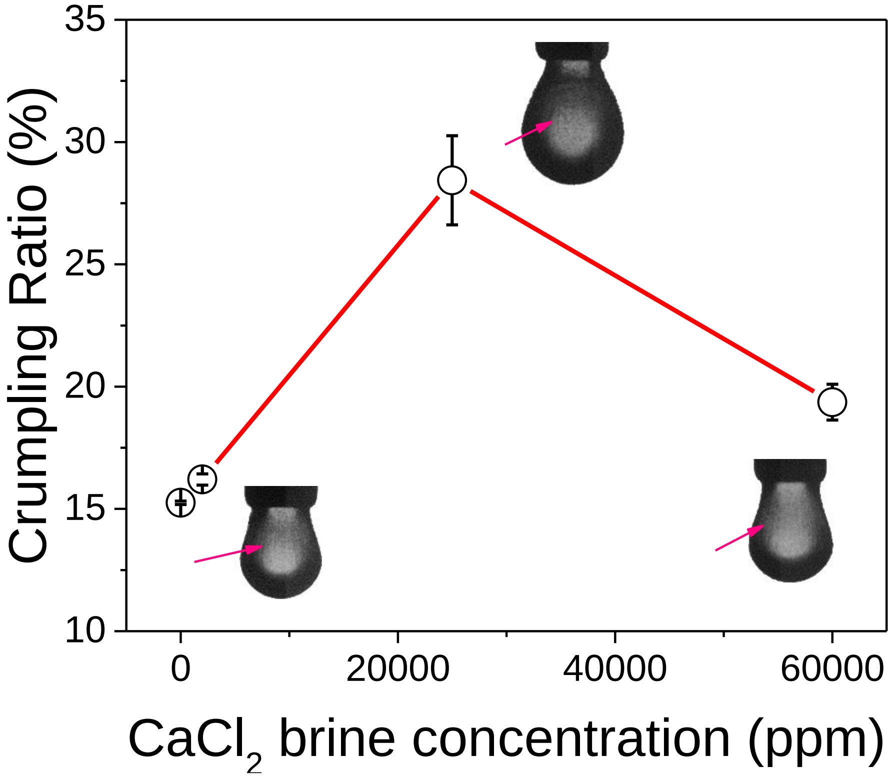

Figure 5.5. Crumpling ratio as a function of $CaCl_2$ brine concentration. Inset images are crumpling asphaltene in 1:1 heptol droplet at each brine concentration. Pink arrows point the droplet wrinkles. Lines to guide the eye.

Comparing $CaCl_2$ and NaCl, **Figure 5.4** shows the reduction in interfacial tension at equivalent brine concentrations is greater for $CaCl_2$ than NaCl, with stronger coordination of the divalent cation (Ca^{2+}) to naphthenic acids likely attributing to this effect.[112] Cation partitioning at an oil-water interface is influenced by its hydration-state,[213] with the more hydrated Na^+, compared to Ca^{2+}, contributing to stronger interfacial repulsion and consequently less favourable conditions to bind with naphthenic acids.[214, 215] Divalent cations have also been shown to strongly interact with asphaltenes, and thus a reduction in interfacial tension *via* asphaltenes partitioning at the oil-water interface becomes more favourable.[82, 83, 216] Considering the crumpling ratio (**Figure 5.5**), the brine concentration dependent crumpling ratio was found to be the inverse of the oil-brine interfacial tension, and may indicate that the dominant interfacially active species for the case of heavy crude oil is asphaltenes. The prevalence of asphaltenes at the oil-water interface is reasonable based on the very high asphaltene content in the heavy crude oil, 39.5 wt%. Moreover, divalent cations are thought to interact more strongly with aromatic oil *via* cation–π interactions.[217, 218] With the cation–π interaction energy correlated to the electrostatic potential,[219] the more positively charged cations strongly interact with the aromatics of the hydrocarbon fluid. The heavy crude oil used in the current study has a high aromaticity (H/C ~1.34), and thus favours such interaction with the divalent cations resulting in more hydrocarbon-cation binding and its consequent the much reduced interfacial tension as recently reported by Kakati and Sangwai.[88]

5.4.3 Equilibrium contact angle

At the end of the oil droplet dewetting process, the equilibrium contact angle was measured, see **Table 5.1**. **Figure 5.6** compares the equilibrium contact angles for NaCl and $CaCl_2$ brines at three concentrations and shows (i) all contact angles are lower than the pure water system (θ = 43.2°); (ii) θ_e increases with increasing brine concentration; and (iii) heavy crude oil droplets dewet more in NaCl brines than $CaCl_2$ brines (θ_e are comparatively lower by ~5-10° at equivalent brine concentrations). For the latter, this behaviour has previously been observed and attributed to divalent cation bridging between the oil droplet and negatively charged solid surface.[80] The lowest equilibrium contact angles were measured at 2,000 ppm: NaCl (18.1°) and $CaCl_2$ (27.2°) and do not correspond to the minimum in oil-brine interfacial tension. Reduced dewetting at higher brine concentrations confirms that low-salinity brine is desired to enhance oil dewetting to promote greater oil recovery.[76, 220]

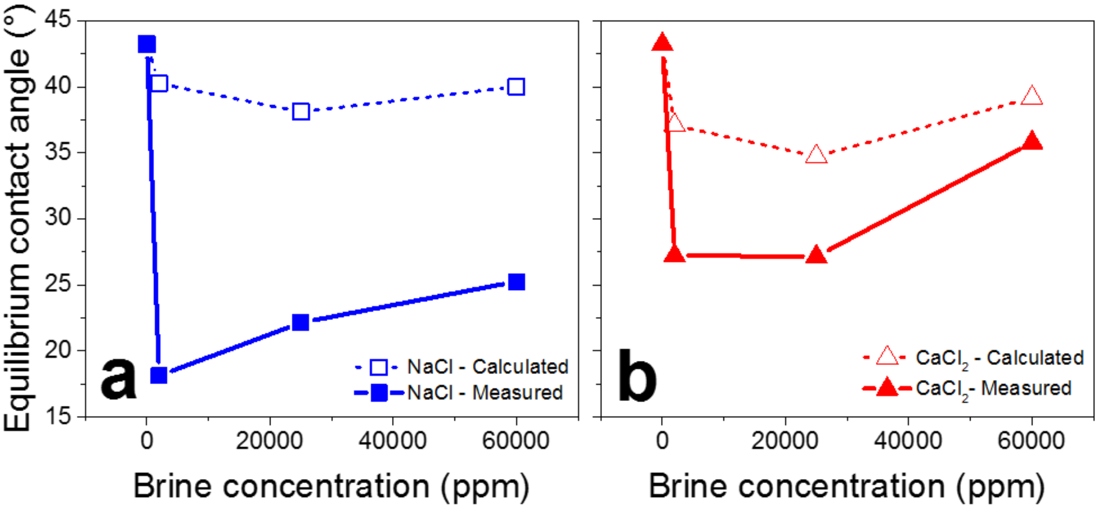

Figure 5.6. Oil droplet equilibrium contact angles as a function of brine type, NaCl (a) and $CaCl_2$ (b), and brine concentration at 60 °C. The measured and calculated equilibrium contact angles (Equation (5.1)) are shown by the open and closed symbols, respectively.

The contribution of the oil-water interfacial tension (σ_{OW}) on the equilibrium contact angle can be pseudo-quantitatively assessed by the Young's equation,[9] Equation (2.4), without considering the changes in σ_{SO} and σ_{SW} (although the brine will influence σ_{SW} by adsorption of hydrated salts on solid surface).[221] Considering the measured contact angle in the pure water system as the Young's contact angle (without brine), Equation (2.4) can be given as:

$$\sigma_{OW}^{0} \cos(\theta^{0}) = \sigma_{OW}^{Brine} \cos(\theta_{IFT}) \tag{5.1}$$

where σ_{OW}^{0} and θ^{0} are the oil-water interfacial tension and contact angle in pure water (no brine), respectively. σ_{OW}^{Brine} is the oil-brine interfacial tension, θ_{IFT} the calculated contact angle that solely depends on the σ_{OW}^{Brine}.

Figure 5.6 compares the measured and calculated contact angles (θ_{IFT}), and while the trends with brine concentration are consistent, interestingly, θ_{IFT} significantly over predicts the measured contact angles, with the effect more pronounced for NaCl brine. As such, changes in the heavy crude oil-water interfacial tension cannot directly describe the changes in equilibrium contact angle with other forces contributing the equilibrium condition.

Disjoining pressure describes the thin film stability between two interfaces (*i.e.* oil-water-solid),[102] and in the case of high brine concentrations, a positive disjoining pressure (repulsive interaction) has been attributed to a dominant hydration force that screens the electrical double layer interaction forces. This repulsive force arises due to an increase in the hydration free energy of salt ions in the thin water film separating two interfaces.[222] This repulsion is observed above a ‘critical’ hydration concentration when the hydrated cations bind to negatively charged substrate.[103]

To measure the disjoining pressure between oil-water and water-solid interfaces, a colloidal probe coated by surface-active components in the heavy crude oil (hard solid), mimicked the surface properties of an oil droplet, although the interface is rigid and does not deform. The force curves measured in brine fluids at 20 °C between the coated-colloidal probe and uncoated glass substrate represents the configuration of the dewetting experiment. Brine fluids were prepared by storing the fluid in contact with the heavy crude oil at 60 °C for 3 h (details in Chapter 3) to better represent the real phenomena occurring in the dewetting experiment at 60 °C, *e.g.* releasing of naphthenic surfactants into brine fluid. The measured force curves were then interpreted using Hertz theory as described in Chapter 3. **Figure 5.8** shows the disjoining pressures measured in NaCl and $CaCl_2$ at brine concentrations: 2,000, 25,000 and 60,000 ppm. The classical DLVO force contribution (van der Waals and electrostatic repulsion) was theoretically calculated using a Hamaker constant of 3×10^{-21} J[108] and the electrostatic force determined using the Poisson-Boltzmann equation assuming constant potential boundary conditions with measured zeta potentials reported in **Figure 5.7**.[223, 224]

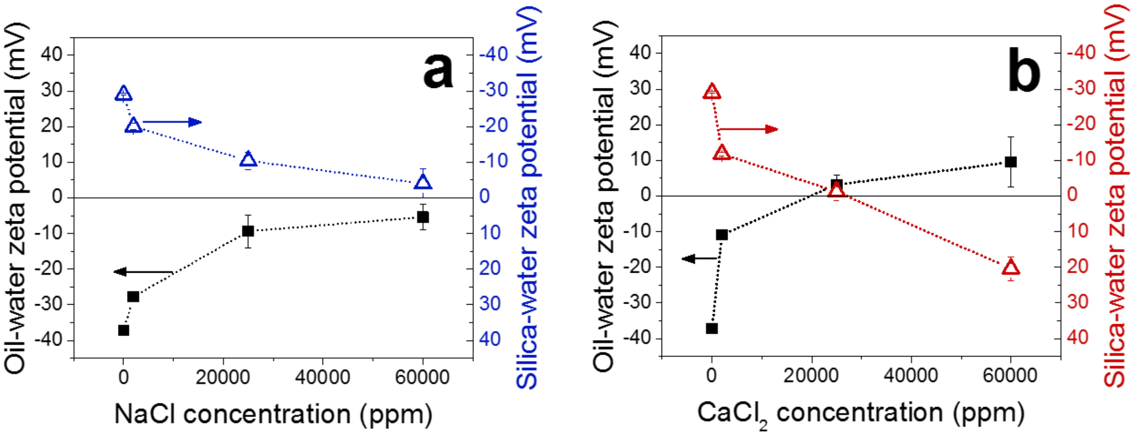

Figure 5.7. Zeta potentials of heavy crude oil-in-water and silica particle-in-water as a function of NaCl (a) and $CaCl_2$ (b) brine concentrations. The error bars are the standard deviations. Lines to guide the eye. Note that the left y-axes are the inverse of those presented in the right.

Figure 5.7 shows the zeta potentials of heavy crude oil droplets and silica particles as a function of brine type and concentration, and the results were found to be in good agreement with published data.[107, 108, 109] For both brine types, the negative zeta potential decreased with increasing brine concentration due to increased ionic screening of the heavy crude oil surface potential.[104, 105, 106] The zeta potential of the heavy crude oil is known to be attributed to the dissociation of acidic materials in the crude oil. Since the solution pH (~7) was much higher than the acid dissociation pH (~4.5),[34, 35] the heavy crude oil droplets were negatively charge when dispersed in aqueous solutions. Silica is also strongly negatively charged when dispersed in aqueous phase due to disassociation of surface hydroxyls. For the heavy crude oil, divalent cations (*i.e.* Ca^{2+}) can bind with dissociated acidic components forming positively charged $R–COO–Ca^{2+}$ complexes at the interface, with the divalent ions also able to bind to negatively charged silica, hence a significant reduction in the negative zeta potentials for both heavy crude oil and silica.[105, 112] **Figure 5.7**b shows that the divalent cation (Ca^{2+}) eventually neutralised charge and reversed the silica and heavy crude oil surface potential, unlike the monovalent (Na^+) which only lowered the negative zeta potential to -5 mV (**Figure 5.7**a).

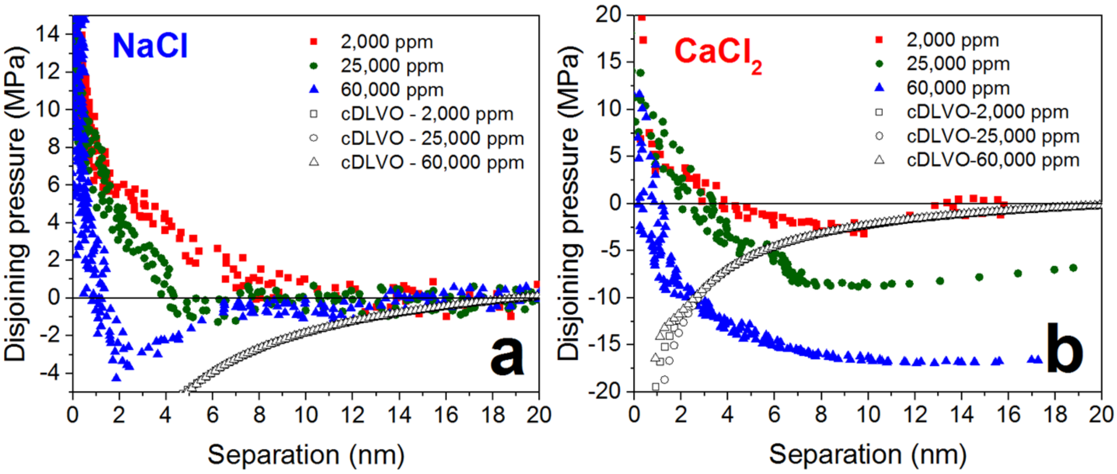

Figure 5.8. Oil-brine-glass disjoining pressures in NaCl (a) and $CaCl_2$ (b) of increasing brine concentration. All measured data as shown by the closed symbols were collected at ambient conditions. The open symbols represent the contributions from the van der Waals and electrostatic forces only.

In NaCl, the DLVO force was unable to predict the short-range interactions, with the disjoining pressure almost independent of the brine concentration and purely attractive. Similarly for the case of $CaCl_2$, both long-range and short-range behaviours was not satisfactorily described by classical DLVO force. The strongly attractive DLVO force, which would imply a less stable water film, results from the van der Waals force component exceeding the electrostatic forces. Measured short-range forces in brines are strongly repulsive indicating hydration force constructed as found by Yang *et al.*[108, 109]

For NaCl, the short-range behaviour is shown to depend on the brine concentration with the disjoining pressure at a fixed distance (*c.a.* 4 nm) decreasing in the order: 2,000 ppm > 25,000 ppm > 60,000 ppm. At higher brine concentrations, the positive disjoining pressure is weakened and this is attributed to weakening hydration of cations at higher ion concentrations.[103] Similarly, the dependence on ion concentration is observed for $CaCl_2$, however, the long-range interaction is dominated by negative disjoining pressures, which eventually become positive at very short separation distances. This long-range attraction is thought to result from a hydrophobic force[225, 226] between the oil-coated sphere and glass substrate. By contacting the heavy crude oil with brine solution prior to measurement, native surfactants in the heavy crude oil (naphthenic acids) transfer to the brine solution. The naphthenic acids are anionic and can adsorb on negatively charged surfaces (glass substrate) *via* divalent cation bridging,[226, 227] with the hydrophobic tail of the surfactant molecule increasing the hydrophobicity of the glass substrate. At higher brine concentrations, the hydrophobic force is stronger due to increased surfactant adsorption *via* cation bridging on the glass substrate. The influence of brine concentration on the amount of surfactant released from the heavy crude oil is negligible, thus the bulk surfactant concentration can be considered to be constant. As shown in **Figure 5.9**, the absence of naphthenic acids in brine solution shows the disjoining pressure to be totally repulsion (hydration force) confirming an effect of native surfactant contributing to a hydrophobic force.

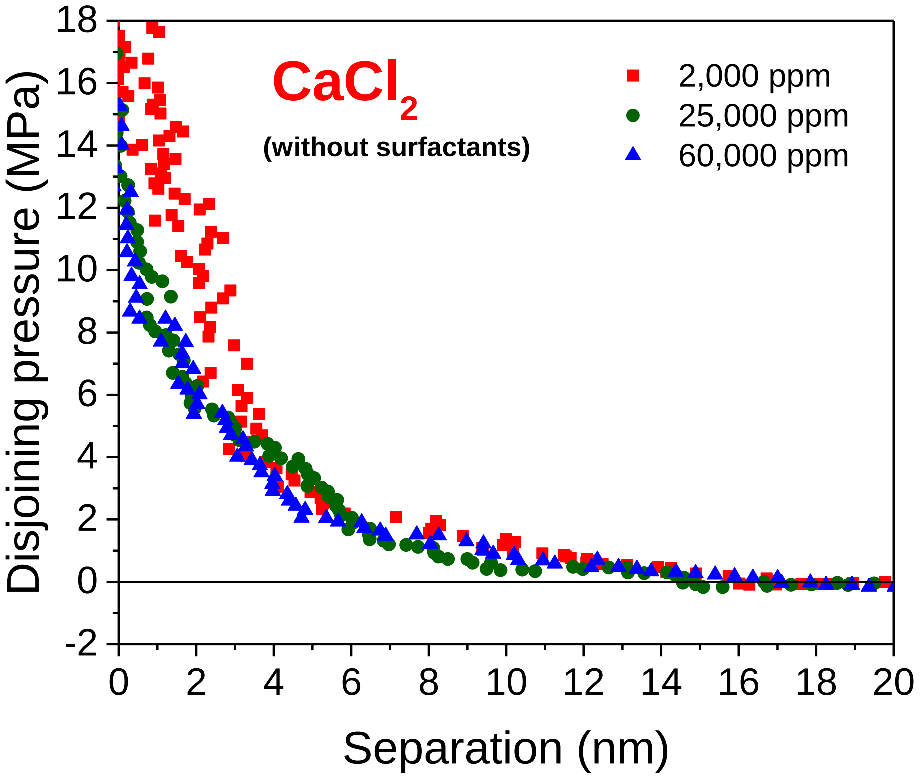

Figure 5.9. Measured disjoining pressures in fresh $CaCl_2$ brines (no natural surfactants). The data shows no attractive long-range hydrophobic force between a hydrophilic silica substrate and oil-coated colloidal probe.

The measured force interactions qualitatively correlate with the equilibrium contact angles in **Figure 5.6**. For brine solutions, increasing the cation concentration led to larger equilibrium contact angles (lower oil dewetting), and thus increased stability of the thin water film (by decreasing cation concentration) resulting in increased oil droplet dewetting. The comparison between NaCl and $CaCl_2$ (**Figure 5.6**) is reasonably consistent as well, with the more stable water films in NaCl leading to increased oil droplet dewetting compared to $CaCl_2$. While the disjoining pressure in $CaCl_2$ is dominated by the hydrophobic force contribution, it is worth noting that the weaker hydration of Ca^{2+} compared to Na^+ may also contribute to a weaker hydration force at short separation distances.[210]

The contact angle data in **Figure 5.6** is similar to the 'wettability map' proposed by Israelachvili and co-workers[76] who underlined the extended-DLVO theory including the hydration force. The authors stated that for low-salinity EOR, decreasing the brine concentration benefits oil recovery up to an 'optimum' concentration with further dilutions leading to reduced performance, consistent with the findings by Wei *et al.*[220] At concentration lower than the optimum, the repulsive hydration force might fail to form and consequently de-stabilises the water film while the attractive van der Waals becomes more pronouncing.[103]

In addition to the static wetting of thin film stability, the disjoining pressure could also attribute to the wetting dynamics[228, 229] as found in nanofluids system with structural force reported by Wasan *et al.*[230] In the present study, the measured disjoining pressure was related to the initial receding rate. The higher disjoining pressure shows stronger repulsion between the oil-water and water-solid interfaces and hence a rapid oil droplet dewetting.

5.4.4 Effect of temperature and pressure

The influence of high temperature and high pressure was also considered with brines. As discussed in Chapter 4, the study at 140 °C was necessary to observe at 10 bar to avoid water boiling. The pressure dependent effect was observed for all three brine concentrations (**Figure 5.10**a), which the increasing σ_{OW} with increasing pressure suggests that the surface-active molecules (*i.e.* asphaltenes) less partitioned at oil-water interface as discussed in Chapter 4. Considering the pressure effect on θ (**Figure 5.10**b), there is a clear dependency on the brine type. For NaCl, higher pressure results in higher equilibrium contact angles which is consistent with the behaviour described by the Young's equation. For $CaCl_2$, the pressure effect at a fixed brine concentration is negligible and this can be attributed to the strongly negative disjoining pressure (**Figure 5.8**b) that results from a long-range hydrophobic force that creates a preferred environment for oil droplet wetting. It is clear that the small changes in σ_{OW} with pressure are insufficient to affect the equilibrium contact angle.

Figure 5.10a clearly shows that the temperature increase from 60 °C to 140 °C led to a significant reduction in σ_{OW} for both brines due to a greater adsorption of surface-active species (*e.g.* asphaltenes and naphthenic acids) at the oil-water interface (details in Chapter 4). For NaCl, increasing the temperature led to a decrease in σ_{OW} from 21.7 to 13.2 mN/m at 2,000 ppm brine and 21.6 to 3.9 mN/m at 60,000 ppm brine. The substantial reduction in σ_{OW} at the highest brine concentration likely results from higher charge neutralised at the interface due to the more partitioning of salt ions. Due to increase in thermal energy, salt ions further partitioned at the interface leading to less negative surface charge and then promoted interaction with asphaltenes and naphthenic acids.

It worth noting that at 140 °C, the phase behaviour as observed in **Figure 5.4** is not consistent and the minima in σ_{OW} up to brine concentrations of 60,000 ppm is not measured (only Phase I obtained). Previously, the mechanism for the increase in σ_{OW} was attributed to the Jones-Ray effect and also the dipole-ion interaction that the adsorbed cations prefer to interact with water rather than asphaltenes. At higher temperatures, higher amount of salt can still adsorb at interface with increasing brine concentration. As such, the saturated brine concentration where the minima in σ_{OW} expected is believed to be much higher concentration at 140 °C.

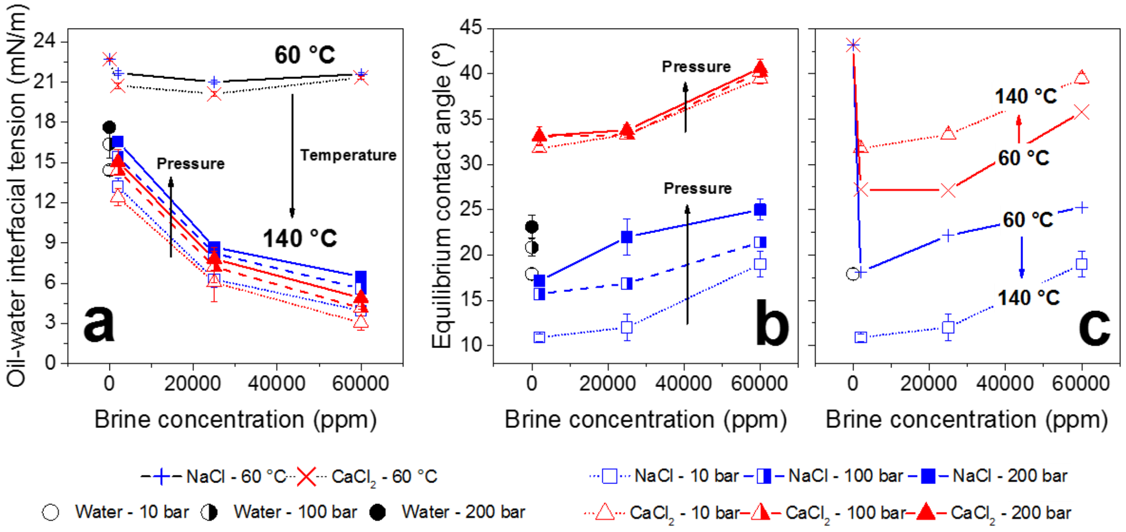

Figure 5.10. Influence of temperature (60 – 140 °C) and pressure (10, 100 and 200 bar) on the heavy crude oil-brine interfacial tension (a). Influence of pressure (b) and temperature (c) on heavy crude oil equilibrium contact angles (measured through water phase) at brine concentrations of 2,000, 25,000 and 60,000 ppm. Lines to guide the eye.

The temperature effect on θ also depends on brine type (**Figure 5.10**c). In NaCl, reducing in σ_{OW} decreased the contact angle distinctively described by Young's equation. The θ decreased ~10° from 60 to 140 °C with > 10 mN/m σ_{OW} reduction. For $CaCl_2$, strong attraction (hydrophobic force) is found to dominate the contact angle rather than σ_{OW} reduction effect. With much reduced σ_{OW} indicating highly adsorbed divalent cations at oil-water interface, such increasing divalent cations would bridge oil droplet onto substrate hence less oil dewetting at this high temperature.

It is noted that the disjoining pressure would have slightly altered as a function of temperature, which is negligible at the studied temperatures. Increasing thermal energy could reduce the Debye length but these temperatures were not high enough to distinctively affect the electrostatic force in the present study. The oil-water-silica Hamaker constant could have increased with increasing temperature,[17] thus possibly increasing the van der Waals attractive forces but it appeared that the effect was minima due to the contact angles observed. The hydration force is also not strongly temperature-dependent.[103] As such, increasing contact angle as a function of brine concentration was still observed due to the brine concentration effect itself, not the temperature change.

5.4.5 Implication for EOR and underlined mechanism

To liberate oil droplet from substrate, an adhesion of oil-water-substrate system needs to be decreased. The adhesion can be quantified by the adhesion work ($W_A = \sigma_{OW}(1 - cos\theta)$) or adhesion force ($F_A = \pi r \sigma_{OW} sin(\pi - \theta)$) as discussed in Chapter 2. Reducing in σ_{OW} or θ decreases those adhesions and thus favours the oil droplet liberation.

In brine system, the equilibrium state of the oil dewetting, *i.e.* the contact angle, strongly depends on the hydration force which does not exist in the pure water. With brine salinity decreasing, the θ has been found to change substantially whereas the σ_{OW} was merely constant. Therefore, it is worth to emphasise that the main EOR interfacial mechanism to reduce the oil-substrate adhesion is wettability alteration rather than a reduction in oil-water interfacial tension ($\Delta\theta$ >> $\Delta\sigma_{OW}$) for low-salinity EOR.

Considering reservoir condition, it is inevitable to note that the temperature screens the pressure effect at high pressure and high temperature condition. The high temperature mainly controlled the steady state of the oil dewetting *via* a great enhancement on the oil-water interfacial adsorption. Substantial reduction in σ_{OW} compared to θ ($\Delta\sigma_{OW} > \Delta\theta$) underlines the crucial mechanism under reservoir environment to be concerned on oil-water interfacial energy.

Figure 5.11 illustrates the oil-substrate adhesion depending on σ_{OW} and θ influenced by (i) high pressure and high temperature condition and (ii) brine salinity. Increasing temperature and pressure results in a massive reduction in oil-substrate adhesion contributed to oil-water interfacial tension decrease although the contact angle slightly increases, a white route (a) in **Figure 5.11**. On the contrary, the brine salinity effect much influences the adhesion decrease by reduction in contact angle while the oil-water interfacial tension has a minor effect, a black route (b) in **Figure 5.11**.

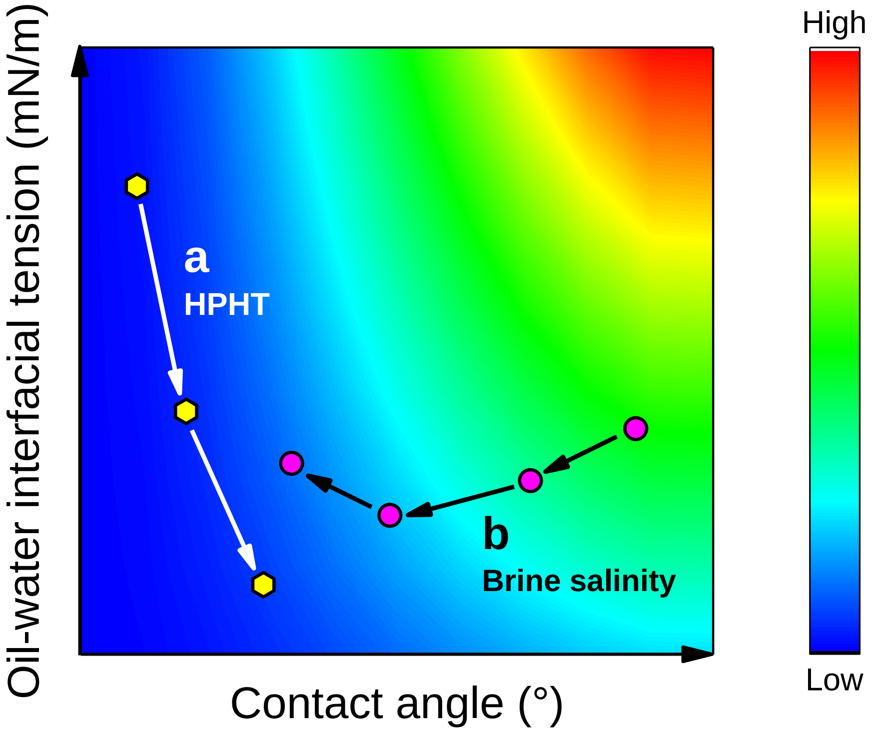

Figure 5.11. Contour map illustrates oil-substrate adhesion changed as a result of (a) increasing pressure and temperature (HPHT) and (b) decreasing brine salinity.

5.5 Conclusion

Oil droplet dewetting dynamics in brines, with equivalent concentration ranges from formation water to EOR low-salinity fluid, have been investigated. Brine influences the oil-water interfacial behaviour through crude oil surface-active materials and salt ions adsorption. Diluted brines dewetted more oil from substrate resulting in lower contact angles which generally favour oil droplet liberation. The repulsive hydration force existing in brines was found to be an influencing factor in the dewetting of oil droplet rather than the oil-water interfacial tension. With increased brine concentration, oil droplets dewetted less and the contact angles increased due to weaker interfacial repulsive forces. In the divalent brines, the solid substrate became hydrophobic due to divalent cations bridging the natural surfactants on the substrate resulting in attractive hydrophobic force between the oil droplet and hydrophobic substrate. This hydrophobic force caused less oil to be dewetted and hence the higher contact angle obtained.

In NaCl brines at high temperature (140 °C), a reduction in oil-water interfacial tension led to reduced contact angles. Although the pressure effect was minimal, it increased the oil-water interfacial tension, leading to slightly higher contact angles. For $CaCl_2$, the hydrophobic force strongly dominates the oil dewetting rather than the interfacial tension hence the contact angles were lower at this high temperature, with negligible pressure influence. Despite thermal energy increasing, the disjoining pressure likely remained unchanged.

The recent findings suggest that salt-dependent trends observed under ambient conditions do not represent those interfacial behaviours found at reservoir conditions. In considering the oil-substrate adhesion energy, a reduction in interfacial tension was found to be less important than wettability alteration, which is considered as the main interfacial mechanism for low-salinity EOR. On the contrary, in high pressure high temperature condition the influencing factor was a reduction in oil-water interfacial tension to reduce the oil-substrate adhesion. As high temperature induces a more effective interfacial adsorption than the high pressure demoting the adsorption.

Chapter 6

Surface-Active Nanoparticles:

Interfacial Activity and Oil Droplet Dewetting

6.1 Synopsis

Nanoparticles typically used in EOR applications have negligible surface activity (i.e. the particles weakly partition at the oil-water interface, hence the reduction in interfacial tension is minimal), and their contribution to modifying the oil-substrate contact angle by changing the interfacial tension is negligible. In the current work, surface-active nanoparticles (PNIPAM) were synthesised and their contribution to modifying the oil-water interfacial tension and dynamic dewetting of a heavy crude oil droplet was considered in the presence of an anionic surfactant (SDS). Adsorption kinetics of PNIPAM and SDS blend (1:1 mass ratio) showed that the surface excess (two components) of each surface-active species was a function of the total bulk concentration. Adsorption of SDS exceeded PNIPAM at low bulk concentration (5 × 10^{-4} *wt%), while PNIPAM showed greater surface excess than SDS at high bulk concentration (5 × 10*$^{-3}$ *wt%), with the balance of both species residing at the oil-water interface as a function of their size (bulk diffusion) and surface activity. The larger PNIPAM particles diffuse slower than SDS, hence limitations in diffusion can be overcome at high concentrations when the increased surface activity of PNIPAM compared to SDS is evidenced.*

The interfacial activity of both PNIPAM and SDS was shown to contribute to modify the rate of oil dewetting. PNIPAM + SDS blend at low concentration (5 × 10^{-4} wt%; where SDS > PNIPAM at the interface) displaced the heavy crude oil droplet faster than at high concentration (5 × 10^{-3} wt%; where PNIPAM > SDS at the interface: initial receding rate: 1.72 °/s → 5.66 °/s) and reached a lower contact angle (60.9° → 37.0°), even though the oil-water interfacial tension remained relatively high (25.3 mN/m). This behaviour results from the presence of excess PNIPAM particles remaining in the bulk fluid and self-assembling in the oil-water-substrate "wedge" (region close to the three-phase contact line) to induce a structural disjoining pressure that promoted greater oil droplet dewetting. At high concentration (PNIPAM + SDS; at 5 × 10^{-3} wt%), the PNIPAM particles strongly adsorbed at the oil-water interface and were able to bridge the solid-liquid and liquid-liquid interfaces, thus reducing the oil dewetting rate.

The performance of the PNIPAM + SDS blend was studied in low-salinity brines. In the presence of brines, PNIPAM particles reduced in size (less solvated) but remained dispersed with a weakly negative surface charge, and this led to the faster bulk diffusion of PNIPAM and greater adsorption at the oil-water interface to increase the reduction in oil-water interfacial tension. In NaCl, a hydration force resulting from the accumulation of hydrated ions in the oil-water-substrate wedge enhanced oil droplet dewetting, and in the presence of PNIPAM, disjoining pressures resulting from hydration and structural forces led to the gradual liberation of the oil droplet from solid surface, even though the droplet buoyant force did not exceed the oil-substrate adhesion force.

The benefit of using temperature-responsive particles was considered by studying the stability of water-in-oil emulsions. PNIPAM stabilised emulsions at T > LCST were less stable when T < LCST and this was due to reduced partitioning of PNIPAM at the oil-water interface. Under such conditions, the PNIPAM particles were more hydrated *and preferred to stay in the bulk aqueous phase as confirmed by the higher oil-water interfacial tension. Using functional particles to switch the stability of an emulsion could be advantageous when separating emulsions after the well-head.*

6.2 Introduction

Due to its broad performance, nanoparticles are increasingly of interest in a number of applications including the oil recovery process. Although typical nanoparticles (*e.g.* SiO_2) have been reported to have no ability to adsorb at the oil-water interface,[19, 231] research suggested that nanoparticles could partition at the interface with particle surface modified. This could reduce the apparent interfacial tension, hence suggesting surface wettability alteration (contact angle decreases) as reviewed in Chapter 2. The nanofluid injection has also been reported to change the contact angle *per se* by constructing the structural disjoining pressure at the three-phase contact line.[133]

It has been found that the blend of silica nanoparticles and surfactant (SDS) can reduce the oil-water interfacial tension greater than the sole surfactant system because the surfactant functionalised the particles to be more hydrophobic and able to partition at the interface.[143, 144] Research by Wasan's group[11, 33, 221] has investigated the silica nanoparticle self-arrangement at the water wedge forming the structural disjoining pressure. As discussed by the authors, the nanofluids contained small amount of surfactant in order to generate enough water wedge room for particle self-arrangement. The formation of structural disjoining pressure by nanoparticles was also found in other particle type that were also not surface-active, *i.e.* polymer-coated nanoparticles.[145] Such structural disjoining pressure has been suggested to be main nanoparticle EOR mechanism.[133] However, the study of clay particles (modified to be hydrophobic by asphaltenes) that could also partition at the oil-water interface caused detrimental oil dewetting.[57] It is believed that the asphaltenes on clay could bridge the oil onto solid surface and hence resists oil dewetting. So far, it has not been clear that how the adsorption/partitioning property of nanoparticles at the oil-water interface affects the oil dewetting that governed by the structural disjoining pressure.

As such, an interest in the current chapter is of specific nanoparticles that can energetically adsorb at the oil-water interface *per se*, hence the interfacial energy reduced. This brings to the hydrogel nanoparticles *viz* poly(*N*-isopropylacrylamide) or PNIPAM. These particles are soft and known to be interfacially active.[21, 152, 232] The PNIPAM particles are suitable to investigate what actually the nanofluids need to construct the disjoining pressure (with or without surface-active property). It is worth to note that adsorption of PNIPAM at the interface is quite unique. Li *et al*.[20, 152] differentiated the particle adsorption into two steps: (i) diffusion-controlled adsorption and then (ii) particle deformation and spreading on the interface. PNIPAM is also size-responsive with temperature: large at T < the lower critical solution temperature (LCST ~32 °C) and small at T > LCST.[233] This would benefit the oil-water separation process (demulsification).[234, 235] In addition to interfacial phenomenon, PNIPAM could also benefit the flow in porous media. Particle softness could prevent severe particle jamming into porethroat after the flow, which occurs with solid particles causing a serious productivity decline and formation damage.[73, 236] Routh and co-workers[237, 238] have found that the particle thermal responsivity can control the nanofluid viscosity and flow permeability. The authors reported the particles precipitating at T > LCST leading to blockage of flow paths. Nanofluid viscosity was found to increase at T < LCST where the particles were hydrated.

The present chapter focuses on the interfacial activity with competitive adsorption of PNIPAM and SDS at the oil-water interface. Oil droplet dewetting dynamics was investigated to examine effects of oil-water interfacial activity and nanoparticle structural force. Following the previous chapter, workability of the particles in brine environment was assessed. Demulsification test of particle-stabilised water-in-oil emulsions was also studied at T > LCST and < LCST.

6.3 Materials and Experimental Methods

6.3.1 Nanoparticle characterisation

The ZetaSizer Nano ZS (Malvern Instrument, UK) was used to measure the hydrodynamic diameter and zeta potential of PNIPAM particles dispersed in aqueous solutions with the temperature varied from 20 to 65 °C. The temperature was controlled within ± 1 °C, with the dispersion left for 10 min to attain the steady-state temperature. Particle size measurements were repeated at least 3 times and zeta potentials were an average of 12 measurements.

6.3.2 Preparation of nanofluids

The PNIPAM + SDS blend was compared to the individual components, and the base fluid in the absence of any surface-active species. The PNIPAM + SDS blend was prepared by mixing the same concentration of PNIPAM and SDS at a 1:1 mass ratio, therefore the total concentration of the blend remains unchanged. The PNIPAM solution was added to SDS solution under gentle agitation. The PNIPAM + SDS blend was then mixed for 30 min to ensure good dispersion. All solutions were prepared fresh and sonicated for 5 min prior to use. To prepare the PNIPAM + SDS blend in brine solution, SDS and PNIPAM were first prepared separately in the brine solution at the desired concentration. These solutions were then mixed together at a 1:1 mass ratio to obtain the blend.

It should be noted that the SDS concentrations considered in the current study are lower than the CMC of SDS (**Figure 4.11**), therefore no micelles were present in the nanofluids. At the brine concentration (2,000 ppm) used in the current study, the CMC of SDS was not reduced (CMC in brine ≈ CMC in water), hence no micelles are expected to be present in either fluid.

6.3.3 Interfacial tension and contact angle measurements

The technique to measure the oil-water interfacial tension and contact angle has been described in Chapter 3. The aging time for oil-water interfacial tension measurements was ≤ 4,000 s. The experimental conditions were kept constant at T = 60 °C and ambient pressure. The control test of Milli-Q water only (T = 60 °C and ambient pressure) has been reported in Chapter 4.

6.3.4 Destabilisation of water-in-oil emulsions

Destabilisation of water-in-oil emulsions stabilised by PNIPAM particles was considered by changing the temperature of the emulsion ($T_{emulsion}$ < and > LCST) to induce a conformational change of the PNIPAM particles.[239, 240] To minimise the contribution from a changing fluid viscosity, the experimental temperatures were selected close to the LCST of PNIPAM: lower temperature equal to 30 °C where T < LCST, and higher equal to 33 °C where T > LCST.

Due to the opaqueness of the heavy crude oil, a transparent base oil (220R, Chevron, Belgium) was used with PNIPAM particles dispersed in Milli-Q water at 5×10^{-4} wt% and pH 7. Water-in-oil emulsions (10 vol% water) were prepared in 20 mL glass vials and homogenised (IKA T25 Ultra-Turrax instrument, Germany) at 10,000 rpm for 1 min at 60 °C. The emulsions were placed in the Turbiscan^{TM} Lab (Formulaction, France) stability analyser and the phase separation monitored immediately by changes in the backscattered signal (ΔBS) along the sample cell.[241] The cell temperature was maintained at either 30 or 33 °C. The ΔBS was recorded at 1 min intervals for 1 h. Destabilisation performance was evaluated according to the rate of phase separation.

6.4 Results and Discussion

6.4.1 Nanoparticle characterisation

Figure 6.1a shows the thermal response of the PNIPAM particles. In Milli-Q water and at T < LCST, the particle hydrodynamic diameter increases from ~152 to 225 nm with decreasing temperature (30 to 20 °C), and at T > LCST the particle size is ~55 nm and independent of temperature. The LCST is found to be in the region ~32 – 35 °C and similar to values reported in the literature.[20, 233, 242]

It has been shown that SDS binds to PNIPAM chains *via* hydrophobic interactions and can increase the LCST of PNIPAM.[243, 244] However, low concentration SDS (*i.e.* < 2×10^{-2} wt%) was reported to have minimal SDS-PNIPAM interaction and negligible effect on the LCST. Therefore, in the current study the presence of SDS ($\leq 5 \times 10^{-3}$ wt%) led to no change in the LCST of PNIPAM.

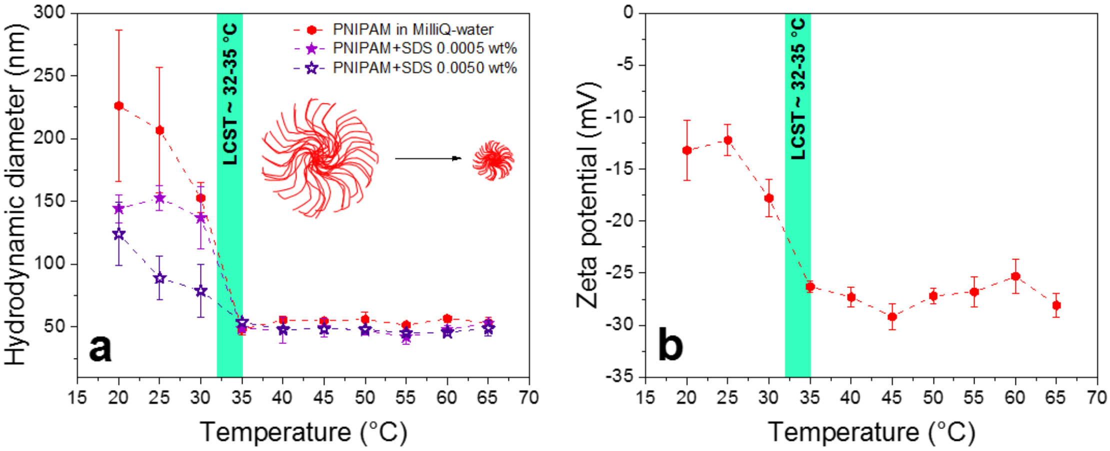

Figure 6.1. Hydrodynamic diameter of PNIPAM particles in Milli-Q water, and Milli-Q water + SDS of increasing concentration (a). Zeta potential of PNIPAM particles in Milli-Q water as a function of temperature (b). The green shaded region indicates the LCST threshold. The error bars are the standard deviation and lines are added to guide the eye.

A change in the hydrodynamic diameter was observed at T < LCST, but at T > LCST the effect on PNIPAM size was minimal. Below the LCST the hydrodynamic diameter decreased with increasing SDS concentration, which has been shown to result from fragmentation of the PNIPAM into smaller clusters by the SDS.[245, 246] Some of PNIPAM chains from the particle may disperse into a single chain stabilised by the SDS.[246] At T > LCST, PNIPAM de-swelled into a highly dense globule, thus the presence of SDS to fragment the PNIPAM particles was less.

The zeta potential of PNIPAM particles dispersed in Milli-Q water is slightly negative (**Figure 6.1**b) due to residual sulfate groups of the KPS initiator.[20] Below the LCST the zeta potential was *ca*. -14 mV at 20 °C and increased to *ca*. -27 mV when T > LCST.[20, 247] The change in PNIPAM zeta potential corresponded to the change in particle size[20, 21, 242] and this can be attributed to the changing surface density of sulfate groups when the temperature transitions above (high surface density of sulfate groups due to PNIPAM globule) and below (low surface density of sulfate due to PNIPAM coil) the LCST.[248]

6.4.2 Oil-water interfacial activity

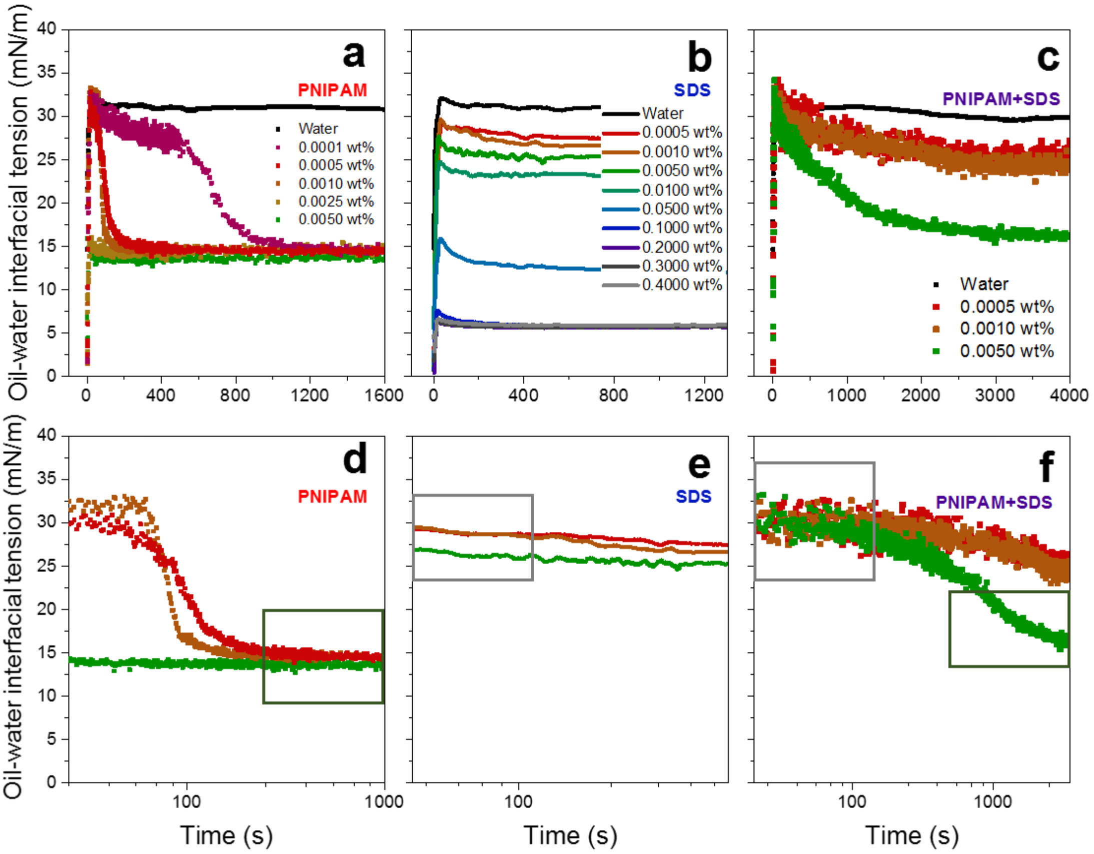

Figure 6.2. Dynamic oil-water interfacial tensions at 60 °C: PNIPAM (a), SDS (b) and PNIPAM + SDS blend (c). Equivalent systems shown as semi-log plots (d) – (f) to highlight the difference in interfacial tension immediately following droplet induction. The boxes are included to show similarity between the PNIPAM + SDS blend and the individual components. The grey box highlights good agreement between the blend and SDS only (*i.e.* high σ_{OW} following droplet induction (< 100 s)), and the green box highlights good agreement between the blend and PNIPAM only (σ_{OW} decreased to a value closer to PNIPAM).

Dynamic and equilibrium interfacial tensions: **Figure 6.2** compares the heavy crude oil-water dynamic interfacial tension with the aqueous phase containing either PNIPAM particles, SDS, or both. For PNIPAM (**Figure 6.2**a), the steady-state (t > 1,000 s) oil-water interfacial tension was shown to be independent of the PNIPAM concentration (~14 mN/m, see **Figure 6.3**), although the dynamic interfacial tension was a function of the PNIPAM concentration, and the change in interfacial tension corresponded to a two-step adsorption: (i) initial diffusion-controlled and (ii) relaxation/re-organisation of the PNIPAM particles.[20, 152] At concentrations $\geq 5 \times 10^{-3}$ wt% PNIPAM, the heavy crude oil-water interfacial tension decreased rapidly reaching a steady-state value within the first few hundred seconds. Higher PNIPAM concentrations increased the rate of interfacial tension reduction, and this would agree with Fick's laws of diffusion. At 1×10^{-4} wt% PNIPAM, the interfacial tension was characterised by three-phase classical kinetics: (i) diffusion of PNIPAM to the oil-water interface; (ii) adsorption of PNIPAM at the oil-water interface; and (iii) relaxation/reorganisation of PNIPAM to a steady-state condition, similar to previous data.[249, 250]

For SDS (**Figure 6.2**b), the equilibrium interfacial tension was reached within 200 s following droplet induction. Since the SDS is in equilibrium with the bulk fluid and oil-water interface, the equilibrium values are a function of the SDS concentration until the CMC is exceeded, ~0.1 wt%. At equivalent concentrations, the reduction in heavy crude oil-water interfacial tension by SDS is lower than PNIPAM. Over an order of magnitude increase in the SDS concentration is needed for the interfacial tension reduction to exceed that resulting from PNIPAM particles.

Figure 6.2c shows the heavy crude oil-water interfacial tension for the PNIPAM + SDS blend, with SDS concentrations below the CMC to demonstrate the concentration effect. Compared to the individual species, the time required for the interfacial tension to attain steady state is substantially longer, ~3,000 s, and the steady-state values show a dependence on the total component concentration. Qualitatively, the rate of change in interfacial tension is higher at 5 × 10^{-3} wt% compared with the two lower component concentrations. These characteristics result from the changing composition of the interface which is discussed below.

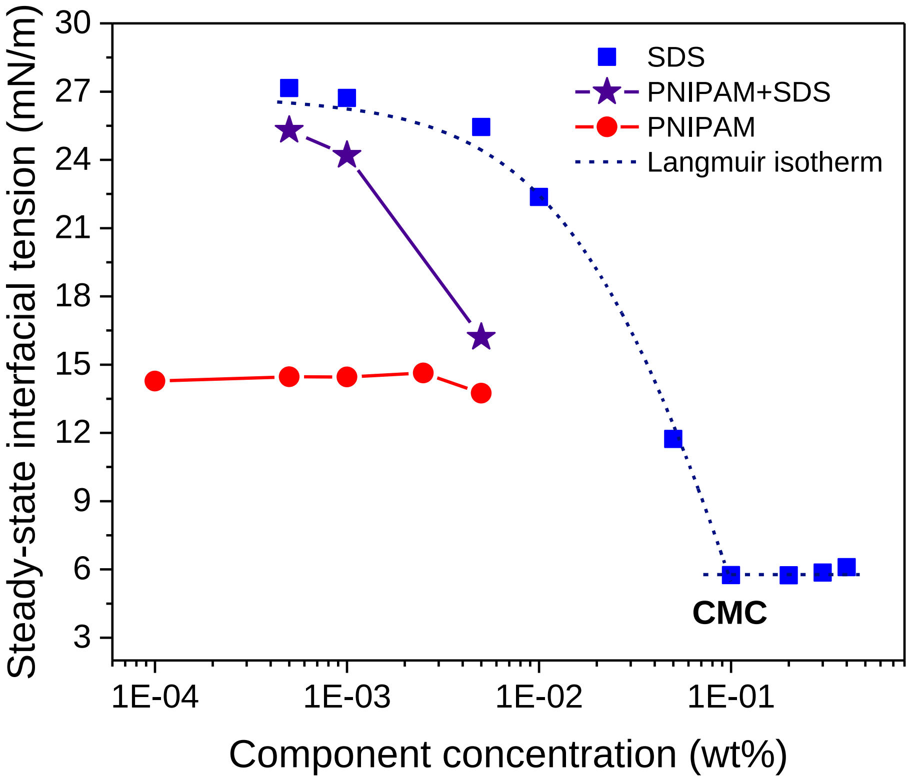

Figure 6.3. The steady-state heavy crude oil-water interfacial tensions as a function component concentration: PNIPAM, SDS and PNIPAM + SDS blend, at 60 °C. The dash line is Langmuir isotherm fit of the SDS data. The red and purple solid lines are added to guide the eye.

Similar to SDS, adsorption of PNIPAM particles at an oil-water interface is shown to be a diffusion-controlled,[251] with desorption (irreversible adsorption) considered to be negligible due to the high particle detachment energy (E = 5,900 k_BT) from the interface, as described by $E = \pi a^2 \sigma_{OW}(1 \pm cos\theta)^2$.[252, 253] Diffusion-controlled adsorption can be described by the Ward-Tordai equation: [253]

$$\Gamma_t = 2\sqrt{\frac{D_{Interface}}{\pi}} C_0 \sqrt{t} \tag{6.1}$$

where Γ_t is the interfacial concentration of material at time t, $D_{Interface}$ the diffusion coefficient at the interface and C_0 the material bulk concentration. Here, the interfacial concentration (Γ_t) equates to the surface pressure ($\sigma_0 - \sigma_t$) by:[254, 255]

$$\sigma_0 - \sigma_t = \Gamma_t RT. \tag{6.2}$$

Combining Equations (6.1) and (6.2), the relationship for the time-dependent interfacial tension is given by:

$$\sigma_t = \sigma_0 - 2RT\sqrt{\frac{D_{Interface}}{\pi}} C_0 \sqrt{t}. \tag{6.3}$$

According to Equation (6.3), σ_t is proportional to $\sqrt{t}$ for a diffusion-controlled process and the slope (k) of σ_t versus $\sqrt{t}$ is proportional to the bulk concentration (C_0), where:

$$k = 2RT\sqrt{\frac{D_{Interface}}{\pi}} C_0. \tag{6.4}$$

For the data shown in **Figure 6.4**, the slope (k) is directly proportional to C_0 for both PNIPAM and the PNIPAM + SDS blend, confirming that adsorption in both these systems is diffusion-controlled. It should be noted that the slopes (k) of the PNIPAM + SDS blend were calculated after t > 400 s, where PNIPAM likely started to adsorb at the oil-water interface following SDS adsorption, see **Figure 6.2**b and c. The diffusion coefficient at the interface ($D_{Interface}$) is calculated using Equation (6.4), and the bulk diffusion coefficient (D_{Bulk}) is calculated *via* the Stokes-Einstein equation:[256]

$$R_h = \frac{k_B T}{6\pi\mu D_{Bulk}} \tag{6.5}$$

where R_h is particle hydrodynamic radius, k_B the Boltzmann constant and μ bulk fluid viscosity.

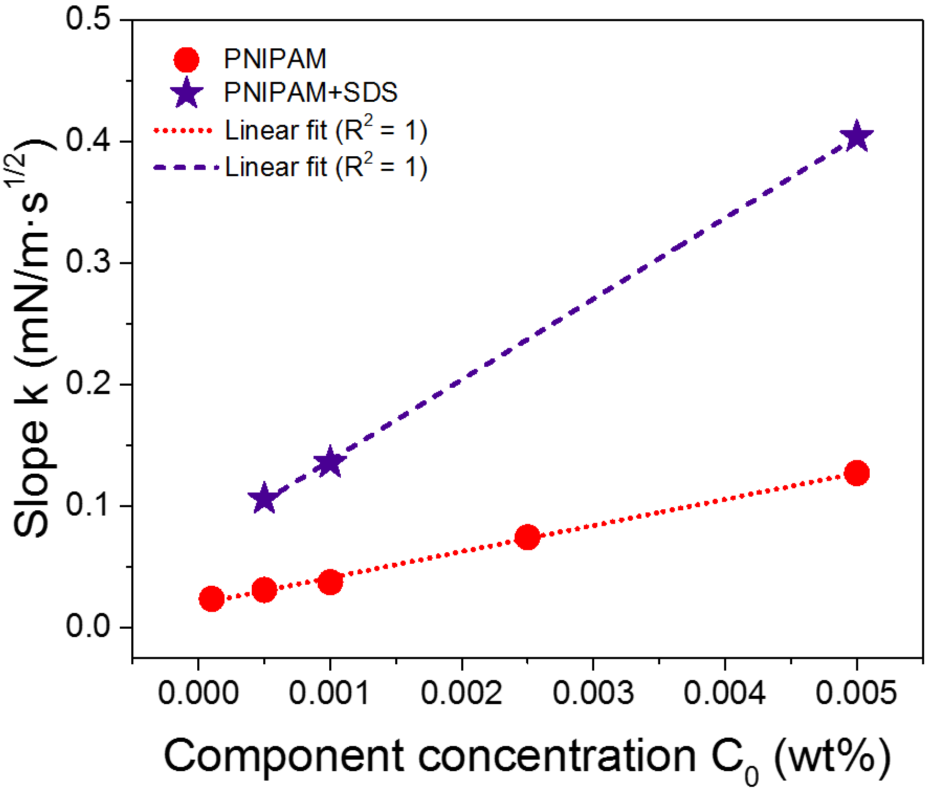

Figure 6.4. Slope k as a function of the component concentration (C_0). The lines are linear fits and confirm diffusion-controlled adsorption for PNIPAM and the PNIPAM + SDS blend.

Since C_0 is given as wt% and not mol/m^3, the units of $D_{Interface}$ and D_{Bulk} are not consistent. Therefore, the normalised diffusion coefficients are used to compare D rather than absolute values as discussed by Li *et al.*,[21, 252] (**Table 6.1)**. At equivalent component concentrations, the PNIPAM + SDS blend showed higher bulk diffusion coefficients compared to PNIPAM particles only, a result of the decrease in particle size. The negatively charged SDS molecules were believed to promote an electrostatic repulsion with negatively charged PNIPAM particles,[143, 257] hence higher dispersion and increased diffusivity towards the interface. $D_{Interface}$ reduced with increasing component concentration (C_0) and this implies that adsorption of surface-active species is hindered at high concentrations, likely a result of a random-sequential adsorption mechanism and particle jamming dominating behaviour at longer times.[152, 258] Increasing particle concentration has been shown to change the adsorption process from a diffusion-controlled to interaction-controlled mechanism as a result of collisions between approaching particles and particles already partitioned at the oil-water interace.[250, 259]

Table 6.1. Diffusion coefficients at the interface ($D_{Interface}$) and in the bulk (D_{Bulk}).

Concentration (wt%)	**Diffusion coefficient at the interface**		**Diffusion coefficient in the bulk**	
	$D_{Interface}$ (mol^2/m^4·s)	***Normalised $D_{Interface}$ [a]***	***D_{Bulk} (m^2/s)***	***Normalised D_{Bulk} [a]***
PNIPAM particles in Milli-Q water				
1×10^{-4}	0.552	1.00	1.85×10^{-11}	1.00
5×10^{-4}	0.039	0.07	1.85×10^{-11}	1.00
1×10^{-3}	0.014	0.03	1.85×10^{-11}	1.00
2.5×10^{-3}	0.009	0.02	1.85×10^{-11}	1.00
5×10^{-3}	0.007	0.01	1.85×10^{-11}	1.00
PNIPAM + SDS in Milli-Q water				
5×10^{-4}	0.456	0.83	1.85×10^{-11}	1.00
1×10^{-3}	0.188	0.34	2.18×10^{-11}	1.18
5×10^{-3}	0.067	0.12	2.29×10^{-11}	1.24

[a] D is normalised by D at 1×10^{-4} wt% in Milli-Q water.

Surface-active contributions and interfacially dominating regimes: In PNIPAM + SDS blend, both PNIPAM and SDS adsorb to the oil-water interface and this is confirmed by the steady-state interfacial tension of PNIPAM + SDS blend being intermediate of the two individual components (**Figure 6.3**).

Figure 6.2d and e show σ_{PNIPAM} and σ_{SDS} on semi-log plots at three equivalent component concentrations. At the two lowest concentrations (5×10^{-4} and 1×10^{-3} wt%), the short-time behaviour of σ_{PNIPAM} is almost independent of time until ~100 s after which the heavy crude oil-water interfacial tension gradually decreases to the steady-state value. At the highest concentration (5×10^{-3} wt%), the interfacial tension remains low and shows no time dependence, indicating a rapid decrease in heavy crude oil-water interfacial tension to the steady-state value immediately following droplet induction. In contrast, at all component concentrations, σ_{SDS} shows only a small time-dependence and the heavy crude oil-water interfacial tension remains higher than σ_{PNIPAM}.

Compared to the individual components, $\sigma_{PNIPAM+SDS}$ (**Figure 6.2**f) showed a similarity to σ_{SDS} (grey box) immediately following droplet induction a similarity to σ_{PNIPAM} (green box) at longer times. This effect is emphasised at the highest component concentration, 5×10^{-3} wt%. For the PNIPAM + SDS blend, this behaviour would imply that SDS initially partitions at the heavy crude oil-water interface before competitive adsorption by PNIPAM particles changes the interfacial composition at longer aging times. This is reasonable since PNIPAM particles (at an equivalent component concentration) are more interfacially active than SDS.

To determine the potential of the individual components in the PNIPAM + SDS blend to lower the oil-water interfacial tension, the decrease in interfacial tension can be described by $-\Delta\sigma = \sigma_0 - \sigma$ (*i.e.* the surface pressure), where σ_0 = 33.5 mN/m (initial oil-water interfacial tension in the absence of surface-active species). **Figure 6.5** shows the interfacial composition depends on the component concentration (wt%) with $-\Delta\sigma_{PNIPAM+SDS}$ (star symbol) between $-\Delta\sigma_{SDS}$ (square symbol) and $-\Delta\sigma_{PNIPAM}$ (circle symbol). Taking a first-order approximation, the contribution of increasing $-\Delta\sigma$ from both PNIPAM and SDS can be taken as a weighted-arithmetic mean of the steady-state $-\Delta\sigma$ for each individual component, enabling an approximation of the surface-active contribution (A) from PNIPAM and SDS in the blend.

For one component, at a given component concentration and aging time, the single component contributes to the increase in $-\Delta\sigma$ (A = 1). For the blend ($A_{PNIPAM+SDS}$), the increase in $-\Delta\sigma$ ($-\Delta\sigma_{PNIPAM+SDS}$), is taken to be the summation of both components (A_i) and the individual $-\Delta\sigma_i$:

$$-\Delta\sigma_{PNIPAM+SDS} = \frac{\sum_{i=1}^{n} -\Delta\sigma_i A_i}{\sum_{i=1}^{n} A_i}$$

$$-\Delta\sigma_{PNIPAM+SDS} = \frac{-\Delta\sigma_{PNIPAM}A_{PNIPAM} + -\Delta\sigma_{SDS}A_{SDS}}{A_{PNIPAM+SDS}} \tag{6.6}$$

Since the blend is a two component system, the interfacial activity ($A_{PNIPAM+SDS}$ = 1) is equal to the combined contribution of PNIPAM and SDS ($A_{PNIPAM+SDS} \approx A_{PNIPAM} + A_{SDS}$ = 1), thus Equation (6.6) becomes:

$$-\Delta\sigma_{PNIPAM+SDS} = \frac{-\Delta\sigma_{PNIPAM}(1 - A_{SDS}) + -\Delta\sigma_{SDS}A_{SDS}}{1} \tag{6.7}$$

The surface-active contribution of each component (A_i) partitioned at the heavy crude oil-water interface is then determined by Equation (6.7).

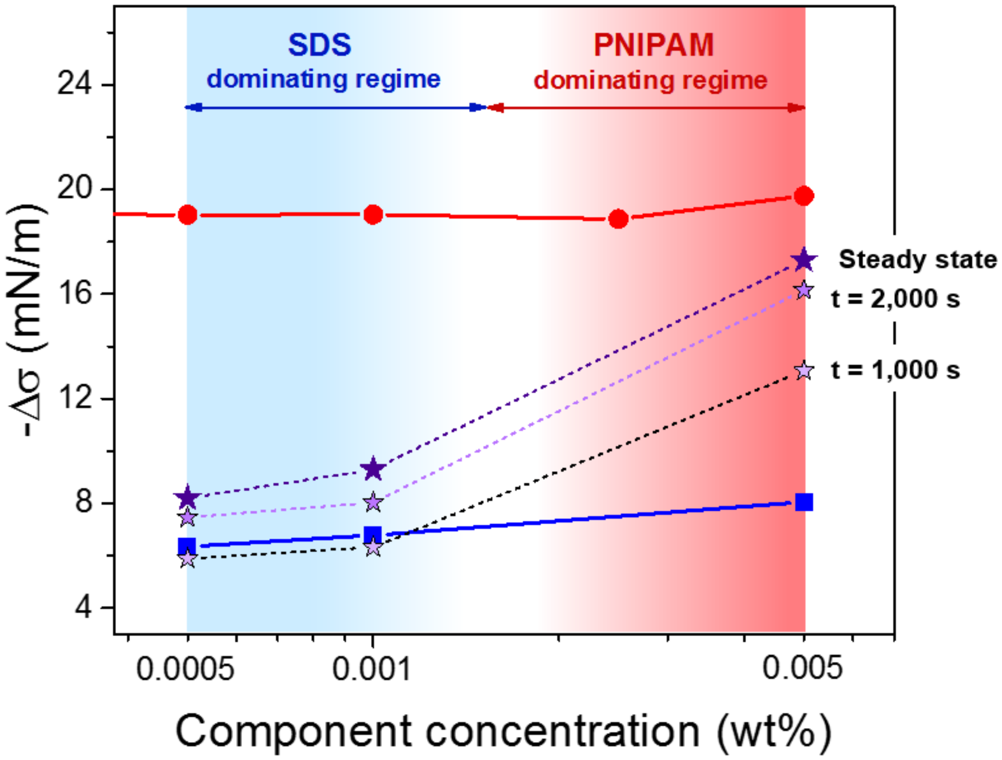

Figure 6.5. Steady-state values of $-\Delta\sigma_{SDS}$ (blue squares), $-\Delta\sigma_{PNIPAM}$ (red circles), and dynamic and steady-state $-\Delta\sigma_{PNIPAM+SDS}$ (purple stars) as a function of component concentration. Shaded regions define the two dominating component regimes: SDS (blue) and PNIPAM (red). The lines are added to guide the eye.

The surface-active contribution (A) from PNIPAM and SDS in the blend are calculated by Equation (6.7), and **Figure 6.6** shows that A_{SDS} decreased while A_{PNIPAM} increased with time and the total component concentration. At low concentrations (5×10^{-4} and 1×10^{-3} wt%), SDS is the dominant species at the heavy crude oil-water interface (due to high bulk diffusion coefficient = 2.9×10^{-9} m^2/s), but with increasing time PNIPAM gradually displaces SDS, and at the near steady-state condition the composition of the interface approaches equal fractions of SDS and PNIPAM. At the high concentration (5×10^{-3} wt%), the interfacial composition at t = 1000 s is almost an equal balance of PNIPAM and SDS, with PNIPAM predominately occupying the oil-water interface as the steady-state condition is reached.

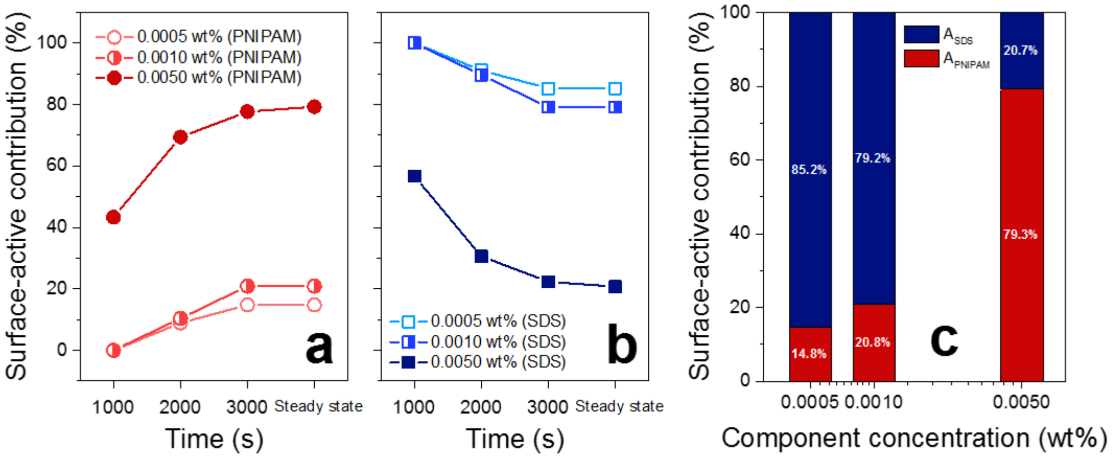

Figure 6.6. Surface-active contributions from PNIPAM (a) and SDS (b) as a function of aging time and component concentration. The steady-state conditions are compared in (c). Lines to guide the eye.

The preferential adsorption (higher interfacial activity) of PNIPAM was confirmed by studying the oil-water interfacial tension following the consecutive addition of the two components (**Figure 6.7**). First adding PNIPAM (**Figure 6.7**a and c) followed by SDS showed no change in the oil-water interfacial tension. The slight reduction in oil-water interfacial tension for 5 × 10^{-3} wt% PNIPAM to SDS may have resulted from a disturbance of the droplet. First adding SDS followed by PNIPAM (**Figure 6.7**b and d) showed a measurable reduction in oil-water interfacial tension when the component concentration was 5 × 10^{-3} wt%, and confirms the ability of PNIPAM to co-adsorb/displace SDS at oil-water interface. This simple experiment validates our understanding that at high component concentrations PNIPAM preferentially partitions at the oil-water interface. This is because PNIPAM is strongly adsorbed (particle detachment energy >> $k_B T$)[252] and can spread and pack more densely at the oil-water interface.[232, 260]

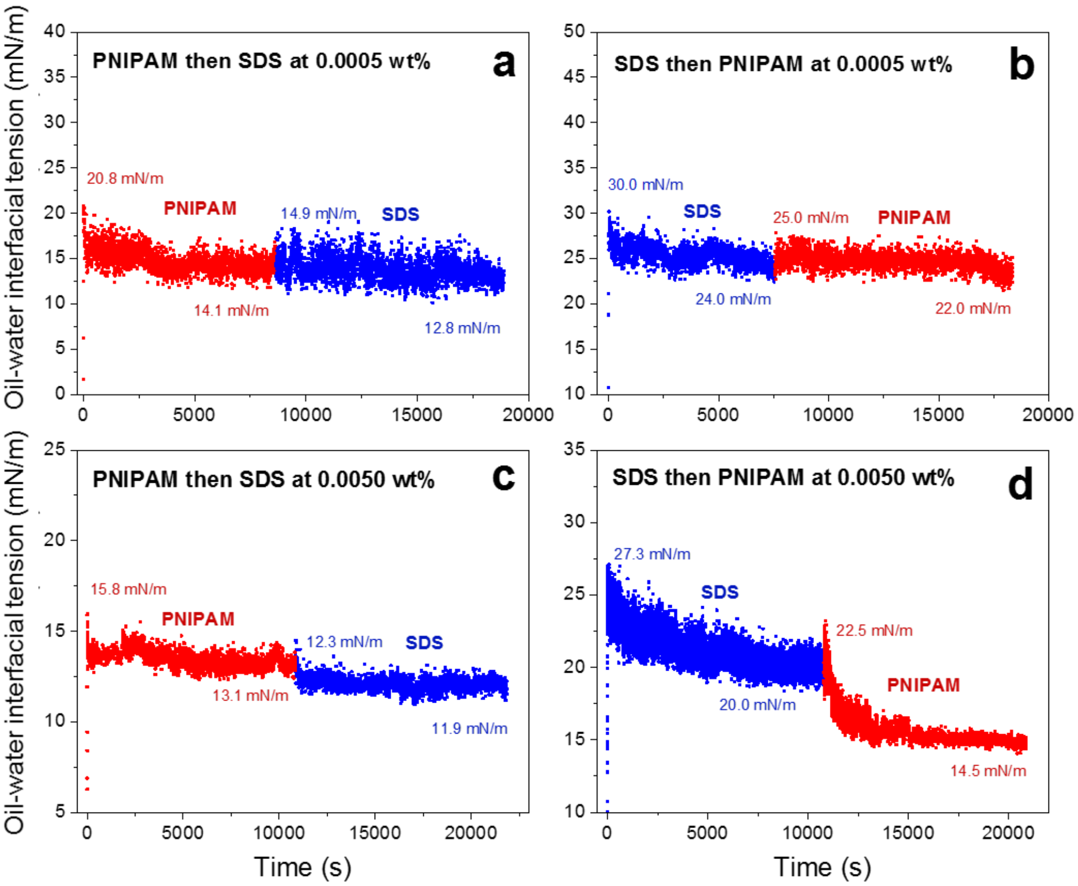

Figure 6.7. The effect of adding PNIPAM and SDS consecutively to change the interfacial tension of heavy crude oil-water. PNIPAM → SDS (a) and (c), and SDS → PNIPAM (b) and (d). σ_{OW} studied for low (5×10^{-4} wt%) and high (5×10^{-3} wt%) component concentrations. Addition of the second component occurred once the first component had reached steady state.

Figure 6.5 has been annotated to clearly define the SDS and PNIPAM dominant phases as a function of component concentration. The SDS dominant phase describes the component concentration where the interfacial tension of the blend is approximated to that of SDS (~5 × 10^{-4} – 1.5 × 10^{-3} wt%), while the PNIPAM dominant phase describes the component concentration where the interfacial tension of the blend is approximated to that of PNIPAM (~1.5 × 10^{-3} – 5 × 10^{-3} wt%).

6.4.3 Dewetting dynamics of heavy crude oil droplet

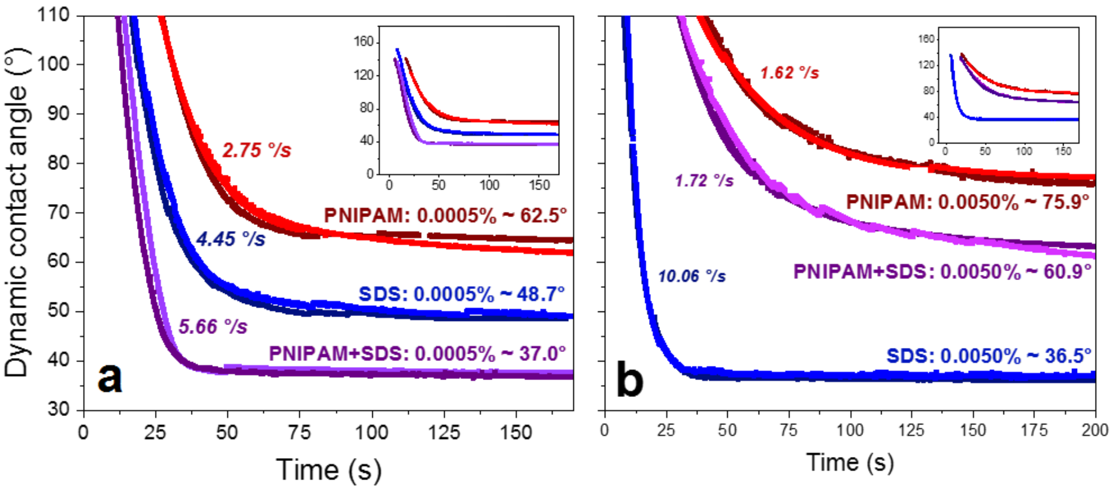

Figure 6.8. Heavy crude oil droplet dewetting on a hydrophilic glass substrate. Dynamic contact angles measured with either PNIPAM (red symbol), SDS (blue symbol) or PNIPAM + SDS (purple symbol) in the aqueous phase at component concentrations of 5 × 10^{-4} wt% (a) and 5 × 10^{-3} wt% (b). Two repeats are shown. Inset shows the dynamic contact angle > 110°.

Figure 6.8 compares the dynamic contact angle of a heavy crude oil droplet dewetting on a hydrophilic glass substrate, with the aqueous phase containing either PNIPAM, SDS, or PNIPAM + SDS blend. The dewetting dynamics were compared using the theoretical dewetting models: (i) hydrodynamic and (ii) molecular kinetic, see **Figure 6.10**. In the case of pure water (*i.e.* no added surface-active species), the oil droplet dewetting dynamics are slightly slower (1.80 °/s) than the those observed at the low component concentration (5×10^{-4} wt%), with the equilibrium contact angle attained after ~100 s, see **Figure 4.3**. The oil droplet dewetting rate, equilibrium contact angle and steady-state oil-water interfacial tension are summarised in **Table 6.2**.

Table 6.2. Experimental data for heavy crude oil droplet dewetting on a hydrophilic glass substrate.

Component and concentration	**Dewetting properties**		
	θ_e *(°)*	σ_{OW} *(mN/m)*	***Initial receding rate (°/s)***
PNIPAM 5×10^{-4} wt%	62.5	14.6	2.75
SDS 5×10^{-4} wt%	48.7	27.2	4.45
PNIPAM+SDS 5×10^{-4} wt%	37.0	25.3	5.66
PNIPAM 5×10^{-3} wt%	75.9	13.8	1.62
SDS 5×10^{-3} wt%	36.5	25.4	10.06
PNIPAM+SDS 5×10^{-3} wt%	60.9	16.2	1.72

At the lowest component concentration, 5×10^{-4} wt% (**Figure 6.8**a), the heavy crude oil droplet receding rate increases and the steady-state contact angle decreases in the following order: PNIPAM < SDS < PNIPAM + SDS. Conventional dynamic dewetting theories (Chapter 2) correlate σ_{OW} and θ_e to describe the dewetting process. The initial receding rate of the heavy crude oil does not follow the trend in σ_{OW} but does agree with the trend in θ_e, *i.e.* the oil droplet recedes faster as θ_e decreases, see Equations (2.8) and (2.10). This implies that the receding rate of the heavy crude oil droplet is less affected by σ_{OW}. In these nanofluids, changes in σ_{SW} and σ_{SO} are assumed to be negligible relative to the change in σ_{OW},[221] hence a decrease in σ_{OW} should result in the contact angle decreasing (*i.e.* the Young's equation), however, this contradicts to the results observed. Therefore, it is suggested that other factors from the nanoparticles influence θ_e such as a structural disjoining pressure.[11, 133] It is commonly discussed in the literature that nanoparticles enhance displacement of an oil droplet from a solid substrate by self-assembling in the region of the three-phase contact line by inducing a structural disjoining pressure (repulsive force), and this effect is independent of the interfacial energies.[132, 133, 230] At low component concentration, SDS is preferentially partitioned at the oil-water interface with the PNIPAM particles mostly in the bulk fluid (minimal partitioning at the oil-water interface) as discussed previously, and the increased oil droplet receding rate from SDS to PNIPAM + SDS likely results from contributions from the structural disjoining pressure. Applying Wasan's theory of nanoparticle structural force, for the PNIPAM + SDS blend at the low component concentration, the disjoining pressure of the water film between the heavy crude oil droplet and solid surface is 15.7 Pa, as described by $\Pi = \frac{2\sigma_{OW}\cos(\pi-\theta)}{r}$.[261] Using the structural disjoining pressure (Equation (2.15)) and assuming 30 vol% PNIPAM particles, the incipient film thickness is ~62.5 nm and can therefore accommodate the 50 nm PNIPAM particles.

At high component concentration, 5×10^{-3} wt% (**Figure 6.8**b), the droplet receding rate increases and the steady-state contact angle decreases in the following order: PNIPAM < PNIPAM + SDS < SDS. For SDS only, a substantially higher oil droplet dewetting rate (10.06 °/s) is observed, and unlike the low component concentration system, the heavy crude oil droplet receding rate in the presence of SDS exceeds the droplet receding rate in the presence of PNIPAM + SDS blend. Compared to PNIPAM and PNIPAM + SDS blend, for SDS only the σ_{OW} is high but θ_e is low, which cannot be described by the Young's equation, and results from a stronger repulsion between the oil droplet surface and solid surface due to SDS adsorption at the oil-water interface. SDS is an anionic surfactant which is more negatively charged than PNIPAM.[262] The faster oil droplet dewetting process is also contributed to low θ_e as described by the dynamic dewetting theories. At the high component concentration, the oil droplet dewetting in the presence of PNIPAM + SDS blend and PNIPAM are very similar, which agrees with the understanding that PNIPAM dominates the interfacial composition at high component concentrations.

The synergistic enhancement of PNIPAM + SDS to enhance oil droplet dewetting is not seen at the high component concentration. While PNIPAM preferentially partitions at the oil-water interface, PNIPAM also adsorbs on the glass substrate. This is confirmed by the QCM (Q-Sense, Biolin Scientific, Gothenburg, Sweden) experiment in **Figure 6.9** where a decrease in resonance frequency and increase in dissipation of the 5 MHz silica sensor is characteristic of mass deposition. Using the Sauerbrey theory,[263] the deposited mass is ~6.4 ng/cm^2. Assuming the density of PNIPAM particles = 1.1 g/cm^2, the deposited particle density is ~90 M particles/cm^2. Since PNIPAM partitions at both the oil-water and solid-water interfaces, it is believed that the reduction in heavy crude oil droplet dewetting results from hindrance caused by the PNIPAM particles bridging the liquid-liquid (droplet) and solid-liquid (droplet-substrate) boundaries.[264]

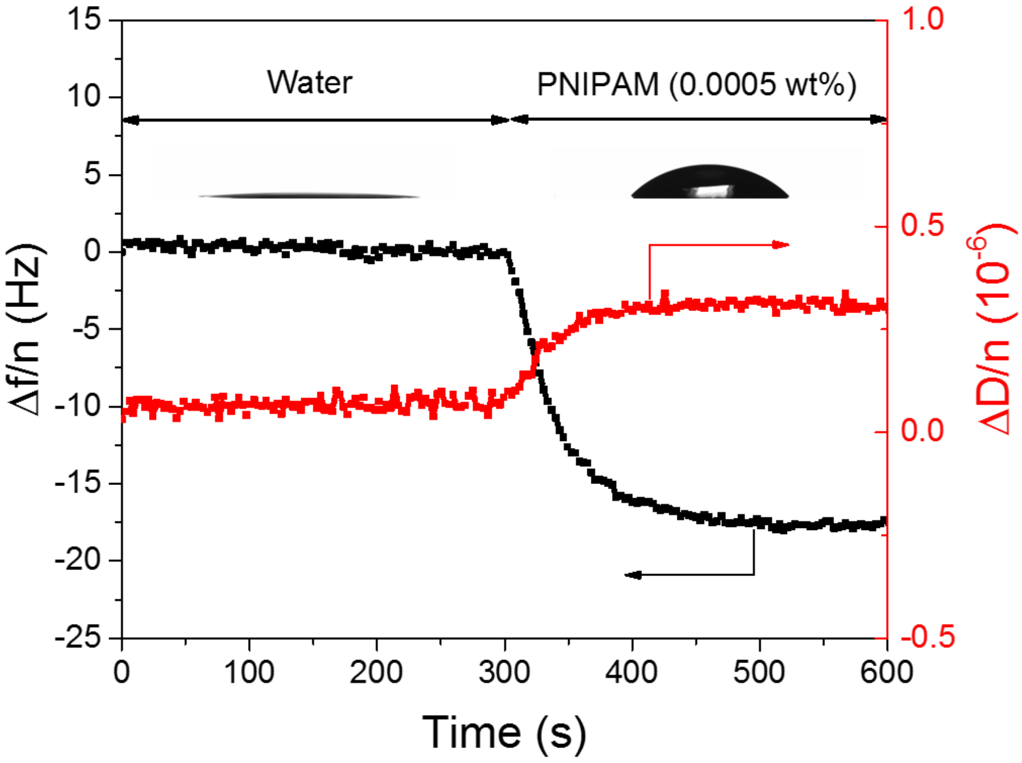

Figure 6.9. QCM showing the changes in resonance frequency and dissipation of the 7th overtone for PNIPAM particles (5×10^{-4} wt%) adsorbing on a 5 MHz silica sensor. Inset: Contact angle of a water droplet on a clean QCM silica sensor (~0°) and the same silica sensor following adsorption of PNIPAM particles (~45°).

Dynamic dewetting model: The dynamic contact angles were fitted using the dewetting models described in Equations (2.8) and (2.10). **Figure 6.10** shows the best fits for all dewetting experiments with $ln(L/L_S)$ and ζ used as the variable parameters. The best fits were obtained by a least-squares difference between the experimental and theoretical θ_d, Equation (4.1).

The best fits were obtained at the high component concentration and in general the HD and MK variable parameters, $ln(L/L_S)$ and (ζ), decreased with increasing initial receding rate (*i.e.* the slip length L_S is increased and the contact-line fraction decreased)

(**Figure 6.11**a and b). The mechanism to describe the change in initial receding rate is discussed below.

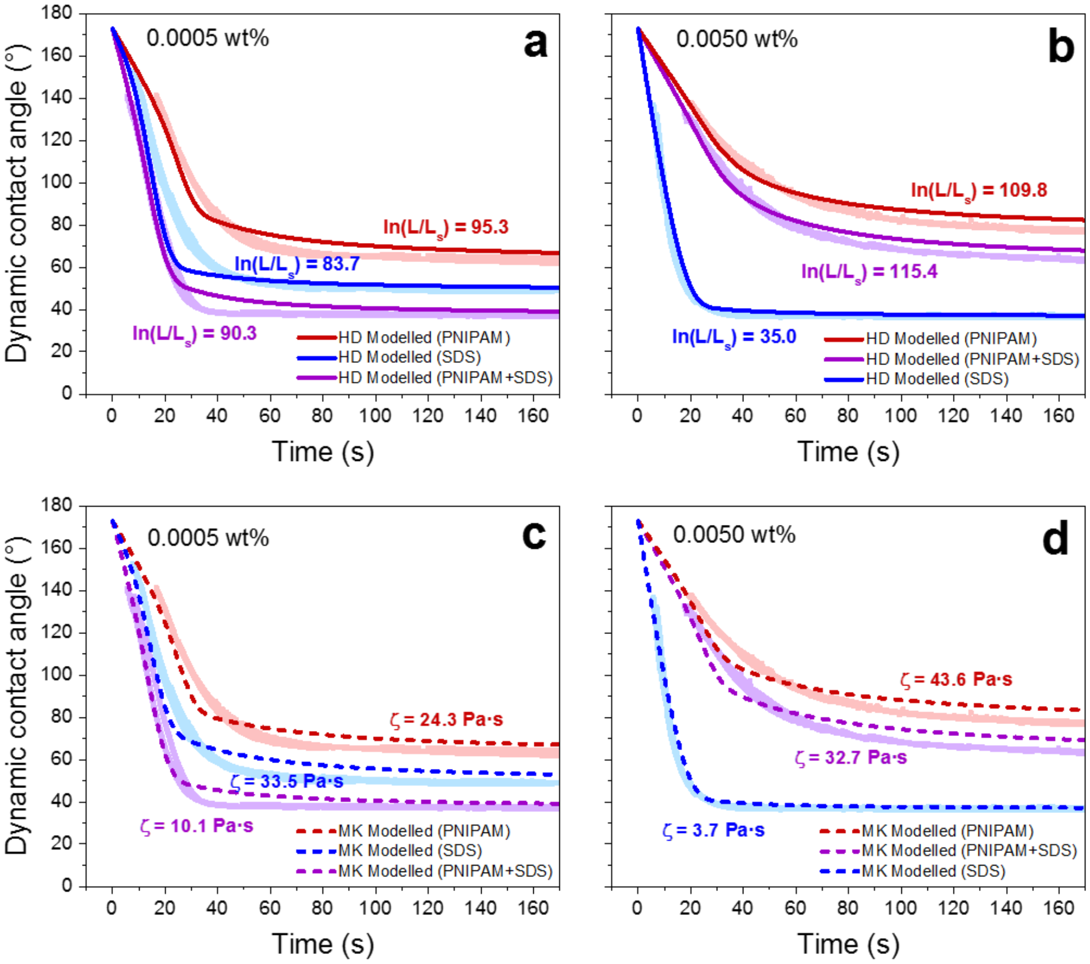

Figure 6.10. Dynamic contact angles of heavy crude oil droplet dewetting (shaded symbols) fitted using HD (solid lines) and MK (dash lines) models. Component concentrations of 5×10^{-4} wt% (a) and (c) and 5×10^{-3} wt% (b) and (d) are compared. The model fitting parameters are shown in the Figures.

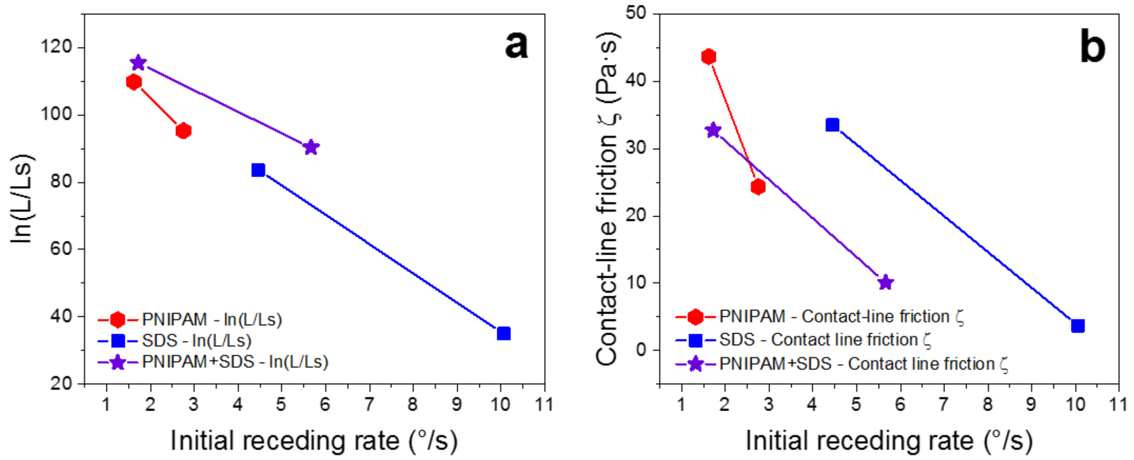

Figure 6.11. Comparison of HD (a) and MK (b) models fitting parameters as a function of initial receding rate and component type: SDS, PNIPAM, PNIPAM + SDS at 5×10^{-4} and 5×10^{-3} wt%.

Proposed dewetting mechanism: Based on the experimental data, the following mechanisms are proposed for the dewetting of heavy crude oil in the presence of the two optimal systems at (i) high component concentration (SDS) and (ii) low component concentration (PNIPAM + SDS).

(i) High component concentration (SDS): Adding SDS at 5×10^{-3} wt% decreases θ_e from 54.1° → 36.5°, and the rate of heavy crude oil droplet dewetting increases from 1.80 → 10.06 °/s according to the dewetting dynamic theories. As discussed in Chapter 4, decrease in θ_e by surfactant is less likely governed by the reduction in σ_{OW} but more the electrostatic repulsion between the oil droplet and solid surface. Due to charge repulsion between the anionic head group of SDS and the negatively charged silica substrate, SDS does not deposit on solid substrate,[265, 266, 267] hence no bridging occurs and greater oil dewetting is observed.

(ii) Low component concentration (PNIPAM + SDS): While SDS is preferentially adsorbed at the oil-water interface, the change in σ_{OW} (~4 mN/m) in the absence and presence of the component blend is negligible, hence the contribution to the significant increase in oil droplet receding rate and lower θ_e result from a structural disjoining pressure as the PNIAPM particles self-assemble in the water-wedge between the oil droplet and solid substrate near the contact line (as illustrated in **Figure 6.12**). Low θ_e contributes to faster oil droplet dewetting in this low component concentration (PNIPAM + SDS) based on the dewetting dynamic theories. σ_{OW} does not influence the dewetting dynamics since it is screened by larger change in θ_e (~17.1°) driven by disjoining pressure.

To pseudo-quantitatively assess particle ordering (concentration as a function of distance) in the water wedge, Cryo-SEM (LEMAS, University of Leeds) was performed on the low component system of PNIPAM + SDS. An oil film was deposited on glass substrate and left to recede in the nanoparticle fluid at 60 °C until the steady state had been reached in the specially designed cell and then cryo-frozen by submerging in liquid nitrogen and sublimed for 1 min. The glass substrate was then removed allowing the water-oil interface at the three-phase contact line to be imaged (**Figure 6.13**a). Three images of increasing magnification were taken and the particle coverage determined using ImageJ software (**Figure 6.13**b), which showed the particles arranged more densely close to the three-phase contact line and decreased in concentration outwards.

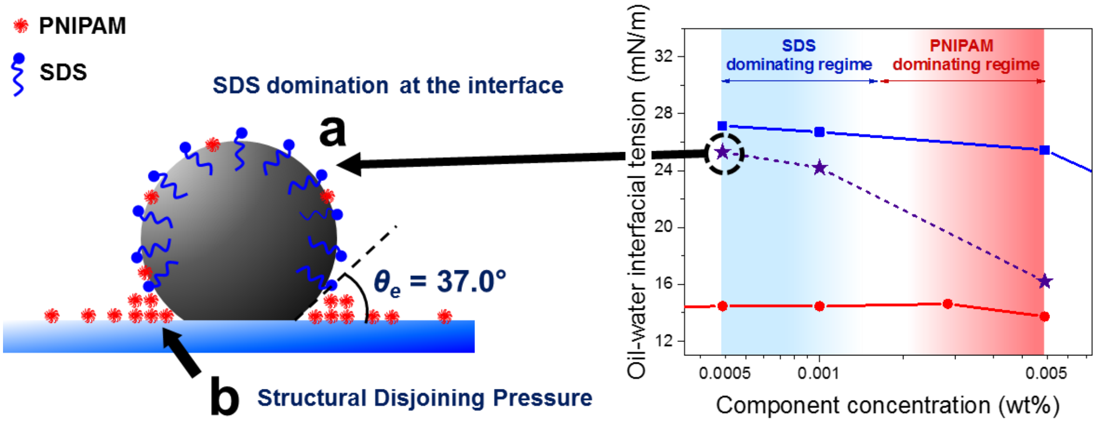

Figure 6.12. Proposed mechanism for oil droplet dewetting in the PNIPAM + SDS blend (low component concentration). SDS preferentially partitions at the oil-water interface (a) and PNIPAM particles accumulate in the liquid-wedge between the oil droplet and solid substrate, inducing a structural disjoining pressure (b).

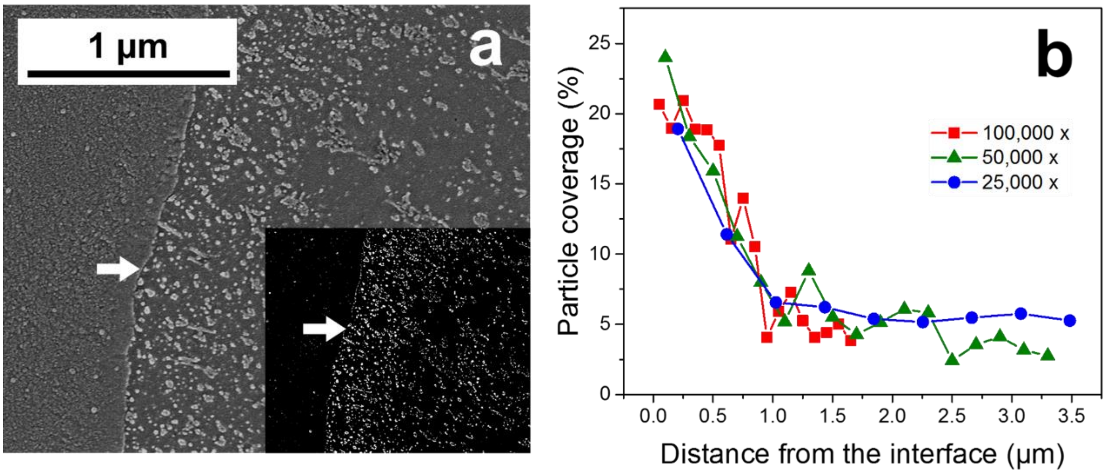

Figure 6.13. Cryo-SEM images showing the particle distribution from the three-phase contact line (arrow) in the water wedge (a). Inset is a black-and-white contrasted image prepared using ImageJ software. Three images of increasing magnification were used to determine the particle coverage distribution outwards from the interface (b).

6.4.4 Performance in low-salinity brines

For PNIPAM + SDS blend at a component concentration of 5 × 10^{-4} wt%, the effect of low-salinity brine (2,000 ppm determined to be the optimal brine concentration, Chapter 5) on the dewetting dynamics of heavy crude oil droplet was considered. Monovalent and divalent (NaCl and $CaCl_2$) brines led to a slight reduction in the hydrodynamic diameter of the PNIPAM particles, see **Table 6.3**. The slight decrease in particle size results from a dehydration of the PNIPAM particles as water molecules interact with excess salt ions,[268, 269] as well as charge screening of the PNIPAM functional groups by cations.[270, 271] The charge screening of the PNIPAM functional groups (sulfate anions) by cations was confirmed by the reduction in particle zeta potential. Even though the ionic concentration was high, no particle aggregation was observed in either NaCl or $CaCl_2$, and this agrees with published literature where aggregation of PNIPAM particles was observed at a much higher salt concentration of 58,445 ppm or 1 M NaCl.[268]

Table 6.3. PNIPAM particle size and zeta potential when prepared in the PNIPAM + SDS blend at a component concentration of 5 × 10^{-4} wt%. The PNIPAM + SDS blend is dispersed in Milli-Q water and monovalent and divalent brines at 2,000 ppm with the dispersion T < LCST of PNIPAM.

In solution	Hydrodynamic diameter (nm)		Zeta potential (mV)	
	20 °C	*60 °C*	*20 °C*	*60 °C*
Milli-Q water	144.2 ± 6.4	47.9 ± 1.6	-26.7 ± 2	-35.4 ± 1
2,000 ppm NaCl	113.5 ± 7.6	43.5 ± 5.3	-9.8 ± 4	-10.5 ± 2
2,000 ppm $CaCl_2$	117.6 ± 5.5	42.5 ± 3.5	-10.2 ± 5	-12.3 ± 5

When compared to the performance in Milli-Q water, adding brines to the PNIPAM + SDS blend substantially lowered the oil-water interfacial tension, see **Figure**

6.14a. The steady-state oil-water interfacial tension decreased from 25.3 mN/m (Milli-Q water) to 12.3 and 11.2 mN/m in NaCl and CaCl$_2$ brines, respectively. The interfacial diffusion coefficients in NaCl and CaCl$_2$ brines were 4.310 and 3.422 mol^2/m^4·s, respectively, and significantly higher than 0.456 mol^2/m^4·s in Milli-Q water, thus the two interfacial components are more favourable to partition at the oil-water interface due to charge screening by brine cations. The presence of brine cations enables charge screening of the negatively charged heavy crude interface, therefore charge repulsion between the oil-water interface and anionic species in the bulk (PNIPAM and SDS) is reduced. This is also favoured by the weaker negatively charged PNIPAM particles, thus the electrostatic repulsion between the oil-water interface and PNIPAM particle is reduced.

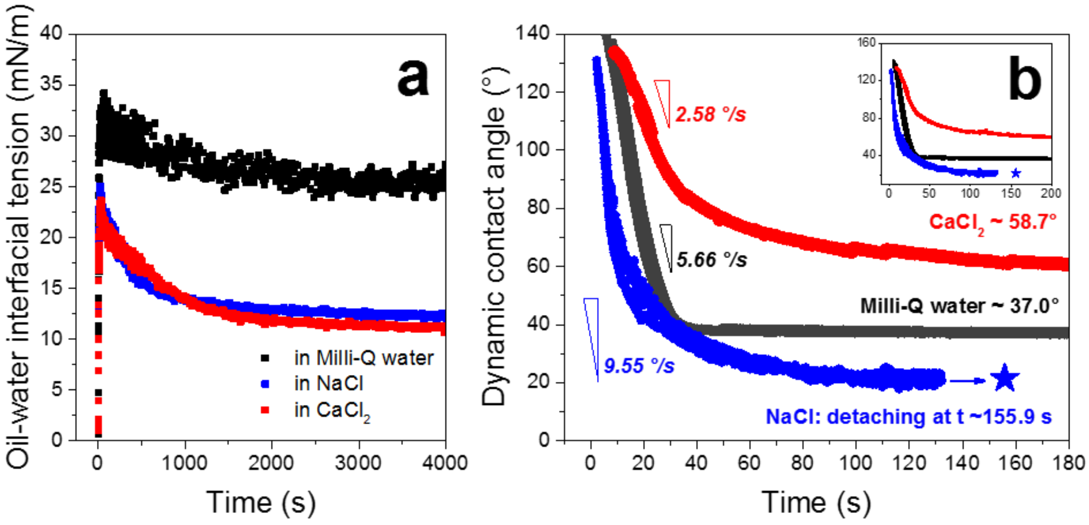

Figure 6.14. Oil-water interfacial tension in the presence of PNIPAM + SDS blend at a component concentration of 5 × 10^{-4} wt% in Milli-Q water, NaCl and CaCl$_2$ brines (a); dynamic contact angle for the three systems and the complete oil droplet dewetting dynamics shown as the inset (b). Solid and dash lines reflect the HD and MK models, respectively. Blue star indicates detachment of the heavy crude oil droplet from the solid substrate in NaCl brine at t = 155.9 ± 4.4 s.

Oil droplet dewetting in NaCl and $CaCl_2$ brines was compared to Milli-Q water, see **Figure 6.14**b. In $CaCl_2$ brine, the dewetting dynamic of the heavy crude oil droplet decreased in comparison to Milli-Q water, with the initial receding rate of the oil droplet equal to 2.58 °/s compared to 7.40 °/s in Milli-Q water. The steady-state equilibrium contact angle was 58.7° and higher than the case of Milli-Q water, but also significantly higher than the case of $CaCl_2$ in the absence of PNIPAM + SDS, θ_e = 27.2°, (**Figure 5.2**d). As previously discussed in Chapter 5, hindrance of oil droplet dewetting signifies stronger adhesion interaction between the heavy crude oil droplet and solid substrate. In $CaCl_2$, PNIPAM bridging between the oil and substrate is the likely cause of the hindrance with contribution from increasing hydrophobicity of the solid substrate as PNIPAM and SDS adsorb through divalent cation binding.[226, 264, 272]

Interestingly, for the PNIPAM + SDS blend in NaCl, the heavy crude oil droplet receded at 9.55 °/s (fastest rate) which eventually detached from the solid substrate at ~160 s (**Figure 6.14**b, star symbol, and **Figure 6.15**). It is likely that the oil droplet detached through the combined contributions from structural disjoining pressure (accumulation of PNIPAM particles in the liquid wedge) and hydration forces associated to structuring of hydrated ions in the liquid wedge. When compared to the oil droplet dewetting in NaCl only (**Figure 5.2**a), the initial droplet receding rate was comparable (9.46 °/s) and thus the rapid oil droplet receding **Figure 6.14**b can be attributed to the hydration forces. Comparing the two steady-state contact angles, 21.5° PNIPAM + SDS in NaCl, and 18.1° NaCl only, it is interesting to note that the heavy crude oil droplet detached in the presence of PNIPAM + SDS blend but not in the absence of the two surface-active species, even though the oil droplet was slightly less dewetting, supporting the hypothesis that the oil droplet detached due to contribution from disjoining pressures resulting from structural and hydration forces. It is worth noting that the reduction in oil-water interfacial tension from NaCl only to PNIPAM + SDS blend in NaCl (21.7 → 12.3 mN/m) did not lower the substrate-oil adhesion force (18.96 → 15.01 µN) below the oil droplet buoyancy (3.77 µN). Also, as shown in **Figure 6.15**, the heavy crude oil droplet remained almost spherical during detachment, unlike detachment induced by very-low interfacial tension when the droplet shape becomes pendant-like in Chapter 4.

It is worth to emphasise that the oil detachment in this system was different from the SDS system where the oil droplet receded at a very slow rate with non-spherical shapes controlled by a strong interfacial repulsion and pinched off by exceeded substrate-oil adhesion force (with long oil filament and oil residual), see **Figure 4.12**. Complete detachment in this study was clearly contributed to continuingly decreasing in oil-substrate contact area (**Figure 6.15**) displaced by the repulsive disjoining pressure, which had no oil filament and left no oil residual on solid surface.

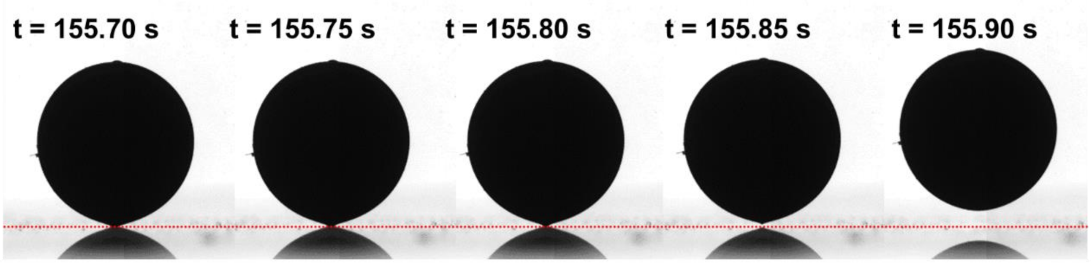

Figure 6.15. Heavy crude oil droplet detachment in the presence of PNIPAM + SDS blend and 2,000 ppm NaCl. The heavy crude oil droplet receded gradually maintaining axisymmetric spherical shape. Red dash line identifies the solid-liquid interface.

6.4.5 Demulsification test

To demonstrate the added benefit of using thermally responsive particles for EOR applications, the stability of water-in-oil emulsions was assessed. Addition of nanoparticles for EOR can lead to the formation of Pickering emulsions, where the two liquid phases are stabilised by a layer of nanoparticles partitioned at the oil-water interface. Since PNIPAM particles are thermally responsive, the hydrodynamic diameter of the particle increases when T < LCST. **Figure 6.16** compares the stability of water-in-oil emulsions stabilised by PNIPAM particles at temperatures above and below the LCST. At T < LCST, water droplets coalesced leading to significantly higher ΔBS, with water droplet coalescence and sedimentation increasing the oil layer thickness, confirming poor emulsion stability (**Figure 6.16**a). The destabilisation of the emulsion when T < LCST results from the larger PNIPAM particles (swelled-state) prefer to reside on the aqueous phase rather than partition at the oil-water interface.[273, 274] At T > LCST, the emulsion was comparably more stable with a lower ΔBS (**Figure 6.16**b). This was because the particles were in the coiled state and favoured to adsorb at the interface. The preference to partition at the oil-water interface as the dispersion temperature is increased has been shown previously, when the oil-water interfacial tension decreased from ~12.5 mN/m to ~11.7 mN/m because the temperature is increased from 30 °C to 33 °C.[152]

The transition to less stable emulsions at T < LCST is good for an application perspective and should promote faster separation of water-in-oil emulsions recovered at the well head. This is not the case for non-responsive particles such as silica, which have been shown to strongly stabilise emulsions when the particle size is sufficiently small.[275, 276]

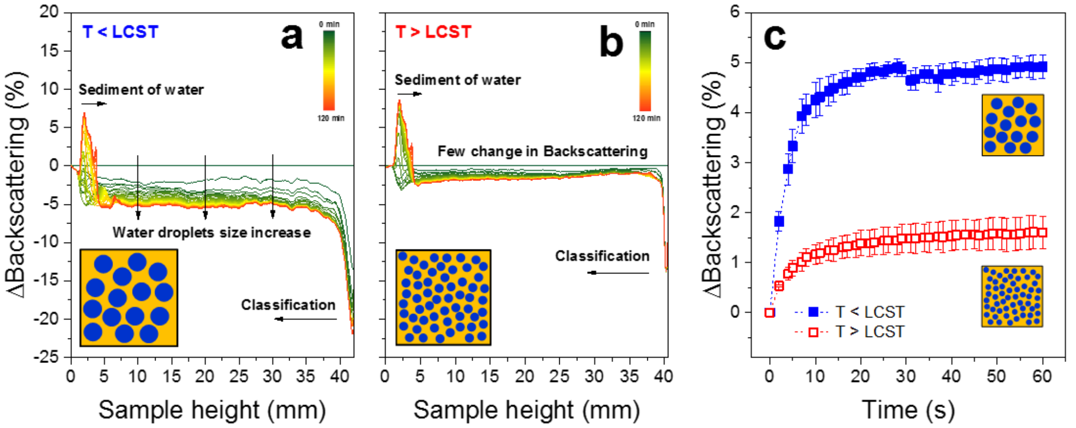

Figure 6.16. Dynamic ΔBS of PNIPAM stabilised water-in-oil emulsions at T < LCST (a) and T > LCST (b) with temperature comparison (c).

6.5 Conclusion

The interfacial activity at the oil-water interface and the dynamic dewetting of heavy oil droplets in the PNIPAM + SDS blend have been studied. Generally known as surface-responsive particles, PNIPAM adsorption has shown to be a diffusion-controlled process similar to SDS. PNIPAM + SDS blend results showed that a competitive adsorption at oil-water interface is a function of concentration. SDS dominates the interface at low component concentration (5×10^{-4} wt%) while PNIPAM partitioning controls the interface at high component concentration (5×10^{-3} wt%).

Adsorption activity at the interface was found to play a role on oil droplet dewetting. PNIPAM + SDS blend at low component concentrations obtained a fast oil droplet dewetting with low contact angle, favouring the oil liberation. Since SDS dominates the oil-water interface, PNIPAM particles are more likely to be suspended in the bulk fluid and self-arrange at the water wedge to construct the repulsive disjoining pressure which displaces further oil. This is considered the main mechanism for nanoparticle EOR. Unlike high component concentration, SDS has shown greater oil dewetting than PNIPAM, as a result of stronger repulsion between oil droplets and the silica surface. This is due to the anionic surfactant adsorbing at the oil-water interface. At high component concentration, PNIPAM partitions the interface and deposits onto the solid surface leading to oil-substrate bridging and hence resisting the oil dewetting. Bridging at the three-phase contact line screens the reduced oil-water interfacial tension caused by PNIPAM, therefore the oil-water interfacial tension effect on oil dewetting is negligible.

Interestingly, the greatest oil displacement was demonstrated using a combination of nanoparticles and low-salinity fluids. The best system (PNIPAM + SDS blend in 2,000 ppm NaCl) displaced the oil droplet rapidly and eventually detached the oil from substrate within two minutes. This enhancement is due to disjoining pressures which result from structural and hydration forces. The study has also demonstrated the temperature-responsive application of the particles. By decreasing temperature to be less than LCST, adsorbed particles which stabilise water-in-oil emulsions become more hydrated into water phase and the oil-water interfacial tension increases, resulting in less stable emulsions. This temperature effect on emulsion stability is a promising application for the separation process of water and oil in the downstream industry.

Chapter 7

Conclusions and Future Work

Heavy crude oil droplet dewetting on model glass substrate is studied in this project. EOR fluids have been examined including effect of pressure and temperature. Comprehensive investigations have been carried out to understand dewetting dynamics, oil-water interfacial energy and disjoining pressure between oil droplet and solid substrate, etc. The following conclusions are drawn from this research works.

7.1 Conclusions

7.1.1 Fundamentals of oil droplet dewetting

After the water phase has been added to substitute air, oil sheet deposited on model glass substrate started to dewet continually until it reached a new equilibrium, forming a steady-state oil droplet with the contact angle defined. Increasing temperature of the system (40 – 80 °C) resulted in faster oil droplet dewetting dynamics (0.07 → 3.73 °/s) due to oil viscosity decrease. Natural surfactants (*e.g.* naphthenic acids) were found to release increasingly from the crude oil to the water phase with increasing temperature, which attributes to a reduction in oil-water interfacial tension (28.3 → 25.5 mN/m) and consequently a decrease in the equilibrium contact angle (63.7° → 51.3°).

The concept of interfacial energy still describes the contact angles in reservoir conditions well, *i.e.* high pressure and high temperature (≤ 200 bar at 140 °C). Oil-water interfacial tension was much decreased (14.4 mN/m) at 140 °C with additional contribution from asphaltene partitioning at the interface, resulting in lower contact angle (17.9°). High solubility of asphaltenes and much lower oil viscosity at this temperature induced a better adsorption which reduced the oil-water interfacial tension. However, at high pressures (10 – 200 bar) asphaltenes have better solubility in crude oil and do not prefer to adsorb at the oil-water interface, hence an increase in interfacial tension (≤ 17.6 mN/m). The contact angles were found to increase (≤ 23.1°) with increasing pressure due to higher oil-water interfacial tension.

The oil droplet dewetting was further enhanced (*i.e.* the contact angle decreased) by adding surfactant (SDS) fluids *via* reduction in oil-water interfacial tension and increase in oil-substrate repulsion. At > CMC, maximum surface coverage at the oil-water interface led to substantial reduction in oil-water interfacial tension (~5.75 mN/m), which decreases the oil-substrate adhesion below the oil droplet buoyancy (2.01 < 3.77 µN). Such low adhesion triggered the oil droplet pinch-off leaving some residual oil on the solid surface. Overall, the findings demonstrated the relationship of the contact angle and the interfacial energy as described by the Young's equation.

7.1.2 Oil droplet dewetting in low-salinity fluids

The performance of low-salinity EOR fluids were investigated in oil droplet dewetting by replacing the water phase in Chapter 4 to be model brines. To examine an effect of interfacial energy on the oil dewetting, the oil-brine interfacial tension was measured. Increasing brine concentration increased the quantity of salt ions adsorbing at the oil-water interface and hence induced heavy-crude-oil surface-active species (*i.e.* asphaltenes and natural surfactants) partitioning due to charge neutralisation and binding with cations. Such adsorption led to a reduction in σ_{OW} with increasing brine concentration up to ~25,000 ppm (22.7 → ≥ 20.1 mN/m) where the salt ions saturated the interface. At > 25,000 ppm, adding further salt resulted in salt negative adsorption (*i.e.* the Jones-Ray effect) and less binding with the oil surface-active materials increasing the σ_{OW} (≤ 21.6 mN/m at 60,000 ppm).

Oil sheet in brines have a better dewetting compared to pure water (θ = 43.2° → ≥ 18.1°). The oil dewetting dynamics was greatly enhanced by decreasing brine concentration (diluted brines), *e.g.* oil droplet receded faster (1.89 → 9.46°/s) and the contact angle decreased (25.3° → 18.1°) from 60,000 to 2,000 ppm NaCl brines. Such dewetting improvement was not controlled by the σ_{OW}, suggesting other influencing factor. By an AFM measurement, repulsive hydration forces were found in brines. As the hydration forces were shown to decrease with higher brine concentration, this shows greater cation hydration is achieved at low concentrations which explains the improved oil dewetting. However, in divalent brine ($CaCl_2$) the disjoining pressures, dominated by attractive hydrophobic forces, led to less oil droplet dewetting compared to the monovalent ($\Delta\theta \leq 10°$). This was due to natural surfactant adsorbed on solid surface by divalent cation bridging, rendering solid surface to be hydrophobic.

Brine effects greatly influenced the oil droplet dewetting under high pressure and high temperature condition. The σ_{OW} continuingly reduced with increasing brine concentration (≤ 3 mN/m), likely resulting from higher charge neutralisation and further partitioning of surface-active species at 140 °C. Higher pressure slightly increased the interfacial tension ($\Delta\sigma_{OW}$ ~2 mN/m) due to less partitioning at the interface as discussed in Chapter 4. Pressure effect on the contact angle strongly depends on the brine type. For NaCl, higher pressure increased the contact angle (≤ 25° at 200 bar) as a result of less oil droplet dewetting at higher σ_{OW} ascribed by the Young's equation. For $CaCl_2$, the pressure effect was negligible ($\Delta\theta \leq 1.3°$), which was attributed to a strong hydrophobic force creating a preferred environment for oil droplet wetting. It is clear that the small changes in σ_{OW} with pressure are insufficient to affect the equilibrium contact angle.

7.1.3 Surface-active nanoparticles: interfacial activity and oil droplet dewetting

Surface-active nanoparticles (PNIPAM) were synthesised and used in the presence of anionic surfactant (SDS) to examine an influence of oil-water interfacial activity on the oil droplet dewetting. The adsorption kinetics of PNIPAM and SDS blend showed that proportion of each surface-active species was dependent on the total component concentration. Adsorption of SDS was greater than PNIPAM at low component concentration (5×10^{-4} wt%). With increasing component concentration (5×10^{-3} wt%), PNIPAM increasingly adsorbed at the interface since PNIPAM needs much higher concentration than SDS to diffuse and partition due to its larger particle size.

The interfacial activity of the two species was also shown to influence the oil droplet dewetting. At low component concentration (5×10^{-4} wt%: SDS > PNIPAM at the interface), PNIPAM + SDS blend dewetted the oil droplet better than high component concentration (5×10^{-3} wt%: PNIPAM > SDS at the interface) with faster initial receding rate (1.72 → 5.66 °/s) and lower steady-state contact angle (60.9° → 37.0°), even though relatively high oil-water interfacial tension (25.3 mN/m) obtained. It is believed that at low component concentration, PNIPAM particles remained in the bulk fluid and self-assembled at the water wedge to induce a structural disjoining pressure and enhance further oil dewetting. Unlike high component concentration, since PNIPAM highly adsorbed at the oil-water interface and also deposited on solid substrate, PNIPAM was able to bridge the solid-liquid and liquid-liquid interface leading to resist oil dewetting.

Much reduced oil-water interfacial tension (16.2 mN/m) also did not pronounce the oil dewetting. The Young's equation did not appear to control the nanoparticle system *via* the oil-water interfacial tension.

PNIPAM + SDS blend was also studied in the low-salinity brines, which is considered in Chapter 5. In the presence of salt, PNIPAM particles reduced in size but remained dispersed which led to faster diffusion and higher adsorption at the oil-water interface, hence much lower oil-water interfacial tension. In NaCl, faster oil droplet dewetting was promoted by a hydration force. Contributions from PNIPAM and brine repulsive structural forces induced the gradual liberation of oil droplet from the substrate, although the droplet buoyancy did not exceed the oil-substrate adhesion. Unlike in $CaCl_2$, co-adsorption of polymeric PNIPAM particles and surfactants on solid surface led to bridging effect and stronger attractive hydrophobic forces, which in turn reduced oil droplet dewetting.

Generally known to be temperature-responsive particles, PNIPAM is more hydrated at T < LCST and dehydrated at T > LCST. Change in particle size was shown to control a stability of water-in-oil emulsions stabilised by the particles. Following stabilisation of the emulsions at T > LCST, decreased stability was observed at T < LCST since the partitioned particles were more hydrated and oil-water interfacial tension was higher than at T > LCST. This would be a promising application for a separation of water and oil after crude oil production.

7.2 Initial Investigations and Future Work

Although a number of fluids can enhance oil droplet dewetting by altering water chemistry and show a great ability to minimise the oil-water-solid contact angle, greater complexity of solid surfaces in reservoir configurations are more difficult to modify and requires in-depth knowledge to better understand its effect on the dewetting mechanisms. Therefore, clear comparisons in performance of the oil droplet dewetting between smooth substrates and rough and/or porous surfaces need to be made.

Equilibrium wetting of liquid droplets stationed on rough substrate have been highly reported, however, dynamic studies of liquid droplet wetting/dewetting have not yet been investigated extensively.[277, 278, 279] Future work will focus on understanding oil dewetting dynamics on model rough surface using the current technique. To observe capillary effects on droplet dynamics, a number of attempts have been carried out on glass frit.

7.2.1 Dewetting dynamics on rough surface: role of solid-liquid retention

Background: According to Wenzel theory, Equation (2.18), an oil droplet stationed on a rough surface in an underwater environment attains lower apparent equilibrium contact angle than flat surface of the same hydrophilic surface.

Hypothesis: Rough surfaces contribute to different dewetting dynamics.

Figure 7.1a shows the oil droplet dewetted on rough surface (RS) much slower compared to smooth surface (SS), having the lower initial receding rate (1.80 → 1.03 °/s) and longer time to the steady-state (100 → 350 s) but equilibrating at a much lower contact angle (54.1° → 16.4°; **Figure 7.1**b and c) as expected. Since the fluid viscosity and oil-water interfacial tension are the same as experimenting in the same temperature and fluids, the slower oil receding rate was solely contributed to the substrate roughness. Droplet three-phase contact line is believed to experience some difficulty or hindrance to move/recede or be peeled along the rougher surface. An actual oil-substrate contact area also increased with roughness, hence the three-phase contact line has to travel or move on a longer distance where more time is needed with the same capillary drive, resulting in a longer equilibrium time. Significant decrease in apparent contact angle shows a promising EOR where an apparent oil-substrate area is much less, requiring a smaller energy requirement to detach or pinch the oil droplet off substrate.

The liquid-solid retention force is believed to be a reason behind such oil dewetting deceleration. This concept has been confirmed with experiments reported by Butt and co-workers[280, 281] and Elliott and co-workers[279, 282, 283] in water-air-solid systems. The retention force (f_R) is increasingly constructed on rougher surface calculated from the change in droplet recession (*i.e.* contact angle and oil-solid contact area):[284, 285, 286, 287]

$$f_R = \frac{k}{2}\sigma D(\cos\theta_r - \cos\theta_a) \tag{7.1}$$

where k is a numerical constant depending on droplet shape and D is droplet width perpendicular to droplet moving direction. θ_r and θ_a are receding and advancing contact angles.

However, the present work focuses on the oil-water-solid system which the retention force calculation (of liquid-liquid rather air-liquid on solid surface) is needed to be confirmed with experiment. It is also expected that the magnitude of the retention force is in accordance with the initial receding rate of the contact angle (the higher the retention force, the slower the initial receding rate) implying that the retention force directly acts as a hindrance on droplet receding dynamics. Since rough surfaces can dewet oil droplets at much lower contact angles, albeit at a reduced rate, further studies should focus on how to accelerate the dewetting without disturbing the steady-state of dewetting (*e.g.* increase repulsion force between oil and substrate).

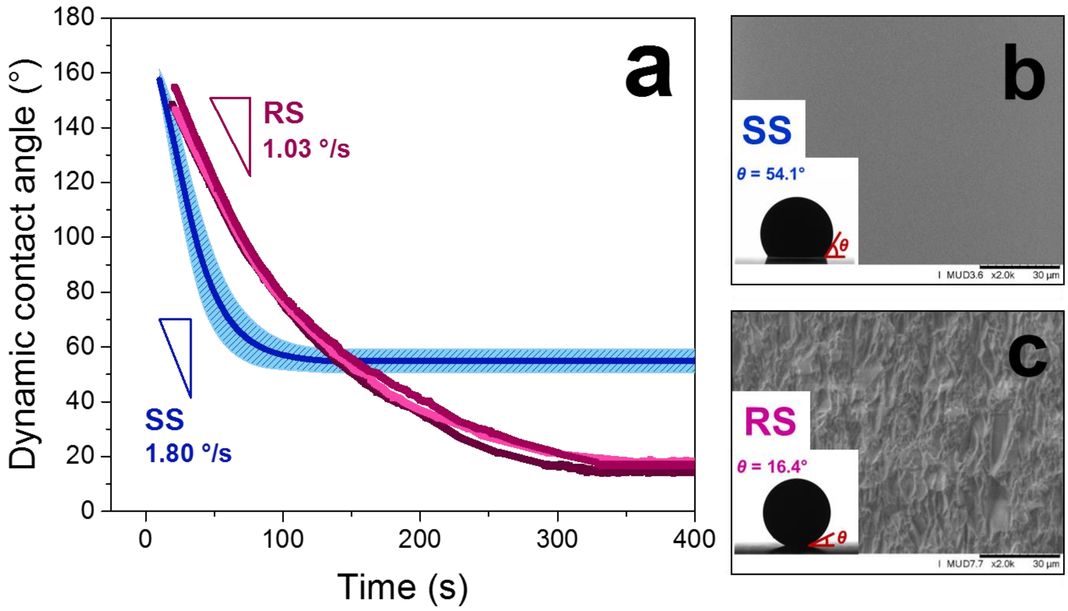

Figure 7.1. Dewetting dynamics of heavy oil film on smooth (SS) and rough (RS) surfaces immersed in Milli-Q water at 60 °C (a). The initial receding rate is reported next to the plot. SEM images of the SS (b) and RS (c) are shown with insets of oil droplet and apparent contact angle at the equilibrium.

7.2.2 Towards the oil imbibition: droplet dynamics on porous substrate

Background: Cassie-Baxter model emphasises the substrate chemical and/or physical heterogeneous on droplet wetting steady-state without considering contribution of capillary pressure from connected pore network.

Hypothesis: Dynamic and equilibrium wetting of droplet on porous surface is dominated by capillary pressure at some condition, which represents the oil imbibition process in petroleum recovery.

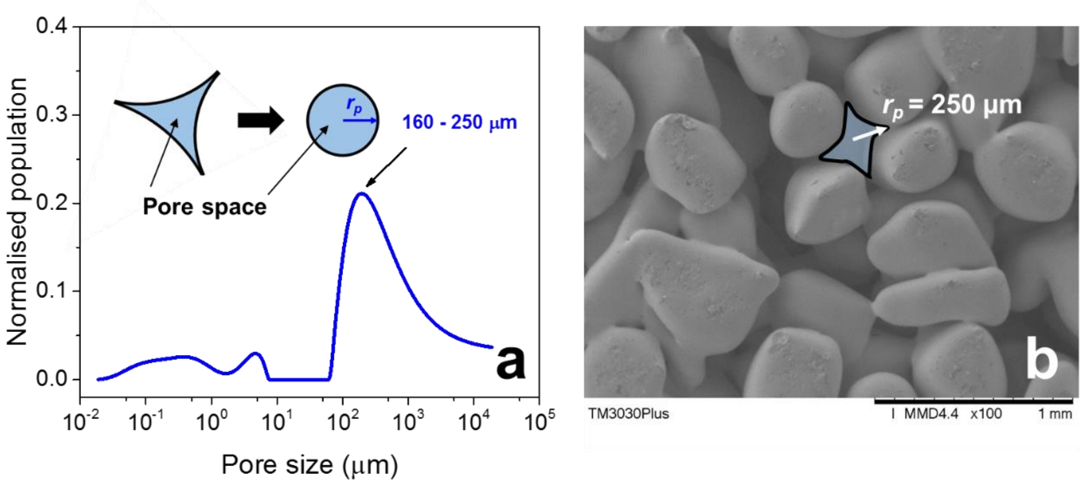

Figure 7.2. NMR pore size distribution (a). The inset shows actual geometry of pore space (left) and its estimated theoretical geometry (right). SEM averaged pore size well validated with the NMR result (b).

A preliminary study was conducted using a glass frit as a model porous substrate. Borosilicate sintered disc (P0, Scientific Glass Laboratories, UK) of 30 mm diameter and 4 mm thick was characterised by nuclear magnetic resonance (NMR: MARAN ULTRA, Oxford Instrument, UK) having pore radius averaged ~160 – 250 μm which agrees with result of SEM image analysis (~250 μm), see **Figure 7.2**. The hydrophilic substrate (toluene-water-surface contact angle = 28.3°) was submerged underneath model oil (toluene) as a non-wetting phase to obtain the initial saturated state of non-wetting phase. Then, a water droplet (~7.5 μL) as a wetting phase was placed on the substrate and the dynamic wetting on and/or imbibition into the substrate was observed by the Theta

Optical Tensiometer. It is noted that toluene was used as a model oil in the present study in order to prevent a viscosity effect and a long-time adsorption of surface-active materials from the crude oil at the oil-water interface (toluene-water σ_{OW} = 35 mN/m).

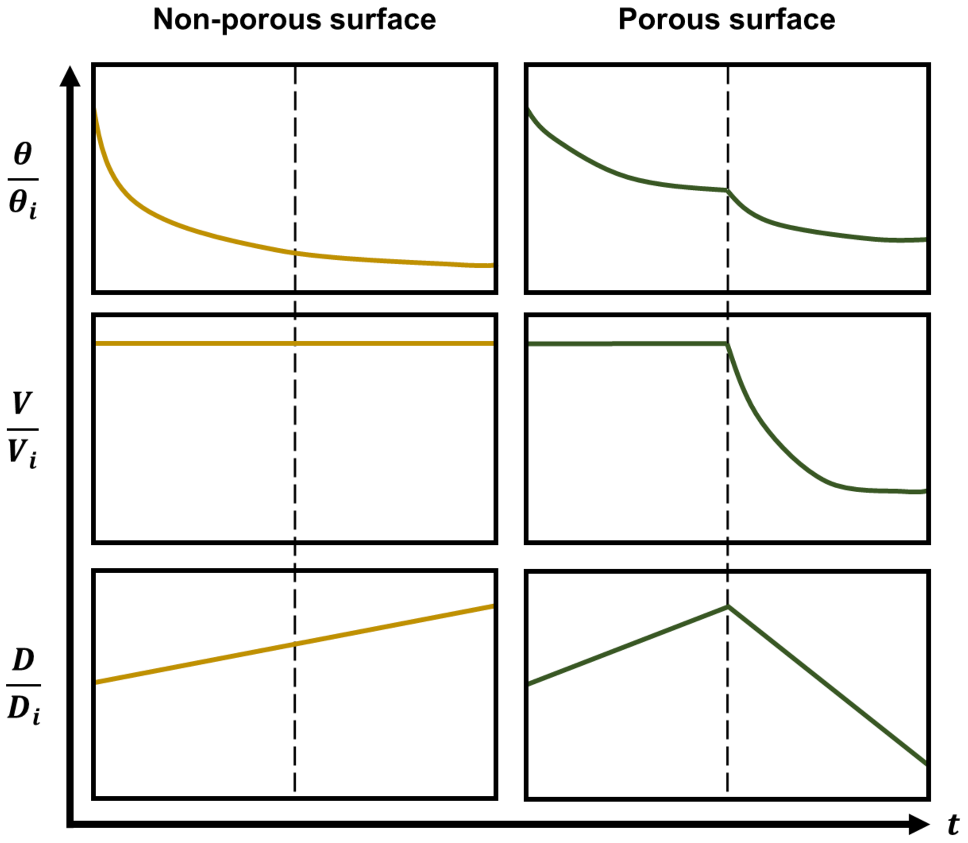

Figure 7.3. Droplet dynamic wetting quantified by normalised apparent contact angle ($\frac{\theta}{\theta_i}$), droplet volume ($\frac{V}{V_i}$) and droplet base ($\frac{D}{D_i}$). Non-porous surface has one stage of wetting: the contact angle decreases, constant droplet volume and droplet base increases. Porous surface is likely to have two stages:^{288} (i) similar to non-porous surface where macroscopic wetting dynamics dominates and (ii) when imbibition occurs dominated by capillary which the contact angle still decreases but droplet volume and base decrease.

The governing forces are the capillary force and those related to body of the droplet itself, *i.e.* buoyancy and gravitational forces.[153, 289] The transition from macro-scopic apparent wetting of droplet on the substrate to droplet imbibition (flow) into the substrate is of interest (dash line in **Figure 7.3**) as it has been simulated but not yet experimentally observed for a liquid-liquid system.[288, 289, 290]

Water droplet contact angle decreased with time until attained equilibrium state at ~70 s and the droplet volume was constant, duplicating the study in the previous chapters observed on a flat surface (**Figure 7.4**a). The hydrophilic flat surface was found to decrease the contact angle to be ~20% of the initial ($0.20\theta_i$). Considering the porous surface (**Figure 7.4**b), the 'apparent' contact angle decreased much slower and attained relatively high contact angle than on the flat surface ($\theta = 0.98\theta_i$ at ~3 h), despite the same hydrophilicity. The droplet volume also decreased ~10% at 3 h indicating an imbibition occurred. Droplet wetting behaviour here appears to be only the second stage of the imbibition in **Figure 7.3**, suggesting the wetting on rough surface due to only Cassie-Baxter is not the case.

To further investigate the role of imbibition, the capillary pressure was reduced by decreasing the oil-water interfacial tension *via* surfactant add. 0.12 wt% SDS (> CMC) droplet (σ_{OW} = 3.4 mN/m) was examined, thus also increasing surface hydrophilicity and the actual contact angle (on flat surface) decreased from 28.3° to 17.2°. The capillary pressure (P_c) can be estimated by:

$$P_c = \frac{m\sigma_{OW}cos\theta}{r_p} \tag{7.1}$$

where m is the dimensionless pore shape multiplier, $2 \geq m \geq 1$.[153] Using the pore radius of 250 µm, therefore the surfactant decreases the capillary pressure ~90% of the water solution. Such substantial decrease resulted in a better droplet imbibition into the substrate, see **Figure 7.4**c. The apparent contact angle decreased rapidly at the beginning and attained ~$0.90\theta_i$ at 3 h. The droplet also imbibed more at a faster speed. This better imbibition performance apparently favours the EOR where the porosity of the substrate is needed to be taken into account. The dynamic wetting on model flat surface could not represent the actual behaviour in the reservoir.

With varying size of the pore space, the capillary pressure is altered and hence the imbibition adjusted. Further investigation should focus on the role of pore radius and the threshold that controls the macroscopic dewetting regime.

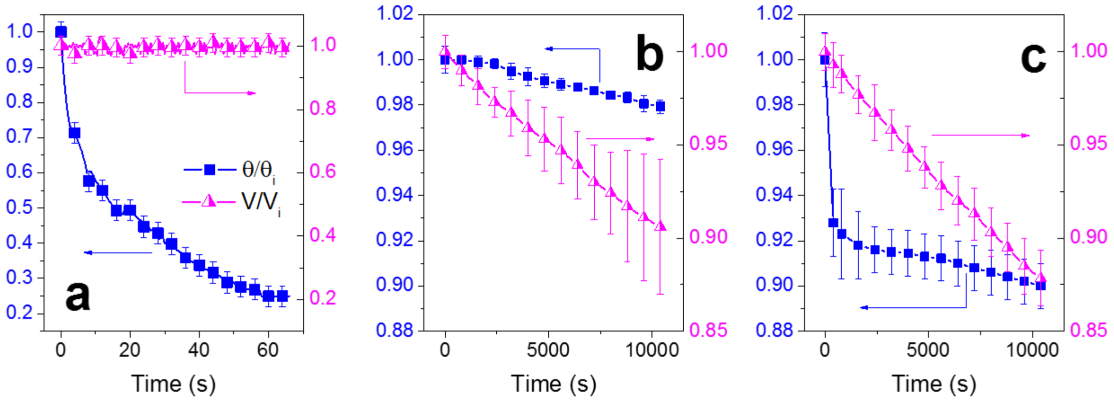

Figure 7.4. Dynamic wetting of water droplet on flat surface (a), water droplet on porous surface (b) and 0.12 wt% SDS droplet on porous surface (c). Blue squared symbols are normalised contact angle ($\frac{\theta}{\theta_i}$) and pink triangle symbols are normalised volume ($\frac{V}{V_i}$). Note that the contact angles in (b) and (c) are apparent.

References

1. Taylor, K. C.; Hawkins, B. F. Emulsions in enhanced oil recovery. *Emulsions (Laucier Schramm Ed.), Adv. Chem. Series* **1992,** *231*.

2. Basu, S.; Nandakumar, K.; Masliyah, J. H. A Model for Detachment of a Partially Wetting Drop from a Solid Surface by Shear Flow. *Journal of Colloid and Interface Science* **1997,** *190* (1), 253-257.

3. Török, J.; Tóth, J.; Gesztesi, G. Polydispersed O/W emulsions in porous media: Segregation at low-tension conditions. *Journal of Colloid and Interface Science* **2006,** *295* (2), 569-577.

4. O'brien, N. R.; Thyne, G. D.; Slatt, R. M. Morphology of hydrocarbon droplets during migration visual example from the Monterey Formation (Miocene), California. *Aapg Bulletin-American Association of Petroleum Geologists* **1996,** *80* (11), 1710-1718.

5. Sheng, J. J. *Modern chemical enhanced oil recovery: theory and practice*; Gulf Professional Publishing2010.

6. Lake, L. W. *Enhanced Oil Recovery*; Prentice Hall: New Jersey, 1989.

7. Sheng, J. J. Status of surfactant EOR technology. *Petroleum* **2015,** *1* (2), 97-105.

8. Raffa, P.; Broekhuis, A. A.; Picchioni, F. Polymeric surfactants for enhanced oil recovery: A review. *Journal of Petroleum Science and Engineering* **2016,** *145*, 723-733.

9. Young, T. An Essay on the Cohesion of Fluids. *Philosophical Transactions of the Royal Society of London* **1805,** *95*, 65-87.

10. Czarnecki, J.; Radoev, B.; Schramm, L. L.; Slavchev, R. On the nature of Athabasca Oil Sands. *Advances in Colloid and Interface Science* **2005,** *114*, 53-60.

11. Wasan, D. T.; Nikolov, A. D. Spreading of nanofluids on solids. *Nature* **2003,** *423* (6936), 156-159.

12. Drummond, C.; Israelachvili, J. Surface forces and wettability. *Journal of Petroleum Science and Engineering* **2002,** *33* (1), 123-133.

13. Basu, S.; Nandakumar, K.; Masliyah, J. H. A Study of Oil Displacement on Model Surfaces. *Journal of Colloid and Interface Science* **1996,** *182* (1), 82-94.

14. Basu, S.; Nandakumar, K.; Masliyah, J. H. On bitumen liberation from oil sands. *The Canadian Journal of Chemical Engineering* **1997,** *75* (2), 476-479.

15. Basu, S.; Nandakumar, K.; Masliyah, J. H. Effect of NaCl and MIBC/kerosene on bitumen displacement by water on a glass surface. *Colloids and Surfaces A: Physicochemical and Engineering Aspects* **1998,** *136* (1), 71-80.

16. Bartels, W. B.; Mahani, H.; Berg, S.; Hassanizadeh, S. M. Literature review of low salinity waterflooding from a length and time scale perspective. *Fuel* **2019,** *236*, 338-353.

17. Xie, Q.; Brady, P. V.; Pooryousefy, E.; Zhou, D.; Liu, Y.; Saeedi, A. The low salinity effect at high temperatures. *Fuel* **2017,** *200* (Supplement C), 419-426.

18. Suleimanov, B. A.; Ismailov, F. S.; Veliyev, E. F. Nanofluid for enhanced oil recovery. *Journal of Petroleum Science and Engineering* **2011,** *78* (2), 431-437.

19. Binks, B. P. Particles as surfactants—similarities and differences. *Current Opinion in Colloid & Interface Science* **2002,** *7* (1), 21-41.

20. Li, Z.; Geisel, K.; Richtering, W.; Ngai, T. Poly (N-isopropylacrylamide) microgels at the oil–water interface: adsorption kinetics. *Soft Matter* **2013,** *9* (41), 9939-9946.

21. Li, Z.; Harbottle, D.; Pensini, E.; Ngai, T.; Richtering, W.; Xu, Z. Fundamental Study of Emulsions Stabilized by Soft and Rigid Particles. *Langmuir* **2015,** *31* (23), 6282-6288.

22. Treiber, L. E.; Owens, W. W. A Laboratory Evaluation of the Wettability of Fifty Oil-Producing Reservoirs. **1972**.

23. Chilingar, G. V.; Yen, T. F. Some Notes on Wettability and Relative Permeabilities of Carbonate Reservoir Rocks, II. *Energy Sources* **1983,** *7* (1), 67-75.

24. Pu, W.-F.; Yuan, C.-D.; Wang, X.-c.; Sun, L.; Zhao, R.-k.; Song, W.-j.; Li, X.-f. The Wettability Alteration and the Effect of Initial Rock Wettability on Oil Recovery in Surfactant-based Enhanced Oil Recovery Processes. *Journal of Dispersion Science and Technology* **2016,** *37* (4), 602-611.

25. Natarajan, A.; Kuznicki, N.; Harbottle, D.; Masliyah, J.; Zeng, H.; Xu, Z. Understanding Mechanisms of Asphaltene Adsorption from Organic Solvent on Mica. *Langmuir* **2014,** *30* (31), 9370-9377.

26. Standal, S.; Haavik, J.; Blokhus, A. M.; Skauge, A. Effect of polar organic components on wettability as studied by adsorption and contact angles. *Journal of Petroleum Science and Engineering* **1999,** *24* (2), 131-144.

27. Kupai, M. M.; Yang, F.; Harbottle, D.; Moran, K.; Masliyah, J.; Xu, Z. H. Characterising rag-forming solids. *Canadian Journal of Chemical Engineering* **2013,** *91* (8), 1395-1401.

28. Zeng, H.; Zou, F.; Horvath-Szabo, G.; Andersen, S. Effects of Brine Composition on the Adsorption of Benzoic Acid on Calcium Carbonate. *Energy & Fuels* **2012,** *26* (7), 4321-4327.

29. Jadhunandan, P. P.; Morrow, N. R. Effect of Wettability on Waterflood Recovery for Crude-Oil/Brine/Rock Systems. **1995**.

30. van Dijke, M. I. J.; Sorbie, K. S. The relation between interfacial tensions and wettability in three-phase systems: consequences for pore occupancy and relative permeability. *Journal of Petroleum Science and Engineering* **2002,** *33* (1), 39-48.

31. Wijaya, N.; Sheng, J. J. Effect of desiccation on shut-in benefits in removing water blockage in tight water-wet cores. *Fuel* **2019,** *244*, 314-323.

32. Zhao, B.; MacMinn, C. W.; Juanes, R. Wettability control on multiphase flow in patterned microfluidics. *Proceedings of the National Academy of Sciences* **2016,** *113* (37), 10251-10256.

33. Chengara, A.; Nikolov, A. D.; Wasan, D. T.; Trokhymchuk, A.; Henderson, D. Spreading of nanofluids driven by the structural disjoining pressure gradient. *Journal of Colloid and Interface Science* **2004,** *280* (1), 192-201.

34. Bakhtiari, M. T.; Harbottle, D.; Curran, M.; Ng, S.; Spence, J.; Siy, R.; Liu, Q. X.; Masliyah, J.; Xu, Z. H. Role of Caustic Addition in Bitumen-Clay Interactions. *Energy & Fuels* **2015,** *29* (1), 58-69.

35. Flury, C.; Afacan, A.; Tamiz Bakhtiari, M.; Sjoblom, J.; Xu, Z. Effect of Caustic Type on Bitumen Extraction from Canadian Oil Sands. *Energy & Fuels* **2014,** *28* (1), 431-438.

36. Swiech, W.; Taylor, S.; Zeng, H. The Role of Water Soluble Species in Bitumen Recovery from Oil Sands. In *SPE Heavy Oil Conference-Canada*; Society of Petroleum Engineers: Calgary, Alberta, Canada, 2014.

37. Liu, J.; Zhou, Z.; Xu, Z.; Masliyah, J. Bitumen–Clay Interactions in Aqueous Media Studied by Zeta Potential Distribution Measurement. *Journal of Colloid and Interface Science* **2002,** *252* (2), 409-418.

38. Sharma, A. Disintegration of macroscopic fluid sheets on substrates - a singular perturbation approach. *Journal of Colloid and Interface Science* **1993,** *156* (1), 96-103.

39. Srinivasa, S.; Flury, C.; Afacan, A.; Masliyah, J.; Xu, Z. Study of Bitumen Liberation from Oil Sands Ores by Online Visualization. *Energy & Fuels* **2012,** *26* (5), 2883-2890.

40. Bertrand, E.; Blake, T. D.; De Coninck, J. Dynamics of dewetting. *Colloids and Surfaces A: Physicochemical and Engineering Aspects* **2010,** *369* (1–3), 141-147.

41. Cox, R. G. The dynamics of the spreading of liquids on a solid surface. Part 1. Viscous flow. *Journal of Fluid Mechanics* **1986,** *168*, 169-194.

42. Cox, R. G. The dynamics of the spreading of liquids on a solid surface. Part 2. Surfactants. *Journal of Fluid Mechanics* **1986,** *168*, 195-220.

43. Blake, T. D.; Haynes, J. M. Kinetics of liquid/liquid displacement. *Journal of Colloid and Interface Science* **1969,** *30* (3), 421-423.

44. Blake, T. D. The physics of moving wetting lines. *Journal of Colloid and Interface Science* **2006,** *299* (1), 1-13.

45. Blake, T. D.; De Coninck, J. The influence of solid–liquid interactions on dynamic wetting. *Advances in Colloid and Interface Science* **2002,** *96* (1–3), 21-36.

46. de Gennes, P. G. Wetting: statics and dynamics. *Reviews of Modern Physics* **1985,** *57* (3), 827-863.

47. Brochard-Wyart, F.; de Gennes, P. G. Dynamics of partial wetting. *Advances in Colloid and Interface Science* **1992,** *39*, 1-11.

48. Acevedo, S.; Escobar, G.; Ranaudo, M. A.; Khazen, J.; Borges, B.; Pereira, J. C.; Méndez, B. Isolation and Characterization of Low and High Molecular Weight Acidic Compounds from Cerro Negro Extraheavy Crude Oil. Role of These Acids in the Interfacial Properties of the Crude Oil Emulsions. *Energy & Fuels* **1999,** *13* (2), 333-335.

49. Havre, T. E.; Sjöblom, J.; Vindstad, J. E. Oil/Water-Partitioning and Interfacial Behavior of Naphthenic Acids. *Journal of Dispersion Science and Technology* **2003,** *24* (6), 789-801.

50. Schramm, L. L.; smith, R. G.; Stone, J. A. A surface-tension method for the determination of anionic surfactants in hot water processing of athabasca oil sands. *Colloids and Surfaces* **1984,** *11* (3), 247-263.

51. Schramm, L. L.; Stasiuk, E. N.; Turner, D. The influence of interfacial tension in the recovery of bitumen by water-based conditioning and flotation of Athabasca oil sands. *Fuel Processing Technology* **2003,** *80* (2), 101-118.

52. Takamura, K.; Chow, R. S. A Mechanism For Initiation of Bitumen Displacement From Oil Sand. *PETSOC-83-06-01* **1983,** *22* (06), 10.

53. Zhang, Y.; Zeng, J.; Qiao, J.; Feng, X.; Dong, Y. Investigating the Effect of the Temperature and Pressure on Wettability in Crude Oil–Brine–Rock Systems. *Energy & Fuels* **2018,** *32* (9), 9010-9019.

54. Nowrouzi, I.; Manshad, A.; Mohammadi, A. *Effects of dissolved binary ionic compounds and different densities of brine on interfacial tension (IFT), wettability alteration, and contact angle in smart water and carbonated smart water injection processes in carbonate oil reservoirs* 2018; Vol. 254. p 83-92.

55. Yang, D.; Gu, Y.; Tontiwachwuthikul, P. Wettability Determination of the Crude Oil−Reservoir Brine−Reservoir Rock System with Dissolution of CO 2 at High Pressures and Elevated Temperatures. *Energy & Fuels* **2008,** *22* (4), 2362-2371.

56. Basu, S.; Nandakumar, K.; Lawrence, S.; Masliyah, J. Effect of calcium ion and montmorillonite clay on bitumen displacement by water on a glass surface. *Fuel* **2004,** *83* (1), 17-22.

57. Basu, S.; Kanda, W. C.; Nandakumar, K.; Masliyah, J. H. Effect of Hydrophobic and Hydrophilic Clays on Bitumen Displacement by Water on a Glass Surface. *Industrial & Engineering Chemistry Research* **1998,** *37* (3), 959-965.

58. Menon, V. B.; Wasan, D. T. Particle—fluid interactions with application to solid-stabilized emulsions part I. The effect of asphaltene adsorption. *Colloids and Surfaces* **1986,** *19* (1), 89-105.

59. Somasundaran, P.; Zhang, L. Adsorption of surfactants on minerals for wettability control in improved oil recovery processes. *Journal of Petroleum Science and Engineering* **2006,** *52* (1), 198-212.

60. Standnes, D. C.; Austad, T. Wettability alteration in chalk: 2. Mechanism for wettability alteration from oil-wet to water-wet using surfactants. *Journal of Petroleum Science and Engineering* **2000,** *28* (3), 123-143.

61. Wu, Y.; Shuler, P. J.; Blanco, M.; Tang, Y.; Goddard, W. A. An Experimental Study of Wetting Behavior and Surfactant EOR in Carbonates With Model Compounds. **2008**.

62. Jarrahian, K.; Seiedi, O.; Sheykhan, M.; Sefti, M. V.; Ayatollahi, S. Wettability alteration of carbonate rocks by surfactants: A mechanistic study. *Colloids and Surfaces A: Physicochemical and Engineering Aspects* **2012,** *410*, 1-10.

63. Xie, X.; Weiss, W. W.; Tong, Z.; Morrow, N. R. Improved Oil Recovery from Carbonate Reservoirs by Chemical Stimulation. Society of Petroleum Engineers, 2004.

64. Curbelo, F. D. S.; Santanna, V. C.; Neto, E. L. B.; Dutra, T. V.; Dantas, T. N. C.; Neto, A. A. D.; Garnica, A. I. C. Adsorption of nonionic surfactants in sandstones. *Colloids and Surfaces A: Physicochemical and Engineering Aspects* **2007,** *293* (1), 1-4.

65. Park, S.; Lee, E. S.; Sulaiman, W. R. W. Adsorption behaviors of surfactants for chemical flooding in enhanced oil recovery. *Journal of Industrial and Engineering Chemistry* **2015,** *21*, 1239-1245.

66. Hou, B.; Wang, Y.; Cao, X.; Zhang, J.; Song, X.; Ding, M.; Chen, W. Surfactant-Induced Wettability Alteration of Oil-Wet Sandstone Surface: Mechanisms and Its Effect on Oil Recovery. *Journal of Surfactants and Detergents* **2016,** *19* (2), 315-324.

67. Karimi, M.; Al-Maamari, R. S.; Ayatollahi, S.; Mehranbod, N. Wettability alteration and oil recovery by spontaneous imbibition of low salinity brine into carbonates: Impact of Mg2+, SO42− and cationic surfactant. *Journal of Petroleum Science and Engineering* **2016,** *147*, 560-569.

68. Hou, B.; Wang, Y.; Cao, X.; Zhang, J.; Song, X.; Ding, M.; Chen, W. Mechanisms of Enhanced Oil Recovery by Surfactant-Induced Wettability Alteration. *Journal of Dispersion Science and Technology* **2016,** *37* (9), 1259-1267.

69. Zhang, R.; Qin, N.; Peng, L.; Tang, K.; Ye, Z. Wettability alteration by trimeric cationic surfactant at water-wet/oil-wet mica mineral surfaces. *Applied Surface Science* **2012,** *258* (20), 7943-7949.

70. Hirasaki, G.; Zhang, D. L. Surface Chemistry of Oil Recovery From Fractured, Oil-Wet, Carbonate Formations. **2004**.

71. Gupta, R.; Mohanty, K. Temperature Effects on Surfactant-Aided Imbibition Into Fractured Carbonates. **2010**.

72. Alvarez, J. O.; Schechter, D. S. Wettability Alteration and Spontaneous Imbibition in Unconventional Liquid Reservoirs by Surfactant Additives. **2017**.

73. Pronk, R.; Russell, T.; Pham, D.; Tangparitkul, S.; Badalyan, A.; Behr, A.; Genolet, L.; Kowollik, P.; Zeinijahromi, A.; Bedrikovetsky, P. In *Non-Monotonic*

Permeability Variation During Fines Migration: Laboratory Study, SPE/IATMI Asia Pacific Oil & Gas Conference and Exhibition, 2017; Society of Petroleum Engineers.

74. Al-Sarihi, A.; Zeinijahromi, A.; Genolet, L.; Behr, A.; Kowollik, P.; Bedrikovetsky, P. Effects of Fines Migration on Residual Oil during Low-Salinity Waterflooding. *Energy & Fuels* **2018,** *32* (8), 8296-8309.

75. Hiorth, A.; Cathles, L. M.; Madland, M. V. The Impact of Pore Water Chemistry on Carbonate Surface Charge and Oil Wettability. *Transport in Porous Media* **2010,** *85* (1), 1-21.

76. Chen, S.-Y.; Kaufman, Y.; Kristiansen, K.; Seo, D.; Schrader, A. M.; Alotaibi, M. B.; Dobbs, H. A.; Cadirov, N. A.; Boles, J. R.; Ayirala, S. C.; Israelachvili, J. N.; Yousef, A. A. Effects of Salinity on Oil Recovery (the "Dilution Effect"): Experimental and Theoretical Studies of Crude Oil/Brine/Carbonate Surface Restructuring and Associated Physicochemical Interactions. *Energy & Fuels* **2017,** *31* (9), 8925-8941.

77. Myint, P. C.; Firoozabadi, A. Thin liquid films in improved oil recovery from low-salinity brine. *Current Opinion in Colloid & Interface Science* **2015,** *20* (2), 105-114.

78. Lager, A.; Webb, K. J.; Black, C. J. J.; Singleton, M.; Sorbie, K. S. Low Salinity Oil Recovery - An Experimental Investigation1. *Petrophysics* **2008,** *49* (01), 8.

79. Morrow, N.; Buckley, J. Improved Oil Recovery by Low-Salinity Waterflooding. *Journal of Petroleum Technology* **2011,** *63*, 106-112.

80. Haagh, M. E. J.; Siretanu, I.; Duits, M. H. G.; Mugele, F. Salinity-Dependent Contact Angle Alteration in Oil/Brine/Silicate Systems: the Critical Role of Divalent Cations. *Langmuir* **2017,** *33* (14), 3349-3357.

81. Moeini, F.; Hemmati-Sarapardeh, A.; Ghazanfari, M.-H.; Masihi, M.; Ayatollahi, S. Toward mechanistic understanding of heavy crude oil/brine interfacial tension: The roles of salinity, temperature and pressure. *Fluid Phase Equilibria* **2014,** *375*, 191-200.

82. Ameri, A.; Esmaeilzadeh, F.; Mowla, D. Effect of low-salinity water on asphaltene precipitation. *Journal of Dispersion Science and Technology* **2018,** *39* (7), 1031-1039.

83. Lashkarbolooki, M.; Riazi, M.; Ayatollahi, S.; Zeinolabedini Hezave, A. Synergy effects of ions, resin, and asphaltene on interfacial tension of acidic crude oil and low–high salinity brines. *Fuel* **2016,** *165*, 75-85.

84. Lashkarbolooki, M.; Ayatollahi, S.; Riazi, M. Effect of Salinity, Resin, and Asphaltene on the Surface Properties of Acidic Crude Oil/Smart Water/Rock System. *Energy & Fuels* **2014,** *28* (11), 6820-6829.

85. Jones, G.; Ray, W. A. THE SURFACE TENSION OF SOLUTIONS. *Journal of the American Chemical Society* **1935,** *57* (5), 957-958.

86. Ghorbanizadeh, S.; Rostami, B. Surface and Interfacial Tension Behavior of Salt Water Containing Dissolved Amphiphilic Compounds of Crude Oil: The Role of Single-Salt Ionic Composition. *Energy & Fuels* **2017,** *31* (9), 9117-9124.

87. Kakati, A.; Sangwai, J. S. Wettability Alteration of Mineral Surface during Low-Salinity Water Flooding: Role of Salt Type, Pure Alkanes, and Model Oils Containing Polar Components. *Energy & Fuels* **2018,** *32* (3), 3127-3137.

88. Kakati, A.; Sangwai, J. S. Effect of monovalent and divalent salts on the interfacial tension of pure hydrocarbon-brine systems relevant for low salinity water flooding. *Journal of Petroleum Science and Engineering* **2017,** *157*, 1106-1114.

89. Al-Saedi, H. N.; Flori, R. E.; Brady, P. V. Effect of divalent cations in formation water on wettability alteration during low salinity water flooding in sandstone reservoirs: Oil recovery analyses, surface reactivity tests, contact angle, and spontaneous imbibition experiments. *Journal of Molecular Liquids* **2019,** *275*, 163-172.

90. Kakati, A.; Jha, N. K.; Kumar, G.; Sangwai, J. S. Application of Low Salinity Water Flooding for Light Paraffinic Crude Oil Reservoir. In *SPE Symposium: Production Enhancement and Cost Optimisation*; Society of Petroleum Engineers: Kuala Lumpur, Malaysia, 2017, p 10.

91. Mahani, H.; Menezes, R.; Berg, S.; Fadili, A.; Nasralla, R.; Voskov, D.; Joekar-Niasar, V. Insights into the Impact of Temperature on the Wettability Alteration by Low Salinity in Carbonate Rocks. *Energy & Fuels* **2017,** *31* (8), 7839-7853.

92. Chen, Y.; Xie, Q.; Sari, A.; Brady, P. V.; Saeedi, A. Oil/water/rock wettability: Influencing factors and implications for low salinity water flooding in carbonate reservoirs. *Fuel* **2018,** *215*, 171-177.

93. Suleimanov, B. A.; Latifov, Y. A.; Veliyev, E. F.; Frampton, H. Comparative analysis of the EOR mechanisms by using low salinity and low hardness alkaline water. *Journal of Petroleum Science and Engineering* **2018,** *162*, 35-43.

94. Mahani, H.; Keya, A. L.; Berg, S.; Bartels, W.-B.; Nasralla, R.; Rossen, W. R. Insights into the Mechanism of Wettability Alteration by Low-Salinity Flooding (LSF) in Carbonates. *Energy & Fuels* **2015,** *29* (3), 1352-1367.

95. Zaeri, M. R.; Hashemi, R.; Shahverdi, H.; Sadeghi, M. Enhanced oil recovery from carbonate reservoirs by spontaneous imbibition of low salinity water. *Petroleum Science* **2018,** *15* (3), 564-576.

96. Saikia, B. D.; Mahadevan, J.; Rao, D. N. Exploring mechanisms for wettability alteration in low-salinity waterfloods in carbonate rocks. *Journal of Petroleum Science and Engineering* **2018,** *164*, 595-602.

97. Zhang, L.; Zhang, J.; Wang, Y.; Yang, R.; Zhang, Y.; Gu, J.; Zhang, M.; Ren, S. Experimental Investigation of Low-Salinity Water Flooding in a Low-Permeability Oil Reservoir. *Energy & Fuels* **2018,** *32* (3), 3108-3118.

98. Mohammadi, S.; Kord, S.; Moghadasi, J. An experimental investigation into the spontaneous imbibition of surfactant assisted low salinity water in carbonate rocks. *Fuel* **2019,** *243*, 142-154.

99. Tetteh, J.; Janjang, N. M.; Barati, R. Wettability Alteration and Enhanced Oil Recovery Using Low Salinity Waterflooding in Limestone Rocks: A Mechanistic Study. In *SPE Kingdom of Saudi Arabia Annual Technical Symposium and Exhibition*; Society of Petroleum Engineers: Dammam, Saudi Arabia, 2018, p 22.

100. Farzaneh, S. A.; Carnegie, A.; Sohrabi, M.; Mills, J. R.; Facanha, J. M. F.; Sellers, B. A Case Study of Oil Recovery Improvement by Low Salinity Water Injection. In *Abu Dhabi International Petroleum Exhibition & Conference*; Society of Petroleum Engineers: Abu Dhabi, UAE, 2017, p 43.

101. Moosavi, S. R.; Rayhani, M.; Malayeri, M. R.; Riazi, M. Impact of monovalent and divalent cationic and anionic ions on wettability alteration of dolomite rocks. *Journal of Molecular Liquids* **2019,** *281*, 9-19.

102. Basu, S.; Sharma, M. M. Measurement of Critical Disjoining Pressure for Dewetting of Solid Surfaces. *Journal of Colloid and Interface Science* **1996,** *181* (2), 443-455.

103. Israelachvili, J. N. *Intermolecular and surface forces*; Academic press2011.

104. Hirasaki, G. J. Wettability: Fundamentals and Surface Forces. **1991**.

105. Farooq, U.; Simon, S.; Tweheyo, M. T.; Sjöblom, J.; Øye, G. Electrophoretic measurements of crude oil fractions dispersed in aqueous solutions of different ionic compositions—Evaluation of the interfacial charging mechanisms. *Journal of Dispersion Science and Technology* **2013,** *34* (10), 1376-1381.

106. Liu, X.; Yan, W.; Stenby, E. H.; Thormann, E. Release of crude oil from silica and calcium carbonate surfaces: on the alternation of surface and molecular forces by high-and low-salinity aqueous salt solutions. *Energy & Fuels* **2016,** *30* (5), 3986-3993.

107. Nasralla, R. A.; Nasr-El-Din, H. A. Impact of cation type and concentration in injected brine on oil recovery in sandstone reservoirs. *Journal of Petroleum Science and Engineering* **2014,** *122,* 384-395.

108. Wu, J.; Liu, F.; Chen, G.; Wu, X.; Ma, D.; Liu, Q.; Xu, S.; Huang, S.; Chen, T.; Zhang, W.; Yang, H.; Wang, J. Effect of Ionic Strength on the Interfacial Forces between Oil/Brine/Rock Interfaces: A Chemical Force Microscopy Study. *Energy & Fuels* **2016,** *30* (1), 273-280.

109. Zhang, J.; Liu, F.; Yang, H.; Zhu, Y.; Wang, X.; Hua, Z. Effect of ion type on the interaction between polar model oil and mica substrate: a chemical force microscopy study. *Energy & Fuels* **2018,** *32* (10), 10486-10492.

110. Lu, Y.; Najafabadi, N. F.; Firoozabadi, A. Effect of Temperature on Wettability of Oil/Brine/Rock Systems. *Energy & Fuels* **2017,** *31* (5), 4989-4995.

111. Alotaibi, M. B.; Nasr-El-Din, H. A. Electrokinetics of Limestone Particles and Crude-Oil Droplets in Saline Solutions. **2011**.

112. Taylor, S.; Chu, H. Metal Ion Interactions with Crude Oil Components: Specificity of Ca2+ Binding to Naphthenic Acid at an Oil/Water Interface. *Colloids and Interfaces* **2018,** *2* (3), 40.

113. Haagh, M. E. J.; Schilderink, N.; Duits, M. H. G.; Siretanu, I.; Mugele, F.; Collins, I. R. Salinity-dependent contact angle alteration in oil/brine/silicate systems: The effect of temperature. *Journal of Petroleum Science and Engineering* **2018,** *165*, 1040-1048.

114. Vafaei, S.; Borca-Tasciuc, T.; Podowski, M. Z.; Purkayastha, A.; Ramanath, G.; Ajayan, P. M. Effect of nanoparticles on sessile droplet contact angle. *Nanotechnology* **2006,** *17* (10), 2523.

115. Alomair, O. A.; Matar, K. M.; Alsaeed, Y. H. Nanofluids Application for Heavy Oil Recovery. Society of Petroleum Engineers, 2014.

116. Ehtesabi, H.; Ahadian, M. M.; Taghikhani, V. Enhanced Heavy Oil Recovery Using TiO2 Nanoparticles: Investigation of Deposition during Transport in Core Plug. *Energy & Fuels* **2015,** *29* (1), 1-8.

117. Ehtesabi, H.; Ahadian, M. M.; Taghikhani, V.; Ghazanfari, M. H. Enhanced Heavy Oil Recovery in Sandstone Cores Using TiO2 Nanofluids. *Energy & Fuels* **2014,** *28* (1), 423-430.

118. Glaser, N.; Adams, D. J.; Böker, A.; Krausch, G. Janus Particles at Liquid−Liquid Interfaces. *Langmuir* **2006,** *22* (12), 5227-5229.

119. Soleimani, H.; Baig, M. K.; Yahya, N.; Khodapanah, L.; Sabet, M.; Demiral, B. M. R.; Burda, M. Impact of carbon nanotubes based nanofluid on oil recovery efficiency using core flooding. *Results in Physics* **2018,** *9*, 39-48.

120. Wei, B.; Li, Q.; Jin, F.; Li, H.; Wang, C. The potential of a novel nanofluid in enhancing oil recovery. *Energy & Fuels* **2016,** *30* (4), 2882-2891.

121. Roustaei, A.; Bagherzadeh, H. Experimental investigation of SiO2 nanoparticles on enhanced oil recovery of carbonate reservoirs. *Journal of Petroleum Exploration and Production Technology* **2015,** *5* (1), 27-33.

122. Al-Anssari, S.; Barifcani, A.; Wang, S.; Maxim, L.; Iglauer, S. Wettability alteration of oil-wet carbonate by silica nanofluid. *Journal of Colloid and Interface Science* **2016,** *461* (Supplement C), 435-442.

123. Maghzi, A.; Mohammadi, S.; Ghazanfari, M. H.; Kharrat, R.; Masihi, M. Monitoring wettability alteration by silica nanoparticles during water flooding to heavy oils in five-spot systems: A pore-level investigation. *Experimental Thermal and Fluid Science* **2012,** *40*, 168-176.

124. Dehghan Monfared, A.; Ghazanfari, M. H.; Jamialahmadi, M.; Helalizadeh, A. Potential Application of Silica Nanoparticles for Wettability Alteration of Oil–Wet Calcite: A Mechanistic Study. *Energy & Fuels* **2016,** *30* (5), 3947-3961.

125. Hendraningrat, L.; Li, S.; Torsæter, O. A coreflood investigation of nanofluid enhanced oil recovery. *Journal of Petroleum Science and Engineering* **2013,** *111*, 128-138.

126. Parvazdavani, M.; Masihi, M.; Ghazanfari, M. H. Monitoring the influence of dispersed nano-particles on oil–water relative permeability hysteresis. *Journal of Petroleum Science and Engineering* **2014,** *124* (Supplement C), 222-231.

127. Li, S.; Hendraningrat, L.; Torsaeter, O. Improved Oil Recovery by Hydrophilic Silica Nanoparticles Suspension: 2-Phase Flow Experimental Studies. International Petroleum Technology Conference, 2013.

128. Shahrabadi, A.; Bagherzadeh, H.; Roostaie, A.; Golghanddashti, H. Experimental Investigation of HLP Nanofluid Potential to Enhance Oil Recovery: A Mechanistic Approach. Society of Petroleum Engineers, 2012.

129. Li, S.; Genys, M.; Wang, K.; Torsæter, O. Experimental Study of Wettability Alteration during Nanofluid Enhanced Oil Recovery Process and Its Effect on Oil Recovery. Society of Petroleum Engineers, 2015.

130. Fan, H.; Striolo, A. Nanoparticle effects on the water-oil interfacial tension. *Physical Review E* **2012,** *86* (5), 051610.

131. Chinnam, J.; Das, D. K.; Vajjha, R. S.; Satti, J. R. Measurements of the surface tension of nanofluids and development of a new correlation. *International Journal of Thermal Sciences* **2015,** *98*, 68-80.

132. Kondiparty, K.; Nikolov, A.; Wu, S.; Wasan, D. Wetting and Spreading of Nanofluids on Solid Surfaces Driven by the Structural Disjoining Pressure: Statics Analysis and Experiments. *Langmuir* **2011,** *27* (7), 3324-3335.

133. Zhang, H.; Nikolov, A.; Wasan, D. Enhanced Oil Recovery (EOR) Using Nanoparticle Dispersions: Underlying Mechanism and Imbibition Experiments. *Energy & Fuels* **2014,** *28* (5), 3002-3009.

134. Trokhymchuk, A.; Henderson, D.; Nikolov, A.; Wasan, D. T. A Simple Calculation of Structural and Depletion Forces for Fluids/Suspensions Confined in a Film. *Langmuir* **2001,** *17* (16), 4940-4947.

135. Winkler, K.; Paszewski, M.; Kalwarczyk, T.; Kalwarczyk, E.; Wojciechowski, T.; Gorecka, E.; Pociecha, D.; Holyst, R.; Fialkowski, M. Ionic Strength-Controlled Deposition of Charged Nanoparticles on a Solid Substrate. *The Journal of Physical Chemistry C* **2011,** *115* (39), 19096-19103.

136. Darlington, T. K.; Neigh, A. M.; Spencer, M. T.; Guyen, O. T. N.; Oldenburg, S. J. Nanoparticle characteristics affecting environmental fate and transport through soil. *Environmental Toxicology and Chemistry* **2009,** *28* (6), 1191-1199.

137. Esfandyari Bayat, A.; Junin, R.; Samsuri, A.; Piroozian, A.; Hokmabadi, M. Impact of Metal Oxide Nanoparticles on Enhanced Oil Recovery from Limestone Media at Several Temperatures. *Energy & Fuels* **2014,** *28* (10), 6255-6266.

138. Li, Y. V.; Cathles, L. M.; Archer, L. A. Nanoparticle tracers in calcium carbonate porous media. *Journal of Nanoparticle Research* **2014,** *16* (8), 2541.

139. Li, Y. V.; Cathles, L. M. Retention of silica nanoparticles on calcium carbonate sands immersed in electrolyte solutions. *Journal of Colloid and Interface Science* **2014,** *436*, 1-8.

140. Cassie, A. B. D.; Baxter, S. Wettability of porous surfaces. *Transactions of the Faraday Society* **1944,** *40* (0), 546-551.

141. Wenzel, R. N. Resistance of solid surfaces to wetting by water. *Industrial & Engineering Chemistry* **1936,** *28* (8), 988-994.

142. Nwidee, L. N.; Al-Anssari, S.; Barifcani, A.; Sarmadivaleh, M.; Lebedev, M.; Iglauer, S. Nanoparticles influence on wetting behaviour of fractured limestone formation. *Journal of Petroleum Science and Engineering* **2017,** *149*, 782-788.

143. Zargartalebi, M.; Barati, N.; Kharrat, R. Influences of hydrophilic and hydrophobic silica nanoparticles on anionic surfactant properties: Interfacial and adsorption behaviors. *Journal of Petroleum Science and Engineering* **2014,** *119* (Supplement C), 36-43.

144. Ahualli, S.; Iglesias, G. R.; Wachter, W.; Dulle, M.; Minami, D.; Glatter, O. Adsorption of Anionic and Cationic Surfactants on Anionic Colloids: Supercharging and Destabilization. *Langmuir* **2011,** *27* (15), 9182-9192.

145. Choi, S. K.; Son, H. A.; Kim, H. T.; Kim, J. W. Nanofluid Enhanced Oil Recovery Using Hydrophobically Associative Zwitterionic Polymer-Coated Silica Nanoparticles. *Energy & Fuels* **2017,** *31* (8), 7777-7782.

146. ShamsiJazeyi, H.; Miller, C. A.; Wong, M. S.; Tour, J. M.; Verduzco, R. Polymer-coated nanoparticles for enhanced oil recovery. *Journal of Applied Polymer Science* **2014,** *131* (15).

147. Esmaeilzadeh, P.; Hosseinpour, N.; Bahramian, A.; Fakhroueian, Z.; Arya, S. Effect of ZrO2 nanoparticles on the interfacial behavior of surfactant solutions at air–water and n-heptane–water interfaces. *Fluid Phase Equilibria* **2014,** *361*, 289-295.

148. Nourozieh, H.; Kariznovi, M.; Abedi, J. Density and viscosity of Athabasca bitumen samples at temperatures up to 200C and pressures up to 10 MPa. *SPE Reservoir Evaluation & Engineering* **2015,** *18* (03), 375-386.

149. Institute, E. IP 469: Determination of Saturated, Aromatic and Polar Compounds in Petroleum Products by Thin Layer Chromatography and Flame Ionization Detection. EI Publications, 2011.

150. Green, D. W.; Perry, R. H. *Perry's Chemical Engineers' Handbook/edición Don W. Green y Robert H. Perry* 1997.

151. Millero, F. J.; Chen, C.-T.; Bradshaw, A.; Schleicher, K. A new high pressure equation of state for seawater. *Deep Sea Research Part A. Oceanographic Research Papers* **1980,** *27* (3), 255-264.

152. Li, Z.; Richtering, W.; Ngai, T. Poly(N-isopropylacrylamide) microgels at the oil-water interface: temperature effect. *Soft Matter* **2014,** *10* (33), 6182-6191.

153. Blunt, M. J. *Multiphase flow in permeable media: A pore-scale perspective*; Cambridge University Press2017.

154. Barnes, G.; Gentle, I. *Interfacial science: an introduction*; Oxford University Press2011.

155. Bashforth, F.; Adams, J. C. *An attempt to test the theories of capillary action: by comparing the theoretical and measured forms of drops of fluid*; University Press1883.

156. Lin, F.; He, L.; Primkulov, B.; Xu, Z. Dewetting Dynamics of a Solid Microsphere by Emulsion Drops. *The Journal of Physical Chemistry C* **2014,** *118* (25), 13552-13562.

157. Delgado, A.; González-Caballero, F.; Hunter, R.; Koopal, L.; Lyklema, J. Measurement and interpretation of electrokinetic phenomena (IUPAC technical report). *Pure and Applied Chemistry* **2005,** *77* (10), 1753-1805.

158. von Smoluchowski, M. Contribution à la théorie de l'endosmose électrique et de quelques phénomènes corrélatifs. *Bull. Akad. Sci. Cracovie.* **1903,** *8*, 182-200.

159. George, A.; Singh, R. Correlation of Refractive Index and Density of Crude Oil and Liquid Hydrocarbon. *Int. J. Chem. Environ. Biol. Sci* **2015,** *3*, 420-422.

160. El Ghandoor, H.; Hegazi, E.; Nasser, I.; Behery, G. Measuring the refractive index of crude oil using a capillary tube interferometer. *Optics & Laser Technology* **2003,** *35* (5), 361-367.

161. Liu, J.; Xu, Z.; Masliyah, J. Colloidal forces between bitumen surfaces in aqueous solutions measured with atomic force microscope. *Colloids and Surfaces A: Physicochemical and Engineering Aspects* **2005,** *260* (1), 217-228.

162. Hertz, H. On the contact of elastic solids. *Z. Reine Angew. Mathematik* **1881,** *92*, 156-171.

163. Clark, K. A.; Pasternack, D. S. Hot Water Seperation of Bitumen from Alberta Bituminous Sand. *Industrial & Engineering Chemistry* **1932,** *24* (12), 1410-1416.

164. Moore, T. F.; Slobod, R. L. The effect of viscosity and capillarity on the displacement of oil by water. *Producers Mon. Penn. Oil. Prod. Assoc.* **1956,** *20*, 20-30.

165. Green, D. W.; Willhite, G. P. *Enhanced Oil Recovery*; Society of Petroleum Engineers1998.

166. Johannessen, A. M.; Spildo, K. Enhanced Oil Recovery (EOR) by Combining Surfactant with Low Salinity Injection. *Energy & Fuels* **2013,** *27* (10), 5738-5749.

167. Duvivier, D.; Seveno, D.; Rioboo, R.; Blake, T. D.; De Coninck, J. Experimental Evidence of the Role of Viscosity in the Molecular Kinetic Theory of Dynamic Wetting. *Langmuir* **2011,** *27* (21), 13015-13021.

168. Xie, Q.; Saeedi, A.; Pooryousefy, E.; Liu, Y. Extended DLVO-based estimates of surface force in low salinity water flooding. *Journal of Molecular Liquids* **2016,** *221,* 658-665.

169. Sauerer, B.; Stukan, M.; Buiting, J.; Abdallah, W.; Andersen, S. I. Dynamic Asphaltene-Stearic Acid Competition at the Oil-Water Interface. *Langmuir* **2018,** *34* (19), 5558-5573.

170. Pradilla, D.; Simon, S.; Sjöblom, J.; Samaniuk, J.; Skrzypiec, M.; Vermant, J. Sorption and Interfacial Rheology Study of Model Asphaltene Compounds. *Langmuir* **2016,** *32* (12), 2900-2911.

171. Schramm, L. L.; Smith, R. G. The influence of natural surfactants on interfacial charges in the hot-water process for recovering bitumen from the athabasca oil sands. *Colloids and Surfaces* **1985,** *14* (1), 67-85.

172. Drelich, J.; Miller, J. D. Surface and interfacial tension of the Whiterocks bitumen and its relationship to bitumen release from tar sands during hot water processing. *Fuel* **1994,** *73* (9), 1504-1510.

173. Drelich, J.; Bukka, K.; Miller, J. D.; Hanson, F. V. Surface Tension of Toluene-Extracted Bitumens from Utah Oil Sands as Determined by Wilhelmy Plate and Contact Angle Techniques. *Energy & Fuels* **1994,** *8* (3), 700-704.

174. Jun, L.; Jaroslaw, D.; Zhenghe, X.; H., M. J. Effect of Operating Temperature on Water-Based Oil Sands Processing. *The Canadian Journal of Chemical Engineering* **2007,** *85* (5), 726-738.

175. Rogers, V. V.; Liber, K.; MacKinnon, M. D. Isolation and characterization of naphthenic acids from Athabasca oil sands tailings pond water. *Chemosphere* **2002,** *48* (5), 519-527.

176. Grewer, D. M.; Young, R. F.; Whittal, R. M.; Fedorak, P. M. Naphthenic acids and other acid-extractables in water samples from Alberta: What is being measured? *Science of The Total Environment* **2010,** *408* (23), 5997-6010.

177. Zhang, S.; Zhang, L.; Lu, X.; Shi, C.; Tang, T.; Wang, X.; Huang, Q.; Zeng, H. Adsorption kinetics of asphaltenes at oil/water interface: Effects of concentration and temperature. *Fuel* **2018,** *212*, 387-394.

178. Rane, J. P.; Harbottle, D.; Pauchard, V.; Couzis, A.; Banerjee, S. Adsorption Kinetics of Asphaltenes at the Oil–Water Interface and Nanoaggregation in the Bulk. *Langmuir* **2012,** *28* (26), 9986-9995.

179. Sheu, E. Y.; Storm, D. A.; Shields, M. B. Adsorption kinetics of asphaltenes at toluene/acid solution interface. *Fuel* **1995,** *74* (10), 1475-1479.

180. Masliyah, J. H.; Xu, Z.; Czarnecki, J. A. *Handbook on theory and practice of bitumen recovery from Athabasca Oil Sands: Theoretical Basis*; Kingsley Knowledge Pub.2011.

181. Schramm, L. L.; Stasiuk, E. N.; MacKinnon, M. Surfactants in Athabasca oil sands slurry conditioning, flotation recovery, and tailings processes. In *Surfactants: Fundamentals and Applications in the Petroleum Industry*, Schramm, L. L., Ed.; Cambridge University Press: Cambridge, 2000, pp 365-430.

182. Scott, A. C.; Young, R. F.; Fedorak, P. M. Comparison of GC–MS and FTIR methods for quantifying naphthenic acids in water samples. *Chemosphere* **2008,** *73* (8), 1258-1264.

183. Yu, G.; Karinshak, K.; Harwell, J. H.; Grady, B. P.; Woodside, A.; Ghosh, M. Interfacial behavior and water solubility of various asphaltenes at high temperature. *Colloids and Surfaces A: Physicochemical and Engineering Aspects* **2014,** *441*, 378-388.

184. Yarranton, H. W.; Sztukowski, D. M.; Urrutia, P. Effect of interfacial rheology on model emulsion coalescence: I. Interfacial rheology. *Journal of Colloid and Interface Science* **2007,** *310* (1), 246-252.

185. Mikami, Y.; Liang, Y.; Matsuoka, T.; Boek, E. S. Molecular Dynamics Simulations of Asphaltenes at the Oil–Water Interface: From Nanoaggregation to Thin-Film Formation. *Energy & Fuels* **2013,** *27* (4), 1838-1845.

186. Kuznicki, T.; Masliyah, J. H.; Bhattacharjee, S. Aggregation and Partitioning of Model Asphaltenes at Toluene−Water Interfaces: Molecular Dynamics Simulations. *Energy & Fuels* **2009,** *23* (10), 5027-5035.

187. Gao, F.; Xu, Z.; Liu, G.; Yuan, S. Molecular Dynamics Simulation: The Behavior of Asphaltene in Crude Oil and at the Oil/Water Interface. *Energy & Fuels* **2014,** *28* (12), 7368-7376.

188. Soleymanzadeh, A.; Yousefi, M.; Kord, S.; Mohammadzadeh, O. A review on methods of determining onset of asphaltene precipitation. *Journal of Petroleum Exploration and Production Technology* **2019,** *9* (2), 1375-1396.

189. Carnahan, N. F.; Quintero, L.; Pfund, D. M.; Fulton, J. L.; Smith, R. D.; Capel, M.; Leontaritis, K. A small angle x-ray scattering study of the effect of pressure on the aggregation of asphaltene fractions in petroleum fluids under near-critical solvent conditions. *Langmuir* **1993,** *9* (8), 2035-2044.

190. Cai, B.-Y.; Yang, J.-T.; Guo, T.-M. Interfacial Tension of Hydrocarbon + Water/Brine Systems under High Pressure. *Journal of Chemical & Engineering Data* **1996,** *41* (3), 493-496.

191. Stanimirova, R.; Marinova, K.; Tcholakova, S.; Denkov, N. D.; Stoyanov, S.; Pelan, E. Surface Rheology of Saponin Adsorption Layers. *Langmuir* **2011,** *27* (20), 12486-12498.

192. Szyszkowski, B. v. Experimental studies on capillary properties of aqueous solutions fatty acids. *Z. Phys. Chem* **1908,** *64*, 385-414.

193. Acevedo, S.; Borges, B.; Quintero, F.; Piscitelly, V.; Gutierrez, L. B. Asphaltenes and Other Natural Surfactants from Cerro Negro Crude Oil. Stepwise Adsorption at the Water/Toluene Interface: Film Formation and Hydrophobic Effects. *Energy & Fuels* **2005,** *19* (5), 1948-1953.

194. Rehfeld, S. J. Adsorption of sodium dodecyl sulfate at various hydrocarbon-water interfaces. *The Journal of Physical Chemistry* **1967,** *71* (3), 738-745.

195. Chen, L.-J.; Lin, S.-Y.; Huang, C.-C.; Chen, E.-M. Temperature dependence of critical micelle concentration of polyoxyethylenated non-ionic surfactants. *Colloids and Surfaces A: Physicochemical and Engineering Aspects* **1998,** *135* (1), 175-181.

196. de Gennes, P.-G.; Brochard-Wyart, F.; Quéré, D. *Capillarity and wetting phenomena: drops, bubbles, pearls, waves*; Springer Science & Business Media2013.

197. Rothert, A.; Richter, R.; Rehberg, I. Formation of a drop: viscosity dependence of three flow regimes. *New Journal of Physics* **2003,** *5* (1), 59.

198. Kovalchuk, N. M.; Nowak, E.; Simmons, M. J. H. Kinetics of liquid bridges and formation of satellite droplets: Difference between micellar and bi-layer forming solutions. *Colloids and Surfaces A: Physicochemical and Engineering Aspects* **2017,** *521*, 193-203.

199. Kovalchuk, N. M.; Nowak, E.; Simmons, M. J. H. Effect of Soluble Surfactants on the Kinetics of Thinning of Liquid Bridges during Drops Formation and on Size of Satellite Droplets. *Langmuir* **2016,** *32* (20), 5069-5077.

200. Kamal, M. S.; Hussein, I. A.; Sultan, A. S. Review on Surfactant Flooding: Phase Behavior, Retention, IFT, and Field Applications. *Energy & Fuels* **2017,** *31* (8), 7701-7720.

201. Morrow, N. R.; Tang, G.-q.; Valat, M.; Xie, X. Prospects of improved oil recovery related to wettability and brine composition. *Journal of Petroleum Science and Engineering* **1998,** *20* (3–4), 267-276.

202. Tang, G. Q.; Morrow, N. R. Salinity, Temperature, Oil Composition, and Oil Recovery by Waterflooding. **1997**.

203. Tangparitkul, S.; Charpentier, T.; Pradilla, D.; Harbottle, D. Interfacial and Colloidal Forces Governing Oil Droplet Displacement: Implications for Enhanced Oil Recovery. *Colloids and Interfaces* **2018,** *2* (3), 30.

204. Tangparitkul, S. Evaluation of effecting factors on oil recovery using the desirability function. *Journal of Petroleum Exploration and Production Technology* **2018,** *8* (4), 1199-1208.

205. Sheng, J. J. Critical review of low-salinity waterflooding. *Journal of Petroleum Science and Engineering* **2014,** *120*, 216-224.

206. Serrano-Saldaña, E.; Domínguez-Ortiz, A.; Pérez-Aguilar, H.; Kornhauser-Strauss, I.; Rojas-González, F. Wettability of solid/brine/n-dodecane systems: experimental study of the effects of ionic strength and surfactant concentration. *Colloids and Surfaces A: Physicochemical and Engineering Aspects* **2004,** *241* (1), 343-349.

207. Matthews, C. S.; Russell, D. G. *Pressure buildup and flow tests in wells*; Society of petroleum engineers of AIME Dallas, TX1967.

208. Correia, R.; Kestin, J.; Khalifa, H. Measurement and Calculation of the Viscosity of Mixed Aqueous Solutions of NaCl and KCl in the Temperature Range 25 - 150° C and

the Pressure Range 0 – 30 MPa. *Berichte der Bunsengesellschaft für physikalische Chemie* **1979,** *83* (1), 20-24.

209. Donose, B. C.; Vakarelski, I. U.; Higashitani, K. Silica Surfaces Lubrication by Hydrated Cations Adsorption from Electrolyte Solutions. *Langmuir* **2005,** *21* (5), 1834-1839.

210. Marcus, Y. A simple empirical model describing the thermodynamics of hydration of ions of widely varying charges, sizes, and shapes. *Biophysical Chemistry* **1994,** *51* (2), 111-127.

211. Petersen, P. B.; Saykally, R. J. Adsorption of Ions to the Surface of Dilute Electrolyte Solutions: The Jones−Ray Effect Revisited. *Journal of the American Chemical Society* **2005,** *127* (44), 15446-15452.

212. Gao, S.; Moran, K.; Xu, Z.; Masliyah, J. Role of Bitumen Components in Stabilizing Water-in-Diluted Oil Emulsions. *Energy & Fuels* **2009,** *23* (5), 2606-2612.

213. Collins, K. D.; Washabaugh, M. W. The Hofmeister effect and the behaviour of water at interfaces. *Quarterly reviews of biophysics* **1985,** *18* (4), 323-422.

214. dos Santos, A. P.; Levin, Y. Ions at the Water–oil Interface: Interfacial Tension of Electrolyte Solutions. *Langmuir* **2012,** *28* (2), 1304-1308.

215. dos Santos, A. P.; Levin, Y. Surface and interfacial tensions of Hofmeister electrolytes. *Faraday Discussions* **2013,** *160* (0), 75-87.

216. Lashkarbolooki, M.; Ayatollahi, S. Experimental and modeling investigation of dynamic interfacial tension of asphaltenic–acidic crude oil/aqueous phase containing different ions. *Chinese Journal of Chemical Engineering* **2017,** *25* (12), 1820-1830.

217. Premkumar, J. R.; Sastry, G. N. Cation–Alkane Interaction. *The Journal of Physical Chemistry A* **2014,** *118* (48), 11388-11398.

218. Mecozzi, S.; West, A. P.; Dougherty, D. A. Cation−π Interactions in Simple Aromatics: Electrostatics Provide a Predictive Tool. *Journal of the American Chemical Society* **1996,** *118* (9), 2307-2308.

219. Wheeler, S. E.; Houk, K. N. Substituent effects in cation/pi interactions and electrostatic potentials above the centers of substituted benzenes are due primarily to through-space effects of the substituents. *Journal of the American Chemical Society* **2009,** *131* (9), 3126-3127.

220. Wei, B.; Ning, J.; He, J.; Lu, L.; Wang, Y.; Sun, L. Relation between brine-crude oil-quartz contact angle formed on flat quartz slides and in capillaries with brine composition: Implications for low-salinity waterflooding. *Colloids and Surfaces A: Physicochemical and Engineering Aspects* **2018,** *555*, 660-667.

221. Lim, S.; Horiuchi, H.; Nikolov, A. D.; Wasan, D. Nanofluids Alter the Surface Wettability of Solids. *Langmuir* **2015,** *31* (21), 5827-5835.

222. Basu, S.; Sharma, M. M. Effect of Dielectric Saturation on Disjoining Pressure in Thin Films of Aqueous Electrolytes. *Journal of Colloid and Interface Science* **1994,** *165* (2), 355-366.

223. Hogg, R.; Healy, T. W.; Fuerstenau, D. W. Mutual coagulation of colloidal dispersions. *Transactions of the Faraday Society* **1966,** *62* (0), 1638-1651.

224. Butt, H. J. Electrostatic interaction in scanning probe microscopy when imaging in electrolyte solutions. *Nanotechnology* **1992,** *3* (2), 60-68.

225. Butt, H.-J.; Jaschke, M.; Ducker, W. Measuring surface forces in aqueous electrolyte solution with the atomic force microscope. *Bioelectrochemistry and Bioenergetics* **1995,** *38* (1), 191-201.

226. Zhao, H.; Long, J.; Masliyah, J. H.; Xu, Z. Effect of Divalent Cations and Surfactants on Silica−Bitumen Interactions. *Industrial & Engineering Chemistry Research* **2006,** *45* (22), 7482-7490.

227. Bakhtiari, M. T. Role of Sodium Hydroxide in Bitumen Extraction: Production of Natural Surfactants and Slime Coating. PhD, University of Alberta2015.

228. Williams, M. B.; Davis, S. H. Nonlinear theory of film rupture. *Journal of Colloid and Interface Science* **1982,** *90* (1), 220-228.

229. Ida, M. P.; Miksis, M. J. The Dynamics of Thin Films I: General Theory. *SIAM Journal on Applied Mathematics* **1998,** *58* (2), 456-473.

230. Lim, S.; Zhang, H.; Wu, P.; Nikolov, A.; Wasan, D. The dynamic spreading of nanofluids on solid surfaces – Role of the nanofilm structural disjoining pressure. *Journal of Colloid and Interface Science* **2016,** *470*, 22-30.

231. Binks, B. P. Colloidal Particles at a Range of Fluid–Fluid Interfaces. *Langmuir* **2017,** *33* (28), 6947-6963.

232. Destribats, M.; Lapeyre, V.; Wolfs, M.; Sellier, E.; Leal-Calderon, F.; Ravaine, V.; Schmitt, V. Soft microgels as Pickering emulsion stabilisers: role of particle deformability. *Soft Matter* **2011,** *7* (17), 7689-7698.

233. Schild, H. G. Poly(N-isopropylacrylamide): experiment, theory and application. *Progress in Polymer Science* **1992,** *17* (2), 163-249.

234. Ngai, T.; Behrens, S. H.; Auweter, H. Novel emulsions stabilized by pH and temperature sensitive microgels. *Chemical Communications* **2005,** (3), 331-333.

235. Ngai, T.; Auweter, H.; Behrens, S. H. Environmental Responsiveness of Microgel Particles and Particle-Stabilized Emulsions. *Macromolecules* **2006,** *39* (23), 8171-8177.

236. Russell, T.; Pham, D.; Neishaboor, M. T.; Badalyan, A.; Behr, A.; Genolet, L.; Kowollik, P.; Zeinijahromi, A.; Bedrikovetsky, P. Effects of kaolinite in rocks on fines migration. *Journal of Natural Gas Science and Engineering* **2017,** *45*, 243-255.

237. Tran-Viet, A.; Routh, A. F.; Woods, A. W. Control of the permeability of a porous media using a thermally sensitive polymer. *AIChE Journal* **2014,** *60* (3), 1193-1201.

238. Howe, A. M.; Desrousseaux, S.; Lunel, L. S.; Tavacoli, J.; Yow, H. N.; Routh, A. F. Anomalous viscosity jump during the volume phase transition of poly(N-isopropylacrylamide) particles. *Advances in Colloid and Interface Science* **2009,** *147-148*, 124-131.

239. Byun, J.; Shin, J.; Kwon, S.; Jang, S.; Kim, J. K. Fast and reversibly switchable wettability induced by a photothermal effect. *Chemical Communications* **2012,** *48* (74), 9278-9280.

240. Chhabra, A.; Kanapuram, R. R.; Kim, T. J.; Geng, J.; da Silva, A. K.; Bielawski, C. W.; Hidrovo, C. H. Humidity Effects on the Wetting Characteristics of Poly(N-isopropylacrylamide) during a Lower Critical Solution Transition. *Langmuir* **2013,** *29* (25), 8116-8124.

241. Mengual, O.; Meunier, G.; Cayré, I.; Puech, K.; Snabre, P. TURBISCAN MA 2000: multiple light scattering measurement for concentrated emulsion and suspension instability analysis. *Talanta* **1999,** *50* (2), 445-456.

242. Pelton, R. Temperature-sensitive aqueous microgels. *Advances in colloid and interface science* **2000,** *85* (1), 1-33.

243. Chen, J.; Gong, X.; Yang, H.; Yao, Y.; Xu, M.; Chen, Q.; Cheng, R. NMR Study on the Effects of Sodium n-Dodecyl Sulfate on the Coil-to-Globule Transition of Poly(N-isopropylacrylamide) in Aqueous Solutions. *Macromolecules* **2011,** *44* (15), 6227-6231.

244. Schild, H. G.; Tirrell, D. A. Interaction of poly(N-isopropylacrylamide) with sodium n-alkyl sulfates in aqueous solution. *Langmuir* **1991,** *7* (4), 665-671.

245. Chen, J.; Xue, H.; Yao, Y.; Yang, H.; Li, A.; Xu, M.; Chen, Q.; Cheng, R. Effect of Surfactant Concentration on the Complex Structure of Poly(N-isopropylacrylamide)/Sodium n-Dodecyl Sulfate in Aqueous Solutions. *Macromolecules* **2012,** *45* (13), 5524-5529.

246. Wang, X.; Li, L. How does the anionic surfactant SDS affect the association of hydrophobically end-modified PNIPAM chains in aqueous solution? *Polymer* **2016,** *88*, 123-132.

247. Daly, E.; Saunders, B. R. Temperature-dependent electrophoretic mobility and hydrodynamic radius measurements of poly(N-isopropylacrylamide) microgel particles: structural insights. *Physical Chemistry Chemical Physics* **2000,** *2* (14), 3187-3193.

248. Utashiro, Y.; Takiguchi, M.; Satoh, M. Zeta potential of PNIPAM microgel particles dispersed in water—effects of charged radical initiators vs. OH− ion adsorption. *Colloid and Polymer Science* **2017,** *295* (1), 45-52.

249. Wu, Y.; Wiese, S.; Balaceanu, A.; Richtering, W.; Pich, A. Behavior of Temperature-Responsive Copolymer Microgels at the Oil/Water Interface. *Langmuir* **2014,** *30* (26), 7660-7669.

250. Kutuzov, S.; He, J.; Tangirala, R.; Emrick, T.; Russell, T.; Böker, A. On the kinetics of nanoparticle self-assembly at liquid/liquid interfaces. *Physical Chemistry Chemical Physics* **2007,** *9* (48), 6351-6358.

251. Kinoshita, K.; Parra, E.; Needham, D. Adsorption of ionic surfactants at microscopic air-water interfaces using the micropipette interfacial area-expansion method: Measurement of the diffusion coefficient and renormalization of the mean ionic activity for SDS. *Journal of Colloid and Interface Science* **2017,** *504*, 765-779.

252. Bhushan, B.; Nosonovsky, M.; Jung, Y. C. Towards optimization of patterned superhydrophobic surfaces. *Journal of the Royal Society Interface* **2007,** *4* (15), 643-648.

253. Ward, A. F. H.; Tordai, L. Time-Dependence of Boundary Tensions of Solutions I. The Role of Diffusion in Time-Effects. *The Journal of Chemical Physics* **1946,** *14* (7), 453-461.

254. Adamson, A. W.; Gast, A. P. Physical chemistry of surfaces. **1967**.

255. Rotenberg, Y.; Boruvka, L.; Neumann, A. W. Determination of Surface-Tension and Contact-Angle from the Shapes of Axisymmetric Fluid Interfaces. *J Colloid Interf Sci* **1983,** *93*.

256. Berne, B. J.; Pecora, R. *Dynamic light scattering: with applications to chemistry, biology, and physics*; Courier Corporation2000.

257. Ma, H.; Luo, M.; Dai, L. L. Influences of surfactant and nanoparticle assembly on effective interfacial tensions. *Physical Chemistry Chemical Physics* **2008,** *10* (16), 2207-2213.

258. Geisel, K.; Isa, L.; Richtering, W. Unraveling the 3D Localization and Deformation of Responsive Microgels at Oil/Water Interfaces: A Step Forward in Understanding Soft Emulsion Stabilizers. *Langmuir* **2012,** *28* (45), 15770-15776.

259. Geng, J.; Pu, J.; Wang, L.; Bai, B. Surface charge effect of nanogel on emulsification of oil in water for fossil energy recovery. *Fuel* **2018,** *223*, 140-148.

260. Brugger, B.; Vermant, J.; Richtering, W. Interfacial layers of stimuli-responsive poly-(N-isopropylacrylamide-co-methacrylicacid) (PNIPAM-co-MAA) microgels characterized by interfacial rheology and compression isotherms. *Physical Chemistry Chemical Physics* **2010,** *12* (43), 14573-14578.

261. Nikolov, A.; Wasan, D. Wetting–dewetting films: The role of structural forces. *Advances in Colloid and Interface Science* **2014,** *206*, 207-221.

262. Hartland, G. V.; Grieser, F.; White, L. R. Surface potential measurements in pentanol–sodium dodecyl sulphate micelles. *Journal of the Chemical Society, Faraday Transactions 1: Physical Chemistry in Condensed Phases* **1987,** *83* (3), 591-613.

263. Sauerbrey, G. The use of quarts oscillators for weighing thin layers and for microweighing. *Z. Phys.* **1959,** *155*, 206-222.

264. Long, J.; Li, H. J.; Xu, Z. H.; Masliyah, J. H. Improving Oil Sands Processability Using a Temperature-Sensitive Polymer. *Energy & Fuels* **2011,** *25* (2), 701-707.

265. Li, P.; Ishiguro, M. Adsorption of anionic surfactant (sodium dodecyl sulfate) on silica. *Soil Science and Plant Nutrition* **2016,** *62* (3), 223-229.

266. Thibaut, A.; Misselyn-Bauduin, A. M.; Grandjean, J.; Broze, G.; Jérôme, R. Adsorption of an Aqueous Mixture of Surfactants on Silica. *Langmuir* **2000,** *16* (24), 9192-9198.

267. Vatanparast, H.; Shahabi, F.; Bahramian, A.; Javadi, A.; Miller, R. The Role of Electrostatic Repulsion on Increasing Surface Activity of Anionic Surfactants in the Presence of Hydrophilic Silica Nanoparticles. *Scientific Reports* **2018,** *8* (1), 7251.

268. García-Salinas, M. J.; Romero-Cano, M. S.; de las Nieves, F. J. Electrokinetic Characterization of Poly(N-isopropylacrylamide) Microgel Particles: Effect of Electrolyte Concentration and Temperature. *Journal of Colloid and Interface Science* **2001,** *241* (1), 280-285.

269. Tong, Z.; Zeng, F.; Zheng, X.; Sato, T. Inverse Molecular Weight Dependence of Cloud Points for Aqueous Poly(N-isopropylacrylamide) Solutions. *Macromolecules* **1999,** *32* (13), 4488-4490.

270. Zhang, Y.; Furyk, S.; Bergbreiter, D. E.; Cremer, P. S. Specific Ion Effects on the Water Solubility of Macromolecules: PNIPAM and the Hofmeister Series. *Journal of the American Chemical Society* **2005,** *127* (41), 14505-14510.

271. Koenig, M.; Rodenhausen, K. B.; Rauch, S.; Bittrich, E.; Eichhorn, K.-J.; Schubert, M.; Stamm, M.; Uhlmann, P. Salt Sensitivity of the Thermoresponsive Behavior of PNIPAAm Brushes. *Langmuir* **2018,** *34* (7), 2448-2454.

272. Kasongo, T.; Zhou, Z.; Xu, Z.; Masliyah, J. Effect of clays and calcium ions on bitumen extraction from athabasca oil sands using flotation. *The Canadian Journal of Chemical Engineering* **2000,** *78* (4), 674-681.

273. Ngang, H. P.; Ahmad, A. L.; Low, S. C.; Ooi, B. S. Preparation of thermoresponsive PVDF/SiO2-PNIPAM mixed matrix membrane for saline oil emulsion separation and its cleaning efficiency. *Desalination* **2017,** *408*, 1-12.

274. Kwok, M.-h.; Ngai, T. Emulsions stabilized by pH-responsive PNIPAM-based microgels: Effect of spatial distribution of functional carboxylic groups on the emulsion stability. *Journal of the Taiwan Institute of Chemical Engineers* **2018,** *92,* 97-105.

275. Binks, B. P.; Whitby, C. P. Nanoparticle silica-stabilised oil-in-water emulsions: improving emulsion stability. *Colloids and Surfaces A: Physicochemical and Engineering Aspects* **2005,** *253* (1), 105-115.

276. Binks, B. P.; Yin, D. Pickering emulsions stabilized by hydrophilic nanoparticles: in situ surface modification by oil. *Soft Matter* **2016,** *12* (32), 6858-6867.

277. Tamai, Y.; Aratani, K. Experimental study of the relation between contact angle and surface roughness. *The Journal of Physical Chemistry* **1972,** *76* (22), 3267-3271.

278. Morrow, N. R. The Effects of Surface Roughness on Contact Angle With Special Reference to Petroleum Rocovery *The journal of Canadian petroleum technology* **1975,** *14* (4), 42-53.

279. Koch, B. M. L.; Amirfazli, A.; Elliott, J. A. W. Wetting of Rough Surfaces by a Low Surface Tension Liquid. *The Journal of Physical Chemistry C* **2014,** *118* (41), 23777-23782.

280. Pilat, D. W.; Papadopoulos, P.; Schäffel, D.; Vollmer, D.; Berger, R.; Butt, H. J. Dynamic Measurement of the Force Required to Move a Liquid Drop on a Solid Surface. *Langmuir* **2012,** *28* (49), 16812-16820.

281. Gao, N.; Geyer, F.; Pilat, D. W.; Wooh, S.; Vollmer, D.; Butt, H.-J.; Berger, R. How drops start sliding over solid surfaces. *Nature Physics* **2017,** *14*, 191.

282. Koch, B. M. L.; Amirfazli, A.; Elliott, J. A. W. Modeling and Measurement of Contact Angle Hysteresis on Textured High-Contact-Angle Surfaces. *The Journal of Physical Chemistry C* **2014,** *118* (32), 18554-18563.

283. Koch, B. M. L.; Elliott, J. A. W.; Amirfazli, A. Study of Model Superoleophobic Surfaces Fabricated with a Modified Bosch Etch Method. *Langmuir* **2014,** *30* (46), 14039-14047.

284. Extrand, C. W.; Gent, A. N. Retention of liquid drops by solid surfaces. *Journal of Colloid and Interface Science* **1990,** *138* (2), 431-442.

285. Furmidge, C. G. L. Studies at phase interfaces. I. The sliding of liquid drops on solid surfaces and a theory for spray retention. *Journal of Colloid Science* **1962,** *17* (4), 309-324.

286. Goodwin, R.; Rice, D.; Middleman, S. A model for the onset of motion of a sessile liquid drop on a rotating disk. *Journal of Colloid and Interface Science* **1988,** *125* (1), 162-169.

287. Dussan V, E. B.; Chow, R. T.-P. On the ability of drops or bubbles to stick to non-horizontal surfaces of solids. *Journal of Fluid Mechanics* **1983,** *137*, 1-29.

288. Arjmandi-Tash, O.; Kovalchuk, N. M.; Trybala, A.; Kuchin, I. V.; Starov, V. Kinetics of Wetting and Spreading of Droplets over Various Substrates. *Langmuir* **2017,** *33* (18), 4367-4385.

289. Frank, X.; Perré, P. Droplet spreading on a porous surface: A lattice Boltzmann study. *Physics of Fluids* **2012,** *24* (4), 042101.

290. Lee, K. S.; Ivanova, N.; Starov, V. M.; Hilal, N.; Dutschk, V. Kinetics of wetting and spreading by aqueous surfactant solutions. *Advances in Colloid and Interface Science* **2008,** *144* (1), 54-65.